EPFL

Thèse n° 9639

Single molecule fluorescence and phosphorescence studies using a scanning tunneling microscope

Présentée le 15 septembre 2022

Faculté des sciences de base
Laboratoire de science à l'échelle nanométrique
Programme doctoral en physique

pour l'obtention du grade de Docteur ès Sciences

par

Abhishek GREWAL

Acceptée sur proposition du jury

Prof. O. Yazyev, président du jury
Prof. K. Kern, directeur de thèse
Dr G. Schull, rapporteur
Dr S. Stepanow, rapporteur
Prof. H. Dil, rapporteur

École polytechnique fédérale de Lausanne

2022

To my grandparents, who happened to be my first teacher.

Abstract

This thesis investigates novel single-molecule luminescence phenomena at their inherent, sub-molecular length scale. The flexibility afforded by molecular design and the relative ease of device fabrication by thin films makes organic molecules attractive for optoelectronic and semiconductor applications. The microscopic understanding of luminescence processes will be crucial for their continued improvement.

In this work, a scanning tunneling microscope (STM) is combined with optical spectroscopy and Hanbury Brown and Twiss interferometry to perform topographic imaging, electronic characterization, and analysis of vibrational mode excitations and emission statistics of molecular luminescence, all at the ultimate atomic scale. Moreover, the precise STM tip positioning allows tuning of the coupling between the molecular exciton and the tip-induced plasmon with sub-molecular spatial control, which is key to the decay rate enhancement and thus emission intensity enhancement of molecular phosphors.

A prototypical platinum (II) phthalocyanine (PtPc) molecule, decoupled from a metal substrate by a thin insulating film of NaCl, provides a model platform for examining STM-induced bipolar fluorescence, phosphorescence, and energy upconversion electroluminescence (UCEL). First, an STM investigation of only the ionic insulator NaCl demonstrates that both valence and conduction bands are of anionic Cl^- character. This is relevant for the coupling between the molecule and the metal substrate. Theoretical considerations reveal a dominant contribution from energetically low-lying molecular orbitals under certain conditions. Surprisingly, these orbitals play a more critical role for tunneling energies in the molecular transport gap than the frontier orbitals. STM topography imaging of the molecules at small voltages perfectly confirms the results of this new theoretical description that can explain tunneling at small voltages, where molecules are nominally not conducting.

Voltage and polarity of fluorescence onsets can be controlled using different metal substrates because their different work functions tune the energy alignment of the molecular orbitals with respect to the substrate Fermi level. For PtPc atop an Au(111) substrate, fluorescence is observed at both voltage polarities, even under tunneling conditions where UCEL occurs. This remarkable behavior allows the testing of different emission mechanisms and reveals new general guidelines for designing future optoelectronic devices. An analysis of photon emission statistics from a single molecule under UCEL conditions refutes previously proposed excitation mechanisms. It guides theory towards a novel mechanism, which is briefly introduced in the thesis.

PtPc atop NaCl on Ag(111) exhibits fluorescence, and in this thesis, its phosphorescence is also observed by local excitation in the STM. Electronic characterization reveals a simultaneous voltage onset of both types of emission. Phosphorescence is moreover detected using tip-enhanced resonant photoexcitation of the singlet state. Since direct optical excitation of the triplet state is forbidden, this observation is the first demonstration of intersystem crossing in a tip-controlled single-molecule experiment. Exciton-plasmon coupling can be varied by fine positioning the tip in proximity to the molecule. This allows tuning the triplet emission (phosphorescence) intensity through control of the singlet lifetime. These findings are directly transferrable to highly topical phosphorescent OLEDs that employ plasmonic enhancement.

The phenomenon of plasmonic antibunching is discovered for electron tunneling from a few monolayer thick C_{60} film to the STM tip. The layer thickness and the applied voltage control the sequential tunneling of charges by a Coulomb blockade mechanism. This mechanism eventually causes the emission of one photon at a time. Such a plasmonic source allows for a higher single-photon emission rate than an individual molecule. A close analysis finds that the tip-induced static electric field locally distorts the band structure and pulls discrete states out of the C_{60} conduction band, favoring the observed behavior. The design principles for other semiconducting films are discussed, suggesting a quest for similar nanostructured single-photon emitters.

Keywords: STM-induced luminescence, single-molecule fluorescence and phosphorescence, upconversion electroluminescence, exciton-plasmon coupling, bipolar emission, second-order intensity correlations, single-photon sources, NaCl electronic structure, phthalocyanine, C_{60}

Zusammenfassung

Diese Doktorarbeit untersucht die Lumineszenz einzelner Moleküle auf der mit ihnen verbundenen submolekularen Längenskala. Organische Moleküle sind aufgrund ihrer Vielseitigkeit und der mit ihrer Hilfe relativ einfachen Herstellung von Bauelementen für optoelektronische und halbleiterbasierte Anwendungen interessant. Das Verständnis des Lumineszenzprozesses auf mikroskopischer Skala ist entscheidend für weitere Optimierungen.

In dieser Arbeit werden Rastertunnelmikroskopie (engl. scanning tunneling microscopy, STM), optische Spektroskopie und Hanbury Brown-Twiss Interferometrie zusammengeführt, um auf der ultimativen atomaren Skala topographische Bilder, elektronische Eigenschaften, die Anregung von Schwingungsmoden, sowie die Emissionsstatistik eines lumineszierenden Moleküls zu messen. Darüber hinaus lässt sich durch die genaue Positionierbarkeit der STM Spitze die Kopplung zwischen molekularem Exziton und spitzeninduziertem Plasmon einstellen, was entscheidend für eine verstärkte Zerfallsrate und damit Emissionsintensität des molekularen Phosphors ist.

Ein prototypisches Platin-(II)-Phthalozyanin (PtPc) Molekül, das durch einen isolierenden NaCl Films vom Metallsubstrat entkoppelt wird, stellt die Plattform für Untersuchungen mittels STM-induzierter, bipolarer Fluoreszenz, Phosphoreszenz und energieaufwärtskonvertierender Elektrolumineszenz (engl. energy up-conversion electroluminescence, UCEL) dar. Zuerst wird anhand einer STM Untersuchung allein des ionischen Isolator NaCl gezeigt, dass sowohl Valenz- wie auch Leitungsband anionischen Cl^- Charakter besitzen. Dies ist für die Kopplung zwischen Molekül und Metallsubstrat maßgeblich. Theoretische Betrachtungen offenbaren den unter bestimmten Bedingungen wesentlichen Beitrag energetisch niedriger Molekülorbitale. Überraschenderweise spielen diese Orbitale bei Tunnelenergien innerhalb der Transportlücke eine entscheidendere Rolle als die Frontorbitale. STM-Topographiebilder bei niedrigen Spannungen bestätigen exakt die neue theoretische Beschreibung des Tunnelprozesses bei Spannungen, bei denen die Moleküle eigentlich nicht leiten.

Größe und Vorzeichen der Spannung, bei der die Fluoreszenz einsetzt, kann durch Verwendung verschiedener Metallsubstrate beeinflußt werden, weil ihre unterschiedliche Austrittsarbeit die Energie der Molekülorbitale gegenüber der Fermienergie des Substrats verschiebt. Für PtPc auf einem Au(111) Substrat wird Fluoreszenz bei beiden Spannungsvorzeichen beobachtet, und das sogar unter Tunnelbedingungen, bei denen UCEL auftritt. Dieses bemerkenswerte Verhalten erlaubt die Überprüfung verschiedener Emissionsmechanismen und führt zu allgemeinen Leitlinien für die zukünftige Entwicklung optoelektronischer Elemente. Die Photonenemissionsstatistik eines einzelnen Moleküls unter UCEL Bedingungen

schließt bisher vorgeschlagene Anregungsmechanismen aus und führt die Theorie zu einem neuen Mechanismus, der in der Arbeit kurz eingeführt wird.

PtPc auf NaCl bedecktem Ag(111) emittiert Fluoreszenz. In dieser Arbeit wird darüberhinaus auch Phosphoreszenz nach lokaler Anregung mit dem STM beobachtet. Die Untersuchung der elektronischen Eigenschaften zeigt, dass beide Emissionsarten bei derselben Spannung einsetzen. Darüberhinaus wird Phosphoreszenz auch nachgewiesen, wenn eine spitzenverstärkte optische Anregung in Resonanz mit dem Singlet-Zustand erfolgt. Da eine direkte optische Anregung des Triplet-Zustands verboten ist, handelt es sich damit um die erste Beobachtung des Übergangs vom Singlet- zum Triplet-System (engl. intersystem crossing) in einem mit einer Spitze gesteuerten Einzelmolekülexperiment. Die Exzitonen-Plasmonen Kopplung kann durch kleine Positionsänderungen der Spitze nahe am Molekül verändert werden. Dadurch wird die Intensität der Triplet-Emission (Phosphoreszenz) über eine Veränderung der Singlet-Lebensdauer gesteuert. Die Ergebnisse können unmittelbar auf hochaktuelle phosphoreszierende OLEDs übertragen werden, die auf plasmonischer Verstärkung basieren.

Das Phänomen plasmonischer Antibündelung (engl. antibunching) wird im Tunnelprozess zwischen einem mehrlagigen C_{60} Film und der STM Spitze entdeckt. Die Filmdicke und die angelegte Spannung bewirken durch eine Coulomb-Blockade ein sequenzielles Tunneln von Ladungen. Dieser Mechanismus bewirkt schließlich die Aussendung von nur einem Photon zu einem gegebenen Zeitpunkt. Solch eine plasmonische Lichtquelle stellt eine höhere Einzelphotonenemissionsrate bereit als ein einzelnes Molekül. Die genaue Analyse zeigt, dass das statische elektrische Feld der Spitze die Bandstruktur in einem räumlich begrenzten Bereich verzerrt und einzelne Zustände aus dem C_{60} Leitungsband herauszieht, was das beschriebene Emissionsverhalten begünstigt. Das Prinzip wird auch für andere Halbleiterfilme erörtert und eine Suche nach ähnlichen nanostrukturierten Emittern vorgeschlagen.

Stichwörter: STM-induzierte Lumineszenz, Einzelmolekülfluoreszenz und -phosphoreszenz, energieaufwärtskonvertierende Elektrolumineszenz, Exziton-Plasmon Kopplung, bipolare Emission, Korrelation zweiter Ordnung, Einzelphotonenquellen, elektronische Struktur von NaCl, Phthalocyanin, C_{60}.

Contents

List of Figures

Acronyms

CB	conduction band
CCD	charged-couple device
DFT	density functional theory
DOS	density of states
fcc	face-centered cubic
FWHM	full width at half maximum
H_2Pc	free-base phthalocyanine
HBT	Hanbury Brown-Twiss
hcp	hexagonal close-packed
HOMO	highest occupied molecular orbital
IC	internal conversion
IDOS	integrated density of states
IES	inelastic scattering
IETS	inelastic electron tunneling spectroscopy
ISC	intersystem crossing
LUMO	lowest unoccupied molecular orbital
ML	monolayer
NEGF	nonequilibrium Green's function
OLEDs	organic light emitting diodes
PTCDA	3,4,9,10-perylenetetra-carboxylicdianhydride
PtOEP	platinum octaethylporphyrin
PtPc	platinum (II) phthalocyanine
SEM	scanning electron microscope
SNOM	scanning near-field optical microscopy
SOC	spin-orbit coupling
SPAD	single photon avalanche diodes
SPP	surface plasmon polariton
STM	scanning tunneling microscopy
STM-EL	STM-induced electroluminescence

STM-PL STM-induced photoluminescence

STML STM-induced luminescence

STS scanning tunneling spectroscopy

TCSPC time-correlated single photon counting

TD-DFT time-dependent density functional theory

TERS tip-enhanced Raman spectroscopy

TTA triplet-triplet annihilation

UCEL up-conversion electroluminescence

UHV ultra high vacuum

VB valence band

X-P exciton-plasmon

Introduction

When a molecule absorbs energy, it moves from its original (ground) state to a higher-energy (excited) state. Fluorescence and phosphorescence are examples of luminescence phenomena in which a molecule emits light from an electronically excited state. A physical (for example, absorption of light or electric field), mechanical (friction), or chemical mechanism can lead to such an excitation. Stokes[1] and Becquerel[2], among others[3,4], provided the first, timescale-related, interpretation suggesting that fluorescence is instantaneous, occurring only as long as the excitation lasts, while phosphorescence is much longer lived. Later, spectroscopic studies[5,6] combined with the determination of quantum yield[7] of fluorescent solutions and dyes allowed a deeper understanding of the phenomena. With the emergence of quantum theory[8,9] in the early twentieth century, the phenomenological description of the two emission processes improved. It came to light that phosphorescence involves a change in the spin-multiplicity of the molecule, typically from the triplet to the singlet or vice versa, while fluorescence does not[10–13]. Since a spin-flip is forbidden for optical excitation, for a singlet ground state, the lifetime of the lowest excited triplet state is a few orders of magnitude longer than that of the lowest excited singlet state.

Further developments in the understanding of fluorophores and chemical engineering enabled tagging of different cell organelles with dyes, thus making them emit light in the visible range at molecular length scales. This allowed imaging of their distribution, location, transport characteristics, and interactions with other biomolecules[14], revolutionizing the field of cell biology. However, better known is their use as light sources. Becquerel's idea of applying various luminescent materials as a coating to electric discharge tubes later led to the development of commercial fluorescent lamps[15]. Not too long after, the light emitting diode, which converts electrical energy to light, was invented. Developments in production techniques, besides optimization of their composition and structure, transformed lighting and display technologies[16]. Lower power consumption, longer lifetime, improved physical robustness, smaller size, and faster switching capability than incandescent or fluorescence lamps make LEDs omnipresent. For example, the brightness achieved (for 800 lumens) by a 60 watt incandescent light bulb requires an almost ten times lower power of ≈ 8 watts for a LED[17], and this without emission of any toxic mercury vapor associated with recycling of fluorescent lamps.

LEDs composed of organic molecules as light emitters allow even lower power consumption. The relative ease of producing thin molecular films enables compact design, opening many avenues. Their further development may make recently developed flexible, transparent, and wearable technologies mainstream in the near future. Just over the last two decades, organic light emitting diodes (OLEDs) have been incorporated into billions of commercial products[18]. Nevertheless, they may still be improved in terms of efficiency and stability.

The operation of an OLED involves the formation of excitons in organic molecules when a voltage is applied. Because of spin-statistics, the energy transfer to the emitting layer leads to the formation of spin-singlet and spin-triplet excitons in a 1:3 ratio[19]. Given that, it is straightforward that effective use of triplet states for light production is necessary to achieve high electrical energy to the light conversion efficiency of OLEDs[20]. Lowering the operating voltage can also reduce the power consumption of these devices. As a result of the exchange interaction, the triplet state typically has lower energy than the singlet, and thus, solely exciting the triplet emission allows for reducing power consumption[21]. However, the triplet excited state is long-lived[22] making the device vulnerable to degradation by oxidation. Here as well, the inherent flexibility afforded by molecular design allows manipulating the excited state levels to enhance the energy transfer from the triplet to the singlet ground state and increase its radiative rate at the same time[23].

Plasmonic enhancement of excitonic emission at a metal-dielectric interface can significantly reduce the lifetime of the excitons[24]. This typically leads to quenching, a process in which the excitation is lost to the environment in the form of heat instead of light generation. However, intelligent control of the spacing between the metal and the molecule, on the order of a few nanometers, allows accelerating the exciton decay in a controlled manner and has recently been shown to enhance the device lifetime of OLEDs[25] greatly. This highlights the importance of precise characterization at the length scale of a molecule ($\sim$ 1 to 2 nm).

Because vibrational frequencies are specific to a molecule's chemical bonds and symmetry, optical spectroscopy provides a fingerprint for their identification. For a light source of a given wavelength, the spatial resolution is diffraction-limited to some fraction of the wavelength[26] (a few hundred nanometers for visible light). Thus, the electronic and optical information is averaged over an ensemble. As a result, one must rely on theoretical predictions and visualizations to assign the spectroscopic data to specific processes or molecules. In the 1990s, Moerner and Orrit[27–29], using isolated molecules in matrices, could achieve single-molecule sensitivity, paving the way to future single-molecule detection and spectroscopy techniques. Despite recent developments in super-resolution microscopy techniques[27], their spatial resolution has been limited to approximately ten nanometers, still about five times larger than the size of a single molecule. This becomes problematic, especially at dimensions in the range of one nanometer, where quantum mechanics dominates.

On the other hand, a scanning tunneling microscope (STM)[30,31] combined with an optical detection setup, routinely allows topographic imaging, electronic and optical characterization, and electric field control, all with the ultimate, sub-molecular scale resolution[32–34]. Combining precise know-how of the electronic structure and the molecular emission allows scrutiny of the suggested mechanisms behind different emission phenomena and the discovery of new processes. The ability to manipulate the interaction between the molecule and its nano-environment enables the control of efficiencies and onset voltage of molecular emitters. The single-molecule nature of these experiments implies that relatively simple theoretical models can be used to describe novel emission phenomena. Single-photon sources, like single molecules or vacancy defects[35], can also be studied at their true length-scale

with second-order correlation measurements of the emitted photon field. The conversion of electrical excitation to light occurs at a timescale limited by the exciton lifetime (few nanoseconds). Thus, the photons are expected to be emitted one by one with a minimum time delay of the same order[36]. Such light sources have applications in quantum key distribution, quantum repeaters, and quantum information science making a detailed study of their electrical and emission properties imperative.

Organization of the thesis

This thesis reports on the experiments performed to elucidate molecular excitation mechanisms for novel emission processes like STM-induced fluorescence and phosphorescence and up-conversion electroluminescence. Combining atomic-scale electronic and laser excitation with optical spectroscopy and photon intensity correlation measurements provides a rich toolkit for analyzing light emission from a single molecule and tip-induced discrete states in a molecular thin film.

Chapter 1 briefly introduces the background of scanning tunneling microscopy and its associated luminescence from the tunneling junction. How the tunneling electron or the incident light in the tip-sample gap leads to excitation of the molecule and the effect of material properties is also reported. In addition, the current state-of-the-art in the interpretation of various emission processes observed in single-molecule studies using this technique is reviewed.

Few monolayer thick NaCl islands are routinely used to limit the interaction between the system of interest, the molecule, and the underlying metal substrate. This provides access to the intrinsic optoelectronic properties of the molecule while still allowing smooth STM operation, which requires at least a weakly conducting substrate. An understanding of the molecule's interaction with the metal surface, mediated via NaCl, is thus the key to explaining more complex phenomena. Chapter 2 shows that in contrast to the textbook picture, the STM topography of the conduction and valence bands suggests that Cl^- anions are mainly responsible for electron conduction at either voltage polarity. The theoretical consideration[1] that the large Madelung potential reverses the order of the Cl^- 4*s* and Na^+ 3*s* levels helps to reconcile the anionic character of the conduction band for the alkali halide. Given that, the coupling of metal states through Cl^- ions of NaCl affects the tunneling through the molecule adsorbed on top of NaCl. The idea that molecular orbitals much lower in energy than the frontier orbitals participate in conduction at voltages in the transport gap of a molecule is briefly introduced and the consequences for topography imaging at voltages close to the Fermi energy are discussed. These findings suggest that it is essential to reconsider previously proposed mechanisms for processes where electron tunneling through the transport gap plays a central role.

Chapter 3 talks about how the energy level alignment of molecular orbitals with respect

[1]The tight-binding calculations were planned and carried out by Olle Gunnarsson, Max Planck Institute for Solid State Research, Germany.

to tip and sample Fermi energy decides what mechanism leads to the electronic excitation of the emission. Since the minimum voltage which allows excitation and the associated emission efficiency rely on the microscopic mechanism at play, such a study provides ways to tune these parameters. Electronic characterization of a single molecule in a controlled environment facilitates having a detailed discussion of these mechanisms.

The quantum statistics of the molecular emission at sample voltages lower than the singlet state energy are analyzed using photon intensity correlation measurements. Recent studies[37,38] suggest that excitation due to electron tunneling through the transport gap of the molecule may be up-converted by a subsequent tunneling electron. Since the onset of this process is at the energy of the spin-triplet state, it is proposed that it acts as a relay state for upconversion. In light of the new interpretation of tunneling through the transport gap and observations from correlation measurements, a new mechanism based on perturbation theory arguments[1], is proposed for UCEL from a single molecule.

Chapter 4 reports on the observation of phosphorescence of a single platinum (II) phthalocyanine (PtPc) molecule using STM-induced electroluminescence (STM-EL). The ability to precisely position the tip allows atomic-scale control over charge injection and the interaction between the molecule and the tip. It is shown that a decrease in dipole coupling increases the amount of intersystem crossing and thus phosphorescence intensity. Using STM-induced photoluminescence (STM-PL), an energy tunable laser resonantly excites the spin-singlet state of the molecule, and an intense emission from the vibrations involved in the transition is observed[2]. Spectrally-resolved spatial mapping of emission intensity reveals different patterns depending on the symmetry of the vibrational modes, showing the potential of this technique to investigate intrinsic vibrational and electronic properties at a single-molecule level. In the resonant photoluminescence spectrum, a weak triplet emission is also observed. Since direct excitation of the spin-triplet state is forbidden for incident light, intersystem crossing in a tip-controlled single-molecule experiment is reported for the first time.

Chapter 5 shows that the tip can be used as a probe and as a source of local perturbation. Theoretical calculations[1] show that for an applied voltage of a few volts, the electric field generated at the tunneling junction can induce discrete states in a C_{60} molecular film, which results in a sharp peak in the differential conductance of the molecule. We suggest that the discretization of current flow due to a Coulomb blockade triggers the excitation of nanocavity plasmonic modes, which are themselves excited one at a time. Thus, the associated photon emission also occurs one by one, which is confirmed by photon intensity correlation measurements. This design principle of quantum control can be generalized and applied to other wide bandgap narrowband materials.

In the end, it is concluded that the combination of optics with the versatile capabilities of the STM provides a unique platform for studying and manipulating the emission properties of isolated emitters at an atomic scale. The insights gained from these novel experiments

[2]The experimental work presented in this Chapter was performed in collaboration with Prof. Yousoo Kim at Surface and Interface Science Laboratory (表面界面科学研究室), RIKEN (理化学研究所), Japan

now provide new general guidelines for future optoelectronic devices. The effect of exciton-plasmon coupling of molecular fluorescence and phosphorescence is universal and thus transferable to plasmonic OLEDs[25], bioimaging[39,40], and biosensing[41,42], where exciton dynamics play a central role. As an outlook, some suggestions for future work that builds upon the research presented in this thesis are discussed. First STM-EL measurements of platinum (II) octaethylporphyrin molecule show great promise for future studies of intersystem crossing at the sub-molecular level. In addition, molecular-beam epitaxy of molybdenum disulfide[43] atop hexagonal-boron nitride on Pt(111) has been successful. Still, further optimization for the material or the vacancy defects is needed to reveal their intrinsic emission.

1 Concepts and techniques

This thesis documents the use of scanning tunneling microscopy (STM) to induce and study luminescence from a single molecule. This chapter introduces the fundamental principles of STM, scanning tunneling spectroscopy (STS), and STM-induced luminescence (STML) in metallic tunnel junctions and electronically decoupled single molecules. We further differentiate between electronic and optical excitation mechanisms for two-level systems in a plasmonic nanocavity and highlight how it differs from traditional spectroscopy techniques. We also briefly introduce our home-built experimental setup, the so-called *Photon-STM*, and the sample and tip preparation methods.

1.1 Scanning tunneling microscopy

The STM was invented in 1982 by Gerd Binnig, Heinrich Rohrer, Christoph Gerber, and Edmund Weibel[30,44,45]. Based on the quantum mechanical tunneling effect[9], it allowed imaging of surfaces at the atomic scale[30,46,47]. Binnig and Rohrer shared the 1986 Nobel Prize in Physics for their design of the STM[48].

The STM comprises a sharp conducting tip and sample which is scanned with respect to the fixed tip. The sample sits on piezoelectric actuators (piezos), which can position the

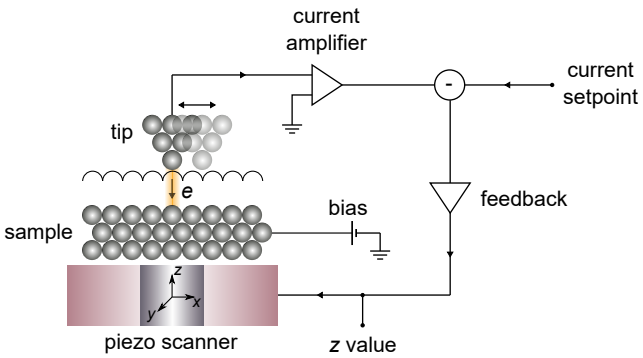

Figure 1.1 — Typical STM experiment. The sample is directly mounted on piezoelectric actuators that control lateral and vertical position of the sample at picometer-scale. Using an electronic feedback loop STM can be operated in the constant current mode. The tunnel gap is controlled to maintain the tunneling current setpoint, allowing the sample to be rastered without coming in contact with the tip.

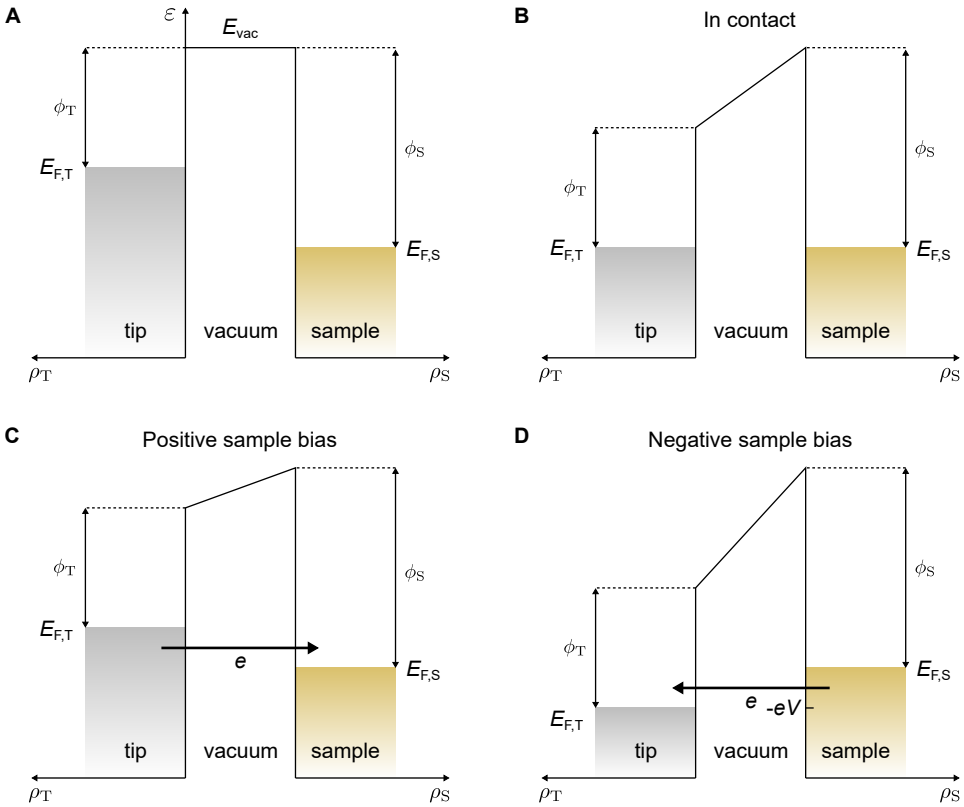

Figure 1.2 — Energy alignment in STM. (A) Before tip and sample are connected in a circuit, their vacuum levels E_{vac} align, while their Fermi levels $E_{F,T}$ and $E_{F,S}$, are different depending on their respective work functions ϕ_T and ϕ_S. ρ_T and ρ_S are the tip and sample density of states, respectively. (B) In the tunneling regime, charges flow to align the Fermi levels by rigidly shifting the band structures. (C) Energy alignment at positive and (D) negative sample bias voltage.

sample in x-, y- and z-direction with sub-Å resolution. The x- and y-piezos scan the sample to obtain an image, while the z-piezo controls the tunnel gap. The tip and sample distance can be brought in the range of a few Å using the z-piezo. In this range, the wavefunctions of the tip and sample overlap and form a metal-vacuum-metal tunnel junction. When a voltage V is applied to the sample, the electrons can tunnel through the vacuum barrier resulting in a tunneling current I_T. The tunnel current can be measured as a function of the (x, y) location, the z-height, and the sample voltage V, enabling topographic imaging and spectroscopy at unprecedented resolution. Figure 1.1 schematically illustrates a typical STM experiment.

As mentioned earlier, the tip and sample are held a few Å from each other to enable electron tunneling across the vacuum gap. When the tip is further apart from the sample, their vacuum energy levels (E_{vac}) are aligned and their respective Fermi levels (tip: $E_{F,T}$ sample: $E_{F,S}$) are distinct by virtue of different tip and sample work functions ϕ_T and ϕ_S, respectively (Fig. 1.2A). As the tip and sample gap approaches a few Å, electrical contact is formed, leading to the Fermi level alignment as shown in Fig. 1.2B. The vacuum levels are now out of alignment leading to a trapezoidal potential barrier. In the STM employed in this thesis, the tip is held to virtual ground while the voltage is applied to the sample. When a positive sample voltage $+V$ is applied with respect to the tip, this raises the tip Fermi level allowing electrons to tunnel from filled states of the tip to unoccupied states of the sample

(see fig. 1.2C). Inversely, at negative sample bias voltage $-V$, the tip Fermi level is shifted below the sample Fermi level allowing electrons to tunnel from the sample to the tip (fig. 1.2D).

Using the framework of time-dependent perturbation theory to treat the current flow between the tip and the sample for states of energy ε for negative sample bias voltage $-V$, the tunneling current due to flow of electrons from filled states of the sample to the empty states of the tip (as in fig. 1.2D) can be written as:

$$I_{\mathrm{S}\to\mathrm{T}} = -2e \cdot \frac{2\pi}{\hbar}|M|^2(\rho_{\mathrm{S}}(\varepsilon)\cdot f(\varepsilon))(\rho_{\mathrm{T}}(\varepsilon+eV)\cdot[1-f(\varepsilon+eV)]) \tag{1.1}$$

where the factor 2 is due to the spin of the electron, $-e$ is the electron charge, $|M|^2$ is the tunneling matrix element, and $f(\varepsilon)$ is the Fermi-Dirac distribution:

$$f(\varepsilon) = \frac{1}{1+\exp(\varepsilon/\kappa_B T)} \tag{1.2}$$

Similarly, the small component of tunneling current due to tunneling from tip to sample across the vacuum barrier can be written as:

$$I_{\mathrm{T}\to\mathrm{S}} = -2e \cdot \frac{2\pi}{\hbar}|M|^2(\rho_{\mathrm{T}}(\varepsilon+eV)\cdot f(\varepsilon+eV))(\rho_{\mathrm{S}}(\varepsilon)\cdot[1-f(\varepsilon)]) \tag{1.3}$$

Then the total tunneling current from sample to tip over all energies ε is:

$$I = -\frac{4\pi e}{\hbar}\int_{E_{\mathrm{F,T}}}^{\infty}|M|^2\rho_{\mathrm{S}}(\varepsilon)\rho_{\mathrm{T}}(\varepsilon+eV)\{f(\varepsilon)[1-f(\varepsilon+eV)]-[1-f(\varepsilon)]f(\varepsilon+eV)\}\mathrm{d}\varepsilon \tag{1.4}$$

Considering that the base temperature of the STM employed in this thesis is $T = 4.3$ K, the Fermi-Dirac function is well approximated by a Heaviside function for bias voltages of the order greater than few meV. Thus, the only contribution to tunneling current is from the electrons occupying the states in the energy range $-eV < \varepsilon < 0$.

$$I \approx -\frac{4\pi e}{\hbar}\int_{-eV}^{0}|M|^2\rho_{\mathrm{S}}(\varepsilon)\rho_{\mathrm{T}}(\varepsilon+eV)\mathrm{d}\varepsilon \tag{1.5}$$

Thus, the total tunneling current is a convolution of tip and sample density of states in the energy range given by the sample bias voltage. Additionally, if the tip is assumed to have a flat density of states in the given energy range, $\rho_{\mathrm{T}}(\varepsilon+eV)\to\rho_{\mathrm{T}}(0)$.

$$I \approx \frac{4\pi e}{\hbar}\rho_{\mathrm{T}}(0)\int_{-eV}^{0}|M|^2\rho_{\mathrm{S}}(\varepsilon)\mathrm{d}\varepsilon \tag{1.6}$$

While treating metal-insulator-metal junctions, John Bardeen introduced the following formalism to obtain a quantitative expression for the tunneling current[49]. In this case, the tip and the sample are treated such that they can be regarded as separate entities, not influenced

by the tail of the wave function from the other. This assumption suggests that the matrix element will be a constant, independent of the energy difference between the two sides.

$$I \approx \frac{4\pi e}{\hbar}|M|^2 \rho_T(0) \int_{-eV}^{0} \rho_S(\varepsilon)\mathrm{d}\varepsilon \tag{1.7}$$

It should be noted that the above discussion is only valid in the limit of small sample bias ($eV \ll \phi$). For a large bias, comparable to sample and tip work functions, the effective barrier height for high and low energy electrons to tunnel across the vacuum barrier would be different, implying that matrix elements will be energy and bias dependent.

In the small applied bias voltage limit, the trapezoidal vacuum barrier can be assumed to be a square (for $\phi_T \approx \phi_S$). Then, approximating the solution using WKB method[50] implies that tunneling matrix element is given by:

$$|M|^2 = \exp(-2\alpha z), \text{ where } \alpha = \frac{\sqrt{2m\phi}}{\hbar} \tag{1.8}$$

where m is the mass of the electron, z is the effective width of the potential barrier, $\hbar$ is the reduced Planck's constant, and ϕ is the height of the barrier, given by the combined work function of the tip and sample materials. Thus the tunneling current becomes

$$I \propto \exp\left(-2z\frac{\sqrt{2m\phi}}{\hbar}\right) \tag{1.9}$$

and consequently, the slope of $\ln I$ versus z can be used to determine ϕ. For a gold sample and tip, which is most commonly used in our experiments, $\phi = 5.3$ eV[51] and thus the decay constant $\alpha \approx 1.2$ Å^{-1}, suggesting that tunneling current decays roughly an order of magnitude per Å increase in the tip-sample gap. The approximately exponential dependence of tunneling current on z-height plays a pivotal role in atomic resolution achieved by STM. However, the same exponential decay makes a determination of the absolute tip-sample gap difficult.

From this discussion it follows that the tunneling current can be well-approximated by

$$\boxed{I \approx \frac{4\pi e}{\hbar} \cdot \exp -z\frac{\sqrt{8m\phi}}{\hbar} \cdot \rho_T(0) \int_{-eV}^{0} \rho_S(\varepsilon)\mathrm{d}\varepsilon} \tag{1.10}$$

An extended discussion of STM fundamentals, for example treatment of tip effects using Tersoff and Hamman approximation[52], can be found in a textbook by Julian Chen[31].

Topography

The sample is scanned at fixed sample bias to determine the sample topography. At the same time, a feedback loop controls the tip-sample gap z to maintain a constant tunneling current, the so-called *constant current mode*. By calibrating the voltage applied to the z piezo

to traverse over a feature of known dimension, we can record the corresponding applied voltage to map the topography of the surface. From the discussion above, it follows that in constant current mode, STM records the contour of the sample density of states (DOS) that decays exponentially in the vacuum.

Scanning tunneling spectroscopy

From equation 1.10, at a given tip (x, y) position for a constant tip-sample gap z at negative sample bias voltage $-V$,

$$I = I_0 \int_{-eV}^{0} \rho_S(\varepsilon) \mathrm{d}\varepsilon \tag{1.11}$$

Thus, by varying bias voltage we can acquire integrated density of states (IDOS) in the bias voltage range. A numerical derivative of IDOS could then be used to obtain DOS. In practice a lock-in amplifier is used to record DOS. The lock-in amplifier modulates the applied bias voltage by a small modulation voltage $\mathrm{d}V$, and by measuring the current modulation $\mathrm{d}I$ signal at the same, chosen, frequency we can obtain the quantity $\mathrm{d}I/\mathrm{d}V$ which corresponds to DOS,

$$\boxed{\frac{\mathrm{d}I}{\mathrm{d}V} \propto \rho_S(\varepsilon)} \tag{1.12}$$

Using lock-in amplifier reduces $1/f$ noise and does not require spectral purity (for e.g., 50 Hz noise does not influence the results).

$\mathrm{d}I/\mathrm{d}V$ mapping

Leveraging the scanning ability of STM, one can spatially map the differential conductance of a distinct resonance, the so-called $\mathrm{d}I/\mathrm{d}V$ *map*. With a fixed sample bias voltage corresponding to the energetic position of the resonance, we raster the sample to obtain a spatial map of the electrons in the resonance state.

Alternatively, the STM can be operated in a *constant height mode*, where the scanning occurs with a fixed tip-sample distance. In this mode, the sample IDOS at a fixed distance from the surface is mapped.

STS in a double barrier junction

STS is a versatile technique and can be used to study the electronic states of metals[53], molecules[54], and semiconductors[55]. For the case of a single molecule, STS allows characterization of their electronic structure by spatially resolving their orbitals. When a molecule is adsorbed atop a metallic substrate, due to hybridization with the underlying substrate, the molecular electronic levels are broadened. In 2003, Qiu *et al.*[56] found that ultrathin

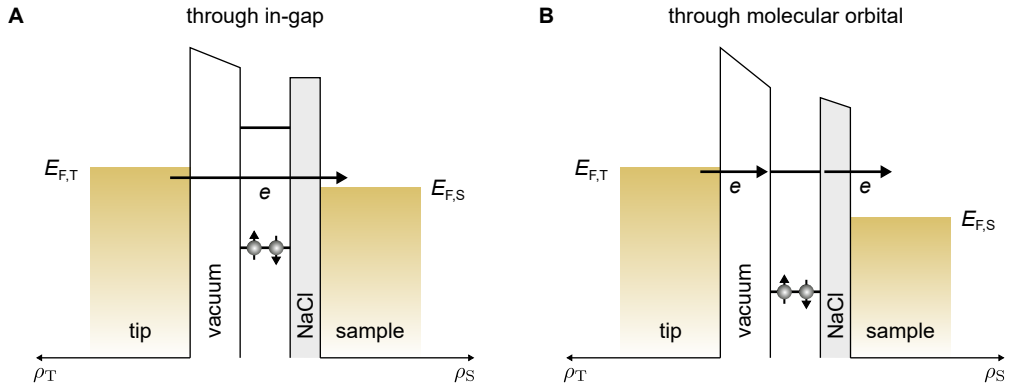

Figure 1.3 — Energy alignment in a double barrier tunnel junction. (A) Direct tunneling at small voltages (in the gap). (B) Sequential tunneling through an unoccupied molecular state when aligned with the Fermi level of the tip. Electrons tunnel from the tip into a molecular state (HOMO or LUMO), and are rapidly extracted via tunneling to the sample.

insulating layers (Al_2O_3) can be used to prevent hybridization between the molecular adsorbates and the metal substrate since they could observe intrinsic emission from a single molecule. Repp *et al.*[54] further showed that large band gap insulators, like NaCl, may also be employed to prevent hybridization of molecular frontier orbitals with the metal substrate. They could map the positive and negative ion resonances of a single Pentacene ($C_{22}H_{14}$) molecule, which correspond to the structures of the lowest unoccupied molecular orbital (LUMO) and highest occupied molecular orbital (HOMO) of the free molecule in a vacuum.

The energy level diagram of a single molecule decoupled from the metal substrate by an ultrathin NaCl layer is sketched in fig. 1.3. The vacuum and the insulator isolating the molecule from the two electrodes form the so-called *double barrier tunneling junction*. The frontier molecular orbitals act as two discrete levels. Assuming the same tip and sample material, when a small positive sample bias voltage is applied, the tip DOS is raised with respect to the sample density of states. The electrons occupying filled states in the tip can tunnel through the potential barrier formed by the vacuum and NaCl. In this case, the unoccupied states of the molecule do not participate in electron transport through the tunnel junction and the electron tunnels through the energetic gap between the HOMO and LUMO level, called the *in-gap* region (see fig. 1.3A). This traditional picture will be revised in Chapter 2, where tunneling through a bulk insulator like NaCl is discussed.

For a large positive sample bias voltage, the Fermi level of the tip aligns with an unoccupied molecular level. Electrons can then resonantly tunnel from the tip to an unoccupied molecular level and then to the free states in the sample (fig. 1.3B). The increased tunneling probability due to resonant tunneling leads to an excess current giving rise to a peak in the $\mathrm{d}I/\mathrm{d}V$ spectra at positive bias voltage. Similarly, for a large negative sample voltage, electrons can tunnel from the occupied sample states, via occupied molecular levels, into the free states in the tip and thus, leading to a peak in $\mathrm{d}I/\mathrm{d}V$ spectra at negative bias voltage.

1.2 Scanning tunneling microscope induced luminescence

In 1976 John Lambe and S. L. McCarthy demonstrated broadband optical emission from tunnel junctions[57]. They interpreted the effect in terms of inelastic tunneling excitation of optically coupled surface plasmon modes present in the metal-oxide-metal tunneling junction. Using Al-Al_2O_3-metal tunnel junctions, they observed stronger light emission for tunneling junctions with highly roughened top metal electrodes. The enhancement of light emission brought about by the roughness reinforced their interpretation since roughness is required for surface plasmons to radiate. The metal-vacuum-metal/semiconductor tunneling junction formed by the tip and the sample in STM is analogous to the oxide-based planar tunneling junction. Thus, light emission stimulated by the tunneling current was anticipated. Gimzewski *et al.* reported the first experimental observation of light emission in STM[58,59], kicking off the field known today as STML. The access to light emission characteristics at sub-wavelength scale provided unparalleled opportunities for studying solid surfaces[58,60], metallic adsorbates[61,62], and molecular layers[63]. Later, the use of ultra thin insulating layers enabled access to intrinsic properties of adsorbates[54,56,64]. In 2003, Qiu *et al.* observed fluorescence spectra on an individual porphyrin molecule[56], demonstrating the feasibility of optical spectroscopy with a nanoprobe for the investigation of single molecules. They later observed vibrational features corresponding to different molecular conformations and from different parts of the molecule[65] confirming that high spatial resolution of STM translates to sub-molecular resolution in STML.

More recently, STML on isolated single molecules has been used to visualize coherent intermolecular dipole-dipole coupling[66,67], intermolecular energy transfer[68,69], single photon emission[70], exciton-plasmon (X-P) coherent interaction[71–75], fluorescence from a molecular ion[38,76,77], explored mechanism enabling selective creation of singlet and triplet excitons[21], and help demystify up-conversion electroluminescence (UCEL)[37,38].

Dong *et al.*[78] followed a different route to access intrinsic molecular emission at the nanoscale, using a multi-monolayer decoupling approach. They observed vibrationally resolved fluorescence from porphyrin nanocrystals, where the molecules in the top layers are electronically isolated by the Schottky-like barrier formed at the molecule-metal interface. STML on molecular nanocrystals has led to observation of hot electroluminescence[79], single photon emission from defects[80] and discrete electronic states[81], bimodal emission[82], self-trapped excitons[83], and provided a rich playground for studying charge and exciton dynamics at play[84,85].

Other approaches, such as suspending a molecular wire comprising an emitter between the tip and sample, have also been proven to provide the necessary isolation for studying intrinsic molecular emission[86,87]. In the same way, suspending graphene nanoribbons in the tunneling junction has also provided access to their optoelectronics[88].

Thus, STML provides sub-nanometer scale access to underlying mechanisms at play for processes such as light harvesting and photosynthesis, making it an excellent tool to study different exciton formation mechanisms and dynamics at the nanoscale that are necessary

for upscaling these technologies. A thorough historical review of STML is also provided by Gustafsson *et al.*[89], Rossel *et al.*[90], and recently by Kuhnke *et al.*[33].

Following a brief survey of the current state of STML, the different modes of light emission observed in STM tunneling junctions, namely *plasmonic* and *excitonic* emission are summarized.

> For a tunneling junction formed of a clean metallic tip and sample surface, the light emission is due to radiative decay of plasmons, the quantum of plasma oscillation with respect to the fixed positive ions in metal, on inelastic excitation by the tunneling current. This mode of light emission is called *plasmonic emission*.
>
> For an isolated molecule, the light emission corresponds to an excited molecule relaxing to its ground state through the emission of a photon. For example, an electron in the LUMO and an electron-hole in the HOMO, and since they are found within the same molecular orbital manifold, the electron-hole state is said to be bound. Such a bound state is called an exciton, and the resulting photon emission upon exciton decay is called *excitonic emission*. Moreover, if the initial and final states have the same (different) spin multiplicities, the corresponding emission is known as fluorescence (phosphorescence).

In the following, plasmonic and excitonic emission from an STML perspective is discussed in more detail.

Plasmonic emission

In classical optics, the behavior and properties of light, including its interactions with matter and optical elements, can be explained by applying Maxwell's equations to the electronic structure at material interfaces. The characteristics of the optical elements rely on their macroscopic properties. However, the tip-sample junction in an STM forms a sub-wavelength gap where the optical properties depend on the local atomic structure[91–97]. The electromagnetic eigenmodes of the tip-sample cavity are well-described within the framework of classical electrodynamics. Besides the dielectric properties of the tip and sample material, they depend strongly on the local geometry of the tip and sample surface[98]. For STML, the tip-sample tunneling junction is electromagnetically strongly coupled. This formalism is distinct from conventional STM experiments where the tip and sample are considered essentially electronically decoupled from each other[52]. The inelastic component of the tunneling current in STM can lose its energy as an excitation of the plasmonic mode, which then decays as a photon[60,99,100]. Since the electrons can lose energy, given by the applied voltage, to a continuum of states, the plasmon exhibits a broad energy distribution (see fig. 1.4C). Figure 1.4B shows a schematic of the light emission process in the vacuum gap of the tunnel junction. The exact composition of the tunnel junction then becomes important since different electronic states involved in the excitation can tune the inelastic tunneling probability.

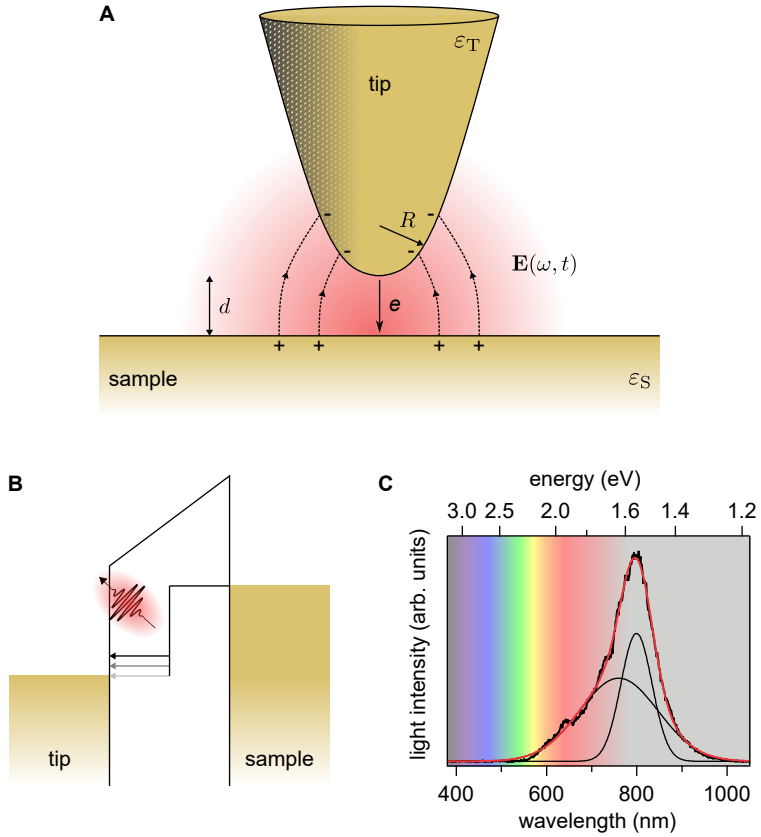

Figure 1.4 — Plasmonic emission in STM. (A) Schematic diagram of plasmonic excitation at the tunneling junction. Adapted from Johansson *et al.*[101]. The tip is biased positively with respect to the sample, which leads to polarization of the junction as shown, with excess negative charges at the tip and excess positive charges at the sample. (B) Energy diagram showing plasmon excitation due to an inelastic tunneling event. (C) STML characteristics of the tip-sample nanocavity on a clean area on the Au(111) substrate using Au wire as tip (set point: $I = 60$ pA, $V = -2.6$ V, $t = 10$ s).

Solving Maxwell's equation at the metal-vacuum interface, one finds that the oscillating plasma leads to an electric field that propagates along the interface[102]. The electric field extends in the vacuum and the metal with an amplitude maximum at the interface. The plasma oscillations at the surface of the metal resonantly couple to the electric field in the vacuum, forming a surface plasmon polariton (SPP). Because their dispersion relations do not cross, the free-space photons cannot directly couple to the SPP, which implies that they cannot decay as free-space photons. For an SPP to decay radiatively, this momentum mismatch needs to be overcome. Kretschmann[103] and Otto[104] showed that a prism can be used to match the photon and SPP wave vectors, and thus, to couple photons into SPPs. The momentum matching can also be achieved using a grating coupler to increase the parallel wave vector component of the SPP. Similarly, surface roughness allows SPP and free-space photons to couple by breaking the translational invariance parallel to the surface[105].

In case of STM, the tip and sample are in close proximity. The resulting electric field from their respective SPPs overlap, leading to formation of a new plasmonic mode, called the gap plasmon (fig. 1.4A). For a sphere in front of a metal surface, Johansson showed that the cavity features resonances ω_l if half a wavelength of the coupled mode equals the gap

distance[101]. Considering a junction formed by a tip and sample composed of same material ($\varepsilon_T = \varepsilon_S$), in the tunneling regime, i.e., at gap distance $d < 10$ Å, Rendell *et al.*[106,107] showed that the frequency-dependent dielectric function $\varepsilon(\omega_l)$ is described by

$$\frac{1}{\varepsilon(\omega_l)} = -\left(l + \frac{1}{2}\right)\sqrt{\frac{d}{2R}}, \qquad l = 0, 1, \ldots \tag{1.13}$$

where ω_l are the distinct resonances of the tip-sample cavity when half a wavelength of the coupled mode equals the tip-sample separation[101]. Then, following the Drude model for metal with plasmon frequency ω_P in the limit $d \ll R$, results in a series of plasmon modes

$$\omega_l \approx \omega_P \sqrt{\left(l + \frac{1}{2}\right)\sqrt{\frac{d}{2R}}}, \qquad l = 0, 1, \ldots \tag{1.14}$$

From the above equation, it directly follows that cavity resonance frequency depends on the tip radius. This effect was indeed experimentally observed by Meguro *et al.*[108] using a scanning electron microscope to image the tip apex and correlate the tip radii with STML spectra. Additionally, shrinking the tip-sample gap would red-shift the gap resonance. Recording STML spectra in parallel to approaching the tip towards the sample, Aizpurua *et al.*[109] recorded a red-shift of few-nm in mean wavelength of the plasmon frequency corroborating electromagnetic coupling between a metal tip and sample.

The plasmon – the SPP related to the tip and sample surface, and the gap plasmon – can be excited by both electrons and photons. In the tunneling regime, the excitation is created by inelastic tunneling excitation of the plasmons (1.4B). Theoretical studies[101,110] showed that for a sample voltage larger than the energy of the plasmon mode, most of the emitted light is due to inelastic tunneling, estimating the maximum yield to be $\approx 10^{-4}$–10^{-3} photons per electron. The estimated yield is in good agreement with the first STML experiments[111]. Berndt *et al.*[60] verified the suggested mechanism experimentally. They obtained no qualitative difference between STML spectra obtained for positive and negative sample voltage polarities, ruling out hot electroluminescence as a probable mechanism. The hot electrons would be fired into the bulk of the metal, scatter, and transfer energy into the bulk plasma leading to the formation of SPP. This would imply that for a distinct tip (W) and sample (Ag(111)) material, the STML spectra would depend on the direction of the tunneling current, i.e., applied voltage polarity. In addition, the light intensity exhibits the same oscillatory behavior as the constructive-destructive interference of electron standing waves in a triangular potential barrier[112,113] for constant current. In other words, it relies on the local DOS, affirming the inelastic tunneling excitation mechanism. Consequently, material selection for the tip and sample is an important aspect of experimental design in STML studies. In the visible spectrum, Al, Ag, Au, or Cu provide the desired large enhancement[21,80,114–117].

Laser light focused on the tip-sample cavity can also be used to excite the plasmonic emission. Similar to electronic excitation, the broken translational invariance due to the tip allows out-coupling of the SPP to free-space photon[118,119].

Besides the spatial variation of light intensity, the emission from the tunneling junction can also be analyzed in time domain. The energy-time uncertainty,

$$\Delta E \cdot \Delta t > \frac{\hbar}{2} \quad \Rightarrow \Delta E = \frac{\hbar}{2\tau}, \tag{1.15}$$

implies that for a state with a short lifetime τ, the energy distribution ΔE will be significant. For a typical linewidth of few hundreds of meV we obtain plasmon lifetime of few fs which agree with previous studies[120,121]. In a realistic STM tunneling junction the tip comprises of several nanoprotrusions[108] forming distinct resonances as shown in fig. 1.4C (smooth Gaussians). Theoretical analysis of field enhancement as a function of tip radius and opening angle by Aizpurua *et al.* [122] showed that sharper tips provide stronger intensity enhancement. In contrast, the energy distribution of the emission depends on the tip aperture. Thus, close attention is paid to tip etching to obtain a tip radius in the range of 10-50 nm and with an acute opening angle of $\approx$ 20-40° [115,123,124]. Tip etching is further discussed in section 1.3.

Excitonic emission

The excitonic emission from single-molecule species or local defects in molecular crystals is the central theme of this thesis. As discussed in section 1.1, molecular adsorbates adsorbed on a metal substrate hybridize strongly, exhibit broadened molecular levels, and thus, short-lived excited states in which the electron from the excited state of the molecule is efficiently transferred to the substrate. Such molecules only modify the local DOS, and thus local plasmonic emission intensity[63]. As the fluorophore-substrate spacing is increased, the molecule-substrate hybridization decreases, and the intrinsic optoelectronic properties of the molecules become accessible[78]. Isolated molecules or clusters atop thin insulator films, 2-4 monolayer (ML) Al_2O_3 [56], NaCl[54,66,68,125], or KCl[83] have also shown intrinsic fluorescence and phosphorescence. Figure 1.6A shows the experimental scheme that allows excitation of the molecular dipole μ by a tunneling electron, leading to STM-induced electroluminescence (STM-EL). Alternatively, laser light focussed at the tunnel junction can also be used to drive the excitation (fig. 1.6B).

The high light emission intensities observed in excitonic STML from single molecules too are by virtue of the tip enhancement effect. The plasmon modes at the tunnel junction lead to an increased local photonic DOS ρ_μ. Using dipole approximation, the spontaneous decay rate γ of a two-level system can be written as[126],

$$\gamma = \frac{\pi\omega}{3\hbar\varepsilon_0}|\mu|^2\rho_\mu(\mathbf{r},\omega) \tag{1.16}$$

where μ is the transition dipole moment. Since γ is directly proportional to ρ_μ, the drastic increase in photonic DOS leads to decay rate enhancement, known as the Purcell effect[127,128]. From equation 1.15, the linewidth in the excitonic spectrum gives a lower estimate of the excited state lifetime. The typical STM-EL depict a sub-ps ($\approx$ 200 fs in fig. 1.6F) lifetime as compared to few ns for molecules in solutions[129] or isolated molecules in frozen host

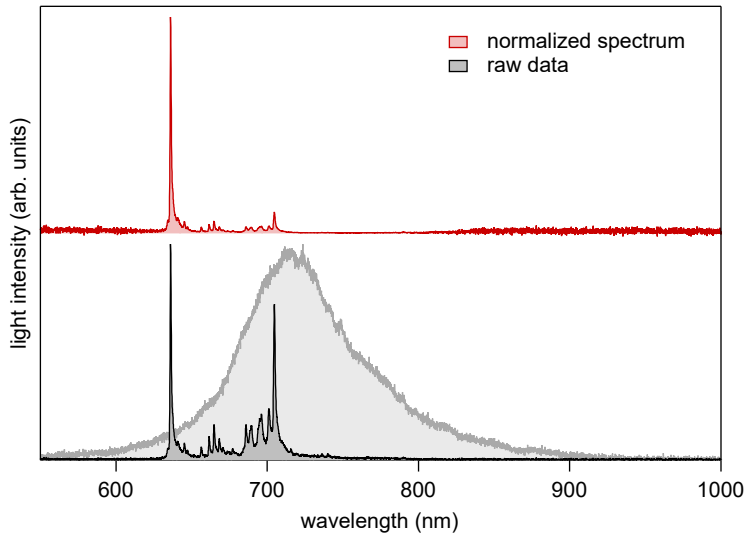

Figure 1.5 — Example of how photonic DOS affects the energy distribution of excitonic intensity. Bottom – Plasmonic and excitonic luminescence (raw data). Top – Normalized excitonic spectrum (set point: $I = 60\,\text{pA}, V = -2.7\,\text{V}, t = 60\,\text{s}$).

crystalline lattices[130,131]. The factors leading to broadening the spectral linewidth are vibrational dephasing (homogeneous broadening) – which is weak at low temperatures, inhomogeneous broadening due to interaction with its environment – which is absent for a single molecule. Within this framework, coherent interaction of adjacent molecular dipoles can also lead to an increase in decay rate, and thus light emission intensity (superradiance)[74]. It is important to note that Purcell enhancement leads to an increase in both radiative and non-radiative decay rates of a molecular excitation[91]. The coupling to the plasmon and increased radiative and non-radiative decay rates also lead to broadening spectral linewidth (discussed in more detail in Chapter 4). The interplay between the two rates also plays a vital role in the observed emission intensity[91,92]. Experimentally, the plasmon influences the intensity distribution of excitonic spectra. Figure 1.5 shows the effect of plasmonic enhancement on the relative intensity of the vibronic peaks. Therefore, only on normalization using the plasmon observed for the same tip can the relative intensities of different emission processes can be compared.

STM induced electroluminescence

For an isolated molecule adsorbed atop a spacer on a metal substrate, at sample voltage $-V$, for which the tip Fermi energy is aligned with the HOMO level of the molecule, an electron of either spin can be extracted from the HOMO (hole creation) (see fig. 1.6C). Next, a charge is injected into the LUMO orbital from the substrate through the spacer layer. Since the two orbitals exist in the same molecular orbital manifold, the electron-hole pair can be said to be bound and be described as an exciton. Depending on the spin-multiplicity of the extracted electron, a singlet S_1 or triplet T_1 exciton could be created leading to *fluorescence* or *phosphorescence*[22,132,133]. The molecule returns to its ground state upon photon emission[56,78,87], which is detected in the far-field spectrum. The above so-called *carrier-injection* mechanism is also valid for a positive voltage where LUMO is aligned with the tip Fermi level. Another debated mechanism for electronic excitation of the molecule is through interaction

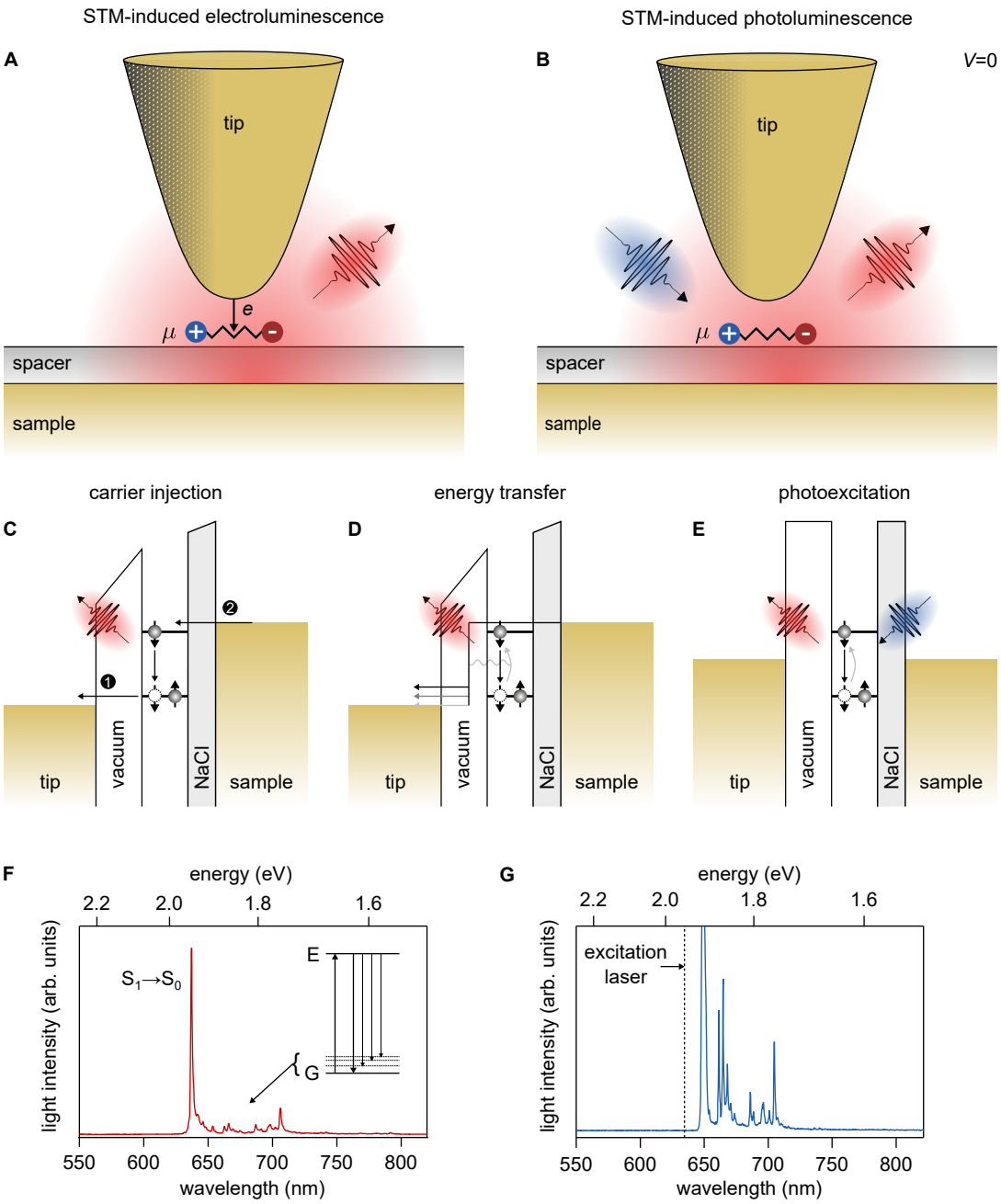

Figure 1.6 — Excitonic emission in STM. Schematic diagram of excitonic emission due to (A) electronic and (B) photoexcitation at the junction. (C) Energy diagram showing ① charge extraction from HOMO, ② charge refilling from substrate to LUMO leading to exciton creation. (D) Plasmonic emission due to inelastic tunneling is adsorbed by the molecule, leading to an excitation where the molecule returns to the ground state on the emission of a photon. (E) Photoexcitation by laser where the molecule returns to the ground state upon photoemission. (F) Typical excitonic STM-EL and (G) STM-PL spectrum.

with the plasmonic emission that occurs due to inelastic tunneling at the tunneling junction (discussed in the previous section). The coupling to the plasmon can lead to an excitation via *energy transfer*, after which the molecule returns to the ground state upon photon emission[134]. For such a process, the voltage onset of the excitonic emission matches the energy of the exciton.

Vibronic spectroscopy – For both excitation mechanisms, the peaks in emission intensity below the $0-0$ line of the fluorescence (fig. 1.6F) are in qualitative agreement with the ones obtained for molecules in frozen matrices[130] and Raman spectra from molecular powder. The peaks are thus assigned to the vibrational modes of the molecule. Utilizing the scanning ability of the STM, spatially resolved isochromatic intensity maps of each peak can be obtained. Such an analysis of single-molecule STML showed that the intensity maps corresponding to the $0-0$ line and the vibrations of distinct symmetries are uncorrelated[65,134,135] allowing for scrutiny of vibronic coupling[136] mechanism at the single-molecule scale. In the Franck-Condon picture[137,138], the stationary nuclear framework does not modify the wavefunctions of the excited or ground states when the molecule undergoes an electronic transition. That would imply that all the vibronic peaks have the same symmetry as the $0-0$ transition. Their relative intensities are given by the square of the overlap integral between the vibrational wavefunctions of the excited and ground states. However, the findings from STML[65,134,135] conclusively show that molecular vibrations can modify the electronic wavefunctions of the excited or ground states strong enough to induce vibrational emission that is forbidden based on the Franck-Condon principle. The intensity maps depicting symmetry of the vibrational modes can be understood based on the Herzberg-Teller contributions[139] where the vibronic transitions depend on the admixture of higher-lying electronic states that contribute to lowest energy transitions[140]. Single-molecule studies of vibronic coupling are discussed further in Chapter 4.

Exciton-plasmon coupling – In STM, the tip position (plasmon) can be controlled precisely relative to the molecule (exciton) to manipulate the exciton-plasmon (X-P) coupling at picoscale lengths. For a sufficiently long distance from the molecule, the STML spectrum exhibits broadband emission characteristic of the plasmon. As the tip reaches ≈ 3 nm from the center of the molecule, an asymmetric dip appears in the broadband plasmonic emission[71–73]. This asymmetric structure in the spectrum, described by a Fano[141] lineshape, is due to a coherent interaction between the continuum of states, i.e., plasmon, and the discrete states of the molecule. This experimental scheme allows one to study how X-P coupling affects not only fluorescence but also other radiative and non-radiative processes, like intersystem crossing (ISC) and phosphorescence. See Chapter 4 for more details.

Emission from a charged molecule – The redox state of an atom or molecule is controlled by its chemical environment. STM can be used to control and probe the charge state of atoms and molecules[142,143]. Energy level alignment at the tunneling junction can be manipulated using a substrate with appropriate work function[144] to control the redox state of a molecule.

An anionic or cationic state of a single molecule can be prepared for STML studies using this strategy. For such a molecule, besides the emission from a neutral molecule (X^0), a sharp emission line corresponding to the radical cation (X^+) or anion (X^-) of the molecule can be observed[38,76,77]. Due to the decoupling from NaCl, upon charge extraction (injection) the radical can be stabilized long enough for the excitation followed by emission to occur. The relative intensity of the lines associated with X^0 or $X^\pm$ relates to the time spent by the molecule in the corresponding redox state.

Up-conversion electroluminescence – UCEL is a phenomena where the intrinsic emission has a higher energy than that of the excitation. Such light emission has been observed in molecular films and isolated molecules in STM-EL[37,79,145,146]. Since multiples of energy quanta are necessary for excitation, mechanism revolving around an intermediate relay state have been proposed. In molecular layers, it was suggested that triplet-triplet annihilation (TTA) between molecules in their excited states could occur[145,146]. In TTA, one molecule transfers its excited state energy to the second molecule and relaxes to its ground state, and the second molecule is promoted to a higher excited state. Recently, observation of UCEL at the single-molecule level has ruled out the TTA mechanism[37]. Another proposed mechanism includes molecular vibration-assisted energy transfer to the molecule[79]. In that case, a short average time between tunneling events is necessary to promote energy transfer. The observation of UCEL at only a few pA current rules out vibration-assisted energy transfer as a mechanism as well. The voltage onset of UCEL corresponding to the triplet emission from the molecule and a quadratic dependence of the intensity on the tunneling current suggests that T_1 state of the molecule could be acting as the relay state, from where the excitation is promoted to the S_1 state due to another inelastic excitation or by the subsequent charge injection[37]. However, the mechanism for UCEL is far from settled. In Chapter 3, we study UCEL from a single molecule and scrutinize the proposed mechanism.

STM induced photoluminescence

The Purcell enhancement in the tip-sample cavity not only allows breaking the Abbe limit[26], at sub-nanometer length scales, it can be done with both electrons[33,56,66,68,134] and photons[96,116,147–150]. For comparison, even though techniques like scanning near-field optical microscopy (SNOM)[151–154] routinely reaches $\approx$ 10 nm resolution, atomic-scale resolution has stayed out of reach. The resolution in near-field microscopy relies on the degree of optical confinement. The probes used for SNOM do not allow as high a confinement as that of the atomically sharp tip characteristic of STM that is just few Å away from the substrate[93,94]. Moreover, for molecules directly adsorbed atop metal substrate the tip-molecule distance can be further reduced to just a few Å enabling tip-enhanced Raman spectroscopy (TERS) at atomic length scales[95,116,155]. The ability to alter the tip at an atomic scale[156,157] allows forming a so-called picocavity[94] which enables the study of atomic scale effects on the Purcell enhancement[96,158]. Fluorescence of isolated molecules could then be probed in a double barrier tunneling junction scheme similar to STM-EL experiments. In this thesis the term

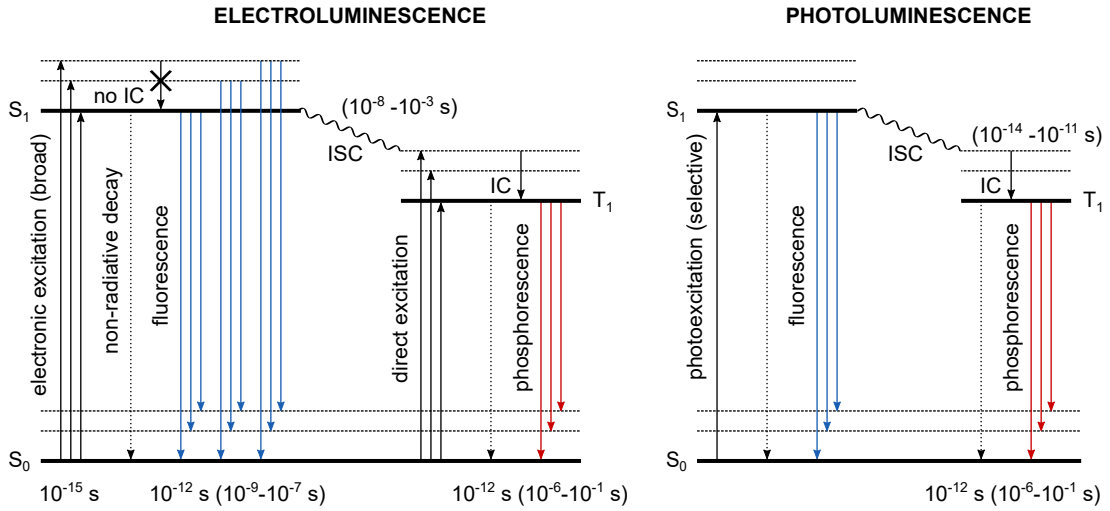

Figure 1.7 — Modified Perrin-Jabłoński diagram of emission processes. Rates of different transitions evaluated from STML peak FWHM are indicated along with the average rates (bracketed) obtained for the transitions for molecules in liquid or frozen solutions.[22,159]

STM-induced photoluminescence (STM-PL) is used to describe the emission from isolated molecules upon photoexcitation by a laser focused at the tunneling junction.

Recently, Yang *et al.*[96] showed the first observation of tip-enhanced photoluminescence in a single molecule STM experiment. Using 532 nm laser light confined between the tip and sample, they detected emission at ≈ 653 nm, related to the molecular fluorescence, when the tip is brought on top of a molecule. Since the sample voltage is set to -1 V (electron energy is less than optical band gap of 1.89 eV), the tunneling electrons cannot lead to fluorescence, thus establishing that they indeed observe photoluminescence. Scanning the tip over the molecule, they observed sub-nanometer resolved fluorescence from single molecules, and how the tip-sample gap distance alters this resolution. Characterizing the spatial distribution of fluorescence spectra also enables studying effects of X-P coupling on STM-PL.

Resonant photoexcitation – Another advantage of using photoexcitation over electronic excitation by tunneling current is the energy distribution of the two excitation sources. The broad energy distribution of the tunneling electrons leads to a poor state selectivity in excitation and thus cannot be used to address single quantum states selectively (see fig. 1.7). However, wavelength-tunable lasers enable monochromatic coherent excitation with precise selection of the state to be excited[160]. Imada *et al.* implemented such a tunable laser excitation in an STM junction, exciting the S_1 to S_0 transition resonantly and observing the vibrational fingerprints in resonant STM-PL from a single molecule. The high energy resolution (μeV range) that this technique offers allowed them to probe subtle changes in vibronic peak positions of a molecule and its deuterated species. In addition to unprecedented resolution in optical spectroscopy at the nanoscale, this technique also allows the study of processes like ISC, the radiation-less energy transfer from S_1 to T_1 state, since the T_1 cannot be directly excited by a photon. Since the decay of T_1 to S_0 involves a spin-flip, phosphorescence is electric dipole forbidden. In the case of electronic excitation, T_1 can be directly excited and thus does not

allow distinguishing between ISC or direct excitation as the source of phosphorescence. We use resonant STM-PL in Chapter 4 to study how X-P coupling affects phosphorescence and ISC at single-molecule level.

Figure 1.7 outlines the differences between electronic and photo-excitation using a Perrin-Jabłoński diagram[161]. The rates indicated for each transition, naïvely evaluated from FWHM of the STML spectrum, highlight the decay rate enhancement due to the Purcell effect in the tunneling junction. Here, it is important to note that processes like internal conversion (IC), which usually face no competition from fluorescence due to their long lifetime, maybe suppressed in STML[72], making studies of molecular emission at high resolution possible.

1.3 Experimental setup and details

All experiments presented in this thesis (except for Chapter 4[1]) are performed using an in-house built low temperature (4.3 K) UHV STM[162,163]. The microscope is located in one of the experimental rooms of the Precision Laboratory at Max Planck Institute for Solid State Research, Stuttgart. The experimental rooms are closed metal shells yielding 60 dB acoustic shielding from the immediate lab environment. Inside, the UHV chamber setup that houses the microscope is attached firmly to a massive 120 t fiberglass reinforced concrete block. The concrete block is suspended on an air spring system (Bilz Vibration Technology AG) to reduce further the floor vibration level below 10 nm s^{-1}. The experimental facility ensures seismic, acoustic, and electromagnetic shielding and enables the extreme stability necessary for highly-sensitive STM studies. The microscope and optical setup are described in more detail in the following.

Photon-STM

The experimental setup, namely *Photon-STM*, comprises two UHV chambers: preparation and STM, separated by a vacuum gate valve. Additionally, a load-lock chamber is installed on the preparation chamber, enabling tip and sample transfer from ambient to UHV environment. The preparation chamber is equipped with a manipulator with a sample heating and evaporation stage, a sputter gun, two molecular beam evaporators, and a metal evaporator. The chamber maintains a base pressure of $\approx 2 \times 10^{-10}$ mbar. The STM chamber with a base pressure $<10^{-11}$ mbar houses the microscope head and the lens system. The microscope head is mounted on the liquid helium bath cryostat (10 l) that hangs on passive air springs, providing additional vibrational isolation. A nitrogen cryostat (40 l) provides radiation shielding, allowing for a standing time of about 48 h.
Figure 1.8 presents a view inside the cryostat showing the microscope head and the three optical lenses (L1, L2, L3). The microscope head comprises a fixed tip stage where an ex-

[1]The experiments presented in Chapter 4 were conducted at a low temperature (4.7 K) ultra high vacuum (UHV) STM, *4-Goki*, at Nanoscience Joint Laboratory, in collaboration with Prof. Yousoo Kim, Surface and Interface Science Laboratory, at RIKEN (理化学研究所), Wakō-shi.

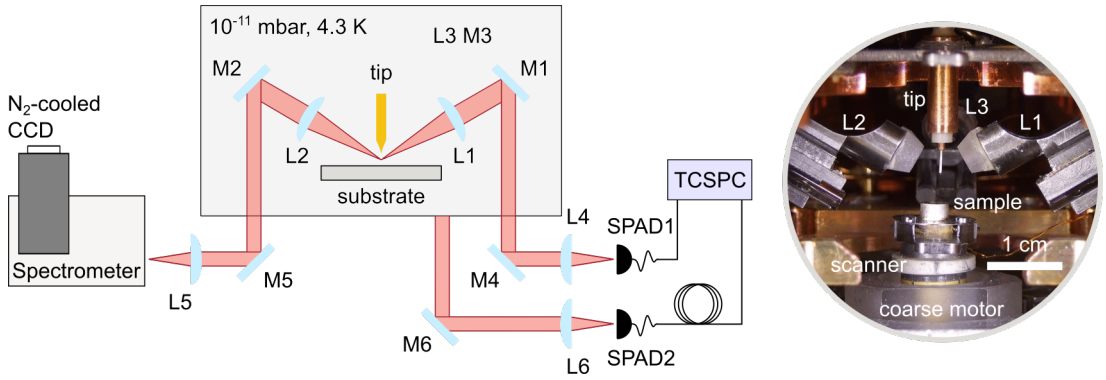

Figure 1.8 — Schematic overview of *Photon*-STM showing the arrangement of optics inside the liquid helium cryostat and the peripheral optics. An inside view of the STM showing optical lenses (described in text) and components of the STM head.

changeable tip holder is mounted. The movable sample (with the tip position fixed) allows utilizing different areas of the crystal for experiments while retaining good optical alignment to the tip apex. Distinct from most STM head designs, the sample stage is mounted on a piezo tube (scanner) that controls the tip-sample gap and horizontal scanning of the sample with respect to the tip. A second slip-stick coarse motor allows for vertical and horizontal positioning of the sample on a millimeter scale.
The instrument control and data acquisition are conducted using control electronics and software *Nanonis Mimea* (SPECS Surface Nano Analysis GmbH) in conjunction with self-written LabVIEW VIs. The data were processed and plotted using Igor Pro or self-written MATLAB or Python code.

Optical access

The light emitted at the tunneling junction is collected by three aspheric lenses (NA = 0.42), marked L1, L2, and L3 in fig. 1.8, located only a few millimeters away from the tip. Since the lenses are housed inside the cryostat, they too are cooled down to 4.3 K. Each lens is placed on a piezo stage that enables in situ adjustments of the focal points of each lens separately with respect to the tip apex. The lenses are mounted at 30° to the surface to optimize light collection, in line with theoretical findings of Aizpurua et al.[122] and are at an azimuthal angle of 90° to each other. The slightly convergent beam is next reflected off a mirror along the surface normal. The beams exit the UHV chamber through the holes in liquid helium (4 mm) and liquid nitrogen (6 mm) cryogenic shields and UHV viewports. The distance of the lenses from the tip is adjusted such that the beam forms an intermediate focus between the liquid helium and liquid nitrogen shields. This allows keeping the beam diameter below a few millimeters throughout the propagation path to avoid any losses. Just outside the UHV viewports, steering mirrors allow guiding the beams towards the detectors. Accounting for the transmission losses at the lenses and viewports, the estimated collection efficiency of each lens is between 7-12%[162]. In this thesis, the detectors used are two single photon avalanche diodes (SPAD) (Micro Photon Devices PDM-R, time resolution: <30 ps,

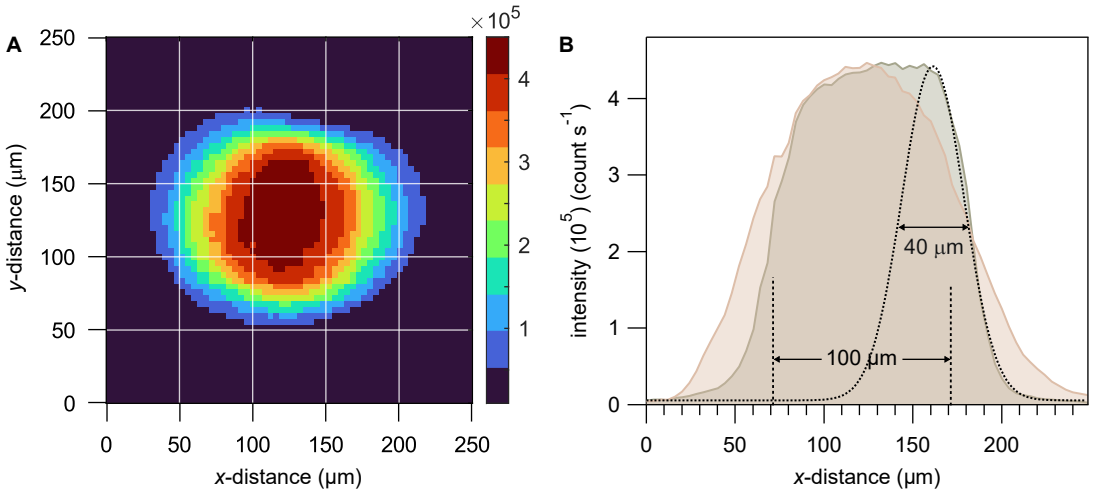

Figure 1.9 — Aligning SPAD. (A) Spatial distribution of light intensity obtained at the SPAD (set point: $I = 1$ nA, $V = -2.7$ V). (B) Horizontal and vertical line cut through the map compared to SPAD chip dimensions. The dotted Gaussian line shape is the approximated line profile.

sensitive area diameter: 100 μm^2, dark counts: <13-18 counts s^{-1}) and a spectrograph (Acton Research SP 300i, 150 grooves mm^{-1} 500 nm blazed grating or 1200 grooves mm^{-1} holographic grating) with a Peltier-cooled electron-multiplying charged-couple device (CCD) (Teledyne Princeton Instruments PI-MAX 4).

We use plasmonic emission from the tunneling junction as the light source to perform the optics alignment. The SPADs are installed on motorized x-, y-, and z-stage (Standa) that allows fine adjustment of the detection chip to the refocused beam. A LabVIEW program sweeps the x-y, y-z, and z-x planes to find the maximum intensity iteratively. Figure 1.9A shows an intensity map obtained for a sweep in the x-y plane where the lens has been focused on the tip apex. The line profile of the intensity map in the horizontal and vertical directions is shown in fig. 1.9B. The focus spot at the SPAD, obtained from deconvoluting a Gaussian peak at the edge of a square-shaped profile, occupies an area of about $\approx 50\times50$ μm^2. For the sensitive area diameter: 100 μm^2, almost all of the emission intensity is detected at the SPAD. For adjustment to the spectrometer, an adjustable mirror is used to manually sweep the beam in the x-y plane to find the maximum intensity at the CCD.

Hanbury Brown-Twiss STM

The Hanbury Brown-Twiss (HBT) effect for photons allows distinguishing between different sources of light by measuring temporal coherence properties of the source by measuring the second-order autocorrelation function $g^{(2)}(\tau)$[36,164–167]. For number of single photons $n(\tau)$ detected at the SPAD, the fluctuation using the second-order correlation function $g^{(2)}(\Delta\tau)$ over all time τ can be written as

$$g^{(2)}(\Delta\tau) = \frac{\langle n(\tau)n(\tau+\Delta\tau)\rangle}{\langle n(\tau)\rangle\langle n(\tau+\Delta\tau)\rangle} \tag{1.17}$$

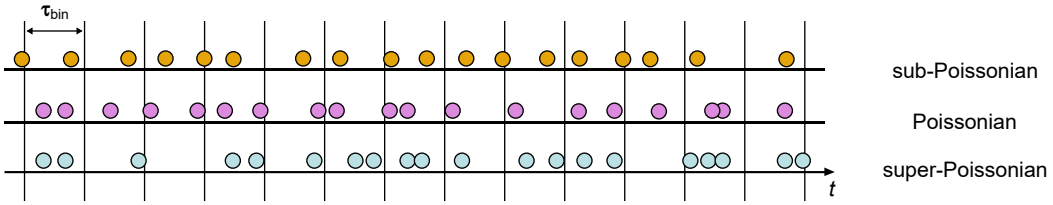

Figure 1.10 — Photon train as a function of time t for top – anti-bunching from a single photon source, center – coherent emission from a laser, and bottom – bunching from a source emitting thermal radiation. τ_c is the coherence time.

where $\Delta\tau$ is the time spanned until detection at the second detector once an event had been detected at the first.

The light sources can also be classified on basis of the photon number fluctuation per time interval τ_{bin}. For a perfectly coherent beam of light, for example from a laser, the photon number fluctuation is described by a Poisson distribution[168] (pink dots in fig. 1.10). Different light sources can then be benchmarked against such a light source. The intensity-intensity correlation $g^{(2)}(\Delta\tau)$ for a laser would result in $g^{(2)}(\Delta\tau = 0) = 1$.

For the case of thermal radiation, for example, from a hot glowing filament, the photons display a tendency to be clustered (blue dots in fig. 1.10). The photon number fluctuation would then exhibit a larger variance than the Poisson distribution (super-Poissonian statistics). Larger number of fluctuations than a coherent state result in $g^{(2)}(\Delta\tau = 0) > 1$[165], a manifestation of so-called *bunching* of photons.

A molecule on the other hand has a tendency to emit photons one at a time[169] (see yellow dots fig. 1.10). The emission intensity in this case has smaller number of fluctuations than a coherent state resulting in *antibunching* in the detection events and thus, $g^{(2)}(0) < 1$[36]. In this case, the photon number fluctuations exhibit a smaller variance than Poisson distribution[170] (sub-Poissonian statistics).

However, these are not the only possible outcomes for $g^{(2)}(0)$. For the particular case of photon pair production, for example, from a tunneling junction at a large bias[171], $g^{(2)}(0)$ can take arbitrarily high values.

HBT-STM combines high spatial resolution with the ability to probe quantum states, which enables the study of single photon sources like single molecules[70,74], color centers[172], crystallographic defects in 2-D materials[173,174] or organic semiconductors[80]. The STM can not only be used to probe the quantum states but also manipulate electronic states by using the tip electric field gradient to discretize the flow of electrons through C_{60} thin films that manifests as single photon emission as shown in Chapter 5. The HBT-STM enables studies of a vast range of systems and processes as proposed in the Perspective article by Rosławska *et al.*[175].

Using two SPADs in conjunction with a time-to-digital converter (TimeTagger, Swabian Instruments) enables time-correlated single photon counting (TCSPC) (see fig. 1.8). Theoretical details and modelling of dynamics in HBT-STM are discussed in more detail in a previous PhD thesis by Anna Rosławska[176].

In studies of single-photon emission from molecules, it is essential to know the time reso-

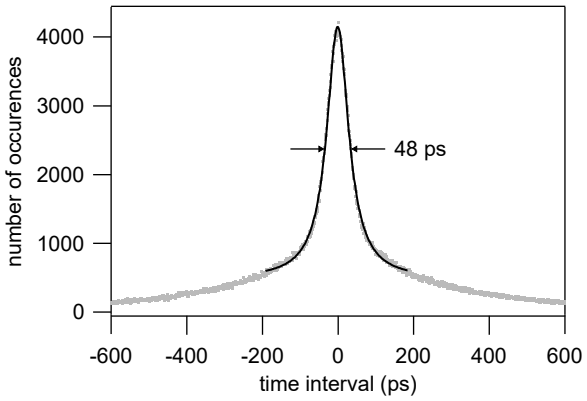

Figure 1.11 — Time resolution of the setup measured using a pulsed laser as the light source.

lution of the intensity interferometer. A laser source (Fianium WhiteLase WL-SC-400-40) with a few tens of picosecond pulse width at 800 nm wavelength is used. Due to the pulsed nature of the laser light, a positive correlation is expected at $\Delta\tau = 0$. As shown in fig. 1.11, a laser autocorrelation width of $\approx$ 48 ps (FWHM) is obtained. This indicates that the setup allows probing dynamics at a few tens of picosecond timescale (see Chapter 3 and 5).

Sample preparation

This section outlines preparation conditions for different samples used in this thesis. The specified parameters are specific to the equipment used.

Single crystals – The Au(111), Ag(111), Cu(111), and Pt(111) single crystals (>99.999%, Suppliers: MaTeck Material-Technologie & Kristalle GmbH or Surface Preparation Laboratory) are prepared in the UHV by repeated cycles of Ar^+ ion sputtering at 10^{-6} mbar range argon pressure with 600 eV acceleration energy. Following the sputtering, the crystals are annealed up to 870 K (Au), 830 K (Ag), 780 K (Cu), and 1170 K (Pt). Pt(111) was additionally exposed to oxygen (10^{-8} mbar) while annealing to get rid of C contaminants. The usual sample heating and cooling rate is about 1 Ks^{-1} to avoid any roughening of the surface due to thermal stress.

Single molecules atop few ML NaCl – NaCl ($\geq$ 99%, Merck KGaA) is thermally evaporated from a Knudsen cell (Dodecon Nanotechnology GmbH) via molecular beam epitaxy held at 890-900 K with substrate held at 300 K. For evaporation time of 5 minutes we obtain a sample partially covered in 2-4 ML thick (100)-terminated NaCl islands. Next, the sample manipulator is cooled down to 65 K using He integrated liquid Helium flow cryostat. Next, the free-base phthalocyanine (H_2Pc), platinum (II) phthalocyanine (PtPc) ($\geq$ 99%, Luminescence Technology Corporation), and platinum octaethylporphyrin (PtOEP) ($\geq$ 99%, Merck KGaA) molecules are thermally evaporated at 668 K, 708, and 608 K, respectively. The sample is then transferred to the STM for characterization using a pre-cooled wobble stick. At the STM instrument at RIKEN (Scienta Omicron), H_2Pc and PtPc were deposited onto the NaCl covered Ag(111) surface directly at the STM head at 4.7-10 K using a homemade

evaporator heated to 575 K and 638 K, respectively.

C_{60} thin films – C_{60} molecules (>99.5%, Merck KGaA) are thermally evaporated at 820-840 K for 45 minutes to obtain multiple layers of C_{60} thin films. The Au(111) substrate is kept at room temperature during evaporation. A shutter, located 2 mm in front of the evaporation stage where the sample is placed, allows partial blocking of the molecular beam from the evaporator. This allows only partial coverage of the sample. For the study presented in Chapter 5, the Ag(111) substrate was kept at a temperature between 213 and 253 K to favor rough island growth. The side free of adsorbates can then be used for tip preparation and characterization without moving to a different crystal.

h-BN monolayer – A closed monolayer of *h*-BN grown by chemical vapour deposition on a Pt(111) single crystal heated to 1025 K and exposing it to 2 L of borazine ($HBNH_3$) gas (Katchem spol s.r.o.) for 1 min followed by increase in partial pressure to 18 L for 4 mins. *h*-BN grows in a self-terminating growth process[177].

Tip preparation

We use an electrochemically etched Au wire (99.999%, Thermo Fisher Scientific) as a tip for all experiments. The wire is etched using a three-electrode etching system developed by Yang *et al.*[124]. The etching system is briefly described in the following.

The system comprises of a 0.25 mm diameter Au wire as the working electrode, a 1 cm diameter ring of 0.5 mm diameter Au wire ring as the control electrode, and an Ag/AgCl/ saturated KCl electrode (Thermo Fisher Scientific) as the reference electrode. A 2.79 mol/L KCl (Merck KGaA) aqueous solution is used as the electrolyte. The Au wire is immersed ≈ 1 mm deep in the electrolyte in the center of the ring for tip etching. A DC voltage of 1.25 V is applied to the working electrode, which is controlled against the reference electrode, while the current at the anode is monitored using a potentiostat (AUTOLAB, Metrohm AG). The etching process is automatically cut off when the anode current drops below the preset limit of 0.1 mA for 1 ms (typical starting anode current ≈ 10 mA). Next, the etched wire is carefully washed in ultrapure water and installed on a tip holder. Figure 1.12 shows an scanning electron microscope (SEM) image of a typical tip etched using this method. The tips are typically 3-6 mm long, with apex radii in the range of a few tens of nanometers and an opening angle of 30-50° which are ideal for a large Purcell enhancement[122]. If the tip

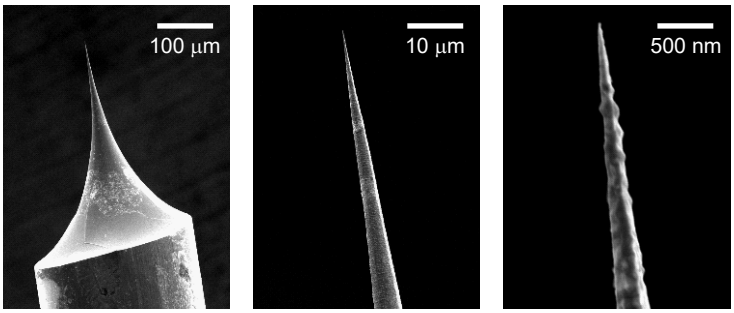

Figure 1.12 — SEM image of a typical tip with scale bars indicated (high voltage = 5 kV).

is found to be smooth and sharp under an optical microscope, it is transferred to the STM using the UHV load-lock of the instrument.

A freshly transferred tip usually requires further preparation in-situ. For tuning the plasmon energy distribution to the molecular emission, the tip is repeatedly indented 3-5 nm into the metal surface at sample voltage on the order of -1 V until the required energy distribution is achieved. In case the cavity exhibits low emission intensity, as measured by the SPAD, the tip is indented $\approx$ 1 nm into the sample with sample voltage on the order of 100 mV. Afterward, the light intensity is monitored. For a prepared tip, typical intensities exceed 40 kcts s^{-1} for -2.5 V, 100 pA. Additionally, we perform dI/dV spectroscopy to verify that the tip exhibits a flat DOS around the Fermi energy. Occasionally, voltage pulses ($\pm$10 V, 10-50 ms) must be applied to the sample to remove NaCl or molecules that spontaneously attach to the tip while measuring.

Partial results of the presented work have been published in: C. C. Leon*, A. Grewal*, K. Kuhnke, K. Kern, and O. Gunnarsson, Nat Commun **13**, 981 (2022).

2

NaCl: more than a decoupling layer

This chapter reports on the findings that ultrathin, insulating NaCl films, regularly used as a decoupling layer in STM and STML experiments, act as more than just an electronically uninteresting buffer to preserve intrinsic electronic properties of adsorbates. A careful investigation of tunneling through the NaCl film, an ionic insulator, for negative and positive sample voltages, shows that tunneling is more efficient through Cl than Na sites. This suggests that both conduction band (CB) and valence band (VB) are mainly of Cl character, strongly contrasting with the widespread textbook picture of the electronic structure of NaCl. Tight-binding calculations[1] show that the topographic features for sample voltages in the gap are located on the same ions as the voltages corresponding to the bands. Given that, assigning topography features related to the ions for voltages in the bandgap, just below the CB and above the VB, is sufficient for understanding the tunneling through the conduction and valence bands themselves. Simple electrostatic considerations show that the large Madelung potential can lead to a reversal in the order of the Cl^- 4*s* and the Na^+ 3*s* levels, leading to a CB, which is mainly of anionic character. Moreover, for a molecule adsorbed atop NaCl, tunneling through the HOMO-LUMO energy gap where there is no appreciable DOS (see section 1.1), we find that the electronic structure of the molecule still determines the STM image. Experimental observations, supported by theoretical considerations, suggest that the molecule's presence typically leads to a considerable increase in the tunneling current through the gap. Theoretical modeling infers that the tunneling, and thus the topography image, is determined by linear combinations of the bound states extending well below the HOMO, even for energies close to Fermi energy. These findings imply that the NaCl substantially influences the tunneling process through the molecule, especially at energies in the gap. This finding helps reconcile other complex observations, like, up-conversion electroluminescence (discussed in section 3.4) and negative differential resistivity[178].

*Equal contribution.

[1]The tight-binding calculations were planned and carried out by Olle Gunnarsson, Max Planck Institute for Solid State Research, Germany.

2.1 Anionic character of the conduction band of NaCl

NaCl, a prototypical alkali halide, is an ionic insulator with both alkali and halogen ions having full shells. The textbook picture of alkali halides dictates that a significant charge transfer from the alkali atoms to the halogen atoms leads to the formation of positively and negatively charged ions. This results in a VB which is primarily of halogen *p* character, while the CB involves an empty alkali *s* level outside a full shell[179–183]. Slater and Shockley[184] were the first to suggest a contrasting picture for NaCl, where the CB and VB both exhibit a substantial Cl 4*s* character. Later, various band structure calculations of NaCl came to the same conclusion, that the CB is mainly located on the Cl^- ions[185–189]. However, due to the lack of experimental evidence and rationale behind the proposed electronic structure, these theoretical findings seem to have been overlooked.

An experimental investigation of the CB of NaCl using STM, provides solid proof of its anionic character (see fig. 2.1 and 2.2). A detailed description of the findings is discussed in the following. Additionally, an empirical calculation reveals that a Madelung potential of roughly 9 eV can result in a reversed ordering of the Cl^- 4*s* (above the vacuum level) and Na^+ 3*s* (at −5 eV) levels, implying that CB is mainly of Cl character. This justifies the anionic character of NaCl CB and is discussed later.

STM topography of NaCl over the entire band gap

Despite many STM studies characterizing the growth and structure of NaCl films[189–194], a detailed study of the CB has been inaccessible, primarily due to spontaneous defect creation at large positive voltages ($V > 1$ V) which produces a high electric field at the tunneling junction[192,195]. The combination of comparatively large tunneling current (small tip-sample gap) necessary to obtain atomic resolution imaging and large voltage results in instabilities at the tunneling junction, which prevent smooth raster scanning of the tip over the surface. We ensure that the integrity of the tip apex is maintained during measurements by repeating topography scans for several voltages. Additionally, the piezo drift over the total measurement time is monitored and corrected.

Figure 2.1 and 2.2 summarize the STM characterization of 2 ML and 3 ML NaCl for sample voltages between −3 V and +3.5 V, thus spanning the entire band gap. An overview image of a NaCl-covered Au(111) region is shown in fig. 2.1A. The apparent height of the NaCl film is 309 ± 3 pm, as obtained from fitting a sigmoid function to the profile of the salt step, which is consistent with earlier studies of 2 ML NaCl on Au(111)[194]. Atop Au(111) (gray ring in fig. 2.1A), the dI/dV spectrum (inset fig. 2.1B) for a small voltage range close to the Fermi energy exhibits a pronounced step with an onset at ≈ −500 mV corresponding to the surface state[196]. For dI/dV spectra acquired atop NaCl, this onset shifts to ≈ −250 mV due to the Pauli interaction at the NaCl-Au interface. The image potential arising from the bare Au(111) surface is polarized and weakened by the presence of NaCl which acts as a dielectric[197,198]. Extending the voltage range for dI/dV spectra, we obtain the DOS of NaCl shown in fig. 2.1 B. The arrows indicate the onset of VB (−3 V) and CB (3.6 V).

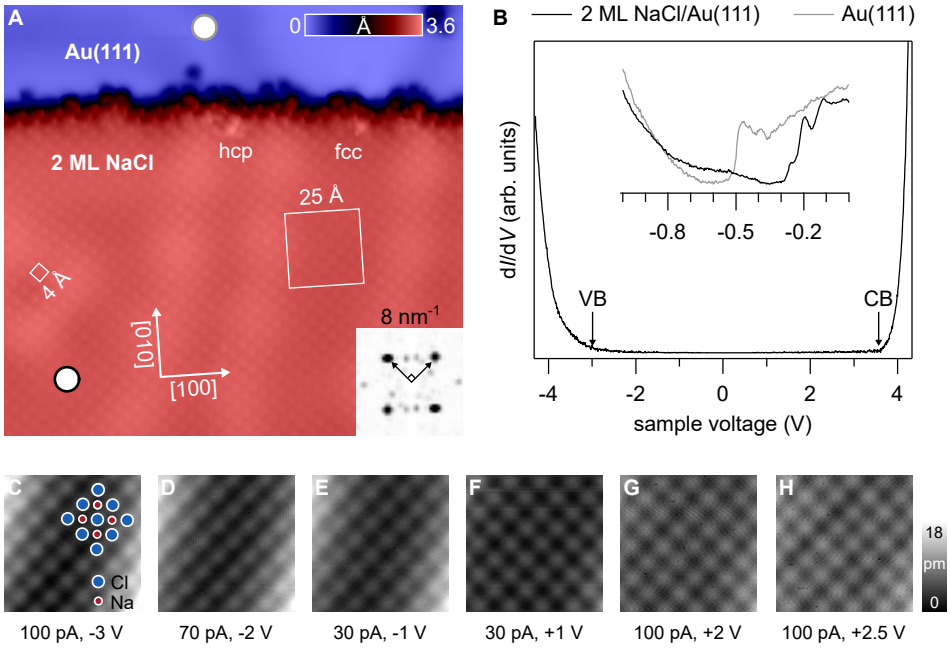

Figure 2.1 — STM topography images of 2 ML NaCl(100) on Au(111). (A) Overview topography image showing the area characterized (set point: I= 8 pA, V= −50 mV, size: 150 × 140 Å^2). 25 × 25 Å^2 region marked by the white box is investigated at sample voltages between −3.0 V and 2.5 V in panels C-H. Inset: Fourier transform of panel F centered over a 8 nm^{-1}×8 nm^{-1} region in the reciprocal space. (B) Large voltage range dI/dV spectra atop 2 ML NaCl(100)/Au(111) (marked by the black ring in A). The arrows indicate onset of VB and CB. Inset. Au(111) surface state and the related interface state atop 2 ML NaCl(100)/Au(111) measured at the gray ring and a black ring in A, respectively. (C-H) Raw STM topography data showing grayscale topography. The current and the voltage indicated in the figure. The red and blue dots indicate the positions of Na and Cl ions of the NaCl(100) lattice, respectively. Adapted from Leon *et al.* [200].

The white box in the face-centered cubic (fcc) area of NaCl/Au(111) (fig. 2.1A) is characterized with high stability for applied voltages in the range of −3 V and 2.5 V (fig. 2.1C-H). First, topographical features close to the VB edge at V= −3 V are analyzed in constant current mode. The grayscale image representing the z-height in fig. 2.1C shows a square lattice of protrusions which is replicated in the Fourier transform image (see inset fig. 2.1A). Each protrusion is assigned to a Cl ion based on earlier studies [189,192,199]. For other negative applied voltages (fig. 2.1C-E), no shift in the position of the square lattice is observed.

At positive voltages, the protrusions remain centered over Cl. In principle, electron extraction at negative voltage is helped at electron-rich Cl^- positions. Naïvely, electron injection at positive voltage would be helped at electron-poor Na^+ positions. The latter argument suggests that at positive voltages, the contrast in the grayscale image (fig. 2.1F-H) should be inverted due to Na^+ ions leading to the maxima instead of Cl^-. A cationic CB would have led to such a contrast inversion, but its absence proves that this cannot be the case. Both VB and CB are anionic in character, with Cl acting as an electron donor and acceptor in NaCl.

On a 3 ML NaCl film (apparent height: 484 ± 5 pm, from sigmoid function fit to NaCl step), the voltage range of topography measurements are extended to 3.5 V, close to the CB edge, as shown in fig. 2.2. In contrast to the data presented above, for 3 ML NaCl, the hexagonal close-packed (hcp) region is studied. This allows excluding differences arising

from the patterned crystal structure of Au(111). Lauwaet *et al.*[201] reported that both Na and Cl lattice sites are resolved in the local DOS map in the hcp region of 2 ML NaCl on Au(111) using a Cl terminated tip. However, in contrast to the experiments, the computed STM images show Cl atoms in both fcc and hcp regions, even when the enhanced electron density in the hcp region is accounted for. Their findings highlight the role of significant electrostatic interactions due to Cl termination of the tip and the small tip-sample distance ($I = 600$ pA, $V = 0.6$ V) used. Even though a metallic termination of the tip employed in the experiments cannot be guaranteed, the much smaller set point used ($I = 8$ pA) rules out any substantial tip effects.

Again, the tip stability is significantly reduced under large positive voltages resulting in an increased number of streaks in the topography images due to tip changes while scanning. Still, the atomic resolution is retained throughout the data set. We use Fourier filtering to remove low and high-frequency noise. Filtered topography images are shown in fig. 2.2H-N with Na lattice positions marked by white dashed lines. During the short data acquisition time of ≈ 10 min, the absolute piezo drift along the x- and y- axis is less than 0.14 Å min^{-1} and significantly smaller than the Cl^--Na^+ ion spacing of ≈ 3 Å.

Topography imaging close to VB, at -3 V, reproduces the square lattice of protrusions assigned to the Cl^- ions. Repeating the measurement at positive voltages ranging from 3 V to 3.5 V, close to the CB edge at ≈ 3.6 V, reveals no evidence for a shift from Cl^- to Na^+. Thus, it can be concluded that this holds for NaCl film thickness, hcp and fcc areas of Au(111), and differently prepared tips (fig. 2.1 and 2.2).

The experiments show that tunneling through NaCl is indeed on Cl at both the valence and conduction band. The electronic structure of NaCl can be visualized as bystander Na^+ cations which bind Cl^- anions that are mainly responsible for electron conduction.

Tight-binding calculations

Tight-binding calculations[2] have been performed for 3 ML NaCl(100) on Au(111) using two different sets of parameters for either CB mainly of Na 3*s* (fig. 2.3A) or Cl 4*s* character (fig. 2.3B). The first set of parameters theoretically reproduces the naïve picture of the NaCl electronic structure, where CB is of Na character. Beside including 3*s* and 3*p* states on the Cl atoms[181], the Madelung potential is neglected. As the energy is increased through the bandgap, the character of the state shifts from being mainly of Cl character close to the VB to having a significant Na character close to the CB. However, this picture contradicts the experimental findings presented earlier.

The second set of parameters includes 3*p* and 4*s* states of the Cl atoms, along with Madelung potential, and yields a CB of mainly Cl character. Not only are the VB and CB of Cl character, but also throughout the bandgap, the gap states[3] are of Cl character in line with the experimental findings shown in fig. 2.1.

[2]A detailed discussion of tight-binding calculations and parameters employed can be found in the supplementary information available online at: `https://doi.org/10.1038/s41467-022-28392-8`.
[3]Metal states of the Au(111) support that are transferred through the ions in NaCl buffer.

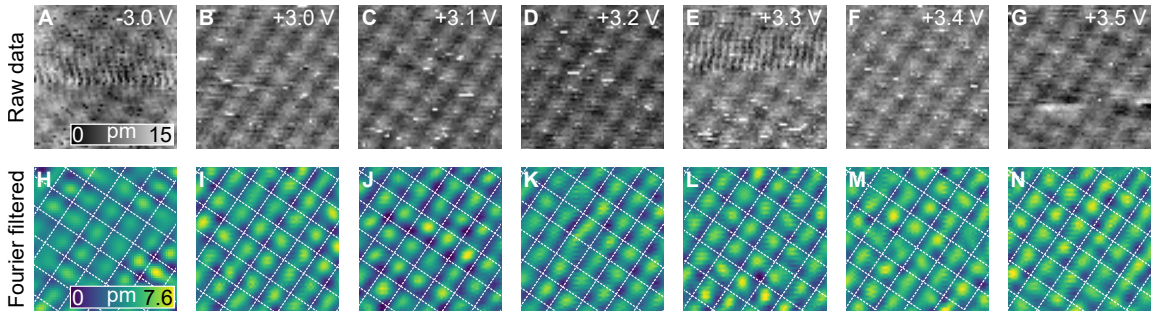

Figure 2.2 — STM topography images of 3 ML NaCl(100) on Au(111) at voltages close to the band edges. (A-G) Raw (grayscale) and (H-N) Fourier filtered (colored) STM topography images at the voltages indicated (set point: I= 15 pA, size: 24 × 24 Å^2). The white dashed lines in panels H-N mark the position of Na ion rows of the NaCl(100) lattice. Adapted from Leon *et al.*[200].

Since tunneling through the bandgap of the insulator proceeds via the electronic states of the nearest neighboring bands, a Cl^- based VB and a Na^+ based CB would result in contrast inversion at a specific voltage within the bandgap as shown in fig. 2.3A. As discussed earlier, such an inversion is absent in the experiments. The tight-binding calculations for the second set of parameters thus corroborate the notion that CB and VB have most of their weight on the Cl^- in NaCl (fig. 2.3B).

A two-pronged argument based on classical electrostatics and higher energetic cost due to having to accommodate the extra tunneling electron in a 4*s* orbital, with Cl^- being negatively charged and having a full shell electron configuration [Ne]$3s^2 3p^6$, it would predict that an electron greatly favors tunneling through positively charged Na^+. In the following, we argue how a Madelung potential of a few eV could flip the order of Na 3*s* and Cl 4*s* states, leading to a CB of mainly Cl character.

Role of Madelung potential

In an ionic crystal, formed of an equal amount of cations and anions, the positive ions experience attraction and repulsion from ions of opposite charge and ions of the same charge. The potential at any ionic position in such a crystal due to the combined electrostatic potential of the infinite number of ions in the crystal is called Madelung constant[202]. Thus, it is related to the crystal structure and depends on the lattice parameters, anion-cation distances, and molecular volume of the crystal. For bulk NaCl composed of fully ionized atoms, the Madelung potential is given by[203]

$$V = 1.7476 \frac{e^2}{4\pi\epsilon_0 d} = 8.92 \text{ V},$$

where $d = a_{\text{NaCl}}/2 = 2.82$ Å is the separation between nearest neighbor Cl and Na atoms[4], ϵ_0 is the vacuum electric permeability and we assume full positive and negative elementary

[4]The calculated reduced lattice parameter $a_{\text{NaCl}} = 5.54$ Å for 3 ML NaCl on Au is used instead of $a_{\text{NaCl}} = 5.63$ Å for bulk NaCl[204].

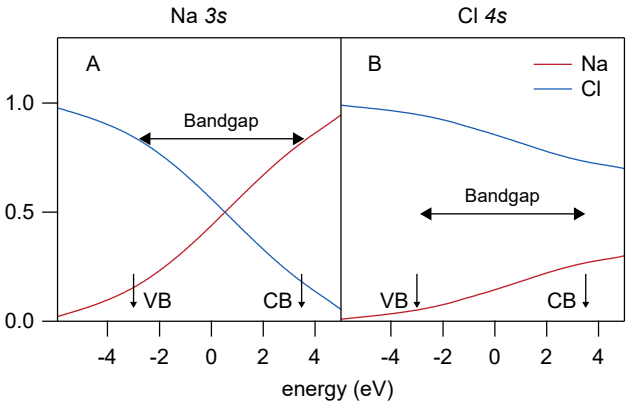

Figure 2.3 — Character of the gap states of NaCl including the contribution of Madelung potential. Normalized relative weight of gap states on the Na and Cl atoms in the outermost NaCl layer as a function of energy *E*. The parameters were tuned (see text) so that the conduction states have mainly (A) Na character and (B) Cl character. Arrows mark the position of valence and conduction band obtained from d*I*/d*V* spectra. Adapted from Leon *et al.*[200].

charges on Na and Cl, respectively. Tight-binding calculations for bulk NaCl give the net charge of 0.805 of the ions, which reduces the Madelung potential to 7.18 V. Nevertheless, a large Madelung potential may lead to a significant upward shift of the Na 3*s* level of a neutral atom from −5.1 eV[205] to above the vacuum level. Then the question arises if the Madelung potential could pull down the 4*s* level of a free Cl^- ion below the Na 3*s* level. To work it out, we use a gedanken experiment where Cl nuclear charge is increased by two. The Cl^- is turned into K^+, for which 4*s* level is determined to be at −4.1 eV[205]. Using Slater's rules[184] the 4*s* state of K^+ can be approximated as

$$\phi_{4s} \approx r^{2.7} \exp(-2.2r/3.7),$$

where 2.2 is the effective nuclear charge, and $n = 3.7$ is the effective principal quantum number. The resultant attractive potential on the 4*s* state due to the increased nuclear charge of Cl by $\Delta Z = 2$ corresponds to the Madelung potential of 8.9 eV. Thus rationalizing the reversed order of the Cl^- 4*s* level and the Na^+ 3*s* level due to Madelung potential, resulting in a CB of mainly Cl character in NaCl. Here, it is essential to note that the atoms in NaCl are not fully ionized, which would lead to a smaller Madelung potential. However, the qualitative discussion is robust since the STM measurements show well-defined topographical features over Cl ions.

Tight-binding calculations show that the interpretation of the NaCl electronic structure presented here for NaCl on Au(111) is also valid for bulk NaCl. The charge transfer to the substrate, evidenced by the work function reduction, results in an increased potential of the outer layers of NaCl. However, the effect on the potential difference between Na and Cl sites in the outermost layer is negligible. The assumed lattice parameter of the NaCl film on Au(111) (smaller) and its finite thickness affect the Madelung potential inversely. Adding up all effects, differences of tens of meV are found between bulk NaCl and NaCl film on Au(111), implying applicability of the effects observed here also for bulk NaCl.

In summary, it is found that the CB of NaCl is of mainly Cl character. A large Madelung potential pushes the Na 3*s* level upwards and pulls the Cl 4*s* level downwards from above the vacuum level. An empirical calculation suggests that the Madelung potential could reverse the order of Cl^- 4*s* and Na^+ 3*s* levels, making a CB mainly anionic in character plausible.

2.2 Role of gap states in tunneling through the molecule

Thin films of NaCl are routinely used as a buffer layer to electronically decouple molecules from metallic substrate for STM[54,206] and STML studies[21,66,76,125]. The voltage range employed in these experiments is −3 V to 3 V so that the electrons tunnel through the NaCl bandgap. The interpretation that CB has an anionic character has consequences for how the molecule couples to the substrate. Since the electrons mainly tunnel through Cl^- states for either voltage polarity, the electrons have wave functions of mainly Cl character. The arising modifications for coupling of an adsorbed molecule to the NaCl are found to favor specific molecular orbitals, which play an essential role in tunneling through the molecule through the HOMO-LUMO gap.

Model calculations[5] of tunneling through the gap show that the HOMO-LUMO gap states can be described as linear combinations of bound molecular orbitals. Moreover, the molecular orbitals at energies far from the gap can play an essential role. Guided by these theoretical findings, we perform experiments on a prototypical single PtPc molecule adsorbed atop 3 ML NaCl for voltages in the HOMO-LUMO gap (see fig. 2.4) and discuss them in the following. A tight-binding calculation for PtPc adsorbed atop 3 ML NaCl on Au(111), accounting for the role of energetically lower-lying orbitals, reproduces the experimental results well and is briefly presented later.

STM topography of a decoupled molecule in the HOMO-LUMO gap

Structurally, the PtPc molecule comprises a Pt atom at the center of four isoindole units linked by a ring of nitrogen atoms (see the ball and stick model in fig. 2.4A). In the optimized geometry for the PtPc obtained using the density functional theory (DFT) (B3LYP), the Pt atom is in the molecular plane, indicating a planar structure. The geometry optimization calculation was performed with the initial geometry, where the Pt atom is moved out of the molecular plane by 0.5 Å. The result indicates that the released geometry obtained by this calculation is, in fact, planar. PtPc has a D_{4h} symmetry, thus having a fourfold rotational symmetry axis through the center of the molecule and four twofold symmetry axes going through the inner lying or the outer lying N atoms, respectively (see fig. 2.4A). Experimentally, atomic resolution STM imaging of the molecule atop 3 ML NaCl shows that the PtPc adsorbs on top of Na and is aligned along the [010] and [100] axis of the NaCl (fig. 3.1A). These observations are taken into consideration for the tight-binding calculation.

PtPc adsorbed atop 3 ML NaCl on Au(111) is characterized by dI/dV spectroscopy (fig. 2.4C) and STM imaging (fig. 2.4B). In the dI/dV spectrum for a decoupled PtPc molecule the two differential conductance maxima observed at ≈ -1.35 V and ≈ 2.1 V are assigned to HOMO and LUMO, respectively. Constant height dI/dV maps at voltages close to these peaks show the two orbitals. The eight-lobed structure of both HOMO and LUMO is in line

[5]The calculations were planned and carried out by Olle Gunnarsson, Max Planck Institute for Solid State Research, Germany.

with previous experimental studies of H_2Pc[54,207] and DFT calculations for PtPc presented in section 3.1.

For the voltages $V = -0.5$ V and 0.5 V in the HOMO-LUMO gap, the STM topography images shown in fig. 2.4D and E differ strongly from the images of either HOMO or LUMO, as it shows a four-lobed structure centered over the isoindole group of the molecule. An STM topography image represents approximately the contour of constant DOS or the local DOS itself (constant height map), both for a selected potential defined by the applied voltage (see discussion in section 1.1). However, it is not straightforward to reconcile the topography imaged by STM inside the gap, where the DOS of a molecule is nominally zero (fig. 2.4C). Repp *et al.*[54] rationalized the in-gap image, which instead of being transparent, appears as a featureless protrusion based on extended tails of the molecular levels which contribute to local DOS at energies close to Fermi level. The orbitals are broadened from a theoretical width of a few tens of μeV to ≈ 100 meV (see fig. 2.4C) due to phonon interaction with the substrate thus resulting in a minute, but non-zero, DOS in the gap. The calculations presented later show that the picture is more complicated, involving states much below the HOMO level that substantially contribute to the tunneling near Fermi energy.

The theoretical images of the PtPc obtained from the tight-binding calculations[6] accounting for the anionic character of the CB (discussed in section 2.1) and considering contributions from energetically lower-lying orbitals are shown in fig. 2.4D and E. The images are in excellent agreement with the STM topography image of the molecule at the same voltages (fig. 2.4D and E), suggesting that the structure in the gap is more than a "featureless protrusion"[54] and can now be explained by theory.

A calculation of their contribution elucidates the role of particular orbitals of PtPc for a theoretical image obtained in the gap region and is presented in the following.

Contributions of low energy orbitals to in-gap imaging of molecules

The wave function of the combined system used for calculations of the in-gap image was expanded in terms of the PtPc molecular orbitals to understand the shape of the theoretical images in figs. 2.4D and E. The wave function inside the molecule can be written as

$$|\psi_i\rangle = \sum_{j=1}^{182} c_j^{(i)} |j\rangle, \tag{2.1}$$

where the sum is over 182 eigenfunctions of the free molecule. The weights can then be calculated as

$$f_j = \sum_{-0.9 \le \varepsilon_i \le 1.3} |c_j^{(i)}|^2, \tag{2.2}$$

adding up the weight of the PtPc jth molecular orbital over states in the energy range $-0.9 \le \varepsilon_i \le 1.3$ eV, in the gap. Figure 2.5 shows f_j for important molecular orbitals of π-character, pointing out the molecular plane and a σ state in the molecular plane. The π-states are

[6] Here, only the resulting images from the said calculations are presented.

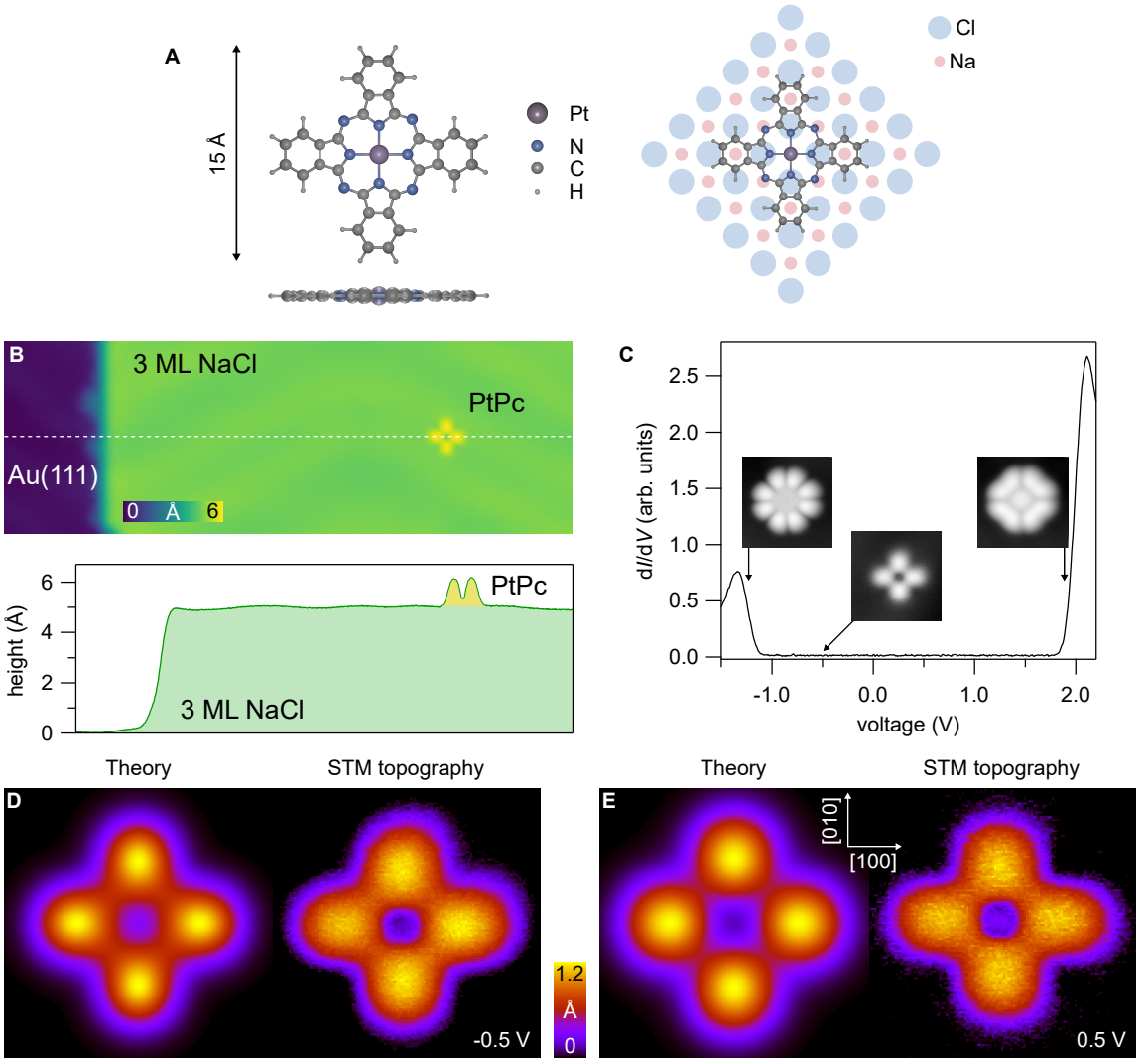

Figure 2.4 — Theoretical and experimental comparison of in-gap images of PtPc. (A). Ball and stick model top view of the PtPc molecule and its side view. Schematic illustration of PtPc adsorbed atop Na lattice site. (B) STM topography of PtPc adsorbed atop 3 ML NaCl on Au(111) (set point: I = 1 pA, $V = -1$ V, size: 30 × 10 nm^2). Height profile along the dashed line marked in B. (C) Constant height dI/dV spectra of PtPc molecule (set point: 20 pA). The insets show HOMO, in-gap, and LUMO images of the molecule at the sample voltages −1.25, −0.5, and 1.85 V, respectively (set point: 600 fA, size: 32 × 32 Å^2). (D, E). Theoretical images (16 × 16 Å^2) and STM topography images (23 × 23 Å^2, $I = 500$ fA) of PtPc for energies $\varepsilon = -0.5$ eV and 0.5 eV for z = 7 Å, tip distance similar to experimental distance of the tip.

Table 2.1 — Contributions to the weights in the interval $-0.9 \leq \varepsilon \leq 1.3$ eV from some π-orbitals with different n_p-values, one σ-orbital, the HOMO and LUMO orbitals. "Other" shows the contributions in Fig. 2.4 from orbitals which were not assigned an n_p value and "Rest" shows the many small contributions not shown in the figure.

$n_p = 0$	$n_p = 1$	$n_p = 2$	σ	HOMO	LUMO	Other	Rest
0.27	0.17	0.05	0.04	0.01	0.09	0.07	0.30

labeled by the number of angular nodal planes n_p, i.e., planes through the center of and perpendicular to the molecule and the surface. In cases where such nodal planes are not well defined, the corresponding state is labeled as "Undef". States with a given value of n_p have different numbers of "radial" nodes, assuring orthogonality. Although the ends of this interval are only 0.4 eV from the HOMO (at -1.3 eV) or LUMO (at 1.7 eV), these states only contribute 1% and 9%, respectively, to the total weight in this interval suggesting that the gap states are not merely linear combinations of the frontier orbitals either. The contributions from states with a well-defined n_p-value are summed up. These results are presented in Table 2.1. Interestingly, three $n_p = 0$ states and six (including degeneracy) $n_p = 1$ states contribute almost half the weight. The $n_p = 2$ states and the σ-state contribute little. States with less well-defined angular nodes shown in fig. 2.5 contributions are of the same order. Many other states, each with a small contribution and not shown in the figure, contribute around one-third of the weights.

The symmetries of these states, and thus their contributions to the DOS, result in the theoretical image of the PtPc in the HOMO-LUMO gap, which is in excellent agreement with the STM topography images. Figure 2.5 illustrates that the Au-PtPc coupling via NaCl is far from trivial and that the coupling to specific molecular orbitals is greatly favored. NaCl provides a buffer between the Au substrate and the PtPc molecule and influences the coupling in non-uniform ways, favoring the coupling to specific molecular orbitals.

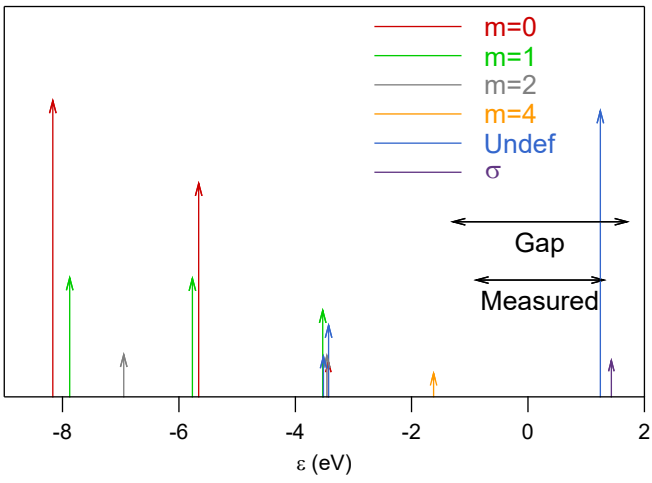

Figure 2.5 — Weights f_j of important molecular orbitals summed over gap states in PtPc between $\varepsilon = -0.9$ eV and 1.3 eV, where the energy range is marked by the arrow "Measured". The π states are labeled by their m values. We also show one σ state, with a strong coupling to Pt. States with more complicated pattern where the nodal planes are not well-defined are labeled "Undef". The states shown in the figure contribute 69% of the total weight. The remaining contribution comes from many molecular orbitals with rather small weights. The $m = 1$ states are doubly degenerate, and the weights of the degenerate states were added.

Conclusion

In summary, the findings presented in this chapter demonstrate that the CB of a prototypical alkali halide, NaCl, is of anionic (Cl) character. Tight-binding calculations reconcile the experimental findings of STM topography images that involve tunneling through NaCl at either voltage polarity by showing that it predominantly occurs through Cl^- ions. It is proposed that a large Madelung potential flips the order of Na 3*s* and Cl 4*s* levels, making a CB of mainly Cl character plausible. These findings suggest taking a closer look at other ionic compounds or other materials whose VB and CB take on unusual combinations of cationic or anionic character[208,209].

The new interpretation of the electronic structure of NaCl, along with including contributions from molecular orbitals at energies well below the HOMO-LUMO gap, allows, for the first time, to understand the molecular in-gap structure. The experiments show that the STM topography image is mainly determined by the electronic structure of the adsorbed molecule, even when the tunneling is through the gap. These findings explain why the molecule's orientation atop NaCl influences tunneling through it substantially. Given these findings, we reconsider mechanisms that involve tunneling through the HOMO-LUMO gap of the molecule, like up-conversion electroluminescence[37] (see discussion in section 3.4). Because of the modified electronic coupling between PtPc-Au via NaCl may also require reanalyzing the proposed role of the dielectric in the plasmonic gap[210,211].

3

Orbital engineering of single molecule STML

This chapter reports on the control of STM-induced luminescence efficiency and onset voltage of a single PtPc molecule. Using substrates with different work functions, the energy of the PtPc orbitals can be engineered to enable bipolar emission and control the associated emission efficiency. Energy level alignment of molecular orbitals plays a central role in governing the excitation mechanism, whether it be carrier injection or energy transfer from the plasmon (see section 1.2). These two mechanisms compete such that one or the other excitation mechanism is dominant at a given applied voltage. We show that local atomic-scale electronic structure influences the PtPc dipole orientation and its excitonic energy due to defect-induced lifting of the degeneracy of the LUMO and LUMO+1 states. The alignment of the orbitals with respect to the Fermi level also controls the voltage onset of S_1 emission. Moreover, related emission phenomena such as up-conversion electroluminescence (UCEL) are also observed at both positive and negative sample voltage polarities. The proposed excitation mechanisms in the literature are discussed based on second-order autocorrelation measurements. A modified mechanism for UCEL based on perturbation theory is also proposed. These findings refine existing design principles to obtain higher emission efficiencies and lower turn-on voltages for molecular optoelectronic devices.

3.1 STM electroluminescence from a single molecule

A comprehensive understanding of the electronic excitation mechanism at the single-molecule level is central for a variety of novel luminescence phenomena observed in STML[21,79,134]. Due to the incipient instability of single molecules on the substrates, few studies have reported bipolar luminescence, and even fewer have studied the STML of the molecule in detail. An ultrathin layer of NaCl on Au(111) provides one such platform where molecular emission can be excited over a large voltage range, and the emission mechanism can be investigated. In the following, substrate and survey measurements are discussed.

Description of PtPc atop 3 ML NaCl on Au(111)

An isolated PtPc molecule decoupled from an Au(111) substrate by a 3 ML thick NaCl island is studied in this section. Figure 3.1A shows three PtPc molecules, each adsorbed atop a Na site of the underlying NaCl lattice, similar to the discussion in the previous chapter. The blue and red dots indicate the Cl and Na lattice sites. Differential conductance spectra obtained for the three molecules (on the positions marked by X) are shown in fig. 3.1D. The spectra exhibit resonance peaks corresponding to the HOMO−1/HOMO−2 (−2.8 V), HOMO (−1.35 V), and LUMO/LUMO+1 (2 V). The black arrows in spectrum II of fig. 3.1D point to the sample voltage used to acquire the topography images presented in fig. 3.1B. Figure 3.1B shows a topography image of molecule II at sample voltages corresponding to the degenerate HOMO−1/HOMO−2, the HOMO, and degenerate LUMO/LUMO+1 which are in agreement with the orbital maps in fig. 3.1C[1]. Note that the calculated DOS is typically represented in the plane of the atoms of a molecule. In contrast, the STM probes ≈ 4 to 7 Å above the molecular plane. This may result in a distortion of the orbital lobes. A more detailed discussion of this difference is provided in section 4.1.

The light emitted at the tunnel junction is recorded simultaneously with dI/dV spectra. To suppress any unwanted contribution of plasmonic light emitted from the tunnel junction (see fig. 1.5), the light is spectrally filtered using a bandpass filter (637 ± 7 nm, Semrock BrightLine). The filter allows only the S_1 emission from the molecule to arrive at the SPAD. The resulting light intensity as a function of sample voltage (filled circles) is shown along with the dI/dV spectra (solid line) in fig. 3.1D. For the voltage range ≈ −2.4 V to 1.8 V, no light intensity is detected by the SPAD, indicating that molecular emission is not excited even though electron transport for $V < -1.3$ V occurs through a molecular orbital (HOMO). Below −2.4 V, the onset of S_1 emission can be observed. The excitonic nature of this light emission is confirmed by STML spectra recorded at −2.8 V (fig. 3.1E). Similarly, for positive sample voltages above 1.9 V, S_1 emission can also be observed – which is a notable demonstration of *bipolar emission*. The voltage-dependent rise in intensity shows two steps due to different excitation mechanisms: direct charge injection from the tip to LUMO and, at higher voltages, to LUMO+1 [38] (inset in fig. 3.1D).

Figure 3.1E shows the STML spectra for the three molecules at −2.8 V and 2.2 V, exhibiting a sharp excitonic peak at ≈ 1.95 eV. Based on earlier work[38] and time-dependent density functional theory (TD-DFT) calculations (see section 4.1) this emission line is assigned to an electronic transition from the lowest singlet excited state S_1 to the singlet ground state S_0. It is important to note that HOMO−1 to LUMO transition is dipole forbidden for PtPc, and thus, no intensity for the corresponding emission is expected. The gray dashed line in fig. 3.1E marks the wavelength 635 nm (1.952 eV), the emission line for STML spectra obtained atop the molecules shown in fig. 3.1A. The almost identical emission energy obtained for the same sample voltage and tunneling current setpoint for molecules II and III compared to

[1]The theoretical calculations were performed by Asst. Prof. Kuniyuki Miwa, Institute for Molecular Science (分子科学研究所), National Institutes of Natural Sciences (自然科学研究機構), Japan.

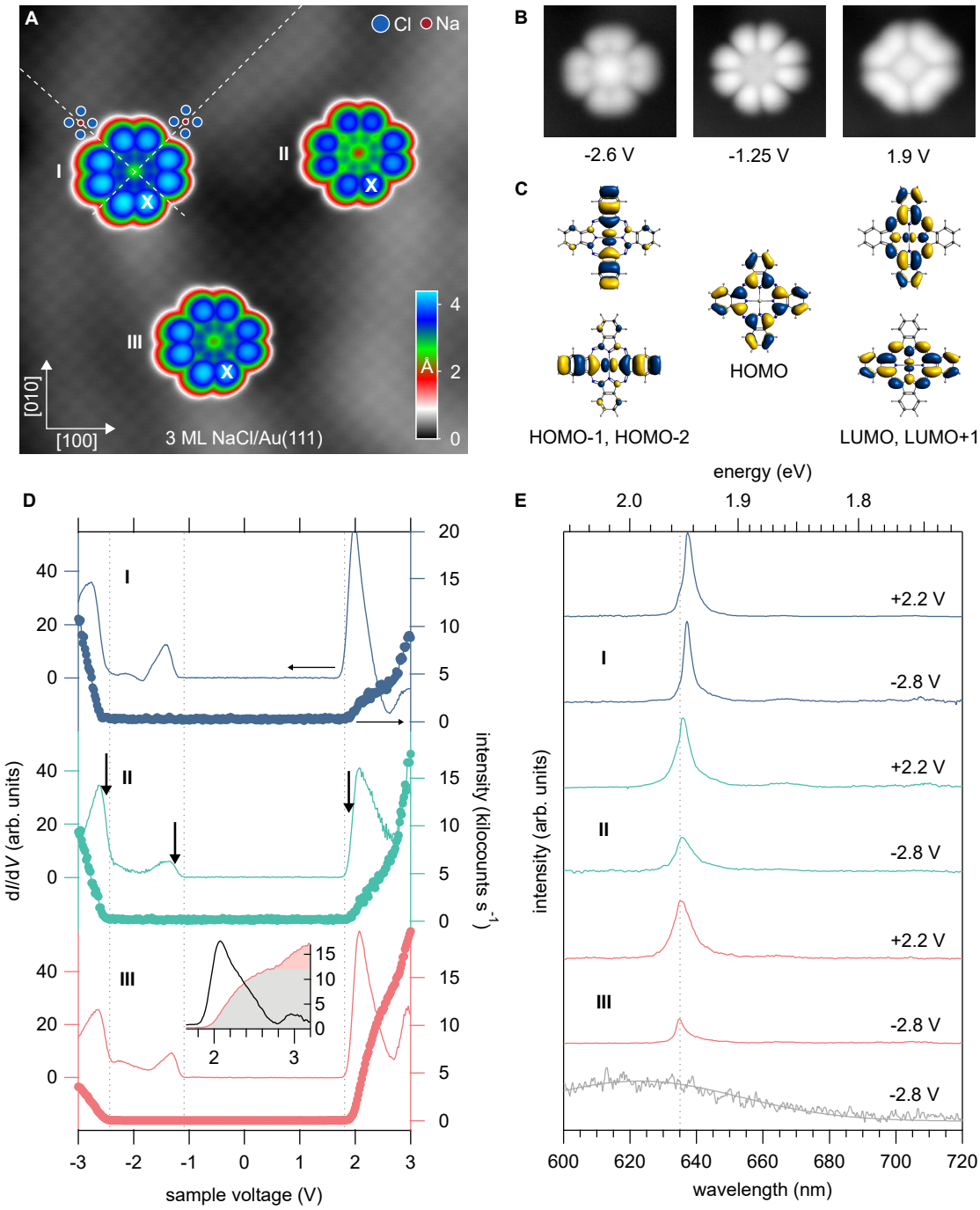

Figure 3.1 — Characterization of PtPc atop 3 ML NaCl on Au(111). (A) Overview topography image of PtPc molecules physiosorbed atop 3 ML NaCl on Au(111) (set point: $I = 20$ pA, $V = -1.23$ V, size: 10×10 nm^2). The white dashed lines are guides to the eye indicating absorption atop Na site. (B) Topography images of the molecule (II) at V corresponding to HOMO−1/HOMO−2, HOMO, and LUMO/LUMO+1 (black arrows in D) of the PtPc (set point: $I = 800$ fA, size: 3.6×3.6 nm^2). (C) Plots of molecular orbitals as obtained from DFT calculations. (D) dI/dV spectra (line) and spectrally-filtered (637 ± 7 nm) S_1 emission intensity (circles) obtained on each molecule (on the position marked by X) (set point: $I = 50$ pA, $V_{mod} = 20$ mV). The gray dotted lines mark the onset of molecular orbitals for III. Inset. Blow up of III showing two different emission regimes (gray and red, see section 3.1). (E) STML spectra obtained for the three molecules I, II, and III, and plasmon background (gray) on top of NaCl. Sample voltages are indicated next to the spectrum (set point: $I = 50$ pA, $t = 50$ s, plasmon: $t = 1$ s). The smooth gray line is the plasmon background used to normalize the excitonic spectra.

molecule I indicate that the modification of excitonic spectra due to tip effects is similar for different molecules. Small shifts, on the order of ≈2 meV (1.952 eV to 1.950 eV), are often observed for STML spectra of a molecule at different voltage polarities. These line shifts can be assigned to the Stark and Lamb effect due to different tip heights that result from constant current operation at a fixed tunneling current set point[212]. However, the emission line for molecular emission corresponding to molecule I at the same sample voltage and tunneling current setpoint appears at 639 nm (1.940 eV), exhibiting a shift of ≈ 12 meV (1.952 eV to 1.940 eV) compared to molecule II and III. The rigid peak shift of molecular orbital energies is evidenced by the different LUMO and HOMO onset for molecules I and II (see fig. 3.1D).

A similar shift of emission line has been reported by Doppagne *et al.*[207] for a free-base phthalocyanine (H_2Pc) molecule atop NaCl on Ag(111). NaCl on Ag(111) forms a Moiré pattern such that different absorption positions of H_2Pc molecule lead to differences in the local electronic environment of a molecule. Minor changes (≈ 20 to 30 mV) in molecular orbital peak positions are reflected in modified peak energies of the H_2Pc emission line. If the degeneracy of the molecular transition (see fig. 3.2E) is lifted, two emission lines are observed. The herringbone reconstruction of Au(111)[213] leads to an apparent height modulation of ≈ 15 pm which can be observed atop NaCl islands[194]. This results in a perturbation of the local electronic environment of the molecule similar to the Moiré pattern of NaCl on Ag(111) and thus, gives rise to the observed shift of molecular orbitals and S_1 emission.

Probing the local nano-environment

Changes in molecular emission can conversely be used to probe local electronic structure. Figure 3.2 shows the effect of Cl vacancies on the optoelectronic properties of a single molecule. The influence of a defect on the transition dipole moment is reflected in the observed STML spectra.

Figure 3.2A shows a topography image of an isolated molecule atop 3 ML NaCl island on Au(111) at a sample voltage $V = -1.7$ V. The HOMO of the molecule is imaged along with the atomically-resolved Cl lattice of the NaCl. As in fig. 3.1, it is straightforward to infer that the molecule is adsorbed atop a Na lattice site. This absorption position holds for the observations and discussion that follows. For a fixed tunneling current, differential conductance spectra are recorded on different lobes of the HOMO (I-V in fig. 3.2A). Experimentally, the tip height is defined by set point: I=4 pA, −1.6 V at tip position I. Employing the atom tracking module of the measurement software *Nanonis*[214], the highest position atop each lobe is determined and employed for data acquisition. In brief, in constant current mode, the tip moves along a circle with a radius of 50 pm. The tip height along the orbit is evaluated. Then, the center of the circle follows the gradient for about 1 min until the highest z-position is found. The piezo-drift for the measurement time of ≈ 3 mins is negligible. The dI/dV spectra obtained in this manner exhibit resonances at −1.4 and 1.9 V corresponding to the HOMO and LUMO of the molecule, respectively. For all tip positions, the HOMO onset is at −1.22 V, although an energy shift smaller than the amplitude of the Lock-in modulation

($V_{\mathrm{mod}} = 20$ meV) cannot be ruled out. At tip positions I, III, IV, and V, the LUMO onset is at ≈ 1.6 V compared to 1.65 eV at tip position II, indicating an upward shift of the LUMO by ≈ 47 meV (inset in fig. 3.2D).

STML spectra obtained at the same tip positions as dI/dV measurements are shown in fig. 3.2E. At tip position II, the emission from the molecule appears at ≈ 1.92 eV, redshifted from its energy of 1.95 eV. This opposite shift of the emission line and the HOMO-LUMO energy gap is counterintuitive and will be discussed later. At tip position I, the emission energy is 1.91 eV. This is because it involves excitation of the same molecular transition along the x-axis as position V, which exhibits an upward shift of LUMO (fig. 3.2F). For tip positions III and IV, a second peak is observed at 1.96 eV, which is the unperturbed transition of the molecule. Determining peak positions using Lorentzian peak fittings yields an energy difference of 42 meV, which is close to the upward shift of the LUMO level at position II (≈ 47 meV).

In the case of an unperturbed molecule, the two orthogonal molecular transition dipole moments are of the same magnitude as is evidenced by a single S_1 emission line (fig. 3.1E). Assuming that the dipole along the x-axis (yellow) is perturbed while the dipole along the y-axis (blue) is not, one would expect emission energy at tip position V to be 1.96 eV. The STML spectrum for tip position V reveals precisely that. Only a weak intensity is observed at the energy of the perturbed transition (1.91 eV) compared to the unperturbed transition.

Figure 3.2G presents a polar plot of the normalized intensities for the two emission lines, integrated over a width of 10 meV around the peak maxima. A sinusoidal fit to the data unambiguously reveals a phase shift of $\approx 15°$ in emission intensity maxima for the emission at 1.91 eV from the molecular axis, corresponding to the perturbed transition.

To analyze the nature of perturbation, we remove the molecule using tip manipulation and analyze the NaCl area on which the molecule had been adsorbed. Figure 3.2B presents the topography image of the area after the molecule has been removed. The blue halo marks the position of the molecule with respect to two blue dots, which are positioned on pre-existing Cl vacancy defects[215]. The molecule's ball and stick model shows roughly the benzene ring's position and isoindole unit over the Cl vacancies. Figure 3.2C illustrates the position of the adsorbed PtPc molecule with respect to the position of the vacancies, which are ≈ 2.8 and 8.4 Å away from the center of the molecule. Cl vacancies in the NaCl lattice imply that previously occupied Cl-derived states are now unoccupied and have now been moved above $E_{\mathrm{F,\,S}}$. Assuming that the energy of the new, unoccupied states is between $E_{\mathrm{F,\,S}}$ and the energy of the LUMO E_{LUMO} may explain the upward shift of LUMO because of Coulomb interaction. The role of Cl-derived states is supported by the highly localized spatial position of the degeneracy lifting, precisely above the vacancies (see fig. 3.2B and D). Here, it is essential to note that the above argument would also result in a downward shift of HOMO, which is not observed in the experiments.

On a detailed analysis of the topography (fig. 3.2A), a slight rotation of the molecule by 3° with respect to the [010] axis of the NaCl is observed. We propose that the defects change the local energy minimum and result in the rotation of the molecule from asymmet-

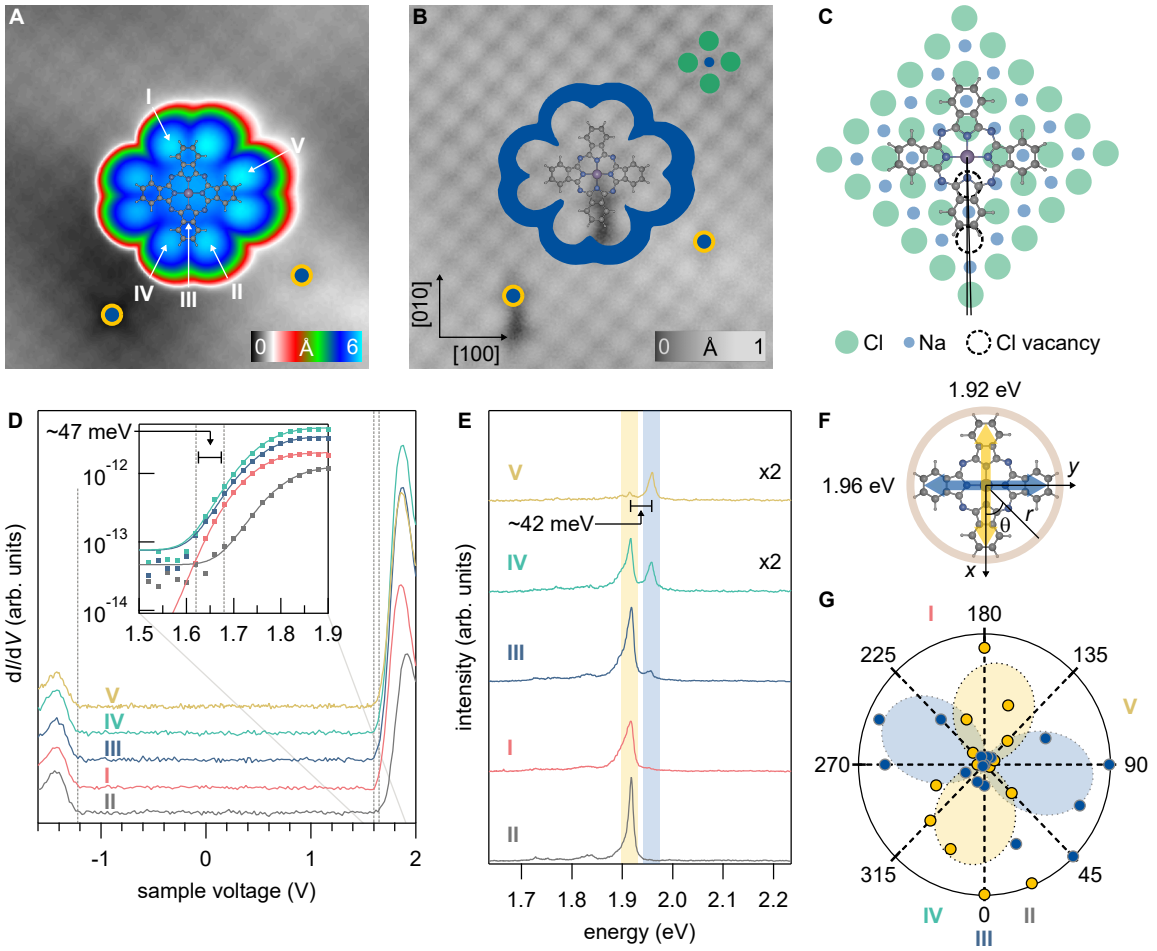

Figure 3.2 — Effects of local defects on the molecular transition dipole at the single molecule level. (A) STM topography image of PtPc adsorbed atop 3 ML NaCl on Au(111) (set point: $I = 2$ pA, $V = -1.7$ V, size: 5×5 nm^2). The blue dots mark positions of Cl vacancies. (B) STM topography image of the same area with the molecule moved away after the STML measurements had been performed (set point: $I = 1$ pA, $V = -1.3$ V). The blue halo, along with the ball and stick model of the molecule, marks the position of PtPc relative to the idealized defects (blue dots). (C) Schematic of PtPc adsorption atop a Na lattice position and the Cl vacancy defects (black dashed circles). (D) dI/dV spectra obtained atop the molecule at the positions I-V indicated in A (set point: $I = 4$ pA, $V = -1.6$ V, $V_{mod} = 20$ mV). Gray dashed lines mark the position of HOMO and LUMO onset. Inset – Blow up of LUMO onset showing a difference of ≈ 47 meV as obtained from fit using error function. (E) STML spectra showing two distinct excitonic lines at ≈ 1.96 eV and 1.92 eV obtained at the same positions atop PtPc as data shown in D (set point: $I = 100$ pA, $V = 2.2$ V, $t = 60$ s). The top three spectra are scaled by a factor of 2 for clarity. (F) Schematic showing the labeling of different parameters indicating tip position with respect to the molecular symmetry axes. (G) Polar plot of normalized intensities at the two peak positions 1.92 eV (yellow) and 1.96 eV (blue) obtained using Lorentzian peak fitting. The dotted lines are sinusoidal fits to the data.

ric absorption geometry (see fig. 3.1A). The rotation leads to the mixing of the previously degenerate LUMO and LUMO+1, leading to enhanced interaction between them (weak hopping element directly between the two orbitals or through NaCl). Besides the electrostatic effect of the vacancies, the hopping between the two LUMOs may amplify their rotation. The above arguments help rationalize the significant rotation of the transition even though a comparatively small rotation of the molecule.

The lifting of the degeneracy of the transition dipole moments may also be due to the strain induced in the molecule due to the tilting of the molecular plane induced by the vacancies. It has been shown that a strain of 5% along the molecular axis for H_2Pc can induce an energy difference of a few tens of meV[207] using TD-DFT calculations. PtPc being almost identical to H_2Pc except for the central Pt atom, is expected to behave similarly. This argument would also explain the change in transport gap at tip position II, above the Cl vacancies. In line with the discussion presented here, the DFT calculations show that for molecules of a size ranging from 1-2 nm, an upward shift of the LUMO is expected for increasing strain[216].

A degeneracy lifting of similar energy due to a nearby Cl vacancy (14 Å away) has been observed for an optical transition using STML[75]. One could speculate that this strain may also result in a rotation of the transition dipole moment and shift the energy of the molecular emission. The combined spatially-resolved electronic and optical characterization of PtPc allows probing minute perturbations in electronic structure due to local influences of vacancy defects on molecular transitions. However, further theoretical studies are necessary to elucidate the exact relationship between molecular orientation, molecular environment, and molecular dipole transitions on surfaces.

3.2 Effect of work function on STML

Differential conductance and STML voltage onset measurements show that orbital positions for PtPc atop NaCl on Au(111) span a large voltage range, for example, from ≈ -2.5 V to -1.2 V for HOMO and ≈ 0.7 V to 2.1 V for LUMO (see fig. 3.3). Since the charge injection into the molecule is necessary for its excitation, the S_1 emission onset depends on the energy level alignment of the HOMO with respect to the Fermi energy and the optical gap of the molecule[66,68,87] (see discussion in section 1.2). Thus, the large voltage range of the orbital energies enables examining varying conditions where different emission mechanisms can be at play.

For the majority of molecules analyzed, the orbital energies of HOMO and LUMO lie in the ranges $-1.6\,\text{V} \leq E_{\text{HOMO}} \leq -1.2\,\text{V}$ and $1.8\,\text{V} \leq E_{\text{LUMO}} \leq 2.2\,\text{V}$, respectively. However, a few molecules exhibit a rigid shift of their molecular orbitals, probably because of a sizeable local perturbation due to unidentified defects, with E_{HOMO} at much lower energies (-2.2 V to -2.6 V). The LUMO energies, too, are shifted down accordingly. In fig. 3.3A, the energy positions of the orbitals, along with the voltage onset of S_1 emission, are summarized. For the typical case with the symmetric alignment of the orbitals, bipolar electroluminescence is observed as reported in section 3.1. UCEL is observed at both voltage polarities for PtPc, whose orbitals

are shifted to ≈ −2.2 V. A detailed analysis of bipolar UCEL will be presented later in section 3.4. For further lowering of orbitals $E_{\mathrm{HOMO}} = -2.6$ V, comparatively intense S_1 emission sets in at $V = E_{\mathrm{HOMO}}$. Then, no S_1 emission is observed for positive sample voltages up to 2.5 V, even at high tunneling currents. In the following section, we rationalize different voltage onsets and efficiencies observed for STML. A new framework is introduced in section 3.4 to capture the role of orbital alignment in UCEL.

Since the measurements were performed for different sample preparations over a year, varying defect densities could play a role in these observations. Since the energy of HOMO and LUMO with respect to the Fermi energy is due to the substrate's work function, a shift in molecular orbital energy most likely stems from a work function variation at the nanoscale. It was shown earlier that defects in the top layer of NaCl (fig. 3.2) or herringbone reconstruction (fig. 3.1) can lead to a shift in orbital energy of about 100 meV. However, the origin of large shifts (≈ 1 eV) seen in fig. 3.3 could not be experimentally clarified. We assume that a high concentration of defects hidden underneath the molecule in the topmost or lower layers of NaCl or at the NaCl/Au(111) interface may be responsible for a significant local work function variation.

Figure 3.3B and D show typical $\mathrm{d}I/\mathrm{d}V$ spectra for, respectively, asymmetric and symmetric energy alignment of molecular orbitals. Since the orbital positions in the asymmetric case are similar to the one of a molecule atop NaCl on Ag(111)/Ag(100), the corresponding emission exhibits properties similar to prior studies[37,38,66,68,134]. The linear current dependence of the S_1 intensity at negative voltage $V < E_{\mathrm{HOMO}}$ shown in fig. 3.3E reflects a single electron transfer to the tip (hole transfer to HOMO), followed by electron hopping from the substrate through the NaCl barrier into the LUMO of the molecule. Electron-hole recombination results in the observed S_1 emission. This excitation mechanism is discussed in more detail in the next section. On the other hand, for very positive voltages (V>3 V), the S_1 emission is rarely observed[66]. The alignment of E_{HOMO} with the sample Fermi level, necessary for electron extraction from HOMO, is only achieved at large voltages where the constant current tunneling condition is unstable.

For the case of symmetric alignment of the orbitals around the Fermi energy (fig. 3.3D), the S_1 emission from PtPc is bipolar (as discussed earlier in section 3.1). Studies on ZnPc atop NaCl on Au(111), where the molecular orbitals are similarly aligned, exhibit S_1 emission only from the neutral molecule at positive voltages[76,217]. However, an electronic characterization of the emission, which is central to clarifying the emission mechanism, has not been reported. This calls for a detailed electronic characterization of S_1 emission from PtPc at positive voltages. Figures 3.3D, F, and G show the voltage and current dependence of S_1 emission from the neutral molecule (see discussion for fig. 3.8D) at sample voltages $V = -3$ V and 2.5 V. As reported earlier in fig. 3.1, for symmetric alignment of molecular orbitals, at negative voltage −2.4 V, the S_1 emission starts at the onset of the HOMO−1 state, indicating that electron extraction from HOMO−1 is the first step in molecular emission. Again, a linear dependence of the emission intensity on the current implies that only one charge transfers to the tip. The data shown in fig. 3.3F suggests that the intensity increases superlinearly as

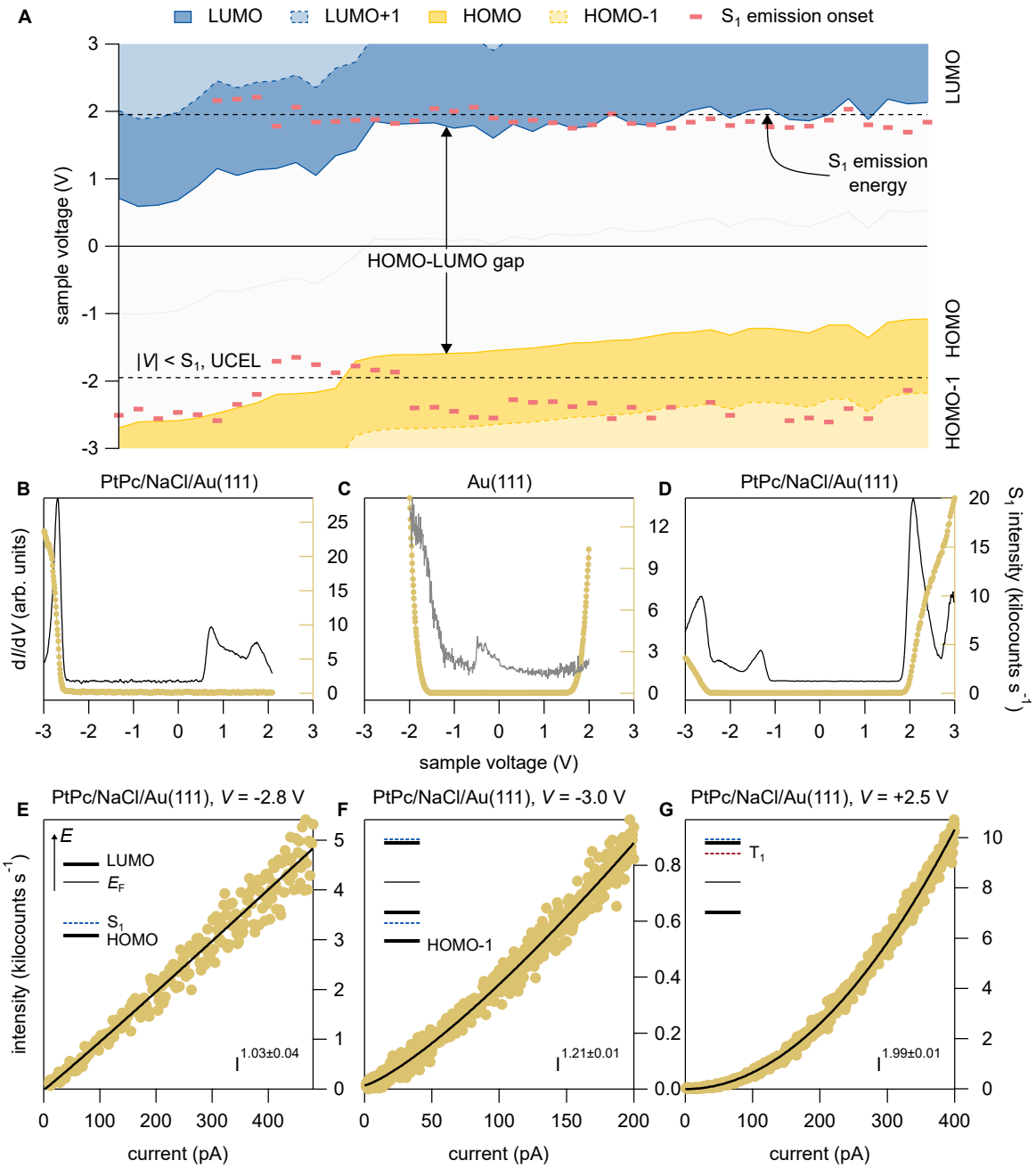

Figure 3.3 — Energy shift of molecular orbitals atop NaCl on Au(111). (A) Positions of HOMO (yellow) and LUMO (blue) obtained from fitting error functions to the onsets of conductance and valence resonance peaks. The dashed, lighter shaded areas represent the same for HOMO−1 and LUMO+1. Red dashes mark the voltage onset of S_1 emission. The black dashed lines mark the energy of S_1. The gray solid line indicates the center of the HOMO-LUMO gap. (B) d*I*/d*V* spectra for asymmetric energy alignment of PtPc orbitals, (C) for bare Au(111) substrate, and (D) for symmetric energy alignment of PtPc orbitals (set point: $I = 50$ pA, $V_{mod} = 20$ mV, 5 mV, and 20 mV). (E-F) Current dependence of spectrally-filtered S_1 intensities from PtPc atop 3 ML NaCl on Au(111) for the indicated sample voltages (integration time per point: $t = 50$ ms).

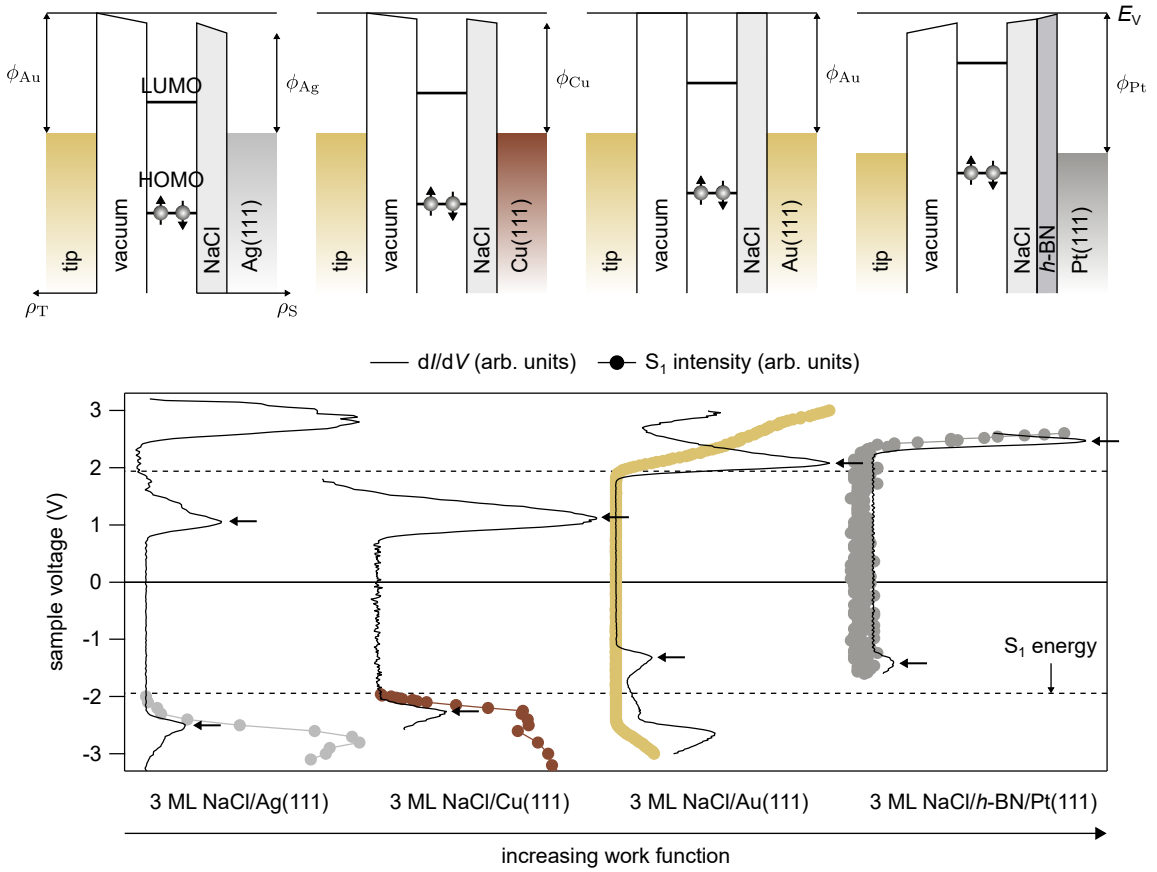

Figure 3.4 — Energy alignment of PtPc orbitals atop different substrates. *Top* – Schematic energy diagrams showing HOMO and LUMO with respect to the Fermi level on different metal substrates at sample voltage $V = 0$ V (left to right - increasing work function). *Bottom* – dI/dV spectra (black) and onset of S_1 light emission for a PtPc molecule atop the indicated substrates (Ag(111): $I = 20$ pA, V_{mod}=20 mV, $t = 50$ ms, Cu(111): $I = 20$ pA, $V_{mod} = 20$ mV, $t = 10$ s, Au(111): $I = 50$ pA, $V_{mod} = 20$ mV, $t = 50$ ms, and Pt(111): $I = 50$ pA, $V_{mod} = 20$ mV, $t = 50$ ms). The black arrows mark the HOMO and LUMO. The black dashed lines indicate the energy of S_1.

the current is increased. This may be due to an additional contribution from the plasmonic emission. Section 3.3 discusses the excitation mechanism through HOMO−1 in more detail.

For positive voltage polarity, the S_1 emission sets in at ≈ 1.9 eV, close to the onset of LUMO. This observation indicates electron injection from the tip to the LUMO as the first step in the excitation process. Since injection of only one charge is required for excitation, the S_1 intensity is expected to depend linearly on the current. Surprisingly, a quadratic dependence is observed (see fig. 3.3G), even in a regime in which the sample voltage $V > E_{S_1}$, where the energy from one charge injection event should be sufficient for S_1 excitation. In literature, a quadratic dependence of emission on the current has only been reported for UCEL (see section 1.2), where the applied voltage is below the S_1 energy and thus the excitation is mediated by the T_1 acting as a relay state[37,38]. The persistence of quadratic dependence calls for a deeper analysis of the emission mechanism. Under these tunneling conditions, even though there may be a linear contribution, the quadratic one remains dominant.

To explore different emission mechanisms without the unknown element that leads to work function variations for NaCl on Au(111) (fig. 3.3A), different metallic substrates were

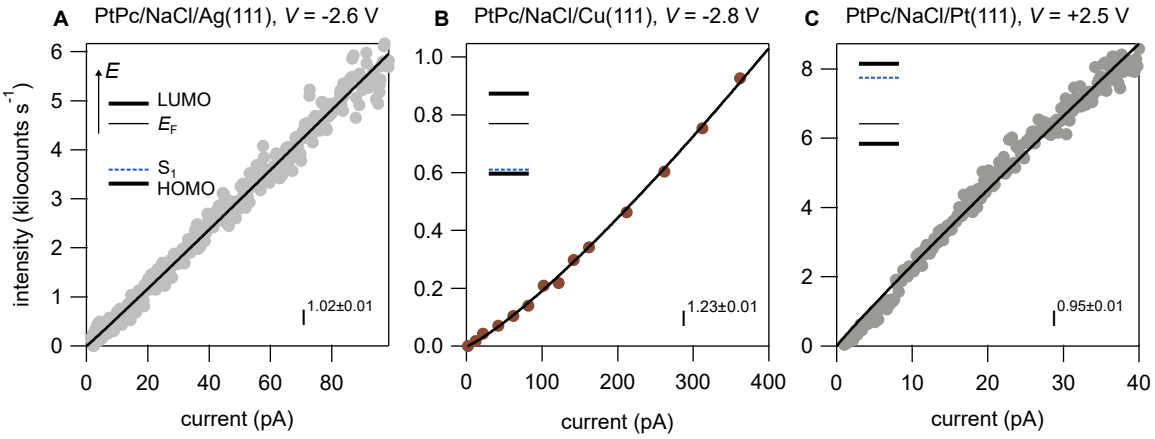

Figure 3.5 — Current dependence of S_1 emission intensity (spectrally filtered) for a single PtPc molecule atop 3 ML NaCl on the metal substrates indicated. The black solid line is a power law fit to the raw data with the respective power (and its error) indicated at the bottom right of each panel.

Table 3.1 — Work function ϕ_S values determined by *I(z)* spectroscopy (see discussion in section 1.1) at $V = -0.2$ V for 3 ML NaCl atop different substrates. The decay constants from exponential fit current versus tip-sample gap atop bare substrate κ_S and 3 ML NaCl κ_{NaCl} convert to a work function change ($\Delta\phi$) as: $\Delta\phi = 0.01905(1/\kappa^2_{NaCl} - 1/\kappa^2_{Au})$ (nm^{2}eV). The work function change with respect to ϕ_S from literature [218] is reported.

NaCl/Ag(111)	NaCl/Cu(111)	NaCl/Au(111)	NaCl/*h*-BN/Pt(111)
3.5±0.1 eV	3.8±0.1 eV	4.3±0.1 eV	4.6±0.1 eV

employed. Using NaCl on Ag(111), Cu(111), Au(111), and *h*-BN/Pt(111), the energy of the orbitals can be tuned in a well-defined manner from the asymmetric case as defined in fig. 3.3B, close to a symmetric alignment in fig. 3.3D. The data presented for PtPc atop 3 ML NaCl on Cu(111) is evaluated using intensities obtained from Lorentzian fitting of the optical spectrum for increasing currents. Interestingly, for PtPc atop NaCl on *h*-BN/Pt(111), the orbital alignment is asymmetric in favor of the excitation for positive voltages. Figure 3.4 shows a schematic of orbital energy alignment for the different substrates. Table 3.1 lists the work functions of the substrates covered with NaCl. On 2 ML NaCl/*h*-BN/Pt(111), the LUMO is higher in energy than on 2 ML NaCl/Au(111), at ≈ 2.4 V as compared to 1.9 V (fig. 3.4). Correspondingly, the S_1 emission sets in at the energy of LUMO. However, differently from PtPc atop NaCl on Au(111), the S_1 emission intensity shows a linear dependence on current (fig. 3.5C). This finding indicates that the S_1 excitation by electron injection from the tip to the LUMO involves a one-electron process. No molecular emission is observed at negative voltages between 0 and -2.7 V. The energy alignment on Cu(111) is still asymmetric, with the HOMO energy at ≈ -2.2 V. A voltage for which an electron may resonantly tunnel through HOMO would be larger than the energy of S_1. Qualitatively, the voltage dependence of the emission onset (fig. 3.4), and the current dependence of the S_1 intensity (fig. 3.5A and B) for PtPc atop NaCl on Cu(111) follow the same trends as PtPc atop NaCl on Ag(111). This indicates that the same S_1 excitation mechanism is at play.

3.3 Excitation mechanism for asymmetric and symmetric energy alignment

In the following, the excitation mechanism at play for the different energy alignments of the molecular orbitals with respect to the Fermi energy is discussed.

Excitation mechanism for asymmetric orbital alignment in favor of HOMO

The voltage dependence of the S_1 intensity shows an onset corresponding to the energy of the HOMO (fig. 3.3B), indicating that electron extraction from HOMO is the first step in molecular excitation. A schematic of the mechanism proposed by Miwa *et al.*[219] for S_1 excitation of H_2Pc atop NaCl on Ag(111) is shown in fig. 3.6A-D. For voltages, $0 > V > E_{\mathrm{HOMO}}$ (energy position of the HOMO), the molecule is in its ground electronic state with the singlet spin state of the molecule $|\mathrm{N}, \mathrm{S}_0\rangle$, where N is the number of electrons in the molecule. For $V < E_{\mathrm{HOMO}}$, the electron can tunnel from the molecule to the tip. The formed electronic cationic doublet spin state $|\mathrm{N}{-}1, \mathrm{D}_0\rangle$ means that the previously Coulomb blocked injection of electrons from the substrate to the LUMO is now possible. The neutral molecule is then in its excited state $|\mathrm{N}, \mathrm{S}_1\rangle$, with the decay of the exciton leading to the observed light emission and the molecule returning to the ground state $|\mathrm{N}, \mathrm{S}_0\rangle$.

Between electron extraction from the molecule to the tip and electron injection from the substrate, only the former can be directly probed by the tunneling current. The process described above results in a linear increase in S_1 intensity as the current increases. This is indeed what is observed for PtPc atop NaCl on Ag(111) and Cu(111) (see fig. 3.5A and B).

Excitation mechanism for asymmetric orbital alignment in favor of LUMO

The mechanism explained above can be easily modified to explain the S_1 excitation mechanism for PtPc atop NaCl on *h*-BN/Pt(111) for both voltage polarities by invoking particle-hole symmetry. Figure 3.6E-F illustrates the schematic for S_1 excitation involving a one-electron process. For a sample voltage $0 > V > E_{\mathrm{LUMO}}$, electron injection from the tip to the molecule (LUMO) is inhibited. For $V > E_{\mathrm{LUMO}}$, the tip Fermi energy aligns with the LUMO promoting resonant tunneling into the orbital. When an electron tunnels to the LUMO, an anionic doublet state $|\mathrm{N}{+}1, \mathrm{D}_0\rangle$ is realized allowing previously blocked tunneling of an electron (hole) from the HOMO (substrate) to the substrate (HOMO). The neutral molecule is now in its excited state $|\mathrm{N}, \mathrm{S}_1\rangle$ and returns to the ground state $|\mathrm{N}, \mathrm{S}_0\rangle$ by electron-hole recombination. The one-electron process directly monitored in the tunneling current is the injection of electrons from the tip to the molecule.

Excitation mechanism for symmetric orbital alignment *at negative voltage*

For PtPc atop NaCl on Au(111), we typically observe S_1 emission from the neutral molecule at both positive and negative voltages (see fig. 3.1E). ZnPc and H_2Pc atop the same substrate

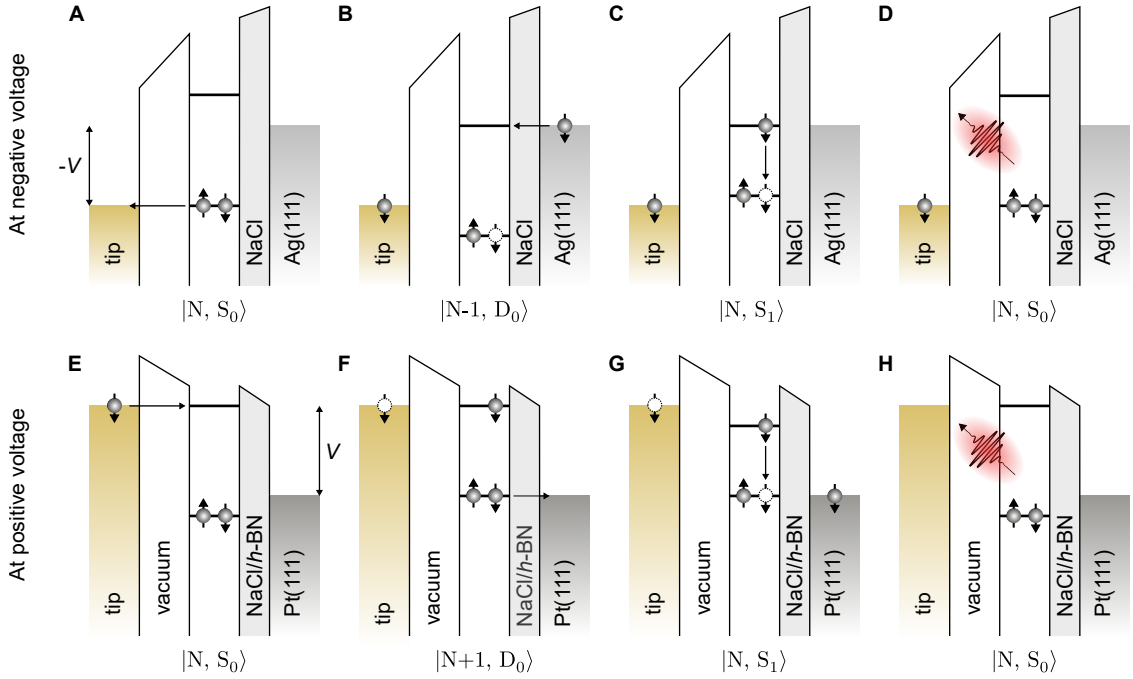

Figure 3.6 — Schematic of the excitation mechanism involving a one-electron process for an isolated single molecule at negative (A-D) and positive (E-H) sample voltage. The electronic states of the molecule are indicated as $|N, S_m\rangle$, where N and S_m denote the number of electrons and the electronic state of the molecule, respectively.

exhibit S_1 emission from the cationic state of the molecule at negative sample voltage[76,77] (see fig. 3.8D). However, for PtPc only the S_1 emission of the neutral state is observed (see discussion in section 3.4). The excitation mechanism for S_1 emission at negative voltage involving the HOMO−1 is discussed below. Even though the electron can be extracted out of HOMO at $V < E_{\mathrm{HOMO}}$, no S_1 emission is observed, even for $|V| > E_{S_1}$ (see fig. 3.1 and 3.4). The lowering of orbital levels upon creation of $|N-1, D_0\rangle$ state (fig. 3.6B) is not large enough to align the LUMO with the substrate Fermi energy. The carrier injection is thus Coulomb blocked. The above discussion helps reconcile the low efficiency of the S_1 excitation due to the energy alignment of PtPc orbitals atop NaCl on Au(111). As seen in fig. 3.3F, the S_1 emission sets in at $V < E_{\mathrm{HOMO-1}}$ and exhibits a linear dependence on current. For $V < E_{\mathrm{HOMO-1}}$, the electron can be extracted out of the HOMO−1, which upon fast internal conversion from HOMO to HOMO−1 leads to the formation of a cationic doublet state $|N-1, D_0\rangle$ (see fig. 3.7). The doublet state makes electron injection from the substrate feasible, which results in the formation of the S_1 excited state of the neutral molecule. The molecule returns to its ground state $|N, S_0\rangle$ by photon emission.

The above arguments explain the different emission onsets and efficiencies corresponding to the participating orbitals' wide range of energy alignments. However, the quadratic current dependence of S_1 intensity for voltages larger than the S_1 energy is not captured within this framework. So far, the quadratic dependence of S_1 intensity for a neutral molecule has only been reported for voltage V less than E_{S_1} energy. Both, Chen *et al.*[37] and Farrukh *et al.*[38], propose that the triplet state acts as a relay state, making available the energies of

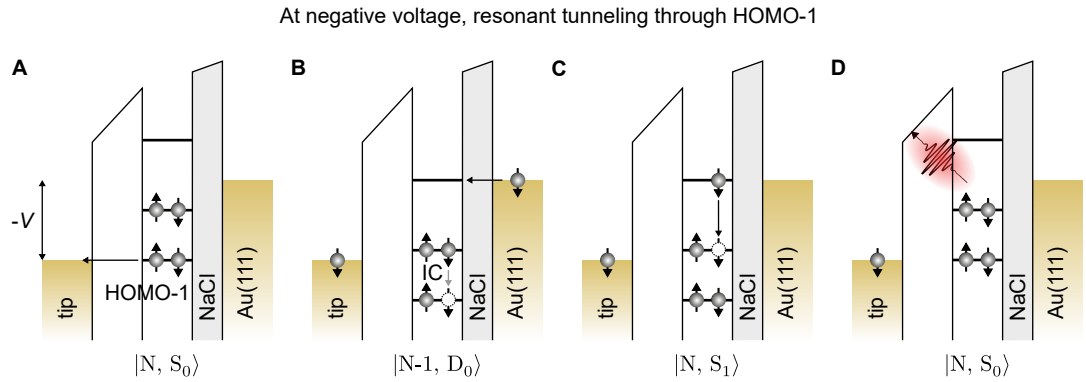

Figure 3.7 — Schematic of the excitation mechanism involving a one-electron process for an isolated single molecule and symmetric position of the HOMO and LUMO with respect to the Fermi level (Au(111) substrate) at large negative sample voltage where resonance tunneling happens through the HOMO—1.

two consecutive tunneling electrons, thus leading to up-conversion. Thereby, the S_1 state can be excited, although the energy conservation does not allow direct S_1 excitation. In the following, a study of UCEL from PtPc atop NaCl on Au(111) is presented using STML and, distinctly, HBT-STM enabled correlation measurements. Guided by these results, Olle Gunnarsson suggested a framework that describes the emission and lower efficiency for S_1 emission at $+V > E_{S_1}$. The key arguments are presented in the following section. Additionally, the implications of energy level alignment for the observed UCEL intensities are discussed, and a new mechanism is proposed which captures these details.

3.4 Spin-triplet mediated up-conversion electroluminescence

In a recent work, Chen *et al.*[37] studied UCEL from an isolated H_2Pc atop NaCl on Ag(100) ruling out a range of previously assigned mechanisms. An intermediate relay state must be invoked to explain the capture of multiples of the electron energy. Observation of UCEL from a single molecule rules out the intermolecular triplet-triplet annihilation[145,146]. Since the emission is observed at low currents in the picoampere range, which is at least two orders of magnitude lower than up-conversion in metallic tunneling junctions, also up-conversion due to co-tunneling of carriers[97,220] cannot be the dominating excitation mechanism. Based on the observation that S_1 emission sets in at the energy of the T_1 state and a quadratic current dependence of the emission intensity, Chen *et al.*[37] suggest that it is the spin-triplet state that acts as the relay state for up-conversion.

The mechanism involves a two-step process. First, the electron is excited into the T_1 state via energy transfer from inelastic scattering (IES). Next, the metastable T_1 state can be promoted to the S_1 state by a similar energy transfer, resulting in the formation of the excited singlet state of the neutral molecule. The mechanism can be summarized as

$$|\mathrm{N}, \mathrm{S}_0\rangle \xrightarrow{\text{IES}} |\mathrm{N}, \mathrm{T}_1\rangle \xrightarrow{\text{IES}} |\mathrm{N}, \mathrm{S}_1\rangle \rightarrow |\mathrm{N}, \mathrm{S}_0\rangle$$

Alternatively, the metastable T_1 state could now lead to the decay of the cationic doublet state

$|N{-}1, D_0\rangle$ as described in fig. 3.6B. The doublet state enables the next electron injection to occur directly into the LUMO, forming the singlet excited state of the neutral molecule $|N, S_1\rangle$, and leading to S_1 emission. This mechanism can be summarized as

$$|N, S_0\rangle \xrightarrow{\text{IES}} |N, T_1\rangle \rightarrow |N-1, D_0\rangle \rightarrow |N, S_1\rangle \rightarrow |N, S_0\rangle$$

Theoretical simulations show that the latter process, involving inelastic excitation and two sequential carrier injections, is ≈ 16 times more efficient than the former process, involving two inelastic excitation steps[37]. However, no experimental evidence for the dominance of the latter process has been reported.

The physical difference between the two excitation mechanisms proposed for UCEL is that the state $|N{-}1, D_0\rangle$ is only realized in the mechanism involving sequential carrier injection steps. The formation of such an intermediate charged state exhibits antibunching in the intensity correlation measurements using HBT-STM[70]. Suppose the time constant for creating the doublet state followed by an electron capture process is larger than the time-resolution of the correlation measurement setup. In that case, the resulting photon emission will be detected one at a time. Given that, the observation of antibunching for UCEL may suggest carrier injection rather than two inelastic scattering or energy transfer events as the leading mechanism.

For an Ag(111) substrate, the energy alignment of the orbitals is asymmetric in favor of emission by charge extraction out of the HOMO, and UCEL is observed only at negative voltages. Using symmetric energy alignment of the orbitals enabled by an Au(111) substrate, we obtain UCEL at both voltage polarities for PtPc atop 2 ML NaCl. Such a study allows scrutiny of the proposed mechanism over a wide range of experimental conditions. HBT-STM measurements under UCEL conditions provide evidence for the dominance of a carrier injection process over the one requiring two IES events (see fig. 3.10).

For the mechanism proposed in the literature, excitation to the T_1 state via a spin-flip of the electron in HOMO of the ground state is essential. Chen *et al.* suggest that IES enables both the electronic excitation and the change in spin-multiplicity necessary for the proposed mechanism. Earlier inelastic electron tunneling spectroscopy (IETS) studies of molecular layers in a metal-insulator-metal tunneling junction have observed triplet excitation of H_2Pc but only for very high currents in the range of few mA[221,222]. Moreover, spin-orbit coupling (SOC) could also provide the required spin-flip. The low currents employed in the single molecule study[37,38] (in pA range) and a very small SOC for the molecules used[159], suggests a very low efficiency for either of these spin-flip mechanisms. We propose a modified mechanism for UCEL (see fig. 3.11) invoking a fourth-order perturbation argument that allows spontaneous carrier extraction from HOMO to the tip (at negative voltages), eliminating the need for spin-flip.

Bipolar up-conversion electroluminescence

Figure 3.8 outlines the observation of UCEL for PtPc atop 2 ML NaCl on Au(111) using STML. An overview topography image is shown in fig. 3.8A. Both H_2Pc and PtPc molecules are found on the same NaCl island physisorbed at slightly different locations of the Au(111) herringbone reconstruction. As discussed in section 3.1, the different local nano-environment affects the energy of the orbitals (fig. 3.8B) and leads to observation of both unipolar and bipolar UCEL (fig. 3.8C). The STML spectra at the voltage $V = -1.84$ V evidences that the electron energy is indeed smaller than the observed S_1 emission energy. The dashed lines mark the quantum cutoff energy given by the applied voltage, and S_1 emission from PtPc (at 1.95 eV) is clearly observed. For the PtPc molecule marked by a blue dot, S_1 emission is still observed at sample voltages of -1.52 V and $+1.6$ V. However, S_1 emission is observed only at positive voltage polarity ≥ 1.67 V for the molecule marked by a green dot. Chen *et al.*[37] showed that S_1 emission sets in at the energy of T_1 emission E_{T_1}, in line with the conclusion that the T_1 state acts as a relay state. However, in our experiments, S_1 emission could not be observed at voltages below the ones reported in fig. 3.8C. Note that for the two PtPc molecules atop NaCl on Au(111), the HOMOs are at -1.3 V (green) and -1.6 V (blue), whereas, for the H_2Pc molecule atop NaCl on Ag(100), the HOMO is at -2.45 V. The reduced intensity of UCEL atop NaCl on Au(111) as compared to Ag(111) may be due to an upward shift of molecular orbitals based on the UCEL mechanism discussed later.

Based on previous studies[76,77], emission from the cationic state is expected at negative voltages for a Au(111) substrate. However, for the PtPc molecule studied here, no electrofluorochromism is observed at voltages up to -2.7 V (fig. 3.8D). This observation suggests that the molecule is not charged at negative voltages, and the analysis of the UCEL mechanism is free of any contribution from a cationic state of the molecule. The top (black) STML spectrum shown in fig. 3.8D exhibits emission lines corresponding to both a neutral (X^0) and a cationic state (X^+) of PtPc atop 3 ML NaCl on Ag(111). Here, proximity to a vacancy in NaCl lifts the degeneracy of LUMO and LUMO+1 and leads to formation of a charged state. The emission line corresponding to X^+ is at 1.38 eV for PtPc, close to the X^+ emission observed for H_2Pc at 1.40 eV. The low quantum efficiency of the CCD detector at energies around 1.4 eV (less than 2%) makes it hard to probe the X^+ emission for PtPc atop NaCl on Au(111) hard. In the voltage range relevant for UCEL -1.95 V $> V >$ 1.95 V, electrofluorochromism is not significant, and thus its role in UCEL is not considered in the following discussion.

The high stability of PtPc atop NaCl on Au(111) enables electronic characterization of the S_1 emission at comparatively high tunneling currents (nA range). Figure 3.8E shows a constant height dI/dV measurement for PtPc in the voltage range from 1 V to 2.4 V. The dI/dV spectrum exhibits the expected LUMO/LUMO+1 and LUMO+2 peaks at 1.7 V and 2.4 V, respectively. An additional peak at 1.16 V is observed, which cannot be easily assigned. For an additional inelastic electronic excitation channel, an increase in conduction of a few percent at the energy of the state ($T_1 \approx 1.27$ eV) is expected[223]. However, it should result in a step and not a peak in the dI/dV spectrum (or a peak in the d^2I/dV^2 spectrum). Expectedly,

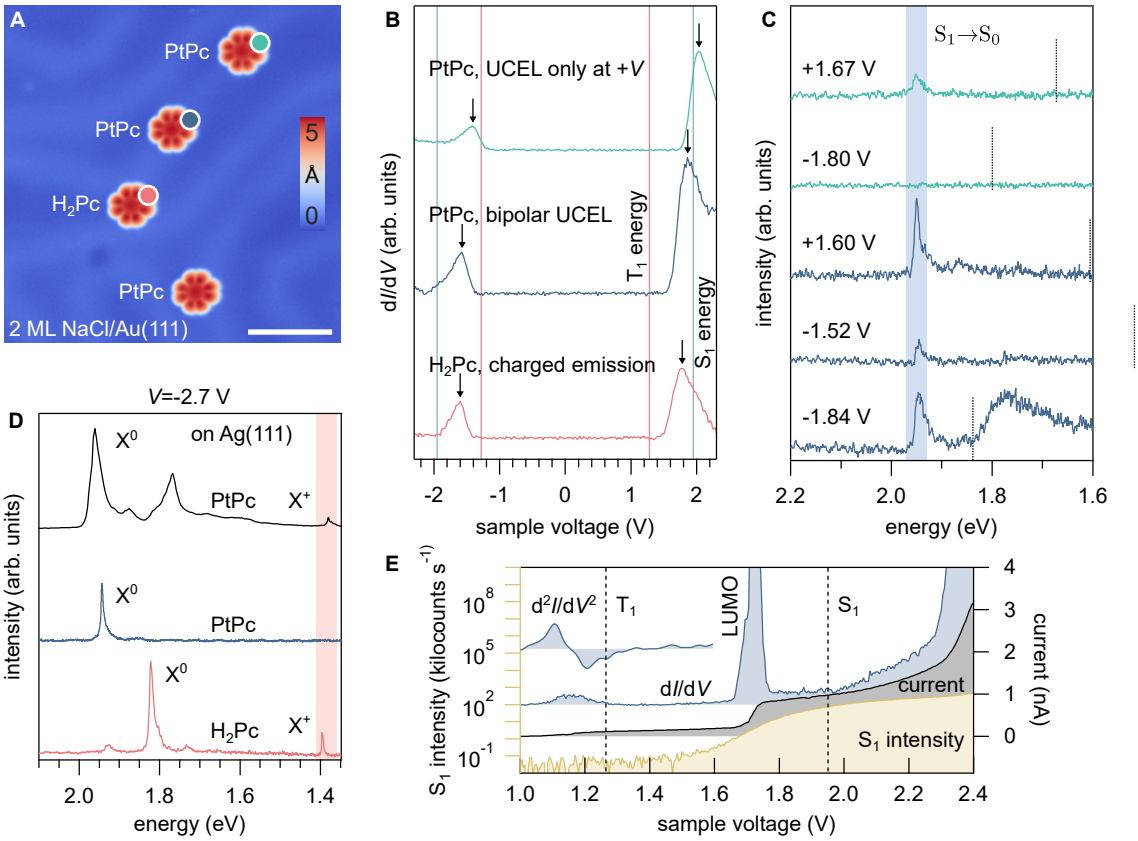

Figure 3.8 — Bipolar UCEL on single phthalocyanine molecules. (A) STM topography image of the overview area showing PtPc and H_2Pc molecules atop 2 ML NaCl on Au(111) (set point: $I = 800$ fA, $V = -1.8$ V, scale bar: 5 nm). The red, blue, and green dots color-code the position of measurements in panel B-D. (B) dI/dV spectra (set point: $I = 5$ pA, $V = -2.3$ V, $V_{mod} = 20$ mV). (C) STML spectra obtained on the PtPc molecules exhibiting UCEL at either sample voltage polarity (set point: $I = 80$ pA, top to bottom: $t = 5$, 10, 5, and 3 mins). The dotted lines indicate the energy cutoff of the tunneling electrons given by the applied sample voltage. (D) STML spectra showing emission lines for the neutral (X^0) and cationic (X^+) state of the molecule. The gray spectrum (top) shows the emission line of the cationic PtPc molecule atop NaCl on Ag(111) (set point: $I = 60$ pA, $V = -2.7$ V, $t = 60$ s). (E) Voltage dependence of dI/dV, current, and S_1 intensity (set point: $I = 4$ nA, $V = 2.5$ V). Inset. d^2I/dV^2 curve obtained from numerical derivation of the dI/dV spectrum. The black dashed lines mark the energies of T_1 and S_1.

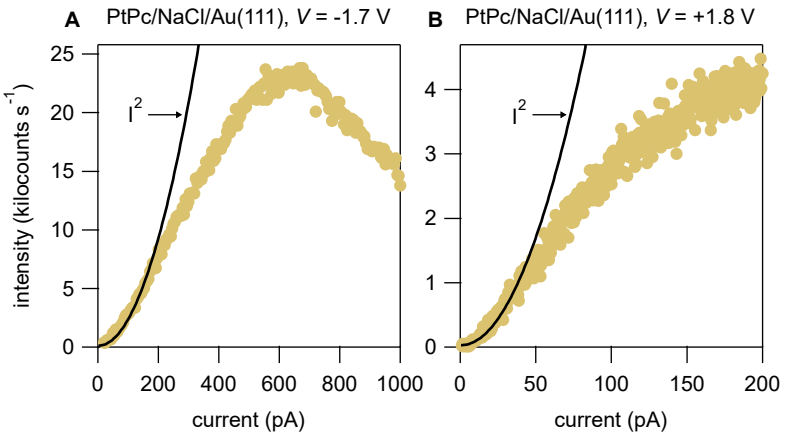

Figure 3.9 — Current dependence of the up-converted S_1 emission intensity (spectrally filtered) for a single PtPc molecule atop 2 ML NaCl on Au(111) at negative (left) and positive (right) sample voltage ($t = 50$ ms). The black solid line is a guide to the eye for intensity scaling quadratically with tunneling current.

for an isolated perylene tetracarboxylic di-imide (PTCDI) molecular layer, a peak in d^2I/dV^2 spectra has been reported at ≈ 1.1 V. The peak energy exhibits a shift from the observed T_1 emission at 1.24 eV, surprisingly similar to the energy mismatch observed between the peak in dI/dV at 1.16 V and T_1 emission for a single PtPc molecule. In conclusion, the appearance of the peak, which could not be rationalized, necessitates a more precise characterization to clarify this observation. The simultaneously recorded S_1 emission intensity turns on at ≈ 1.5 V, clearly exhibiting UCEL.

Characterization of the current dependence of the S_1 emission for UCEL, shown in fig. 3.9, exhibits the expected quadratic dependence corresponding to two sequential carrier injection steps. Extending this measurement to currents of a few hundred picoamperes reveals saturation, followed by quenching, of the up-converted S_1 emission (fig. 3.9A). At these currents, the decreasing electron injection interval competes with the time scale of the up-conversion process. Additionally, the change in tip-sample distance results in a stronger plasmonic enhancement leading to deviations from the quadratic dependence.

HBT-STM at UCEL conditions

As discussed earlier in this section, the S_1 intensity autocorrelation provides additional evidence for the dominance of a carrier injection mechanism for UCEL in single-molecule STML. The basic principle of HBT-STM is described in section 1.3. A schematic of the experimental setup is shown in fig. 3.10A. The light emission from the tunneling junction is passed through bandpass filters (637±7 nm) before it is focused on the SPADs. The filters substantially reduce the plasmonic emission, but its remaining contribution adds a constant offset in the correlation measurement.

Figure 3.10B shows second-order correlation measurements for a voltage $V = 2.2$ V and tunneling currents 120 pA, 250 pA, and 400 pA (bottom to top). Antibunching dips at zero time delay exhibit $g^{(2)}(0) < 0.5$, indicating single-photon emission[224]. The measurements qualitatively reproduce the findings of single-photon emission at negative voltages from single ZnPc molecules in STML reported by Zhang *et al.*[70]. As shown schematically in fig. 3.6, the S_1 excitation mechanism at both voltage polarities is qualitatively identical. The time constant, obtained from fitting exponential functions, decreases with increasing tunneling current. The time constant $\tau = 0.77$ ns at I=120 pA, V=2.2 V is similar to the one reported by Zhang *et al.* at the same tunneling current but at $V = -2.5$ V indicating that the excitation mechanisms at both voltage polarities (discussed in fig. 3.6) are qualitatively similar. Out of the different steps in the excitation mechanism, only the doublet state (fig. 3.6B) may introduce a time constant in the range of 2 ns. For the emission mechanism illustrated in fig. 3.5, the time constant of the doublet state τ_{res} is estimated by

$$\tau_{res} \approx \left(\frac{1}{\tau} - \frac{I}{e}\right)^{-1}, \tag{3.1}$$

where τ is the time constant obtained from the $g^{(2)}(\Delta\tau)$ measurement, I is the tunneling

current, and e is the elementary charge. The estimated τ_{res} for the tunneling currents used in the correlation measurements (shown in fig. 3.10B) are summarized in Table 3.2. Absence of an antibunching dip in $g^{(2)}(\Delta\tau)$ measurements for STM-PL[96] which does not involve a transiently charged state suggests that the exciton lifetime is shorter than the time-resolution of the HBT setup ($\approx$ 50 ps).

A second-order correlation measurement under UCEL conditions, V=1.85 V, at a voltage $\approx$ 100 meV lower than the S_1 emission energy, exhibiting $g^{(2)}(0) < 0.5$ is shown in fig. 3.10C. A small tunneling current I = 30 pA is used for this measurement to rule out any contributions from competing mechanisms that lead to intensity saturation at higher tunneling currents (fig. 3.9B). Given the quadratic dependence of emission intensity on tunneling current and the low intensity ($\approx$ 3000 photons s^{-1}), a long integration time (up to 6 h) is necessary to obtain a good signal-to-noise ratio in $g^{(2)}(\Delta\tau)$. The piezo drift over a few hours is compensated by employing atom tracking atop a LUMO lobe similar to the experiments presented in section 3.1. Due to the smaller tip-sample distance for UCEL ($V < E_{LUMO}$), the plasmonic contribution is significant, and thus, filtering the S_1 line becomes crucial. Observing an apparent antibunching dip in UCEL confirms that the carrier injection mechanism is the dominant mechanism. This finding is considered for the UCEL mechanism proposed in the next section.

Even though a comparatively small tunneling current I=30 pA (average time interval between tunneling electrons $\approx$ 5.3 ns) is employed, the time constant obtained for UCEL (exponential fitting) is similar to that obtained for tunneling currents more than an order of magnitude larger for conventional STM-EL. Using equation 3.1, a residence time of $\approx$ 0.3 ns is obtained for the doublet state, which is an order of magnitude shorter than the one obtained for conventional STM-EL ($\approx$ 2 ns). This can be explained by the reduced tip-sample distance for tunneling conditions used for UCEL ($V < E_{S_1}$) as compared to conventional STM-EL ($V > E_{S_1}$). For voltages in the HOMO-LUMO gap, the tip-sample distance is reduced by at least 2 Å at the same current, as estimated from the z-height values in constant current dI/dV measurements. Besides a larger plasmonic enhancement, the reduced tip-sample distance also increases the tip-induced electric field. This may alter the residence time of the doublet state formed prior to exciton formation in the UCEL process discussed in section 3.4.

This observation is supported by constant height light emission efficiency maps for the PtPc molecule employing sample voltages smaller (fig. 3.10D-F) and larger (fig. 3.10G-I)

Table 3.2 — Residence time of the doublet state τ_{res} as given by equation 3.1, for the time constant τ obtained from second order correlation measurements, and the tunneling current I.

I (nA)	τ (ns)	τ_{res} (ns)
0.12	0.77	1.89
0.25	0.49	2.08
0.40	0.33	1.89

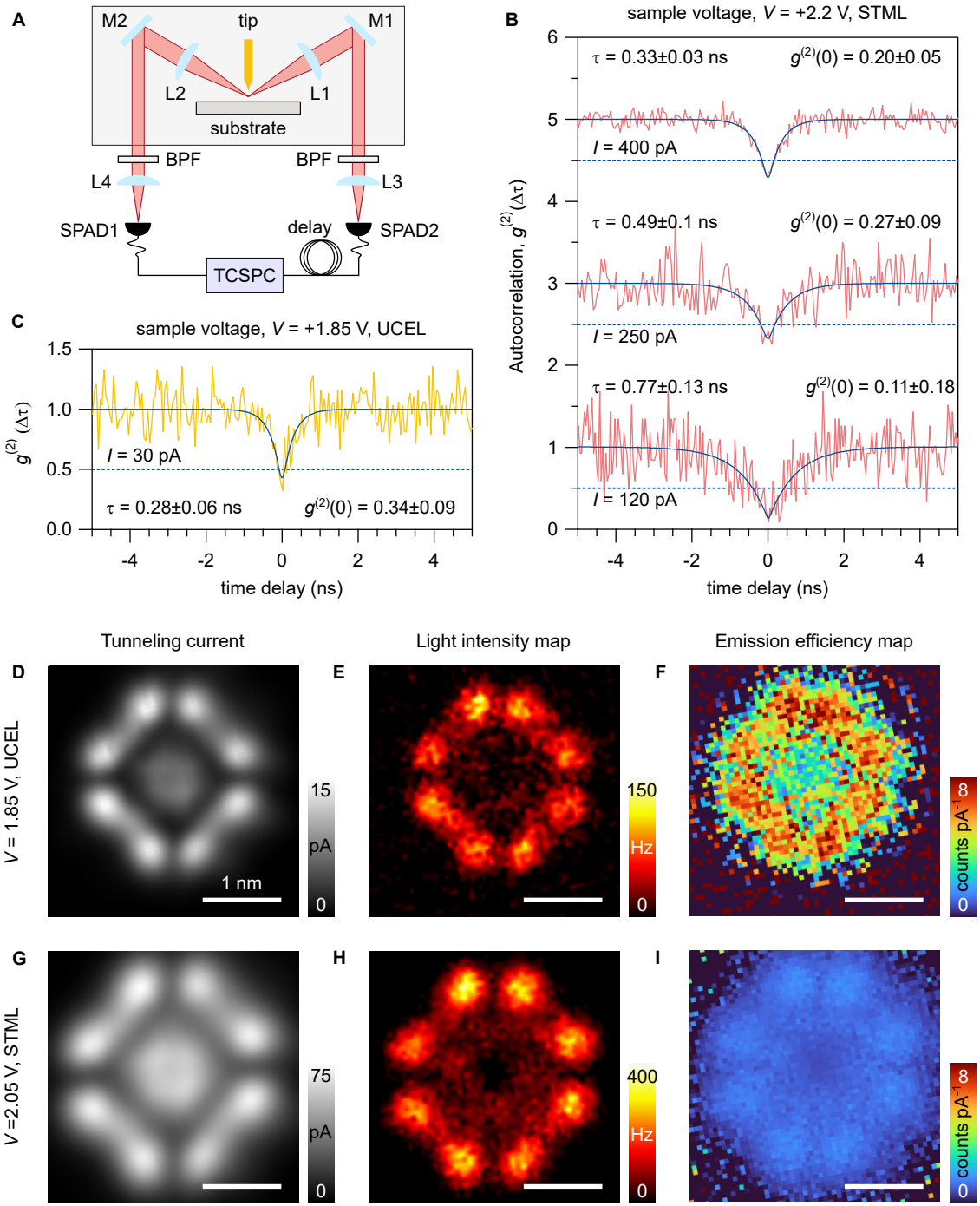

Figure 3.10 — Excitation mechanism for UCEL. (A) Schematic of the HBT-STM setup used for correlation measurements of filtered excitonic light. The SPAD1 acts as timer-start and SPAD2 as timer-stop for TCSPC. (B) Second-order correlation function $g^{(2)}(\Delta\tau)$ (pink) measured for the currents indicated ($V = 2.2$ V, $t = 15$ mins). The curves are vertically shifted for clarity. Blue solid lines are exponential fits to the data. The values of time constants (τ) and $g^{(2)}(0)$ are obtained from the corresponding fits. The blue dashed lines mark $g^{(2)}(0) = 0.5$. (C) $g^{(2)}(\Delta\tau)$ (yellow) measured for UCEL ($V = 1.85$ V, $t = 6$ h). (D, E, G, H) Constant-height STM tunneling current and light intensity map of a PtPc molecule atop 2 ML NaCl on Au(111) at V=1.85 V and 2.05 V, respectively (set point: I=15 pA, V=1.85 V; atop LUMO lobe of the molecule, size: 3.2×3.2 nm^2). (F, I) Emission efficiency map calculated by dividing intensity by current.

than the S_1 energy. The tip-sample gap is fixed for both sample voltages, defined by the set point: $I = 15$ pA, $V = 1.85$ V atop the highest point of the LUMO lobe. The tunneling current map of the molecule represents the symmetry of the degenerate LUMO/LUMO+1 structure and rises from 15 pA for a voltage corresponding to UCEL (1.85 V) to $\approx$ 75 pA at 2.05 V. The high-resolution reveals that the S_1 intensity exhibits the same spatial distribution as the LUMO due to carrier injection into the orbital resulting in S_1 excitation (see fig. 3.6). The extreme confinement of the plasmon in the tip-sample cavity, the lower residence time of the doublet state, and atomically resolved carrier injection result in the high spatial resolution of the molecular fluorescence. A detailed discussion of hyper-resolved fluorescence can be found in the PhD thesis of Benjamin Doppagne[225].

The emission efficiency is obtained by dividing the S_1 intensity by the current. Figure 3.10F and I show efficiency maps for sample voltages corresponding to both UCEL and conventional STM-EL at $V > E_{S_1}$ exhibiting a higher efficiency for UCEL at tunneling currents up to 75 pA. The saturation of the UCEL intensity above 100 pA suggests that a reversal of efficiency for the two cases is expected for high currents.

Mechanism for UCEL

The experimental findings for UCEL for PtPc atop NaCl on Au(111) (bipolar UCEL) can be rationalized by the mechanism discussed in the following. Since up-conversion involves electronic excitation from carriers tunneling through the HOMO-LUMO gap, the gap states, discussed in section 2.2, play an essential role in the S_1 intensities observed. For a comparatively inefficient process (quadratic instead of linear), the slight increase in tunneling probability through the HOMO-LUMO gap can considerably modify the observed UCEL intensities. A preliminary tight-binding simulation of the up-conversion for PtPc atop NaCl on Au(111) (symmetric alignment) suggests that for a voltage $V < E_{S_1}$, a tenfold increase in UCEL intensity is expected for an energy $E_{HOMO} < -1.95$ V (S_1 energy) compared to $E_{HOMO} = -1.3$ V. A further lowering of the orbital energy does not change the observed intensity considerably. The energy $E_{LUMO} = 1.7$ V is favorable for UCEL due to an enhanced tunneling probability at positive voltage, and thus, a larger intensity is expected. Experimentally obtained UCEL spectra reported in fig. 3.8C reproduce exactly these predictions. For the PtPc molecule marked with a green dot ($E_{HOMO} = -1.3$ V and $E_{LUMO} = 1.9$ V), no UCEL is obtained at negative voltages. In contrast, at positive voltage ($|E_S| < E_{S_1}$) a clear peak corresponding to the S_1 emission emerges. The second PtPc molecule, marked with a blue dot, exhibits slightly lower energy of the orbitals $E_{HOMO} = -1.5$ V and $E_{LUMO} = 1.7$ V. Even for such a minor shift in orbital energies, a significant increase of in-gap tunneling current leads to an increased intensity for UCEL. The simulations thus suggest that for H_2Pc atop NaCl on Ag(100), $E_{HOMO} = -2.45$ V[37], much larger UCEL intensities are expected. The observation of UCEL down to the T_1 energy thus becomes more plausible for Ag(100) as substrate. These arguments demonstrate that tunneling through the HOMO-LUMO gap indeed plays a vital role for UCEL and manifests itself in increased emission intensity as the molecular levels are

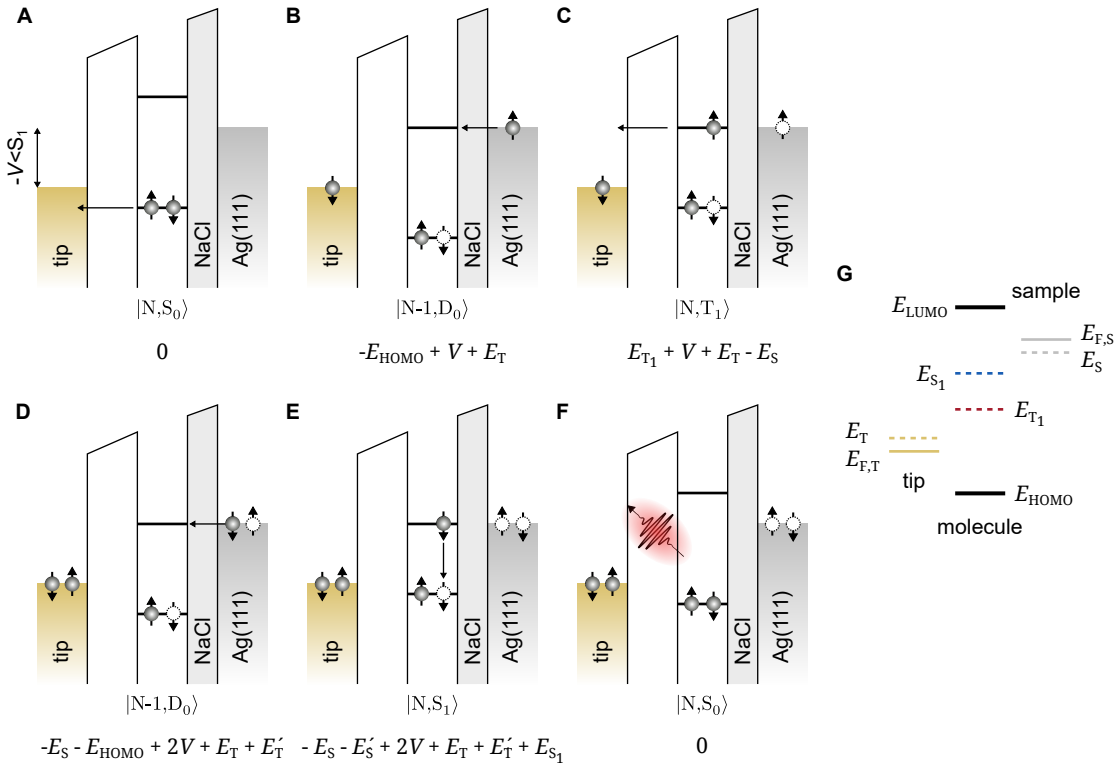

Figure 3.11 — UCEL mechanism. (A-F) Schematic of proposed mechanism for UCEL involving a two-electron process for an isolated molecule at negative sample voltage $V < E_{S_1}$ showing that sequential carrier injection leading to excitation of the singlet state. Perturbation theory requires energy conservation for the initial A and final F state but not for intermediate B-E states. (G) Labels for different energy states used in the text. E_T and E_S are energies of the tip and sample states occupied by the electron. Electrons in tip and the holes in the sample are at some finite energy above $E_{F,T}$ and below $E_{F,S}$, respectively.

shifted in the direction of the applied voltage (lower in energy for the negative voltage and higher in energy for positive voltage).

Next, a mechanism that rationalizes the quadratic power-law dependence of the UCEL intensity with respect to the tunneling current is discussed. Figure 3.11 shows a schematic illustration of the mechanism for asymmetric energy alignment of the molecular orbitals. The energies of different states used in the following discussion are labeled in fig. 3.11G. E_{S_1} and E_{T_1} are singlet and triplet energy levels, and E_S and E_T are electron states in the sample and the tip. The different processes in perturbation theory for PtPc atop NaCl on Ag(111) at the voltage $-V$ are described in the following. The energy of the state described in fig. 3.11A is defined as zero. In the first step an electron tunnels from PtPc HOMO to the tip (fig. 3.11B). A spontaneous electron extraction by the tip violates energy conservation but is allowed in a fourth-order perturbation consideration. Next, the doublet spin state of the cationic charge state of the molecule $|\mathrm{N}{-}1, \mathrm{D}_0\rangle$ is formed with energy: $-E_{\mathrm{HOMO}} + V + E_{\mathrm{T}}$ (fig. 3.11B). The generation of the doublet state enables tunneling of an electron from the substrate to the LUMO leading to the formation of the triplet state of the neutral molecule $|\mathrm{N}, \mathrm{T}_1\rangle$ with energy: $E_{\mathrm{T}_1} + V + E_{\mathrm{T}} - E_{\mathrm{S}}$ (fig. 3.11C). Again, the state $|\mathrm{N}\text{-}1, \mathrm{D}_0\rangle$ is formed for which a second sequential electron injection from the substrate to the LUMO can occur (fig.

Table 3.3 — Energy for different steps of the excitation mechanism described in fig. 3.11 for UCEL at negative sample voltage ($V = -1.5$ V). Energy of the triplet and singlet state are 1.27 eV and 1.95 eV, respectively. E_S and E'_S, and E_T and E'_T are energies of the sample and tip states, respectively. In both cases the energies are measured relative the Fermi energies of the sample ($E_{F,S} = 0$) and the tip ($E_{F,T} = V$). Note that the energy of the neutral ground state $|N, S_0\rangle = 0$.

E_{HOMO}	$\|$N-1, $D_0\rangle$	$\|$N, $T_1\rangle$	$\|$N-1, $D_0\rangle$	$\|$N, $S_1\rangle$
-1.3	$-0.2+E_T$	$-0.23-E_S+E_T$	$-1.7-E_S+E_T+E'_T$	$-1.05-E_S-E'_S+E_T+E'_T$
-1.5	E_T	$-0.23-E_S+E_T$	$-1.5-E_S+E_T+E'_T$	$-1.05-E_S-E'_S+E_T+E'_T$
-2.45	$0.95+E_T$	$-0.23-E_S+E_T$	$-0.55-E_S+E_T+E'_T$	$-1.05-E_S-E'_S+E_T+E'_T$

3.11D). The energy of this state is $-E_S-E_{HOMO}+2V+E_T+E'_T$, where E_T and E'_T correspond to tip states with different energies. Finally, an electron hops from the substrate to the LUMO. Together with the hole in the HOMO, it forms an exciton of the neutral molecule with the energy S_1 (fig. 3.11E). The energy of this state is $-E_S-E'_S+2V+E_T+E'_T+E_{S_1}$. The energy estimates discussed above are presented in Table 3.3 for an applied voltage $V = -1.5$ V and three different energy positions of HOMO: at -1.3 V and -1.5 V for PtPc atop NaCl on Au(111), and at -2.45 V for H_2Pc atop NaCl on Ag(100).

Energy conservation only comes in at the final state of the excitation mechanism and requires that $-E_S-E'_S+E_T+E'_T = 1.05$ eV. Then, for $-E'_S > 0$ ($E_{F,S} = 0$), $-E_S+E_T+E'_T \leq 1.05$ eV. In a time-dependent perturbation theory of UCEL, the energies in the second to fourth columns of Table 3.3 enter in the energy denominators. Given that, the energy of the state $|$N-1, $D_0\rangle$ plays an important role. As the absolute value of this energy is reduced, the UCEL rapidly increases in intensity. Perturbation theory breaks down when the energy denominator is minimal, while a nonperturbative treatment shows how UCEL keeps increasing but is finite. For $E_{HOMO} = -1.3$ V and -1.5 V, the first two cases shown in Table 3.3, the energy of the doublet state is smaller than zero, which implies that the probability of singlet formation is greatly reduced. This explains the low UCEL intensities for PtPc atop NaCl on Au(111) at negative voltages. However, for $E_{HOMO} < -1.95$ V, the energy denominator can vanish, and UCEL becomes prominent. This establishes why the UCEL for H_2Pc on Ag(100) is strong for negative voltages. Invoking electron-hole symmetry for the mechanism described above would suggest a large UCEL at positive voltages for $E_{LUMO} \sim 1.95$ V. The amplitude for UCEL is proportional to V_{MT}^2 since it involves the hopping of two electrons from the molecule to the tip. Here V_{MT} is the hopping matrix element from the molecule to the tip. The photon emission probability is then proportional to V_{MT}^4. The current is determined by processes of the type shown in the top three panels of fig. 3.11, except that the substrate electron in fig. 3.11C tunnels into the HOMO instead of the LUMO. This results in the current being proportional to V_{MT}^2. As the tip is moved towards the surface and V_{MT} grows, the UCEL then grows quadratically with the current.

The mechanism involving a small perturbation enabling carrier injection from the molecule to the tip reconciles the vast differences in emission intensity and voltage onset observed for

UCEL from PtPc atop NaCl on Au versus Ag. The importance of energetically lower-lying molecular orbitals discussed in section 2.2 may be expected to introduce an asymmetry in UCEL intensities for positive and negative voltages. Moreover, two sequential carrier injection steps explain the quadratic dependence of UCEL intensity on current. We had earlier reported that the current dependence of S_1 emission at voltage $V = 2.5$ V also shows a quadratic power-law dependence (fig. 3.3G). The competition between large UCEL intensities and low efficiency of conventional STM-EL observed at low positive voltage could potentially lead to the observed quadratic dependence at $V > E_{S_1}$.

Conclusion

A wide range of emission phenomena, from bipolar electroluminescence to UCEL, is observed for STML of PtPc atop a few ML NaCl on Au(111). Significant work function variations due to the morphology of the substrate allow shifting the energies of molecular orbitals on the order of a few hundred meV, which qualitatively alter the excitation properties of PtPc electroluminescence. The rich molecular emission phenomena corresponding to different energy alignments of the orbitals are characterized using STML and rationalized by theory. The precise optoelectronic characterization enabled by STML and HBT-STM allows for rationalizing different emission efficiencies for unipolar and bipolar STML and UCEL based on different excitation mechanisms. Especially for UCEL, the proposed mechanism captures almost all aspects of the emission and significantly furthers the understanding of spin-triplet mediated energy up-conversion. Some of the proposed tunneling mechanisms in this chapter invoked electron-hole symmetry. This symmetry is broken due to the influence of the NaCl buffer. A deeper theoretical analysis is required to understand its consequences. Nevertheless, arguments based on electron-hole symmetry appear to be reasonable. The insights gained from single-molecule STML studies are crucial for the future design of novel molecular optoelectronic devices. The findings of this chapter could, in principle, be applied to manipulate the efficiencies and energy management of existing molecular emitters by controlling their nano-environment.

The experimental work presented in this Chapter was performed in collaboration with Prof. Yousoo Kim at Surface and Interface Science Laboratory (表面界面科学研究室), RIKEN (理化学研究所), Japan

4

Single molecule phosphorescence and intersystem crossing

This chapter reports on the observation of phosphorescence from a single PtPc molecule coupled to the nanocavity plasmon. The T_1 state can be excited by direct charge injection and intersystem crossing from the S_1 state. Using a recently developed resonant STM-PL[150], we selectively excite the S_1 state and observe phosphorescence. Since the T_1 state can only be excited through ISC in this case, the observation of phosphorescence evidences that observation of ISC at the single-molecule level is possible. The effect of X-P (exciton-plasmon) coupling on phosphorescence is probed using the ability to precisely position the STM tip. Even though resonant excitation of the S_1 state in STM-PL does not allow for studying the fluorescence of PtPc, the high intensities obtained for vibronic peaks allow their spatial mapping. The theoretical simulation of the emission using quantum master equation methods combined with first-principle calculations based on DFT and TD-DFT calculations help rationalize the experimental results[1]. The details of the theoretical methods are briefly discussed alongside the experimental discussion.

4.1 Fluorescence and phosphorescence from a single molecule

Even though most phthalocyanines exhibit phosphorescence in the near infrared range[129,226] its detection, and thus, characterization at a single molecule level has remained a challenge[125]. Recently, Kimura *et al.*[21] reported selective T_1 emission in a charged 3,4,9,10-perylenetetra-carboxylicdianhydride (PTCDA) molecule. Owing to the exchange interaction in the charged molecule, electron extraction from the molecule is spin-selective, which leads to a formation of excitons corresponding to the T_1 state. Their findings inspire a deeper STML investigation of the emission mechanism in prototypical phosphors.

[1]The theoretical calculations were performed by Asst. Prof. Kuniyuki Miwa, Institute for Molecular Science (分子科学研究所), National Institutes of Natural Sciences (自然科学研究機構), Japan.

Due to the heavy atom effect of the central Pt metal atom ($Z = 78$), PtPc exhibits stronger SOC[159,227,228] than other metallophthalocyanines studied by STML[66,68,69,229,230]. In addition, the paramagnetic nature of the Pt atom leads to an increase in radiative and non-radiative rates, thus, boosting phosphorescence and total luminescence yields[159]. In line with theoretical expectations, previous experimental work on PtPc molecules in solutions[129,159,231], embedded in Shpol'skiĭ matrix[130,131] and OLEDs[226], and their molecular crystals[232,233] show comparatively higher phosphorescence yields with respect to other metallophthalocyanines. Temperature dependence of the phosphorescence quantum efficiencies has been reported[234]. The quantum efficiency of phosphorescence drops by two orders of magnitude with decreasing temperature ($\approx 10^{-1}$ at 80 K to $\approx 10^{-3}$ at 4.5 K when normalized to efficiency at room temperature), which presents a challenge for single-molecule STML studies at 4.3 K. Moreover, in STML the picture can be considerably different from earlier studies due to the strong interaction with the underlying substrate as shown in section 2.2 or due to the different coupling strengths of the singlet and triplet excitons to the nanocavity plasmon modes. A brief description of the system and a detailed analysis of the STML signal is given below.

Description of PtPc atop 4 ML NaCl on Ag(111)

A single PtPc molecule adsorbed atop 4 ML thin NaCl island on Ag(111) surface is used as the system for this study. Figure 4.1A shows a large scale 40×10 nm^2 STM topography image. The 4 ML thickness of the NaCl is verified by the step height of the island 589.4 ± 0.6 pm at sample voltage $V = 1$ V as determined by fitting a sigmoid function to the linecut presented in fig. 4.1B. The reported error is the standard deviation obtained from the fit. The measured layer thickness of the NaCl is in line with previous reports[70,144].

The $\mathrm{d}I/\mathrm{d}V$ spectrum shown in fig. 4.1C exhibits the HOMO and LUMO orbitals with onsets corresponding to the energy positions -2.3 V and 0.8 V, respectively. The apparent electronic transport gap of ≈ 3.1 eV is in agreement with other studies on few ML NaCl on Ag(100)[38] and theoretical simulations (gray curve in fig. 4.1C). The details of the spatial characteristics of the molecular orbitals are presented in section 3.1.

Theoretical simulations are performed using a Hubbard nonequilibrium Green's function (NEGF) to describe the transport and optical response of the single PtPc molecule atop NaCl on Ag(111) in proximity to a plasmonic tip. The details of the model can be found in an article by Miwa *et al.*[219]. Molecular many-body states calculated by DFT for the equilibrium isolated molecule are utilized in the Hubbard NEGF calculations as a basis set.

STM-induced electroluminescence of a single phosphor

The previous chapter discussed tunneling current-induced fluorescence from a single isolated PtPc molecule. For molecular emission induced by charge injection, either of the singlet or triplet states can be directly excited depending on the electron spin (see schematic in fig. 4.2A). For a negative sample voltage that allows for an energy alignment of the tip Fermi level

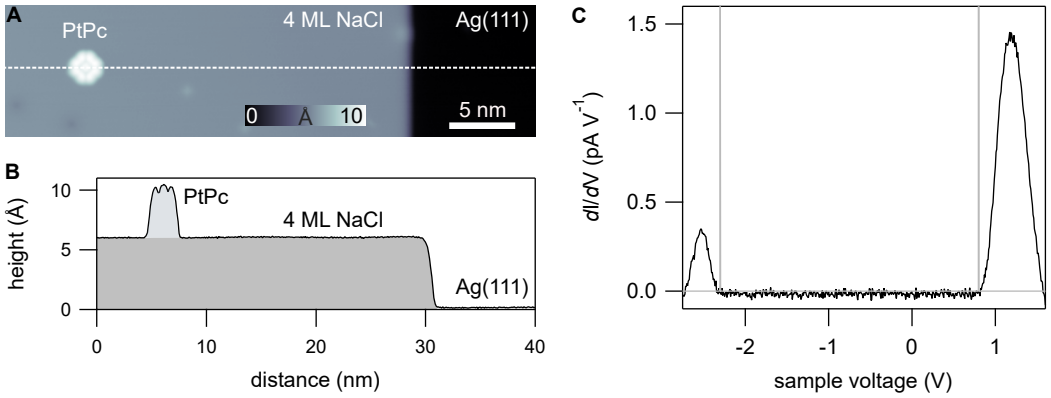

Figure 4.1 — STM characterization of PtPc atop 4 ML NaCl on Ag(111). (A) Overview topography image of one PtPc molecule atop 4 ML NaCl on Ag(111) surface (set point: $I = 3$ pA, $V = 1$ V). (B) Linecut profile along the dashed white line in (A). (C) Experimental dI/dV spectrum (black) showing the transport gap, and theoretical simulation (gray) showing the position of orbitals used for further calculations of an isolated PtPc molecule. The experimental spectrum is obtained for tip position at the center of the molecule (set point: $I = 10$ pA, $V = 1$ V).

with the HOMO, depending on the spin of the electron extracted (see ① in fig. 4.2B), and the spin injected from the sample side to the LUMO (see ② in fig. 4.2B), they form either a spin singlet or triplet state. Unlike optical excitation where absorption by the T_1 state is forbidden, for electronic excitations spin statistics implies that the S_1 and T_1 states are formed in a 1 : 3 ratio. However, as illustrated in fig. 4.2B, not only the spin multiplicity but also the different potential barrier for injection into the two states has to be accounted for. The higher potential barrier for charge injection into the triplet state implies that the T_1 emission intensity would be suppressed in favor of S_1. Figure 4.2C shows a typical STM-EL spectrum obtained for a sample voltage of -2.6 V with the tip placed atop the HOMO lobe of the molecule (gray dot marked in the inset showing STM topography image). The sharp emission lines between 1.95 eV and 1.7 eV are assigned to the electronic transition of fluorescence ($S_1 \rightarrow S_0$) and the corresponding vibronic satellites based on gas-phase calculations and Raman spectroscopy of PtPc powder samples (discussed in more detail in section 4.1 and 4.4, respectively). Here, it is essential to note the large bandwidth of the plasmon employed in the experiment (gray plot in fig. 4.2C). Given that plasmonic enhancement in the tip-sample gap is central to higher intensities observed for molecular emission (see fig. 1.5), the energy overlap between the plasmon mode and the excitons is necessary for the observation of S_1 and T_1 emission.

The emission around 1.272 eV, not reported in the previous Chapter for PtPc atop NaCl on Au(111), is assigned to the $0-0$ transition of phosphorescence ($T_1 \rightarrow S_0$). Prior spectroscopic studies on PtPc in form of a molecular crystal[232,233], dissolved in solution[129,159,234], in Shpol'skiĭ matrix[131], and as an emitter material in OLEDss[226] report phosphorescence energies between 1.276 and 1.313 eV. The emission line is distinct from luminescence corresponding to the anionic species of the molecule (1.36 eV) reported by Farrukh *et al.*[38]. For a PtPc molecule adsorbed atop 3 ML NaCl on Ag(100), at positive sample voltages, they observe luminescence from the anionic species. However, at negative sample voltages, only the fluorescence from the neutral specie (at 1.95 eV) is observed, similar to the findings

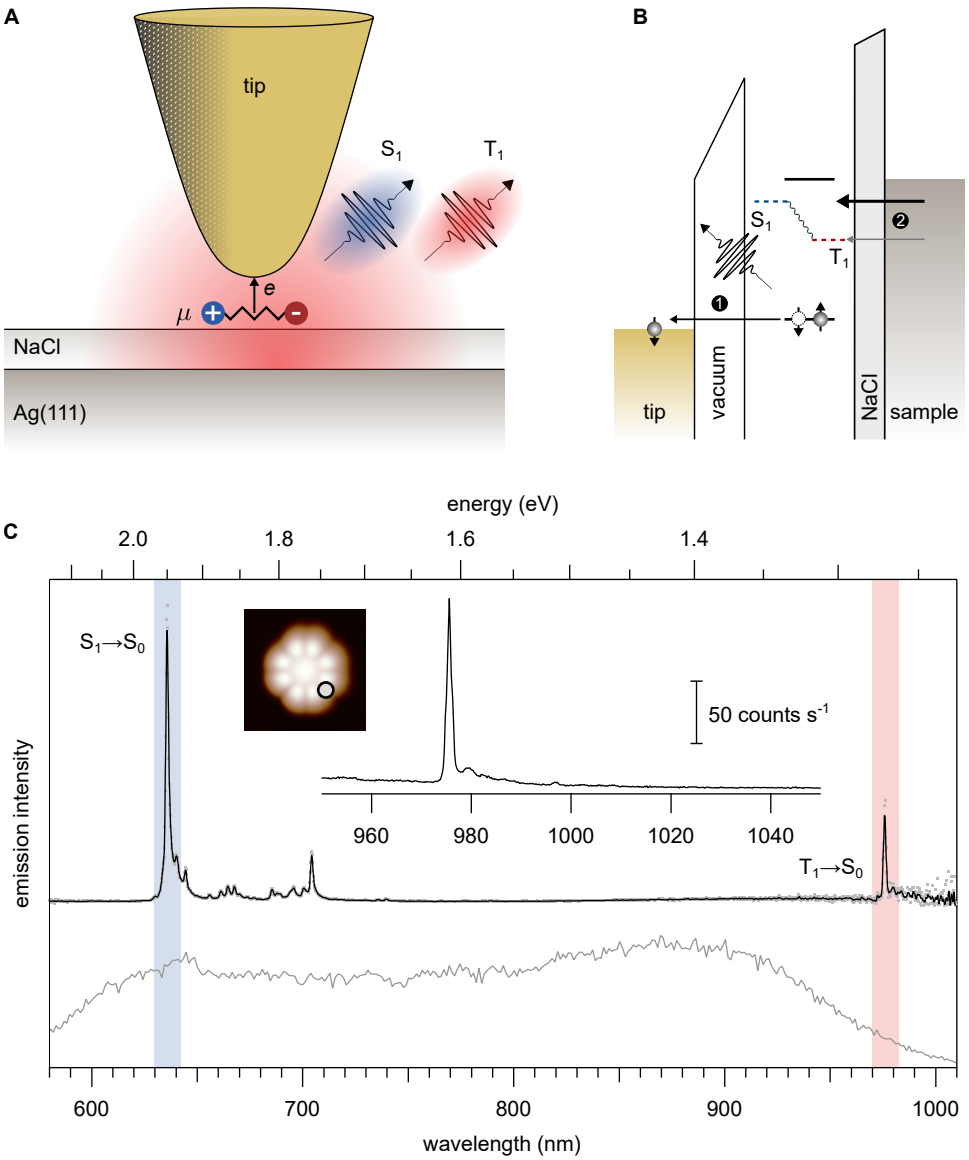

Figure 4.2 — STM-EL fluorescence and phosphorescence from a single PtPc molecule. (A) Schematic of the experiment showing excitonic emission (S_1 and T_1 emission) from a molecule decoupled from the metal substrate. (B) Energy level diagram showing the proposed mechanism for creation of S_1 and T_1 exciton ① on removal of electron from the HOMO followed by ② filling of LUMO from the substrate. (C) Typical STM-EL spectrum of PtPc molecule (set point: $I = 80$ pA, $V = -2.6$ V, $t = 60$ s) using a tip where the nanocavity plasmon (shown in gray) spans the energy range from 2 eV to at least 1.1 eV (set point: $I = 250$ pA, $V = -2.6$ V, $t = 1$ s). The emission lines corresponding to the 0-0 transition of the S_1 (blue) and T_1 (red) are also indicated. A second spectrum shows a blow up of the T_1 spectrum with a longer integration time (set point: $I = 80$ pA, $V = -2.6$ V, $t = 1200$ s). The inset shows a STM topography image of the molecule shown in overview image with tip position indicated (set point: $I = 3$ pA, $V = -2.6$ V, size: 3.5×3.5 nm^2). The excitonic spectrum has been divided by the purely plasmonic spectrum, shown in gray, thus accounting for both spectral enhancement variations and wavelength-dependent detector sensitivity.

reported in Chapter 3.

The TD-DFT calculations substantiate the claim that the emission at 1.272 eV indeed corresponds to phosphorescence. The energy estimates for S_1 and T_1 excitons are 2.02 eV and 1.03 eV, respectively, are in fair agreement with the experiment.

The transition dipole moment $\mu_{S_1 \to S_0}$ for the $S_1 \to S_0$ transition is evaluated at the optimized structure for the S_1 state and is obtained as 2.93 (a. u.). For the $T_1 \to S_0$ transition, $\mu_{T_1 \to S_0} = 0.069$ (a. u.) was obtained at the optimized structure for the T_1 state. The fluorescence and phosphorescence rates are estimated using the formula $\kappa = 4/3\hbar(\omega/c)^3|\mu|^2$, with $\hbar\omega$ being the optical transition energy, $\hbar$ the reduced Planck constant, c the speed of light in vacuum, and μ the transition dipole moment[235]. The rates $\kappa_{S_1 \to S_0} = 5 \times 10^7$ s^{-1} and $\kappa_{T_1 \to S_0} = 5 \times 10^3$ s^{-1} are utilized for the fluorescence and phosphorescence processes in the gas phase, that are on the same order of magnitude as calculated with the values of $\mu_{S_1 \to S_0}$ and $\mu_{T_1 \to S_0}$ reported above.

Based on the theoretically calculated transition dipole moments, the $\mu_{T_1 \to S_0}$:$\mu_{S_1 \to S_0}$ intensity ratio is $\approx$ 1:40. Experimentally, in STM-EL, when accounting for both spectral enhancement variations and wavelength-dependent detector sensitivities, the T_1:S_1 intensity ratio is $\approx$ 1:4 (see fig. 4.2C). The phosphorescence intensities observed are almost an order of magnitude larger than the theoretical estimate, thus suggesting a much larger population of the T_1 than that of the S_1 state.

Timescale of excited states from linewidth

Besides the emission energies of the excited states, another way to characterize the emission is through the excited state lifetime, which can be estimated from the emission linewidth. Phosphorescence requiring a change in spin multiplicity[132] typically exhibits a lifetime two orders of magnitude longer than fluorescence[12,129].

Figure 4.3 shows high energy resolution S_1 (left) and T_1 (right) emission spectra obtained using a grating with 1200 grooves mm^{-1}. The S_1 emission line exhibits an asymmetric shape, requiring more than one Lorentzian peak to be fit accurately. Thus, the spectrum comprises several superimposed electronic transitions from vibrationally excited states rather than only a 0-0 transition. Such a breakdown of Kasha's rule is due to a large plasmonic enhancement of radiative and non-radiative transition rates[79,236,237], leading to comparable electronic transition and vibrational relaxation rates. Nevertheless, a longer lifetime would lead to a sharper line even if the linewidth is composed of several transitions. A longer lifetime also allows vibrational relaxation to the lower-lying vibrational states and lead to a sharper linewidth, even if there is no complete relaxation to the vibrational ground state.

On the other hand, the T_1 emission line is fit well by a single Lorentzian peak, suggesting that the peak corresponds to the 0-0 transition of phosphorescence. As obtained from fitting a Lorentzian line shape to the data, the full width at half maximum (FWHM) of the S_1 emission is 3.25 meV and of the T_1 emission is 0.23 meV. The significantly sharper linewidth of the peak at 1.272 eV further supports its assignment to the phosphorescence.

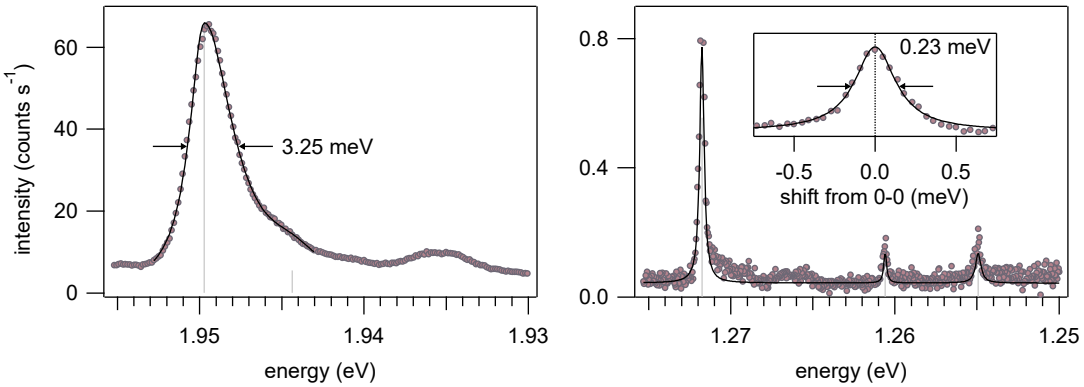

Figure 4.3 — FWHM of the S_1 and T_1 emission peaks. Lorentzian line shape (centered at the gray lines) (black) fitting of the S_1 (left) and T_1 (right) emission line . The grey lines mark the peak position of the Lorentzian line shape. Inset (right). Blow up of the T_1 emission line showing intensity distribution in terms of energy shift from the peak position (1.272 eV) as estimated from the fit (set point: $I = 80$ pA, $V = -2.6$ V, S_1: $t = 5$ min, T_1: $t = 50$ min).

As shown in section 3.4, for PtPc adsorbed atop 3 ML NaCl on Au(111), a time constant of $\approx$ 300 ps is obtained in second-order correlation measurements. This time constant is similar to previous HBT experiments on single ZnPc molecule[70]. Using tip-enhanced photoluminescence, Yang *et al.*[96] recently reported a linewidth of $\approx$ 10 meV for ZnPc adsorbed atop 3 ML NaCl on Ag(100). The linewidth suggests a lifetime on the order of tens of femtoseconds. Then, it is not surprising that using an HBT set up with a time resolution of $\approx$ 80 ps, no antibunching dip is observed[96]. The single photon emission due to a finite exciton lifetime is too fast to detect. A 532 nm (2.33 eV) laser is used in photoluminescence experiments[96]. This leads to excitation to a higher-lying excited state than the lowest singlet excited state at $\sim$ 1.89 eV. Given that Kasha's rule does not hold in a plasmonic nanocavity, it is plausible that the S_1 line reported by Yang *et al.*[96] is composed of several transitions. Thus, care has to be taken when STML spectra is evaluated to provide the lifetime of an exciton.

Recent measurements from Imada *et al.*[150], who used a tunable laser to resonantly excite an H_2Pc molecule to its lowest singlet excited state, find a much sharper linewidth of 0.5 meV for the S_1 excitation. The calculated lifetime ($\tau \sim 700$ fs) is in reasonable agreement with fluorescence lifetime studies of molecules in the proximity of plasmonic bow tie nanoantennas[149]. The findings from Imada *et al.*[150] further substantiate the argument that the time constant obtained for antibunching in single-molecule HBT-STM is related to the lifetime of a different process, for example, an intermediate charged state prior to exciton creation (see section 3.3).

It is important to note that the phenomenological difference between electronic- and photo-excitation mechanisms is the transient charged state involved in the three-state model. In this case, two opposite charges need to be injected into the molecule to observe radiative decay (see section 3.3). In contrast, photoluminescence is a two-state process involving only an excitation by photon absorption and radiative (or non-radiative) decay to the ground state (for example, in photoluminescence from nitrogen-vacancy centers in diamond mem-

brane[172]). Thus, the time constant reported in the previous chapter for PtPc atop 3 ML NaCl on Au(111) of ≈ 300 ps is most probably related to a transient charged state rather than to the exciton lifetime. The understanding of lifetime measurements in STML is not yet complete and thus commands further experimental and theoretical investigations.

Electronic characterization

The sample voltage and tunneling current dependencies of the fluorescence and phosphorescence allow an analysis of the exciton formation mechanism at the single-molecule level. Figure 4.4 shows the S_1 (fig. 4.4A) and T_1 (fig. 4.4B) intensities when the tip is placed atop the molecule (lobe) at constant current. For a sample voltage of −2.1 V, a purely plasmonic spectrum is observed (lowest spectrum in fig. 4.4A). As the sample voltage is decreased to −2.15 V and further, sharp peaks corresponding to the intrinsic molecular emission from the S_1 (at 1.95 eV) and T_1 (at 1.272 eV) state emerge simultaneously. The emission intensity saturates for sample voltages lower than −2.5 V (not shown). The intensity corresponding to the two transitions can be evaluated using Lorentzian peak fitting. A linear fit of the emission efficiency (evaluated by normalizing the intensity with tunneling current and integration time) versus sample voltage (fig. 4.4C) indicates a voltage cutoff at ≈ −2.15 V. An empirical simulation of the luminescence intensity for parameters: coupling of the S_0-S_1 transition with plasmon = 5 meV and coupling of the S_0-T_1 transition with plasmon = 50 μeV, show that both fluorescence and phosphorescence are predicted to occur for sample voltages < −2.3 V (see fig. 4.4D). The estimate of the coupling strength for the S_1 transition is in accordance with the value reported in a previous work[219].

The cutoff voltages of the emission intensity for both experiment (≈ −2.15V) and theory (−2.3 V) match well with the sample voltage (≈ −2.3 V) for which the tip Fermi energy is aligned with the lower edge of the HOMO (see fig. 4.1C). This finding indicates that the charge extraction from the HOMO is the first process in the excitation mechanism. Given that the energy of the electron is larger than both S_1 and T_1 emission, both transitions set on simultaneously (see section 3.3 for a detailed discussion of the excitation mechanism). The different heights of the potential barrier for charge injection from the substrate into the S_1 or T_1 state can also affect the relative emission intensities. As illustrated in fig. 4.4, the generation of a triplet state requires an electron injection through a higher potential barrier than the generation of a singlet state. This suggests that the energy alignment could be changed to suppress the relative intensity of the lower energy triplet state in favor of the higher energy singlet emission, providing an alternative path to tune the intensity of organic emitters[238].

Recording the fluorescence and phosphorescence intensity at a fixed sample voltage while the tunneling current is increased, allows further analysis of the emission dynamics. For higher currents, i.e., the shorter average time between tunneling events which may quench the intrinsic emission, a reduced emission lifetime is expected[80]. With a fixed sample voltage $V = -2.6$ V, the tunneling current is increased from 1 to 100 pA (the tip moves closer

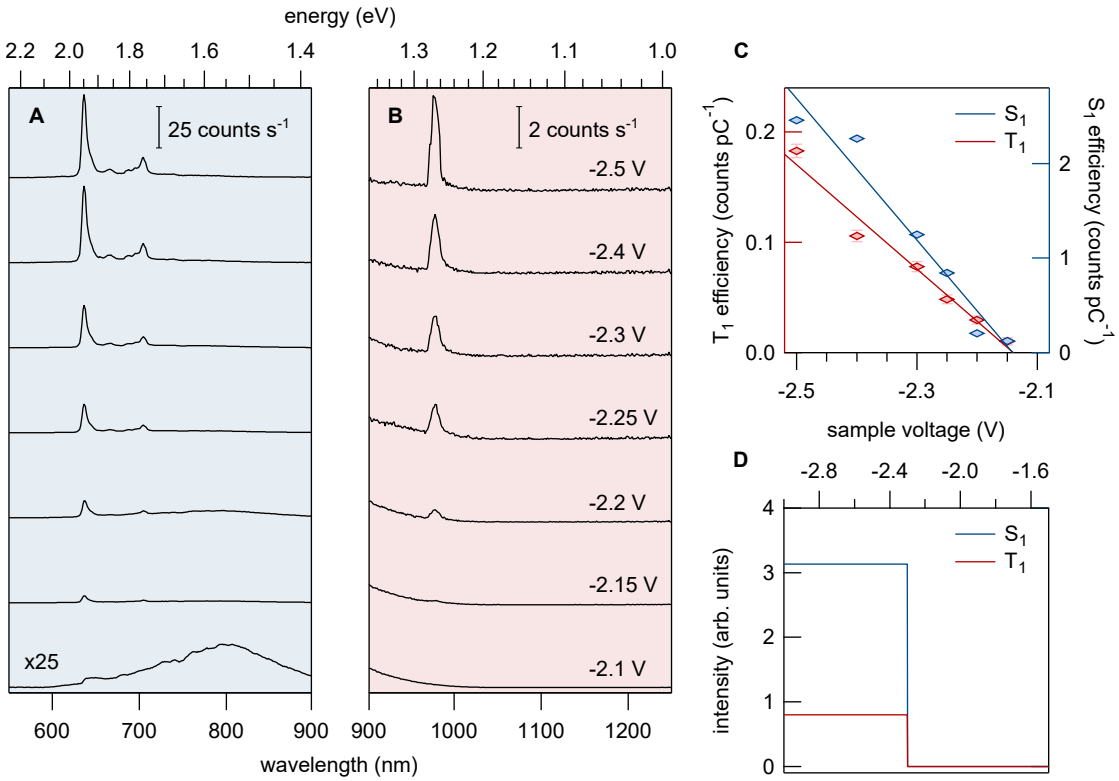

Figure 4.4 — Voltage dependence of fluorescence and phosphorescence. (A) S_1 and (B) T_1 intensities for sample voltages indicated (set point: $I = 200$ pA, $t = 30$ s). The plasmonic spectrum corresponding to sample voltage $V = -2.1$ V is multiplied by a factor of 25 for visualization ($t = 1$ s). (C) Sample voltage cut-off evaluated by linear fit of S_1 and T_1 peak intensities obtained from Lorentzian peak fitting. (D) Theoretical simulation of S_1 and T_1 emission intensities using the quantum master equation method to describe the transitions.

by ≈ 2 Å). For a current higher than 100 pA, spontaneous development of defects in the NaCl layer or hopping of a PtPc molecule to the next Cl lattice site becomes highly probable. This defines the upper limit in the current dependence measurement.

Experimentally, a path-switching mirror behind the spectrometer is used to direct the light to an SPAD (Excelitas SPCM-AQRH). The TTL pulses corresponding to photon detection events from the SPAD are counted using a multi-channel data acquisition device (National Instruments). For voltage $V = -2.6$ V, the observed spectrum is purely excitonic, as seen in fig. 4.2C, with almost no plasmonic contribution. To filter the S_1 and T_1 light emission, a grating with 1200 grooves mm^{-1} centered at the emission energy of each transition is used. Thus, the S_1 and T_1 intensities reported in fig. 4.5 are spectrally integrated over 610-660 nm and 950-1000 nm, respectively.

Both fluorescence and phosphorescence set on linearly as the current is increased. This indicates that the excitation involves a one-electron process which is the electron extraction from HOMO, as discussed above. The charge refilling to the LUMO happens from the substrate side and thus, does not contribute to the tunneling current. The T_1 emission intensity starts to become sub-linear at tunneling currents above ≈ 40 pA as seen in fig. 4.5. A similar behavior for S_1 emission intensity for defects in C_{60} films has been reported by Merino *et al.*[80]. They suggest that the sub-linear behavior arises when an exciton can get quenched

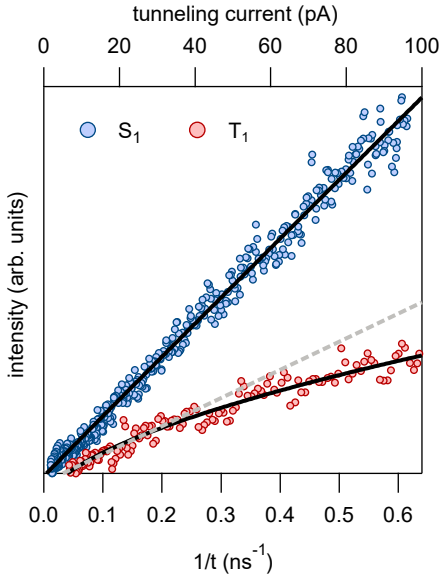

Figure 4.5 — Current dependence of fluorescence and phosphorescence at a fixed voltage $V = -2.6$ V. S_1 and T_1 peak intensities for current range from 1 to 100 pA ($S_1 : t = 200$ ms, $T_1 : t = 1$ s). The S_1 data is fit with $I^{0.99}$ and T_1 data is fit with the three-state model [80]. The dashed gray line is a linear fit for data corresponding to I range: 0-40 pA.

by the subsequent tunneling charge. The sub-linear behavior setting on at ≈ 40 pA would suggest an excited state lifetime of ≈ 4 ns. However, the lifetime estimate from T_1 linewidth (FWHM: 0.23 meV) is ≈ 3 ps. A deviation from strictly linear behavior would then start at a higher current (≈ 500 pA). The lower onset of the sub-linearity instead suggests an increase in non-radiative decay rate as the tip approaches the molecule [70]. For the current range probed, the increase in non-radiative decay rate does not seem to affect the shorter living S_1 state significantly.

4.2 Evidence for intersystem crossing in a single phosphor

Along with the direct electronic excitation of the T_1 state, ISC from the S_1 to the T_1 state also contributes to the phosphorescence intensity. As mentioned earlier, the PtPc molecule exhibits large SOC due to the heavy atom effect and thus, promotes ISC. However, using STM-EL there is no direct way to obtain evidence for ISC at the single-molecule level or its contribution to the phosphorescence intensity since direct charge injection to form a triplet state and ISC cannot be decoupled.

To study the role of ISC in single-molecule phosphorescence a wavelength-tunable laser is employed to resonantly excite the S_1 state, and the corresponding photoluminescence is recorded. No direct charge excitation of T_1 is possible because, in dipole approximation, light cannot induce a spin-flip. Figure 4.6 shows the experimental scheme used to illuminate the STM junction with laser light. In the following, we discuss the details of the experimental setup, the so-called *4-Goki*, that enables resonant STM-PL.

The *4-Goki* STM

The experimental setup consists of two branches, namely illumination, and detection. The optical access to the tunneling junction is enabled by two optical lenses, L2 and L3, each

covering a solid angle of ≈ 0.5 sr, installed on the STM stage (see fig. 4.6).

Illumination – The laser light from a 637 nm, temperature-stabilized laser diode (Thorlabs, Inc.), thermally tuned to 635.52 nm (fig. 4.7C) is used for excitation. The laser power (1-2 μW) is feedback-controlled using a neutral density filter ND installed on a translation stage. The laser light is then coupled to a polarization-maintaining single-mode fiber PM-SMF (Thorlabs, Inc.). Next, a lens L1 collimates the beam, followed by spectral filtering through a short-pass filter SPF (Semrock, Inc.). At this stage, the energy distribution of the excitation line is monitored using a spectrometer (Acton Research IsoPlane-320 with a grating with 1800 grooves mm^{-1}) coupled with a liquid nitrogen-cooled CCD (Teledyne Princeton Instruments Spec10) (not shown in fig. 4.6). A polarizer (P) and a half-wave plate ($\lambda/2$) define the beam's polarization. In this work, a polarization along the tip axis (p-polarization) is used to maximally utilize the tip enhancement[239]. Finally, the laser beam enters the UHV chamber and is focused on the tip-sample nanocavity by lens L2.

Detection – The emitted light is collected and collimated by lens L3 and directed out of the UHV chamber. A long-pass filter LPF (Semrock, Inc.) with the edge at 650 nm blocks the scattered light from the excitation laser[2]. The beam is then focused onto a grating spectrometer (Acton Research SpectraPro 2300i with gratings with 50, 300, and 1200 grooves mm^{-1}) and detected with a CCD (Teledyne Princeton Instruments PyLoN:100). A path switching mirror directs the light towards a SPAD to record the emission intensity integrated over a narrow wavelength range.

STM-induced resonant photoluminescence of a single phosphor

Figure 4.7A shows a schematic of the primary measurement principle for STM-PL. The incident laser excites the molecule, which radiatively decays back to its ground state. A long-pass filter blocks the scattered laser light on the detection end, and only the STM-PL signal reaches the detectors. The excitation laser line profile (635.52 nm) is shown in fig. 4.7C (blue). The line exhibits a FWHM of ≈ 50 μeV which is at the resolution limit of the spec-

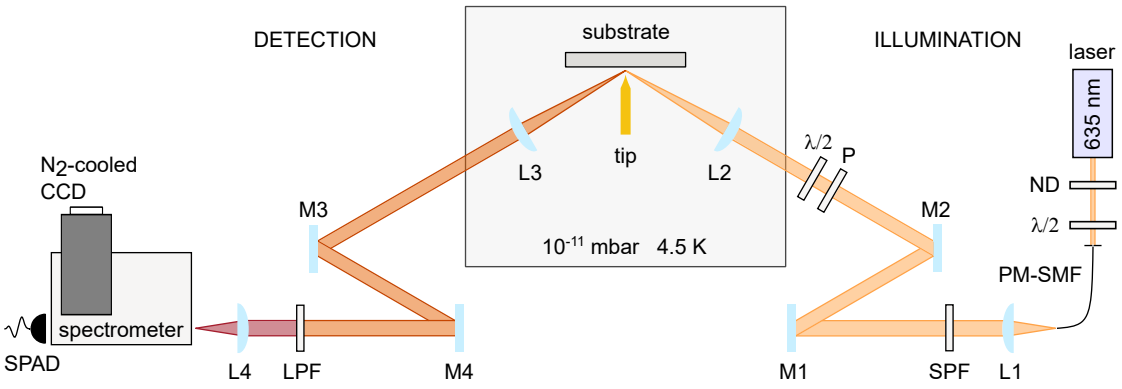

Figure 4.6 — Schematic overview of the *4-Goki* STM including the arrangement of optics components.

[2]The LPF was removed for STM-EL measurements.

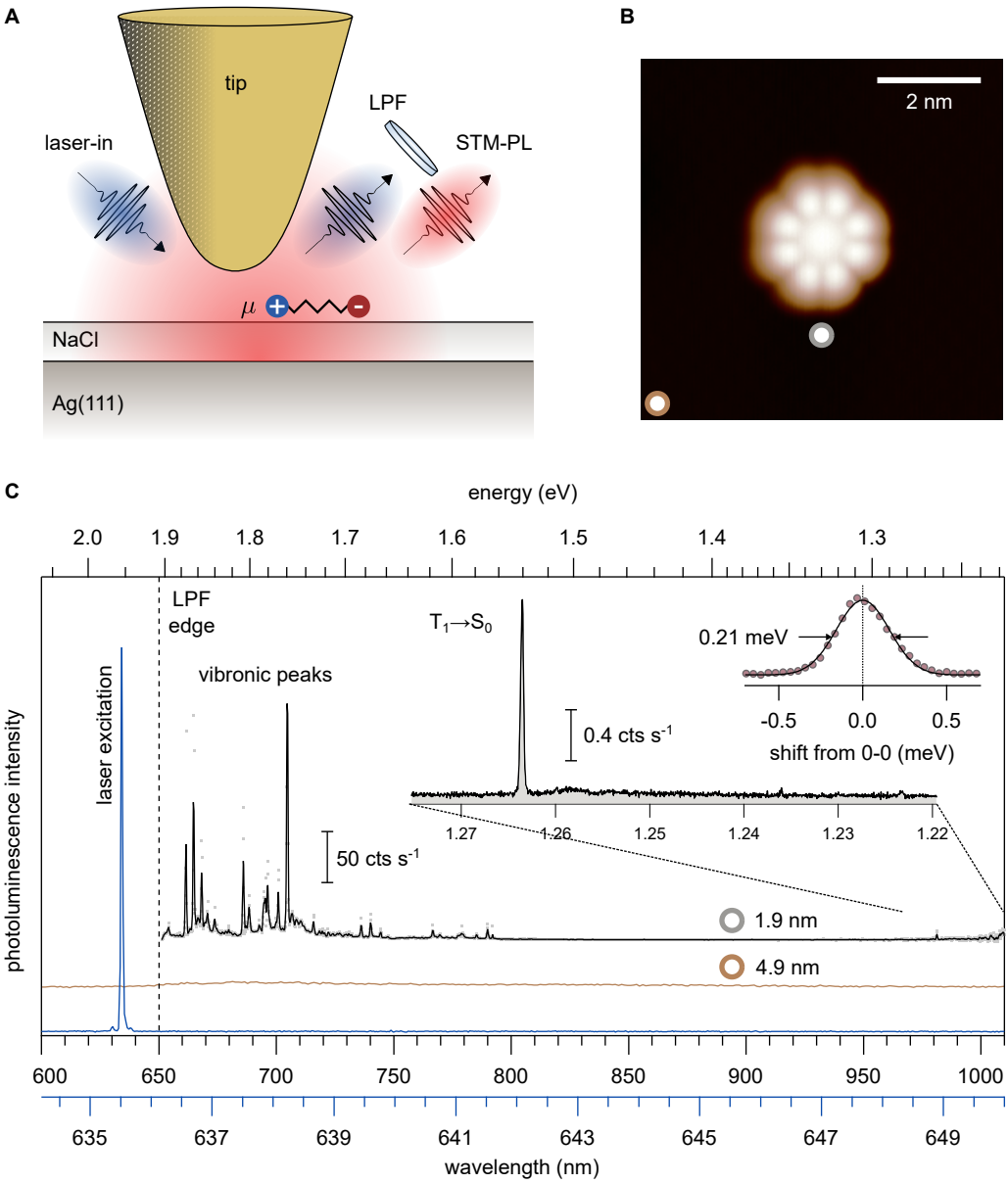

Figure 4.7 — STM-induced resonant photoluminescence. (A) Schematic depiction of the STM-PL principle. The incident laser is suppressed by long-pass filter LPF on the detection side. (B) STM topography image of the PtPc molecule adsorbed atop 4 ML NaCl on Ag(111) (set point: $I = 3$ pA, $V = -2.6$ V). (C) Laser line (635.52 nm) used for photoexcitation. STM-PL spectrum obtained at indicated distances from the center of the molecule depicted by the white dots with colored rings (laser power: 1 μW, $t = 60$ s, grating: 300 grooves mm^{-1}). The dashed line marks the 650 nm edge of the long-pass filter LPF. Inset. Zoom-in on the phosphorescence region of the STM-PL spectrum (set point: $I = 3$ pA, $V = 1$ V; laser power: 1 μW, $t = 60$ min, grating: 1200 grooves mm^{-1}). Lorentzian fit of the T_1 line with FWHM indicated.

trometer (68×68 mm^2 grating with 1800 grooves mm^{-1})[240]. When the tip is placed ≈ 5 nm away from the center of the molecule (brown ring in fig. 4.7B), almost no light emission is observed (see fig. 4.7C). As the tip moves closer (gray ring), a series of vibronic peaks corresponding to the PtPc molecule appears in the STM-PL spectrum. The peak positions match almost perfectly the vibronic peaks observed for STM-EL measurements. A detailed comparison of theoretical and experimentally obtained vibronic peaks is presented in section 4.4. Even though both STM-PL and STM-EL spectra presented here are obtained for the same molecule, the vibronic peaks in STM-PL are much sharper, allowing precise analysis of the vibrational modes. Spatial mapping of these modes allows symmetry analysis of the vibrations similar to TERS mapping in a picocavity[95,155] or by utilizing the resonance Raman effect for a decoupled single molecule[241]. The findings of the vibrational mode mapping are discussed in section 4.4.

In addition to the vibrational modes, a weak peak is observed at 1.264 eV. The peak is assigned to the 0-0 transition of phosphorescence because of the reasons discussed earlier in section 4.1. The inset in fig. 4.7C shows a blowup of the T_1 emission line with longer integration time. The width of the 0-0 peak (0.21 meV) is comparable to the one obtained for STM-EL (0.23 meV) and suggests similar lifetimes for the T_1 state upon excitation via ISC and direct charge injection. The T_1 emission intensity for STM-PL, on the other hand, is very different from the one obtained for STM-EL. Since the $S_0 \rightarrow S_1$ transition is used for excitation, it leads to a strong background intensity at the S_1 line and must be suppressed by a long-pass filter. Thus, the respective integrated photon intensity of the S_1 vibrational progressions (1.9-1.75 eV) has to be used to normalize the T_1 line for both STM-EL and STM-PL. Following this protocol, the T_1 intensity is about two orders of magnitude weaker in STM-PL than in STM-EL.

Considering that only the lowest vibrational ground state of S_1 is excited in resonant STM-PL, and no ISC can occur from the higher-lying vibrational states, the T_1 intensity in STM-PL provides only a lower bound on the contribution of ISC in STM-EL. The excitation using a plasmon with broad energy distribution (≈ 0.8 eV) or with direct charge injection at a sample voltage of -2.6 V implies that the excitation extends to energies well above the S_1 energy. The ISC rate would be increased when occurring from vibrationally excited states[242,243] leading to a larger ISC contribution to T_1 emission intensity for STM-EL.

The observed $T_1 : S_1$ intensity ratio $\approx 1 : 30$ in STM-PL is in fair agreement with the ratio of calculated transition dipole moment of the T_1 and S_1 state $\mu_{T_1 \rightarrow S_0} : \mu_{S_1 \rightarrow S_0} \approx 1 : 40$. This finding suggests that the ISC rate is not significantly perturbed (in comparison to radiative decay rates) upon absorption of PtPc atop NaCl or the proximity to the plasmonic tip compared to PtPc in the gas-phase. The above inference is central to the discussion of how X-P coupling can be used to control the T_1 intensity in section 4.3.

Besides a different excitation mode, photo- versus electronic excitation, different sample voltages were used to stabilize the tip position using the feedback loop in the two measurements, -2.6 V for STM-EL and 1 V for STM-PL. Figure 4.8 shows the T_1 emission spectra for STM-EL (bottom) and STM-PL (top) spectra at the two sample voltages. For STM-EL the T_1

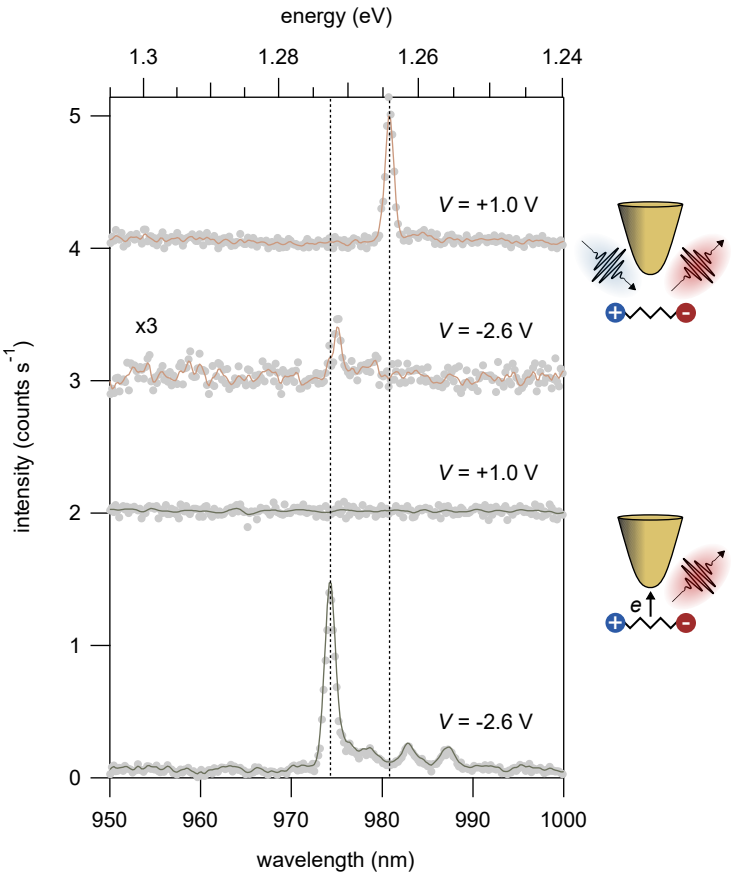

Figure 4.8 — Voltage dependence of the T_1 emission line for STM-EL and STM-PL. Bottom – STM-EL spectra at −2.6 V and 1 V ($I = 60$ pA, $t = 2$ min). Top – STM-PL spectra at −2.6 V and 1 V (laser power: 1µW, $I = 3$ pA, $t = 5$ min) showing the voltage dependent redshift.

line is at 1.273 eV for a sample voltage of −2.6 V, whereas, for 1 V no T_1 emission is observed. This is because, at 1 V, neither the plasmon nor the charge injection through the LUMO has enough energy to excite the molecule. Note that the tip is placed atop the molecule, on the HOMO lobe, for the STM-EL measurement. For STM-PL, with the tip placed ≈ 1.9 nm from the center of the molecule, the T_1 line is at 1.272 eV for −2.6 V, identical to the T_1 energy in STM-EL. In contrast, at 1 V, the T_1 line in STM-PL is redshifted to 1.264 eV (peak shift ≈ 8 meV). Figure 4.9 shows extended STM-PL spectra obtained for voltages −2.6 V and 1 V. The vibronic peak positions are identical, whereas the T_1 emission shows a considerable shift (≈ 8 meV), implying that sample voltage affects S_1 and T_1 differently. The redshift of the T_1 peak at the sub-molecular length scale suggests that the STM tip applies a highly localized electric field that shifts the quantum states in the nanocavity.

A similar peak shift in resonant STM-PL was observed by Imada *et al.*[150] for the S_1 line of H_2Pc, although four times smaller in magnitude. Based on the dependence of the S_1 peak energy on the sample voltage and the lateral distance from the molecule, they attributed the shift to the Stark effect[244]. For constant voltage, as the tip is moved away from the molecule, a combination of both Stark effect and X-P-coupling lead to a shift of the peak position[219]. A similar redshift of the S_1 peak energy for STM-PL (532 nm laser) of ZnPc (S_1: 655 nm) was reported by Yang *et al.*[96]. Spatially mapping the peak position at constant height roughly 2 Å above the molecule, they observe a redshift by ≈ 7 meV, which is quite close to the redshift of the T_1 peak energy observed for PtPc. Rosławska *et al.*[212] too reported a redshift of the

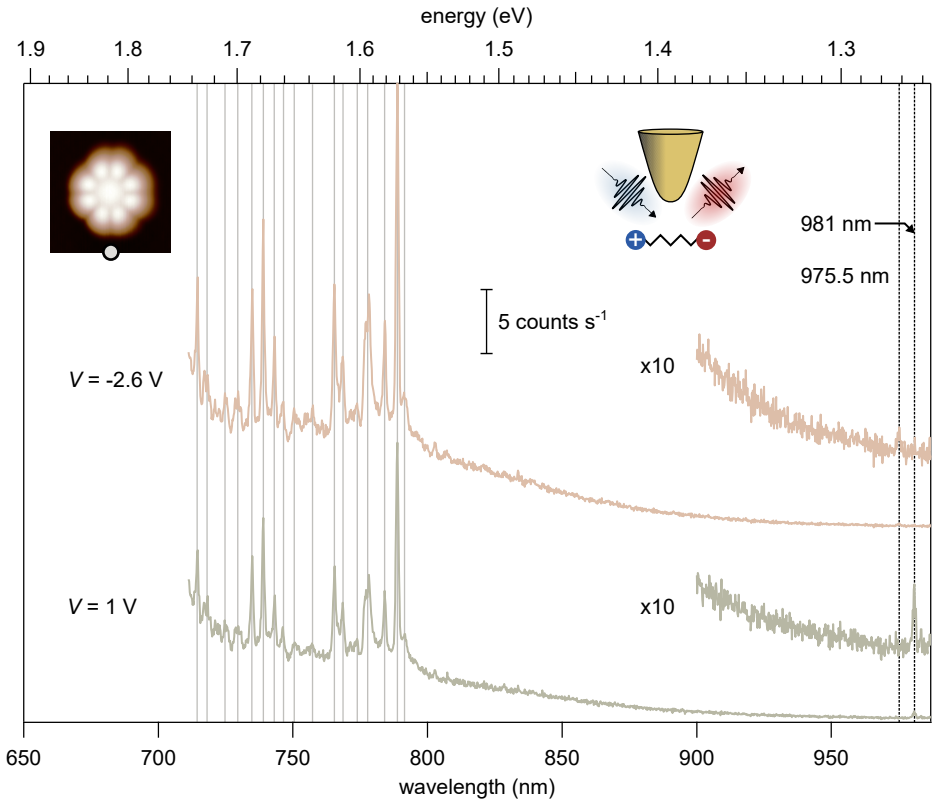

Figure 4.9 — Extended STM-PL spectra at different voltage polarities. STM-PL spectra at sample voltage of −2.6 V (top) and 1 V (bottom) showing vibronic peaks and T_1 emission line (laser power: 1µW, $I = 3$ pA, $t = 5$ min, grating: 300 grooves mm^{-1}). The blowups (×10) of T_1 emission line showing voltage dependent redshift. Inset (top left). STM topography image of the molecule with gray dot marking the tip position (set point: $I = 3$ pA, $V = -2.6$ V, size: 3.5 × 3.5 nm^2).

S_1 peak energy as the STM tip vertically approaches (z-height) an H_2Pc molecule. For a z-distance sweep of 300 pm, they report a redshift of ≈ 5 meV, which they attribute to the Stark effect due to the electrostatic field and the Lamb shift[245].

The tip is stabilized at a different tip height in the constant current mode for different voltages. This changes the X-P coupling and the effect of the tip-induced electric field on the molecule underneath and thus leads to a peak shift as discussed above. The laser line used for resonantly exciting the S_1 state has FWHM of 50 µeV. Given that, a peak shift on the order of a few meV could potentially detune the resonant excitation and reduce the observed emission intensities. As seen in fig. 4.8, an almost tenfold difference in T_1 intensity is observed for the two voltages (−2.6 V and 1 V). For this reason, a sample voltage of 1 V is used for measurements in this chapter. In contrast, the intensity of the vibronic modes is almost identical for the two voltages (fig. 4.9), indicating that the laser line is comparatively well aligned to the S_1 energy. These seemingly contradicting findings show that the effect of X-P coupling and the Stark shift on the T_1 state and ISC are more involved. Further experimental and theoretical considerations are thus needed to elucidate this observation. The next section presents an analysis of this complex tip-molecule interaction (X-P coupling) using STM-EL.

4.3 Influence of exciton-plasmon coupling on phosphorescence and intersystem crossing

The ability to precisely position the STM tip with respect to the molecular transition dipole axes allows investigation of X-P interaction and addressing the question how it affects different emission processes[71–73]. In the previous section, the tip acted as a highly localized source of perturbation for the electronic states due to the Stark, Lamb, and Purcell effects[212]. Here, it enables probing the effect of X-P coupling on ISC and phosphorescence while keeping the charge injection into the molecular orbital constant. Figure 4.11B schematically shows the path along which the tip is placed at a distance r from the center of the molecule. The azimuthal angle θ is defined with respect to the x-axis of the molecular skeleton. In constant current mode, for the tip position at $r = 1.1$ nm, and azimuthal angles $\theta = 0°$ and 45°, an almost identical emission intensity for the S_1 line is observed (see fig. 4.10 – bottom). This finding suggests that the electronic excitation of the singlet state through injection into the same orbital (LUMO) does not differ considerably for the two tip positions. In contrast, the emission intensity of the T_1 line exhibits more than a threefold increase at $\theta = 45°$ in comparison to $\theta = 0°$. Considering that STM-PL measurements (low T_1 intensity) suggest that the ISC from the S_1 to the T_1 state accounts for only a few percent of the observed STM-EL phosphorescence intensity, a threefold modulation in T_1 intensity is probably unrelated to the modulation of the ISC rate for different tip positions.

As discussed earlier in section 3.1, the molecular transition dipole axes are in the direction of the isoindole units of the PtPc molecule. Thus, for a fixed distance $r = 1.1$ nm from the center of the molecule but still atop the HOMO, the tip positioned at $\theta = 0°$ would exhibit stronger X-P coupling than when it is positioned at $\theta = 45°$. Corresponding to $\theta = 0°$ – *stronger* X-P coupling – the peak position of the S_1 line is observed at 1.948 eV (see fig. 4.10 – bottom). The line blueshifts to 1.953 eV ($\approx$ 5 meV) for $\theta = 45°$ – *weaker* X-P coupling. Accordingly, the vibronic peaks are also blueshifted. This observation is in line with previous works reporting peak shifts of S_1 emission atop the molecule using STM-EL[134,212] and STM-PL[96]. Next, with the tip placed at a distance $r = 1.9$ nm to avoid charge injection into the HOMO, STM-PL spectra are recorded for $\theta = 0°$ and 45°. For the two tip positions corresponding to different X-P coupling strength, almost no shift in vibronic peak positions is observed (see fig. 4.10 – top). The local perturbation due to the tip field in the tip-sample cavity, resulting in Lamb shift, is confined to picometer length scales[237,246]. As the tip moves away from the molecule, the effects due to X-P coupling is strongly reduced, and thus, no detectable shifts in vibronic peak positions are observed.

For T_1 emission in both STM-EL and STM-PL, a blueshift of the emission peak of $\approx$ 2 meV and $\approx$ 4 meV, respectively, is observed. This suggests that X-P coupling affects the singlet and triplet coupling differently, similar to the discussion in the previous section. The opposite trend for the peak shift for T_1 and S_1 lines may be due to the Stark effect. The dipole moment is negligible for a centrosymmetric molecule like PtPc, and thus, so is the Stark effect due to the dipole in the electric field of the tip. However, a tip-induced electric field gradient over

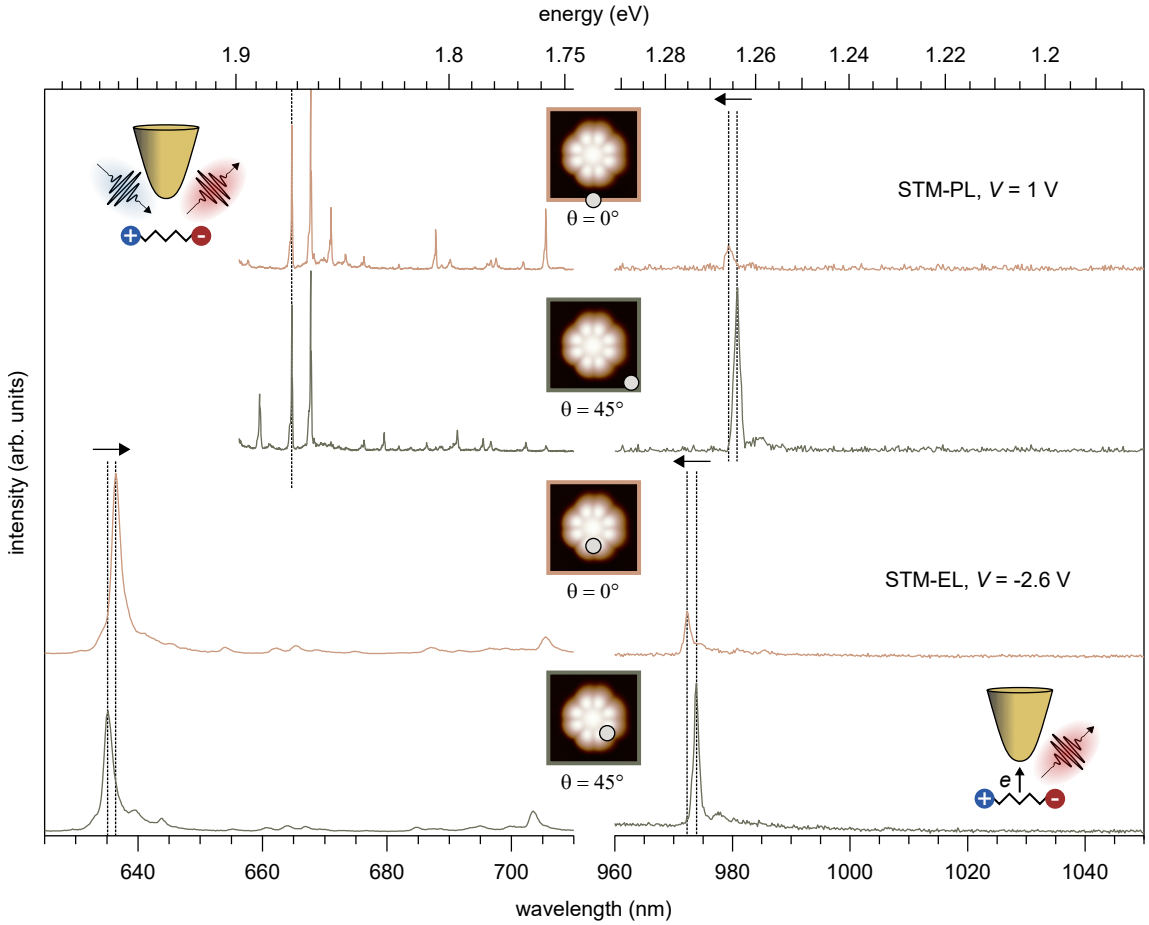

Figure 4.10 — X-P coupling for fluorescence and phosphorescence. Bottom – STM-EL spectra showing S_1 (left) and T_1 emission (right) obtained for azimuths $\theta = 0°$ and $\theta = 45°$, and distance from the molecule $r = 1.1$ nm (set point: $I = 80$ pA, $V = -2.6$ V, S_1: $t = 30$ s, and T_1: $t = 120$ s). Top – STM-PL spectra showing vibronic peaks (left) and T_1 emission (right) for $r = 1.9$ nm, i.e., off the molecular orbital (set point: $I = 3$ pA, $V = 1$ V, $t = 300$ s). The drop in T_1 intensity in STM-PL indicates modulation of ISC by change in tip-position.

the molecule's quadrupole moment also leads to a Stark shift. Then, depending on the sign of the coupling, a redshift or a blueshift may occur.

Furthermore, the phase of the constant that couples the involved oscillators, here the S_1 and T_1 excitons, to the plasmon may also explain the opposite shift of the S_1 and T_1 emission lines. For a complex coupling constant, the two interacting modes (X-P) could energetically attract, repel, or move in phase with each other.[247]. An example for the principle is the difference between *J*- and *H*-aggregates[248–250]. In that case, the direction of energy shift with respect to the single-molecule transition depends on the phase of the intermolecular dynamic dipole coupling, which is determined by the relative orientation of the coupled molecules[74,249,251]. For a polyatomic molecule, the perturbation due to the SOC effect would lead to singlet-triplet mixing and is behind the observed ISC[133]. We speculate that S_1 and T_1 excitons might couple with a different phase to the plasmon. A deeper theoretical investigation would be required to elucidate this point.

As mentioned earlier, the change in azimuthal angle coincides with a significant drop

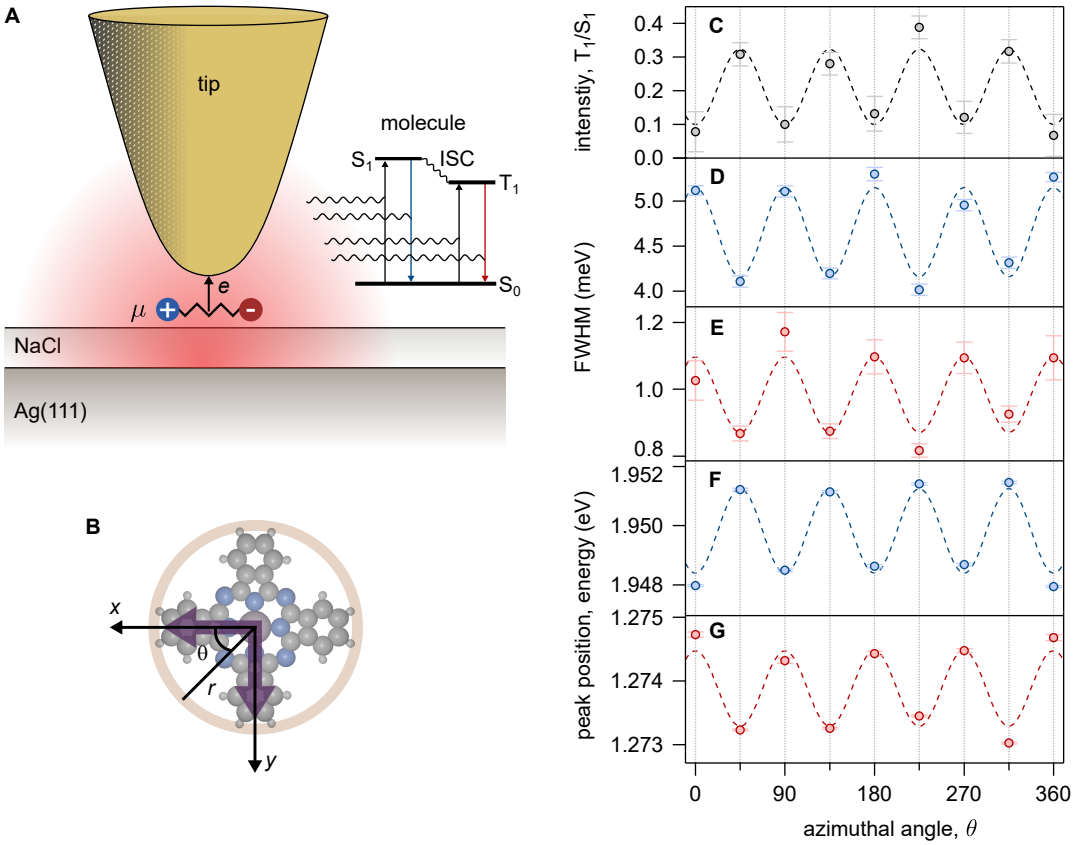

Figure 4.11 — Azimuthal dependence of T_1 emission. (A) Illustration of the interaction between the plasmonic field at the nanocavity and molecule. (B) Schematic defining polar coordinates r and θ with respect to the molecular geometry. (C) Azimuthal dependence of normalized T_1 intensity (set point: $I = 50$ pA, $V = -2.6$ V, S_1: $t = 5$ s, and T_1: $t = 30$ s, grating: 300 grooves mm^{-1}). The intensities were approximated by the area under a Lorentzian peak fit. Error bars represent standard deviation of the peak height from the fit. (D, E) Azimuthal dependence of S_1 (blue) and T_1 (red) FWHM. (F, G) Azimuthal dependence of S_1 and T_1 peak position. The azimuthal dependencies are fit by sine functions (dashed lines in C-G).

($\approx 2/3$) in T_1 emission intensity, while the S_1 emission intensity stays almost constant. A similar drop in T_1 intensity is obtained at $\theta = 0°$, compared to $\theta = 45°$, for STM-PL spectra. Since only ISC results in T_1 excitation for STM-PL, the drop in intensity indicates modulation of ISC magnitude by the change in X-P coupling. It is not straightforward to isolate the reason for the modulation of T_1 intensity. The FWHM and the peak energy of S_1 and T_1 emission is analyzed as a function of the X-P coupling strength in more detail (fig. 4.11).

STM-EL spectra are recorded by placing the tip next to the molecule at $r = 1.1$ nm and azimuths corresponding to $\theta = n\pi/4$, where n is an integer (fig. 4.11B). The relative phosphorescence intensity (T_1:S_1 intensity ratio), position, and FWHM of the emission lines are obtained using Lorentzian fitting. In line with earlier observations (reported in fig. 4.10), the higher phosphorescence intensity corresponds to azimuths $\theta = (2n+1)\pi/4$ and lower intensity to $\theta = n\pi/2$ (fig. 4.11C). The variation of T_1:S_1 is in anti-phase with the width of the S_1 and T_1 lines, both of which broaden due to stronger X-P coupling[212,219,252]. In the following, the origin of this correlation is discussed.

Firstly, the decrease in T_1 intensity might be related to the observation in fig. 4.5 that

stronger X-P coupling to T_1 reduces its emission efficiency via a stronger non-radiative decay as the tunneling current increases. This is supported by the increase in linewidth as the T_1 intensity diminishes (see fig. 4.11C and E).

Since a grating with only 300 grooves mm^{-1} is used to acquire the spectra, we observe considerably broadened spectral lines. Using a grating with 1200 grooves mm^{-1} in fig. 4.3 we observe a FWHM of 0.23 meV, whereas, in fig. 4.11E a FWHM of 0.85 meV is measured. Considering that broadening would affect all spectra similarly, the FWHM obtained with a lower resolution grating can be corrected. On deconvolution[3] of the values in fig. 4.11, the reported variation would range from 0.23 to 0.75 meV (instead of the measured 0.85 meV and 1.1 meV). Thus, the change in FWHM is more significant (×3) than indicated by the raw data values (20%) in fig. 4.11E.

Secondly, the S_1 linewidth increases at $\theta = n\pi/2$ because of the stronger X-P coupling (fig. 4.11D). The broadening of the linewidth implies that the lifetime is reduced. If we assume that the ISC rate stays approximately constant and is unaffected by the tip position, shortening the S_1 lifetime will reduce the amount of ISC in STM-EL, decreasing the T_1 population. This is in line with the relative T_1 intensity and is in fair agreement with the calculated transition dipole moment ratio (see section 4.1). The argument that ISC rate is approximately constant is also supported by the fact that the SOC facilitates ISC due to the central Pt atom[231]. For comparison, the heavy atoms of the tip (Au or Ag) are at least 5 Å away as measured in point-contact experiments[241]. Once more, deconvoluting the FWHM of the S_1 line (see fig. 4.3), we obtain a variation from 3.9 meV to 5 meV (instead of 4 meV to 5.1 meV in the raw data). The resulting change of S_1 lifetime by nominally 28% must be regarded with caution since the line is composed of several transitions as discussed above (see section 4.1) Still, the modulation of non-radiative decay and the magnitude of ISC cannot entirely account for a threefold modulation in T_1:S_1 ratio, as seen in fig. 4.11C.

To further analyze the role of X-P coupling and Stark effect, the radial distance dependence of the T_1:S_1 ratio is studied (shown in fig. 4.12). For a fixed tunneling current setpoint, the tip is placed at an increasing distance from the molecule's center, and fluorescence and phosphorescence are recorded. An increase in relative T_1 intensity is observed as the tip is moved away from the molecule instead of a decrease, as would be expected for the increase in length of the tunneling barrier as discussed above. FWHM and peak position analysis of the spectra shows that for both S_1 and T_1 emission lines, the FWHM decreases with increasing distance from the molecule, indicating a decrease in X-P coupling strength. Similar to the angular dependence, a longer S_1 lifetime (weaker coupling) would increase the magnitude of ISC (assuming constant ISC rate as discussed in the previous section) from the S_1 state, resulting in a larger T_1 population.

The S_1 peak position shows a blueshift with decreasing X-P coupling strength in line with earlier studies[71,72,212]. However, the T_1 peak shows the opposite trend (fig. 4.12C). It redshifts as the tip moves away from the molecule, similar to the observation of its azimuthal

[3] $\mathrm{FWHM}_{\mathrm{corr}} = \sqrt{\mathrm{FWHM}^2_{\mathrm{observed}} - \mathrm{FWHM}^2_{\mathrm{grating}}}$

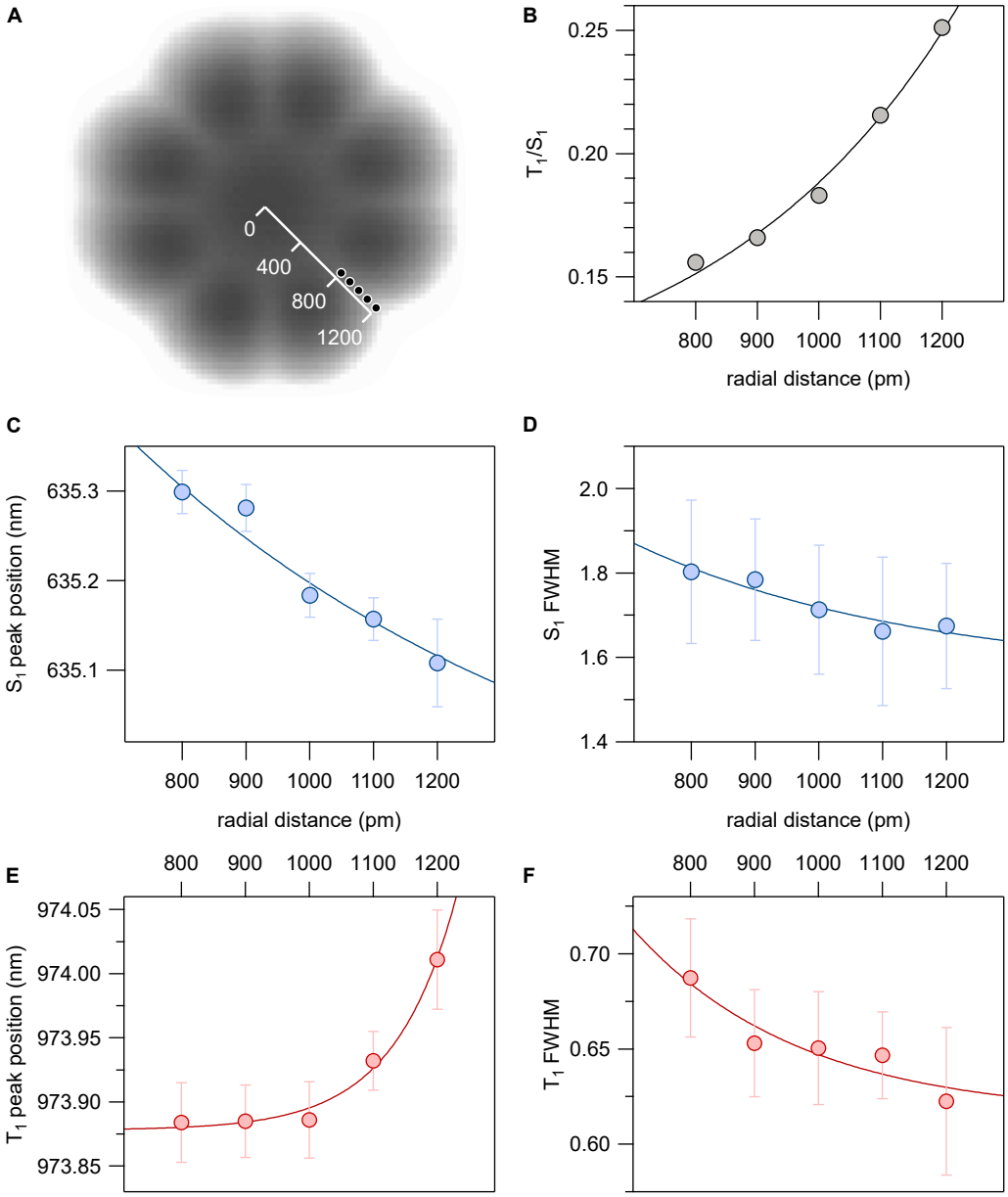

Figure 4.12 — Distance dependence of S_1 and T_1 emission. (A) STM topography of the molecule with tip positions marked for data presented in B-F (set point: $I = 4$ pA, $V = -2.6$ V). (B) T_1/S_1 intensity ratio as a function of radial distance from the molecule (set point: $I = 50$ pA, $V = -2.6$ V, S_1: $t = 10$ s, and T_1: $t = 120$ s, grating: 300 grooves mm^{-1}). (C, D) Peak position and FWHM evaluated using a Lorentzian lineshape fit to the S_1 and (E, F) T_1 emission lines for the tip positions in A. All solid lines are exponential fits to guide the eye.

dependence (4.11G). Moreover, in both cases, the shift of the T_1 line is roughly one-third of the shift of the S_1 line. This finding hints at a weaker plasmon coupling for the T_1 state than for S_1. This is in qualitative agreement with the theoretically calculated ratio of the T_1 and S_1 transition dipole moments (see section 4.1).

In summary, as the tip moves away from a molecule, a weaker X-P coupling leads to a larger ISC magnitude and, thus, higher intensity of T_1 emission. This also leads to narrowing of the S_1 and T_1 lines. Figure 4.12 corroborates the mechanism of non-radiative quenching by tip proximity and is in line with the behavior discussed for fig. 4.5 and fig. 4.11E. Thus, the substantial variation of T_1 intensity with azimuths (fig. 4.11C) is a combination of varying S_1 lifetime and varying non-radiative quenching induced by the proximity of the tip.

4.4 Single molecule vibrational mapping using STM-PL

The chemical fingerprint of a molecule can be routinely obtained via nuclear magnetic resonance[253], infrared[254], Raman[255], and fluorescence spectroscopies[256]. However, to assign the spectroscopic data to specific chemical bonds in a molecule, one must rely on theoretical predictions and visualizations. Combining Raman spectroscopy, which provides rich chemical information, with local probe microscopy offers sub-Å spatial resolution in the form of tip-enhanced Raman spectroscopy (TERS), allowing mapping of the vibrational modes of a single molecule[116,257,258]. Similar to STM-EL[134] and STM-PL[96], the high spatial resolution translates to sub-nanometer resolution in TERS mapping due to the strong confinement of the nanocavity plasmon[93,94]. Recently, spatial maps of individual vibrational modes allowed assignment of atoms involved in the respective vibration[95,155], reaching atomic spatial resolution in chemical sensitivity. However, the experimental conditions that enable these measurements lead to a significant distortion of the geometric and electronic structure of the molecule. The significant plasmonic enhancement of the Raman signals, necessary for atomic-scale spatial mapping, requires that the probe (a single atom at the tip apex) and its distance from the molecule are comparable in size ($\approx$ 2Å). Considering that the tip enhancement exhibits a dominant component along the tip axis (z-component), the Raman modes parallel to the tip axis are strongly enhanced compared to the modes along the molecular plane. The Raman intensity in the *picocavity* is further enhanced by chemisorption of the molecule on a metal substrate[259,260]. The moiety chemically bonded to the metal forms dynamic charge transfer states. When the excitation energy matches the intermediate charge transfer states of the chemisorbed molecule-metal complex, the vibrational mode exhibits resonant Raman enhancement[261]. However, chemisorption on the metal surface leads to distortion of the geometric and electronic structure of the molecule, which also alters its vibrational characteristics.

As discussed in section 1.1, the coupling to the metal substrates can be greatly reduced using a few layers of NaCl. Using this strategy to isolate a copper naphthalocyanine molecule, Jaculbia *et al.*[241] recently reported Raman maps that correspond to the symmetry of the vibrational modes imaged. They propose that resonant excitation conditions and a significant

contribution of the lateral (x and y) components to the overall enhancement enable mapping of the symmetries of the vibrational modes. In contrast to the studies by Lee *et al.* [95] and Zhang *et al.* [155], they perform the spatial mapping at a tip sample distance of ≈ 6Å (instead of 2 Å) which rules out chemical enhancement due to charge transfer to the tip[262].

In principle, resonant photoluminescence is a particular case of resonant Raman spectroscopy in which the excitation laser energy is tuned to the S_1 line. The decay to the vibrational ground state happens directly from the S_1 state and not from the virtual states as in a non-resonant Raman process. Figure 4.13 shows a schematic diagram of the underlying measurement principle. For STM-EL spectra recorded with the tip placed at $r = 1.4$ nm from the center of the molecule, a Fano lineshape is observed at ≈ 635.6 nm related to the broadband plasmonic emission and the excitonic molecular transition is observed (fig. 4.13). The plasmon acts as a local excitation source for single molecule absorbance spectroscopy[71–73]. Figure 4.14 (left) shows the vibronic satellites of the S_1 emission from a single PtPc molecule adsorbed atop 4 ML NaCl on Ag(111) using STM-EL and STM-PL. A Raman spectrum obtained for PtPc powder is shown for comparison. The vibrational peak positions for the three measurements are almost identical, demonstrating the viability of chemical characterization in the plasmonic nano junction. Finally, the spectra are compared with theoretical simulations based on gas-phase DFT calculations for the optimized geometry of the molecule. Besides a slight discrepancy for the peak at 1526 cm^{-1}, the agreement with the experimental data for vibrations belonging to the singlet ground state is striking.

Since PtPc belongs to the D_{4h} point symmetry group, vibrational modes with A_{1g}, B_{2g}, and B_{1g} symmetries are Raman active. Table 4.1 lists vibrational modes of various symmetries and their assignments for Raman, STM-EL, and STM-PL spectra. The vibronic structure of the resonant STM-PL spectrum is rich in features, and a few peaks could not be assigned to vibrational modes. A theoretical calculation taking into account resonant excitation, tip enhancement, and surface effects may overcome the observed discrepancies but is out of scope for the current study. In light of the findings reported in Chapter 2, we envision that the molecule's interaction with Cl ions might affect the vibrational modes.

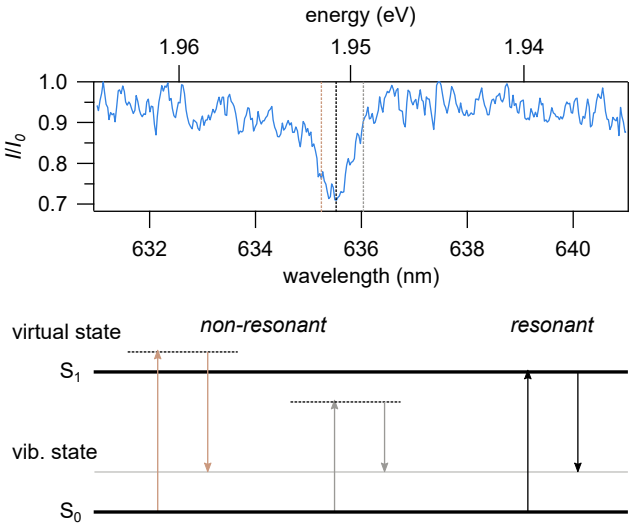

Figure 4.13 — Resonant STM-PL as a special case of resonant Raman spectroscopy. Top – STML spectrum showing a Fano lineshape due to the interaction between the plasmon and the molecular transition (set point: $I = 60$ pA, $V = -2.8$ pA, $t = 60$ s). The intensity is normalized to 1. Bottom – Schematic of the Raman process at different excitation energies demonstrating excitation of virtual levels and resonant energy condition at which S_1 is directly excited.

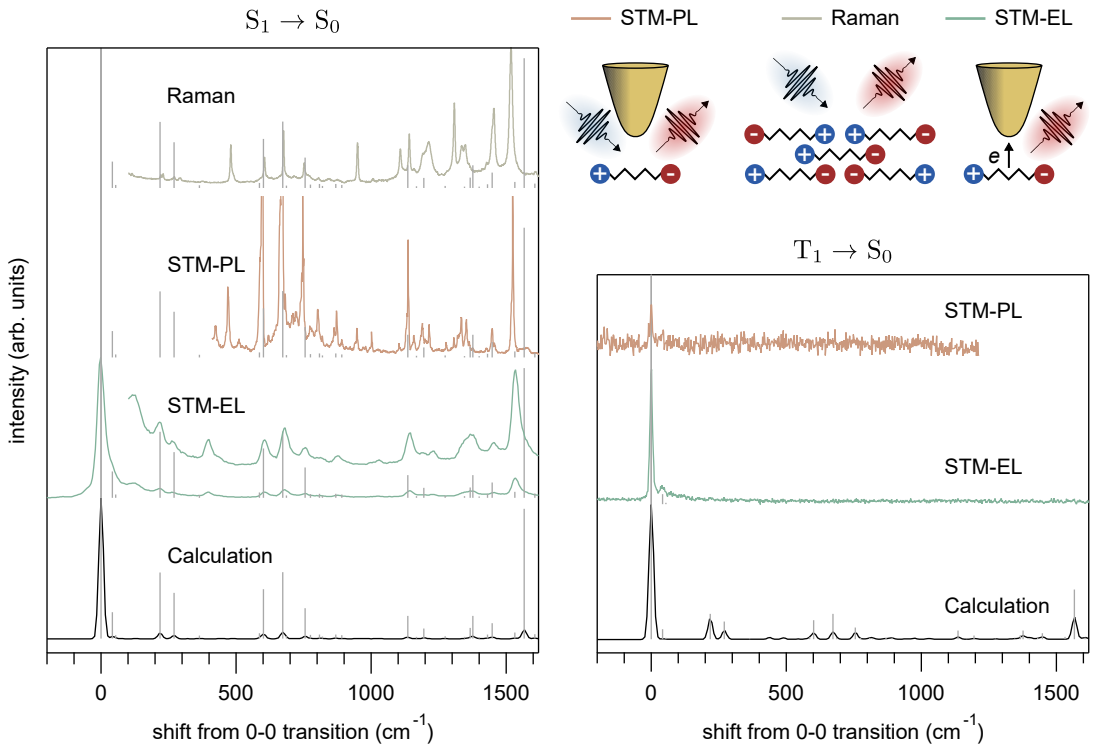

Figure 4.14 — Comparison of vibronic satellites for $S_1 \rightarrow S_0$ (Left) and $T_1 \rightarrow S_0$ (Right). Left – (Top to bottom) Raman spectrum for PtPc powder using a 532 nm laser (grating: 600 grooves mm^{-1}), STM-PL spectrum next to a PtPc molecule atop 4 ML NaCl on Ag(111) (set point: $I = 3$ pA, $V = 1$ V, laser power: 1 µW, $t = 30$ s, grating: 1200 grooves mm^{-1}), STM-EL spectrum for the PtPc molecule obtained with the tip placed atop a HOMO lobe (set point: $I = 60$ pA, $V = -2.6$ V, $t = 120$ s, grating: 300 grooves mm^{-1}), and calculated vibronic spectrum of a neutral PtPc molecule in the gas phase for the $S_1 \rightarrow S_0$ transition. Right – (Top to bottom) STM-PL ($t = 120$ s), STM-EL, and calculated optical spectrum of a neutral PtPc molecule for $T_1 \rightarrow S_0$ transition.

Surprisingly, for the T_1 emission almost no vibrational satellites are observed (fig. 4.14 – right). In an earlier study, vibronic peaks of the T_1 transition for a PTCDA molecule could be observed and assigned to modes obtained from gas-phase calculations[21]. The discrepancy may be due to the lack of plasmonic enhancement as the tail of the plasmon barely reaches $\approx$ 1000 nm as observed from STM-EL spectra (see fig. 4.2). A drop in detector quantum efficiency from $>$ 90% at 750 nm to $<$ 10% above 980 nm contributes to the difficulty in detecting the vibrational peaks of the T_1 transition. Using tips that exhibit enhancement in the near-infrared (larger tip radii $\approx$ 100 nm[263]) and near-infrared sensitive CCD may relax some of these limitations.

Figure 4.10 shows that vibrational peaks in STM-PL show no shift for different angular positions of the tip. It was proposed that due to the larger distance from the molecule $r = 1.9$ nm compared to the STM-EL measurement for $r = 1.1$ nm (where a shift of vibrational peaks is observed), the change in X-P coupling is negligible. STM-PL spectra for azimuths $\theta = 0°$ (blue), 22.5° (gray), and 45° (red) show for some modes, a modulation in intensity (see fig. 4.15). For example, the vibrational mode at 476.3 cm^{-1} is absent for tip position $\theta = 0°$ but its intensity increases sharply at $\theta = 22.5°$ and further at $\theta = 45°$. The vibrational peak at 1528.5 cm^{-1} shows the opposite trend, exhibiting maximum intensity at $\theta = 0°$. Remark-

ably, the mode at 605.2 cm^{-1} shows no intensity modulation. Considering that the tip is placed far from the molecule and the plasmonic enhancement is constant over the displayed energy range, the X-P coupling would play only a minor role, if any, in the azimuthal dependence. The intensity modulation of specific vibrational modes is thus assigned to their spatial symmetry, similar to the resonant Raman measurements[241].

Next, spatial mapping of the resonant STM-PL (resonance Raman) intensity for representative vibrational peaks is performed. For the parameters: $I = 3$ pA, $V = 1$ V, the tip is scanned over the surface at 6 nm s^{-1}. The grating with 300 grooves mm^{-1} is for each scan centered on the selected mode to deflect the light into the SPAD (see discussion on *4goki*). These maps are shown in fig. 4.15B-D with vibrational modes assigned to each of the spatial maps. The symmetry is determined by the azimuthal angle at which the intensity maximum occurs. The obtained patterns in the spatial maps resemble the mode symmetries perfectly and support the notion that the intensity modulation of vibronic peaks is indeed related to the symmetry of the vibrational modes[241].

The intensity of each vibrational mode is governed by its Raman tensors $\alpha_{\rho\sigma}$ where ρ and σ represent the cartesian coordinate axes x, y and z. For the symmetries in fig. 4.15, $\alpha_{\rho\sigma}$ is given by

$$A_{1g}: \begin{pmatrix} a & 0 & 0 \\ 0 & a & 0 \\ 0 & 0 & b \end{pmatrix} \quad B_{1g}: \begin{pmatrix} c & 0 & 0 \\ 0 & -c & 0 \\ 0 & 0 & 0 \end{pmatrix} \quad B_{2g}: \begin{pmatrix} 0 & d & 0 \\ d & 0 & 0 \\ 0 & 0 & 0 \end{pmatrix} \tag{4.1}$$

Since B_{1g} and B_{2g} modes do not have any component along the tip axis, they are not expected to exhibit large intensities, in line with the observations reported above. A molecule adsorbed atop a few ML NaCl on Ag(111) is closer to the tip than to the metal surface[241]. Thus, the image charges do not compensate each other, suggesting an increased lateral plasmonic enhancement. Since resonant Raman spectroscopy relies on light absorption, the Laporte rule[4] plays a central role. For PtPc, HOMO and LUMO exhibit odd parity along the z-axis, and thus the electronic transition between them is Laporte forbidden (see fig. 4.15F). However, in the x-y plane, the two orbitals exhibit different parities, and the HOMO-LUMO transitions are parity allowed for excitation in the molecular plane.

The three different patterns for resonant STM-PL images can be assigned within the above framework. For the A_{1g} mode, the induced dipole due to the vibrations can be anywhere in the molecular plane since the tensor is diagonal and $\alpha_{xx} = \alpha_{yy}$. Then the lateral component of the plasmonic enhancement would be parallel to the induced dipole and thus detectable for all azimuths around the molecule, as in fig. 4.15C. When the tip is placed along the molecular axes $\theta = n\pi/2$, the dipole induced due to the B_{1g} mode would be paral-

[4]The Laporte Rule is a selection rule in electron absorption spectroscopy that applies to centrosymmetric molecules. It says that transitions between states of the same symmetry with respect to inversion are forbidden. A detailed derivation of the Laporte rule can be found in the following textbook[264].

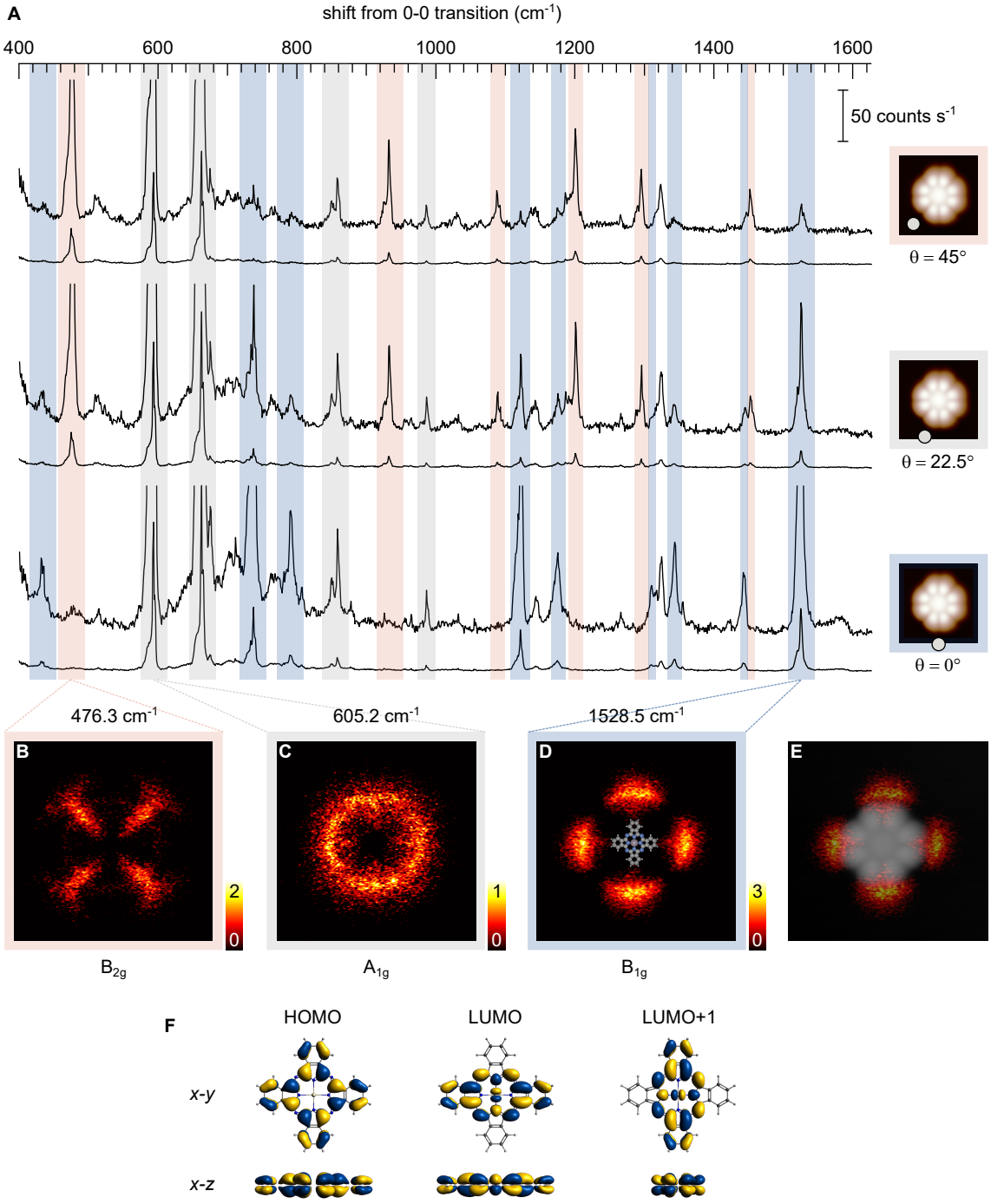

Figure 4.15 — STM-PL mapping of vibrational modes. (A) High resolution STM-PL spectra at angular positions indicated in the STM images on the right (r = 1.9 nm, laser power: 1 μW, set point: $I = 3$ pA, $V = -2.6$ V, $t = 120$ s). A vertically shifted blow up of the spectra (×7) is shown for clarity. The color-coding highlights the specific modes whose intensities are modulated by tip position at $\theta = 0°$ (blue), $\theta = 22.5°$ (gray), and $\theta = 45°$ (red). (B-D) Maps of STM-PL intensity for modes at wavenumbers 476.3 cm^{-1}, 605.2 cm^{-1}, and 1528.5 cm^{-1} showing distinct patterns representative of the vibrational modes and their respective symmetries (size: 6 × 6 nm^2). (E) Grayscale STM image (size: 3.5 × 3.5 nm^2) overlaid with the B_{1g} STM-PL map showing the light intensity distribution with respect to the HOMO. (F) Calculated maps of the electronic molecular frontier orbitals of PtPc along *x-y* (top) and *x-z* (bottom) planes. HOMO-LUMO transitions with excitation along the *x-y* plane are parity allowed, while the ones with excitation along the *z*-axis are parity forbidden.

lel to the lateral enhancement and thus leads to high intensity along the molecular axes with nodes along with the diagonals (fig. 4.15D). For the B_{2g} mode, the induced dipole is parallel to the lateral enhancement only for $\theta = (2n+1)\pi/4$ and thus detected at the azimuths $\theta = 45°, 135°, \ldots$. Thus, the selection rules enforced by the Raman tensors – taking into account the lateral component of the plasmonic enhancement – are valid for a single decoupled molecule. These findings prove that resonant STM-PL (Raman) allows non-invasive mapping of the symmetry of the observed vibrational modes at a sub-molecular level. The electronic decoupling provided by the ultrathin NaCl film provides an unperturbed playground to study photoluminescence and Raman spectroscopy at the ultimate limit of a single molecule.

Conclusion

The results presented in this chapter provide a comprehensive picture of nanoscale processes at play in plasmon-enhanced fluorescence and phosphorescence. The unique combination of STM-EL and STM-PL allows the analysis of triplet emission and, for the first time, the observation of singlet-triplet ISC of excitons at the single-molecule scale. The S_1 and T_1 exciton coupling to the nanocavity plasmon are studied with sub-Å precision, providing insight into dynamic processes that control the emission intensity, like radiative and non-radiative decay. From distance dependence measurements, it is found that the strong non-radiative damping by the tip quenches the phosphorescence much more efficiently than the fluorescence. A large modulation in phosphorescence intensity is observed with the change in exciton-plasmon coupling for the tip position at different azimuthal angles around the molecule. Thus coupling to plasmonic nanostructures can be used to tune the relative T_1:S_1 intensities of emitters for intelligent control of the emission color[238]. The T_1 emission lifetime, as estimated from the FWHM of the 0-0 transition peak, is in the range of a few picoseconds as compared to microseconds[226], in the absence of plasmonic enhancement. This shows promise for future phosphorescent OLEDs, which use decay rate enhancement of plasmonic nanostructures to boost their emission intensities. A lower steady-state exciton density also helps prevent oxidation of the emitting layer, thus allowing for a longer device lifetime. Despite the novel character of the experiment, the findings of this chapter are transferable to a wide range of systems where exciton dynamics play a central role like plasmonic-OLED devices[25,265], bioimaging[39,40], and biosensing[41,42].

Table 4.1 — Vibrational modes for the S_0 ground state of the PtPc molecule.

Irreducible representation	Theory (cm^{-1})	Raman (cm^{-1})	STM-EL (cm^{-1})	STM-PL (cm^{-1})
B_{1g}	218.2531	221.53		457.6100
A_{1g}	270.2882	230.18		498.4740
B_{1g}	569.7727	271.34	216.138	583.1511
A_{1g}	601.4807	291.08	229.407	656.5677
A_{1g}	672.7821	480.39	395.439	733.7030
B_{1g}	755.7018	605.91	398.780	789.3000
B_{1g}	809.0600	675.96	603.762	859.2470
A_{1g}	869.0328	713.98	617.818	934.6550
B_{1g}	1015.273	752.02	655.035	989.1100
A_{1g}	1016.074	804.91	679.562	1124.140
A_{1g}	1135.702	845.88	755.463	1145.410
B_{1g}	1135.828	1006.2	811.073	1176.440
A_{1g}	1168.702	1108.3	879.086	1201.930
B_{1g}	1195.629	1191.1	1025.30	1293.710
B_{1g}	1335.332	1213.7	1143.15	1319.980
A_{1g}	1366.718	1307.9	1222.12	1339.740
B_{1g}	1377.022	1335.2	1366.79	1405.830
A_{1g}	1400.646	1348.2	1449.41	1435.140
A_{1g}	1431.611	1427.5	1462.79	1511.944
B_{1g}	1448.847	1453.8	1509.81	1558.645
A_{1g}	1532.383	1517.5	1534.64	1594.704
B_{1g}	1566.739	1608.5	1567.29	1635.037
A_{1g}	1606.378	1742.4	1574.10	1740.823
B_{1g}	1606.582	2121.9	1907.65	2123.838
B_{1g}	3129.543	2269.7	2139.48	2198.555
A_{1g}	3129.626	2326.1	2215.51	2277.870
B_{1g}	3145.889	2866.6	2289.29	2332.678
A_{1g}	3146.104	2968.4	2686.63	2666.663
		3038.1	3066.47	2718.688
		3070.9		2847.034
		3123.6		2873.290
				2976.600
				3052.357
				3084.641

Partial results of the presented work have been published in: C. C. Leon, O. Gunnarsson, D. G. de Oteyza, A. Rosławska, P. Merino, A. Grewal, K. Kuhnke, and K. Kern, ACS Nano **14**, 4216 (2020).

5

Coulomb-blockade driven single photon emission from a plasmonic light source

This chapter reports on the observation of single photon emission in the tip-sample gap atop a few monolayer thick molecular films of C_{60} deposited on an Ag(111) surface. Single photon emitters produce a stream of photons such that precisely one photon is emitted at a time. Since an atom-like two-level system requires a finite time for the excitation to relax, the decay rate gives the average time delay between photons. Such light sources play an essential role in a range of proposed quantum technologies, like quantum simulations, precision measurements, and secure communication schemes, among others[266]. Fluorescent atomic defects (vacancy centers in diamond, silicon carbide, or hexagonal-boron nitride) and quantum dots show great promise as single photon sources. However, here we show that at large negative voltages, the STM tip-induced electric field results in split-off states below the C_{60} LUMO band in the bandgap of the C_{60} film, similar to defect states due to atomic vacancies or substitutional defects. The localization of the split-off state on the C_{60} molecule directly beneath the tip leads to significant Coulomb repulsion. The Coulomb blockade encountered by consecutive tunneling charges hopping into these states leads to decay of plasmons one at a time, resulting in single photon emission. We characterize the light emission from the tunneling junction using Hanbury Brown and Twiss STM (HBT-STM) measurements (see section 1.3) and observe quantum emission as evidenced by an antibunching dip ($g^{(2)}(0) < 0.5$) in second-order photon correlations. Since there is no two-level system involved, the associated finite emission lifetime (≈ 1 ns[80,84]) does not limit the single photon emission rate, which, for the proposed mechanism, can be controlled by the tip-sample gap. The experimental findings are rationalized with the help of theoretical modeling of the coupled tunneling gap-C_{60} film system[1]. Further design considerations based on theoretical findings, for example, for choosing molecules comprising the molecular semiconductor, are also proposed for the

[1]The tight-binding calculations were planned and carried out by Olle Gunnarsson, Max Planck Institute for Solid State Research, Germany.

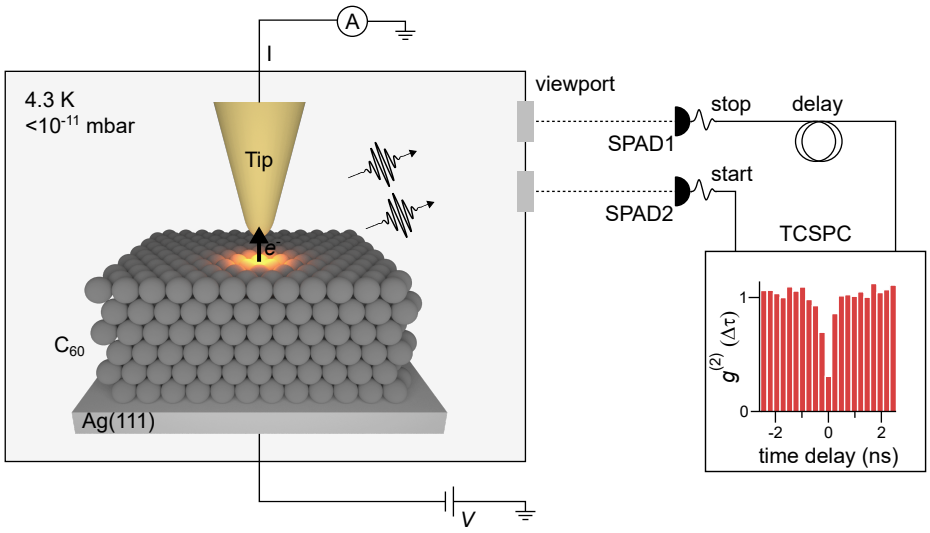

Figure 5.1 — Schematic of HBT intensity interferometer combined with an STM. The light collected at the tunneling junction is guided towards a pair of SPADs which perform time-correlated single photon counting (TCSPC). A third optical path to an optical spectrometer is not shown.

on-demand creation of split-off states in wide bandgap semiconductors. Lastly, we discuss different competing processes which reduce the nominal depth of the photon correlation dip and propose strategies to overcome them.

5.1 Observation of a discrete charging state atop a C_{60} film

Typically, STML spectra acquired atop a few ML thick C_{60} terraces exhibit only broadband plasmonic emission due to the inelastic excitation of plasmonic modes in the tunneling junction[82]. In the absence of local defects in C_{60} films[80,84,85,267] any contribution to the emission spectrum from the corresponding excitonic emission of C_{60} (sharp, few meV broad emission line) is absent. Thus, the observed single photon emission is distinct from that reported for a defect charge trap in a few ML C_{60} films by Merino *et al.*[80]. The average time delay between consecutive photons arises from the Coulomb blockade and is not due to a finite exciton lifetime. The plasmonic origin of single photon emission reported here is further evidenced by an almost an order of magnitude shorter antibunching time constant than the one reported for exciton decay in C_{60} films. The details of the C_{60} on Ag(111) system and its experimental characterization are presented below.

Description of C_{60} on Ag(111)

Figure 5.1 schematically shows the experimental setup used for time-correlated single photon counting (TCSPC) using a pair of SPADs as a photon intensity interferometer in a Hanbury Brown and Twiss configuration[167], which allows measuring $g^{(2)}(\Delta\tau)$ as discussed in section 1.3. A spectrometer coupled to a CCD (not shown) allows simultaneous spectral analysis of the light emitted by the tunneling junction. A representative spectrum acquired

atop a 5 ML thick C_{60} film on Ag(111) is shown in fig. 5.2A. The $\approx$ 100 nm wide spectral band in the visible-infrared region is characteristic of plasmonic emission (see discussion in section 1.2). An energy level diagram of the emission mechanism is shown in fig. 5.2C. The nanocavity plasmon modes in the tunneling junction are excited by subsequent inelastic tunneling events, similar to one comprising purely metal-metal electrodes (see discussion in section 1.2). Tunneling between the tip and sample occurs through an isolated electronic state which has been split off from the LUMO band, in contrast to a metal-metal tunneling junction where the electron tunnels simply through the vacuum, for the tunneling parameters allowing for light emission from the C_{60} film.

The $g^{(2)}(\Delta\tau)$ measured atop a C_{60} terrace for sample voltages $V < -3.3$ V exhibits an antibunching dip ($g^{(2)}(0) = 0.42$) at time delay $\Delta\tau = 0$ (fig. 5.2B). A control $g^{(2)}(\Delta\tau)$ measurement performed over a bare Ag(111) surface shows that $g^{(2)}(\Delta\tau) = 1$, for all $\Delta\tau$, in line with the uncorrelated nature of electron tunneling. The time constant obtained from the Laplace fit yields an antibunching recovery time of $\Delta\tau = 0.13$ ns and is related to the electrons tunneling from Ag(111) to the top C_{60} layer. This time is about an order of magnitude shorter than the average time interval between tunneling electrons in the measurement, which is $\approx$ 1.3 ns for $I = 125$ pA.

Figure 5.3A and B show the tip-sample gap and sample voltage dependence of $g^{(2)}(\Delta\tau)$ at the same tip position as the data presented in 5.2B. For the correlation measurements presented in fig. 5.3A, the sample voltage is fixed at $V = -3.5$ V. The tip-sample gap corresponding to the set point $I = 125$ pA, $V = -3.5$ V is defined as $\Delta z = 0$ and the tip is vertically translated by the z-displacements indicated in fig. 5.3A. This results in an exponential increase in tunneling current and a weak linear increase in the tip-induced electric field. The associated antibunching time constant τ decreases monotonically because the increasing field leads to a decrease in tunneling time from the Ag(111) to the topmost C_{60} layer. The sample voltage dependence of $g^{(2)}(\Delta\tau)$ exhibits antibunching only for voltages $V < -3.3$ V because of the large voltage required to split-off states from the LUMO continuum and pull them below the sample Fermi level $E_{F,S}$ (fig. 5.3B). At $V = -2.7$ V, there is no split-off state visible because it is not yet below $E_{F,S}$, and thus, no single photon emission is observed.

The photon statistics presented above can be rationalized by the electronic properties of the substrate. Figure 5.4A depicts the STM topography image of a 5 ML thick C_{60} molecular island with labels indicating the terrace height. The simultaneously recorded emission efficiency map is shown in fig. 5.4B. Characterization of dI/dV on the C_{60} film reveals the bandgap of the C_{60} nanocrystal for 2 ML and 3 ML C_{60}, while for the 1 ML terrace, only a small gap is seen due to charge transfer and hybridization with the metal substrate. For 4 ML and 5 ML, a pronounced peak close to -3 V becomes visible. The sharpness of the peak (FWHM$\approx$ 50 meV) hints at an additional tunneling channel through a single electronic state[268]. Based on theoretical calculations discussed in section 5.3, we assigned it to a state split-off from the LUMO and pulled down below $E_{F,S}$ by the localized electric field of the tip. This is made possible by the significant negative voltages and small tip-sample gap used in these experiments. If the states were split-off from the HOMO continuum, an expansion in

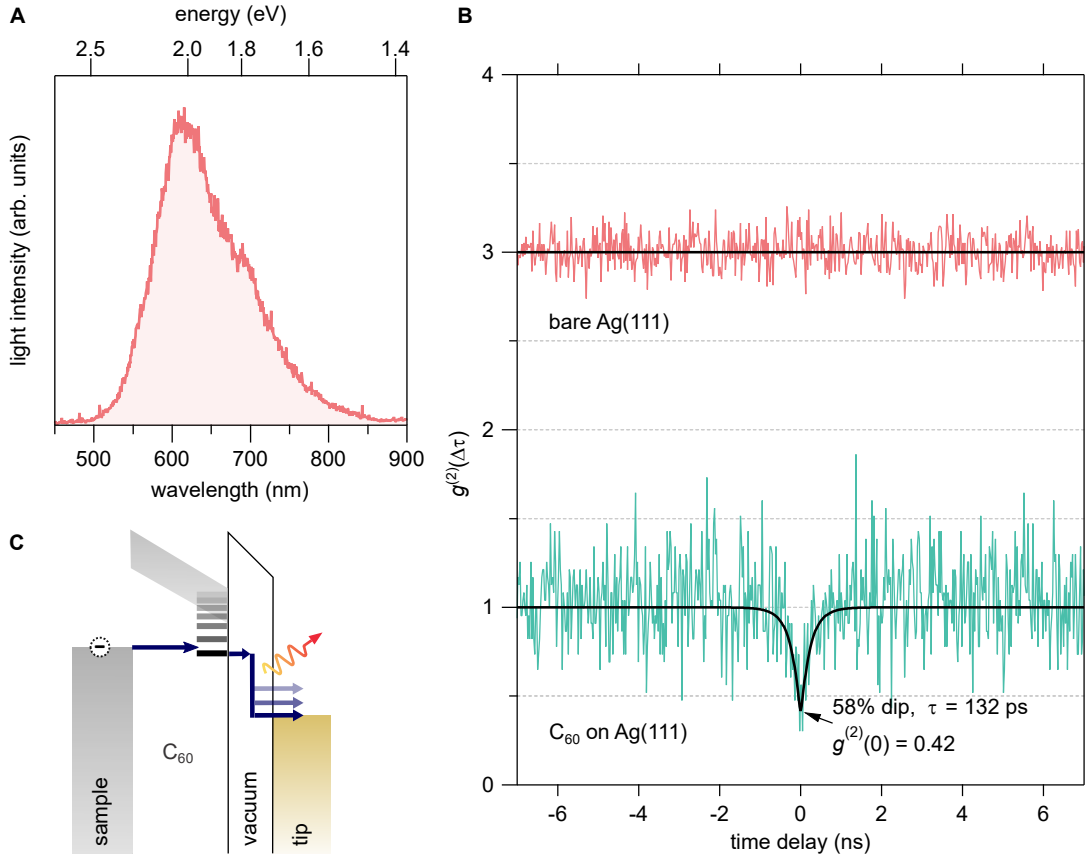

Figure 5.2 — Antibunched plasmonic light emission on 5 ML C_{60} on Ag(111). (A) STML spectrum measured on a C_{60} terrace (set point: $I = 125$ pA, $V = -3.5$ V, $t = 20$ min). (B) Second-order correlations measured *bottom* – at the same tip position as the spectrum in A ($t = 125$ min, time bin width: 24.4 ps) and *top* – atop bare Ag(111) surface (set point: $I = 250$ pA, $V = -3.5$ V). The black curve is a least-squares Poisson-weighted fit to the data, using a constant background, and the detector response time convolved with a Laplace distribution: $1 - \eta\exp(-|\Delta\tau|/\tau)$, whose decay parameter τ is defined as the antibunching recovery time. (C) Schematic illustration of tunneling through the lowest LUMO split-off state and the resulting light emission process. Figure adapted from Leon *et al.*[81].

the apparent bandgap from 4 to 5 ML C_{60} would shift it to lower potentials. However, for dI/dV spectra atop 5 ML C_{60} island in fig. 5.4D, the split-off state is at higher potential than atop 4 ML, indicating that the state is indeed pulled down from the LUMO continuum.

Next, the emission efficiency of 2-5 C_{60} layers is characterized at sample voltages for which antibunching is (−4 V) and is not (−2.78 V) observed (fig. 5.4F and G, respectively). The green contours mark the C_{60} terraces obtained from the topography image in fig. 5.4E. This analysis reveals a twofold increase in emission efficiency when antibunching is observed. The additional tunneling channel signified by the sharp peak observed in dI/dV spectra exhibits increased emission efficiency. A series of dI/dV spectra as a function of tip-sample distance are recorded (fig. 5.5A). The dI/dV spectra show two peaks close to the HOMO onset. As the tip-sample distance decreases, which is directly proportional to the tip-induced electric field, the electronic states in the gap shift to lower energies, as seen in fig. 5.5B. Thus, the onset of quantum emission in C_{60} can be tuned by controlling the tip-sample distance.

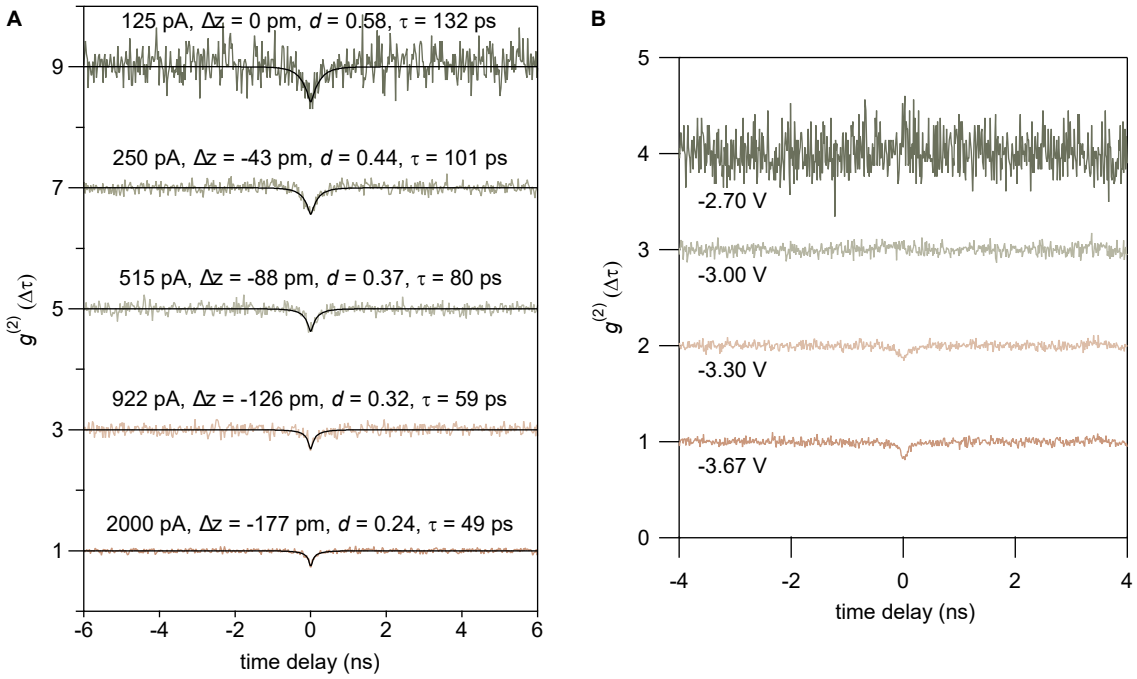

Figure 5.3 — Change of tip-sample distance Δz and sample voltage dependence of $g^{(2)}(\Delta\tau)$. (A) $g^{(2)}(\Delta\tau)$ for z-displacements indicated from initial tunneling current set point $I = 125$ pA ($\Delta z = 0$) shown in fig. 5.2B at fixed voltage $V = -3.5$ V. Resulting depth of the antibunching dip $d = 1 - g^{(2)}(0)$ and the recovery time constants τ for each Δz. (B) $g^{(2)}(\Delta\tau)$ as a function of sample voltage at fixed $I = 2$ nA. The traces are vertically offset for clarity.

5.2 Calculated electronic structure of C_{60} under the influence of a localized electric field

The electronic structure of a C_{60} film on Ag(111) is theoretically modeled using a tight-binding model that includes the five HOMO (H_u) and three LUMO (T_{1u}) states on each C_{60} molecule. The nanocrystal is modeled based on a tight-binding parameterization of $4n$, where n is the number of layers, molecules per unit cell volume, which is then periodically continued to construct an infinite film of C_{60} arranged as a (111) surface, with layers stacked in an fcc crystal structure. The factor of 4 accounts for the four different orientations of the C_{60} molecules in the unit cell[269]. The tip-induced electric potential is modeled in the form of image charges, satisfying electrostatic boundary conditions at the tip and the Ag(111)-C_{60} (metal-dielectric) and C_{60}-vacuum (dielectric-vacuum) interfaces. The electronic structure of the system is calculated in Green's function formalism. It is assumed that for a typical tip radius of a few tens of nm, only a few hundred molecules are affected by the tip potential.

Figure 5.6 shows the projected DOS of the topmost layer of a 4 ML C_{60} film on a metal substrate. The LUMO band ranges from 0.27 eV to 1.02 eV, with a first moment 0.73 eV ("No tip" in fig. 5.6). When a small voltage $V = -0.68$ V is applied to the tip, the electrostatic and image potential lead to a shift of the first moment of the local DOS on the C_{60} molecule directly below the tip towards $E_{F,S}$. For a critical applied voltage V, discrete split-off states are pulled down from the LUMO continuum. The bandwidth of the LUMO band gives the

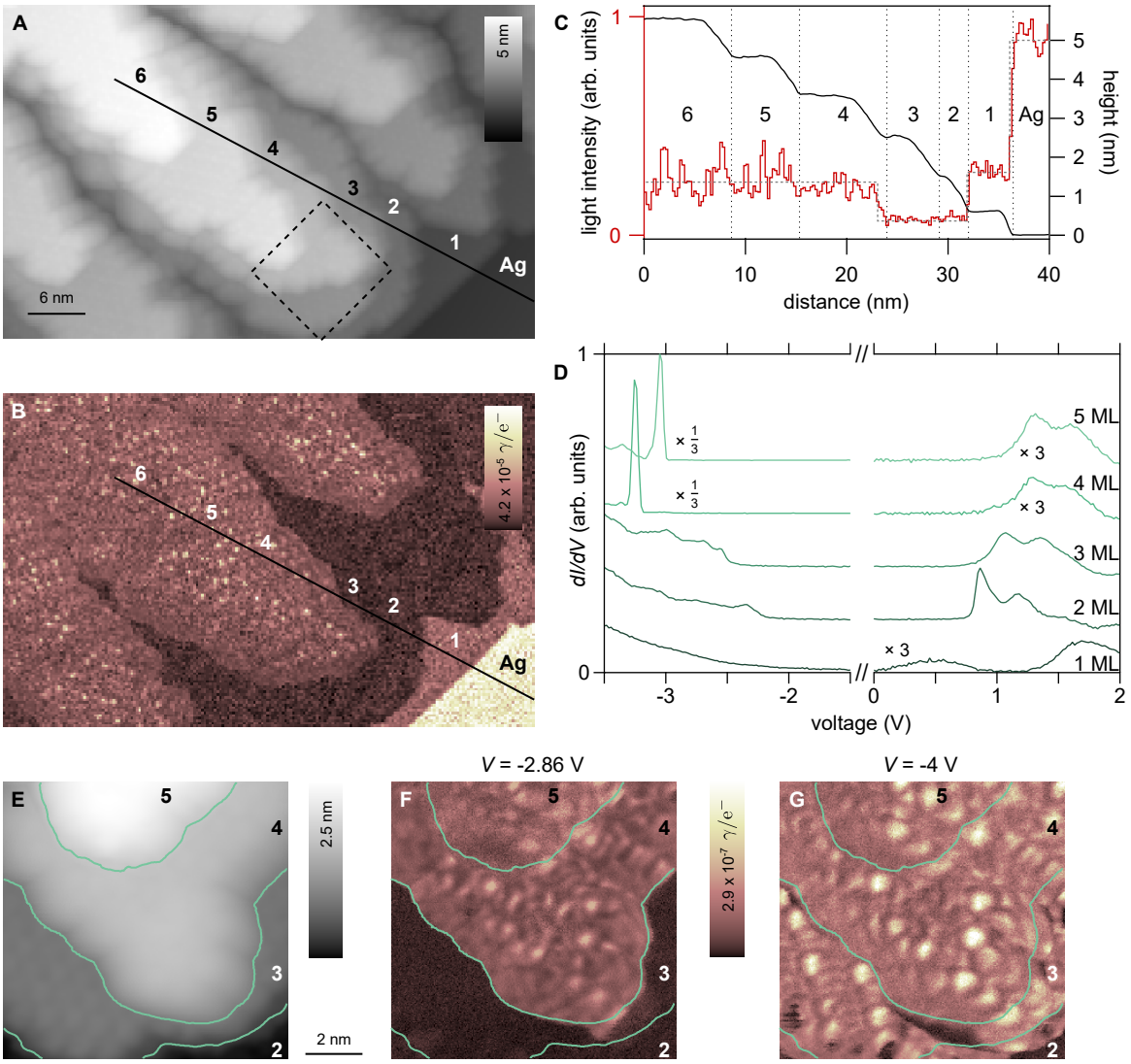

Figure 5.4 — Topography, differential conductance, and emission efficiency of C_{60}/Ag(111). (A) Topography image and (B) Light emission efficiency map (photon counts divided by tunneling current) of 5 ML C_{60} on Ag(111) (set point: $I = 20$ pA, $V = -3.5$ V). (C) Line profile of topography (black) and emission efficiency (red) along the black line marked in A and B. The gray dashed line follows the average efficiency obtained for each C_{60} terrace. (D) dI/dV spectra of 1-5 ML C_{60} on Ag(111) (set point: $I = 100$ pA, $V = -3.5$ V, $V_{mod} = 20$ mV). The spectra are vertically shifted for clarity. (E) Topography image and (F) emission efficiency of the area marked by the black dashed square in A ($I = 100$ pA, $V = -2.86$ V). (G) Emission efficiency at voltage for which the split-off state and antibunching in $g^{(2)}(\Delta\tau)$ is observed ($V = -4$ V). Figure adapted from Leon *et al.* [81].

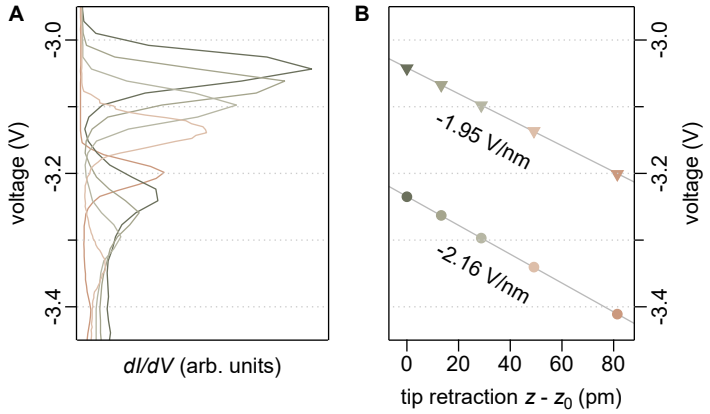

Figure 5.5 — Tip-sample distance dependence of (A) dI/dV spectra on the fourth C_{60} layer and (B) energetic position of the pulled down states (set point: $I = 100$ pA, $V = -3.5$ V). The solid gray lines are fits to the data and show that the energetic position of pulled down states follow lines of constant electric field. Figure adapted from Leon *et al.*[81].

critical voltage. A split-off state may be pulled out of the continuum when the first moment of the DOS on the C_{60} below the tip has moved about half the LUMO bandwidth. For a voltage $V = -3.3$ V, the split-off states are pulled down just below $E_{\mathrm{F,\,S}}$, opening up an additional tunneling channel to the tip. Tunneling through the first split-off state from the LUMO explains the sharp peak in fig. 5.4D for 4 ML and 5 ML C_{60} films. Calculations reveal that the experimentally observed states in fig. 5.5 are split-off states having most of their weight on the first three LUMO states on the C_{60} below the tip. Their difference in peak height is due to the double degeneracy of the first state at ≈ -3 V, well-reproducing the spectral weights in fig. 5.5A. The calculated DOS also shows HOMO split-off states, whose role is discussed later.

Next, the shift of split-off features as a function of tip-sample distance and C_{60} layer distance to the C_{60}/Ag(111) interface is studied. Figure 5.7A and B show the electrostatic potential for tip voltage -3.3 V, and 2 ML, 3 ML, and 4 ML thick C_{60} film with a fixed tip-sample distance of 0.4 nm. For a 4 ML thick C_{60} films, the electrostatic potential is evaluated using tip-sample distances $d = 0.4$ and 0.35 nm. Because of the large relative permittivity of C_{60} ($\varepsilon_{\mathrm{bulk}} = 4.4$)[270], the potential drop occurs mostly over the vacuum gap. However, there is still a considerable potential drop over the C_{60} film, proportional to the layer thickness. Figure 5.7C shows the shift of the lowest split-off state with applied voltage. The blow up of the shaded area in fig. 5.7C shows the V and d dependence of split-off states near $E_{\mathrm{F,S}}$ for 4 ML thick C_{60} film (fig. 5.7D). For -3.32 V, close to the experimental value of -3.26 V, the lowest split-off state moves below $E_{\mathrm{F,S}}$. The additional voltage required to move the second-lowest split-off state 0.22 V (fig. 5.7D) is also comparable to the energy difference between the two peaks observed in the experiment (see fig. 5.5A). Decreasing the tip-sample distance from $d = 0.4$ nm to 0.35 nm while keeping the peak position fixed requires an energy shift of 0.17 and 0.19 V for the lowest and second-lowest states, respectively. The calculated derivative is -3.5 (-3.8) V/nm in qualitative agreement with the experimental electric field -1.95 (-2.16) V/nm for the lowest (second-lowest) peak. The discrepancy ($\times 2$) is expected considering the approximations used in the calculation. Significantly, the radius of the spherical tip (1 nm) in the calculation is sharper than a realistic tip resulting in a stronger electric field dependence.

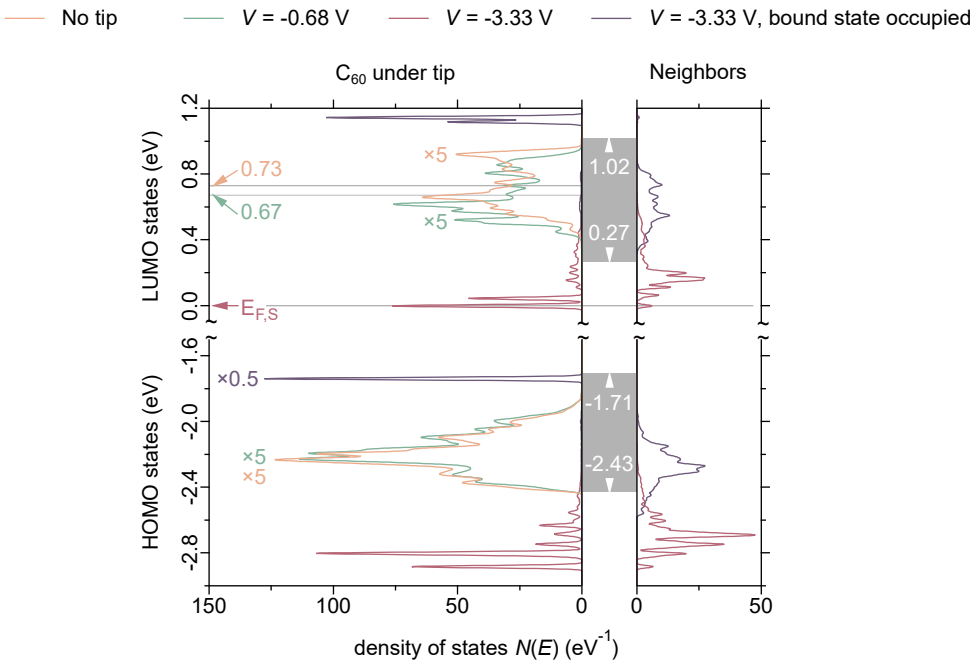

Figure 5.6 — Calculated projected DOS of 4 ML C_{60}/Ag(111) substrate as a function of applied voltage V. Gray-shaded areas mark the energy range and the onsets of the bands. The sharp peaks in "C_{60} under tip" correspond to discrete states split-off from the LUMO band continuum for the C_{60} molecule directly under the tip position. Features overlapping with the bands are the so-called resonances. Gray lines mark the first moment of the LUMO bands. "Neighbors" marks the average DOS of all six nearest-neighbor C_{60} molecules. All features have been broadened with a Lorentzian with FWHM of 0.02 eV. The topmost layer's projected DOS in the absence of any tip-induced perturbation of the electronic structure is signified by "No tip". Figure adapted from Leon *et al.* [81].

5.3 Coulomb blockade driven single photon emission

The antibunching dip observed in photon intensity correlations can be rationalized based on a resulting Coulomb blockade on the split-off states. This interpretation is similar to the one reported in section 3.4 for single PtPc molecules adsorbed atop NaCl. The lifetime of the intermediate charged state formed upon electron hopping from the tip to the LUMO (at negative voltages) prevents another electron from being injected into the orbital due to Coulomb interaction. The charged state then either decays back to the ground state or upgrades to an exciton. However, the antibunching is probably due to the lifetime of the charged state and not the exciton decay. Coulomb blockade for tunneling through the split-off state on C_{60} film manifests itself similarly to the transient charging of the single-molecule prior to excitation. The light emission, however, is plasmonic and due to inelastic tunneling.

As discussed earlier, for $V = -3.33$ V the lowest LUMO split-off state is just below $E_{\mathrm{F,S}}$ (magenta curve in fig. 5.6) and thus, can become occupied by an electron. The resulting Coulomb interaction is substantial because the DOS is mainly localized on the C_{60} directly under the tip. The electron in the split-off state locally increases the electrostatic potential by 1.02 eV, resulting in an upward shift by 1.14 eV of the DOS of the C_{60} directly underneath the tip. The increase in potential on the neighboring molecules is lower in magnitude (0.34 eV), and thus, the DOS is shifted to higher energies (purple curve in fig. 5.6). Since the split-

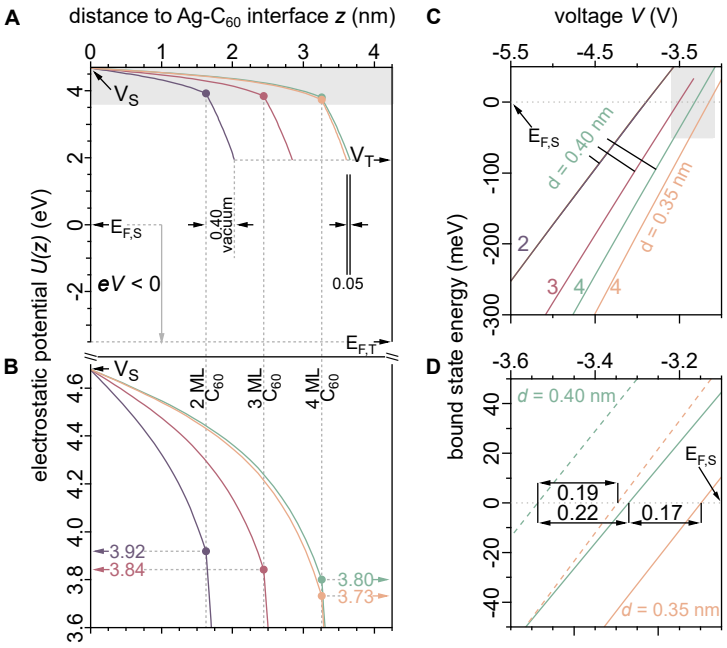

Figure 5.7 — Calculated electrostatic potential and potential energies of the resultant split-off state. The colored solid lines show calculated electrostatic potential $U(z)$ as a function of C_{60} thickness and a tip-C_{60} vacuum gap of $d = 0.4$ nm. For 4 ML thick C_{60}, $U(z)$ is evaluated using $d = 0.40$ and 0.35 nm. The sample and tip Fermi levels ($E_{F,S}$ and $E_{F,T}$), work functions (ϕ_S, ϕ_T) and vacuum levels (V_S, V_T) satisfy $V_S = E_{F,S} + \phi_S$ and $V_T = E_{F,T} + \phi_T$. (A) The potential directly underneath the tip at voltage $V = 3.33$ V. The Ag(111)-C_{60} interface is defined as $z = 0$. The C_{60}-vacuum interface is marked by the solid circles. (B) Blow up of the shaded region shown in A. (C) Voltage V dependence of lowest LUMO split-off state energy. (D) Blow up of the shaded region in C. The dashed lines show the second lowest singly degenerate LUMO split-off state. The differences betweeen the voltages at which this state crosses $E_{F,S}$ for the film thicknesses 3, 4, and 5 are indicated. Figure adapted from Leon *et al.* [81].

off state is now above $E_{F,S}$, tunneling through the LUMO is prohibited. Inelastic tunneling of an electron from such a split-off state to an empty tip state above $E_{F,S}$ leads to a single photon being emitted and to the observation of antibunching (fig. 5.2B).

However, the upward energy shift of the split-off states associated with the HOMO band also contributes to the tunneling process. On electron occupancy of the LUMO derived split-off state, a resonant feature at −1.74 eV, above the top of the HOMO band appears (purple curve in fig. 5.6). Such a state has a substantially higher tunneling rate than a typical electron in the HOMO band since the electron sees a lower tunneling barrier. The sharp feature in the dI/dV spectrum for 4 ML C_{60}, reported in fig. 5.4D, is then related to both tunneling through the LUMO split-off state and an increased tunneling probability through HOMO split-off states. Concomitant tunneling through the HOMO states results in an additional tunneling channel which may reduce the antibunching minimum and destroy single photon emission. The energy difference between the resonance state and $E_{F,S}$ (1.59 eV) suggests that photon emission from this channel may be detected by the SPADs, which are sensitive down to 1.4 eV, however, with lower detection efficiency. Such a mechanism could potentially result in the $g^{(2)}(0) = 0.42$ observed in the correlation experiments. Typically, the energy of the resulting photon emission due to tunneling through the HOMO split-off state would be lower in energy than from tunneling through the split-off state derived from the

LUMO band. Given that, a spectrally filtered photon intensity correlation may discern the effect of two tunneling components on the observed depth of the antibunching dip.

The calculations predict that for an applied voltage $V < -6.2$ V, the tip potential is large enough that even an occupied LUMO split-off state remains below $E_{\mathrm{F,\,S}}$. It would be interesting to systematically find ways to explore tunneling in this regime.

In an earlier work[171], Leon *et al.* reported photon pair emission from the tunneling electron, which results in the so-called photon superbunching ($g^{(2)}(0) \gg 1$), for large tip-sample distances. No bunching peak is observed in the $g^{(2)}(\Delta\tau)$ measurements presented here. This effect is negligible probably because of the smaller tip-sample distance used.

Design guidelines for developing plasmonic antibunching emitters

The above-introduced theoretical calculations using varied parameters provide general design guidelines for developing plasmonic single photon emitting systems beyond the C_{60} films. Doubling the HOMO and LUMO bandwidths and keeping their energetic positions fixed relative to $E_{\mathrm{F,\,S}}$, twice as large a voltage is required to align the LUMO split-off state with $E_{\mathrm{F,\,S}}$. This favors the use of materials with narrow bandwidths. The tunneling contribution from the HOMO needs to be suppressed to reduce the unwanted effect of tunneling through a resonant HOMO state. This can be achieved by reducing the high HOMO degeneracy or lowering the HOMO energy using a larger bandgap material and would reduce the HOMO tunneling component because of the increased potential barrier.

Similarly, using a metal substrate with a low work function could also improve the energy position of the bands in favor of antibunching. The proximity of the LUMO band to $E_{\mathrm{F,\,S}}$ would require a lower voltage for aligning the split-off state to $E_{\mathrm{F,\,S}}$ and reduce the tunneling rate through the resonant HOMO states.

Another path to reduce the HOMO split-off state energy is the use of large molecules for which the effective Coulomb interaction tends to be smaller than for C_{60}. Then electron occupancy of the LUMO split-off state under the tip would result in a lower HOMO split-off state energy, which again leads to a smaller HOMO tunneling component and, thus, potentially favor antibunching. A material with a large dielectric function would also lower the effective Coulomb interaction through screening effects. However, this would also lower the potential drop over the molecular layers and thus increase the voltage required for pulling down split-off states.

Conclusion

The experiments presented in this chapter show that a tip-induced electric field can induce discrete split-off states localized over a single molecule in a C_{60} molecular film on a metal substrate. This leads to a Coulomb blockade for tunneling charges, resulting in antibunching in the photon intensity correlation measurements. As for metal-metal tunneling junctions, the plasmon modes in the tip-sample cavity are excited due to inelastic tunneling resulting

in broadband light emission. The single photon emission rate is not fundamentally limited since the emission process is fast (few tens of fs) compared to exciton lifetimes in two-level systems (few hundreds of ps). The tip-induced electric field, inversely proportional to the tip-sample distance, can control the recovery time constant – enabling single photon emission at high rates. The tunneling of electrons from the substrate to a split-off state in the topmost layer gives the recovery time and, thus, can be tuned by controlling the thickness of the molecular layer.

The alignment of split-off states with the substrate Fermi level is tuned by the applied voltage, thus suggesting the future realization of a single-photon-on-demand light source. These considerations highlight the tunability of a plasmonic antibunching light source. Competing tunneling processes result in more than one photon emission, thus lowering the single photon emission purity. The theoretical findings reveal design strategies to suppress the unwanted tunneling channel and induce split-off states in various materials, spurring a search for new concepts that can be leveraged to design purer quantum emitters.

Conclusions and outlook

This work reports on studies of molecular optoelectronic properties at sub-molecular length scales performed using a scanning tunneling microscope (STM). Different operation modes of an STM, like topography imaging and local electronic spectroscopy, combined with optical spectroscopy techniques and time-resolved detection of photons emitted in the tunnel junction affords a range of tools for detailed analysis of luminescence processes, all with atomic-scale resolution. The ability to not only probe, but also manipulate the interaction between adsorbates and the STM tip allows precise control of the nano-environment and localized electronic states, which directly influences the quantum efficiency, onset voltage, and quantum statistics of the molecular emission.

Thin films of sodium chloride are routinely used to decouple electronic properties of molecules from the metal substrate. Thus, a thorough understanding of the electronic and optical effect of the film on the adsorbates is important. Based on electronic characterization of NaCl at large voltages close to the conduction and valence band edges, it is found that, surprisingly, both bands are of anionic Cl character. Given that NaCl, an alkali halide, is an ionic crystal, textbooks suggest that its conduction band should be of cationic Na character. Cl^- being negatively charged, and a full shell electronic configuration of Na ($[Ne]3s^2 3p^6$) may naïvely suggest that tunneling of electrons at positive sample voltages should be favored through a positively charged Na^+. Topography imaging shows that this is not the case. Tight-binding calculations of the conduction band accounting for the hypothesis that a large Madelung potential flips the order of Cl^- $4s$ and Na^+ $3s$ levels are performed. These findings may also be applicable to other I-VII and II-VI compounds, and prompt a search for materials whose conduction and valence bands take on unusual combinations of cationic and anionic character.

In view of the new interpretation of the NaCl band structure, the electronic coupling of adsorbed molecules to the metal substrate which occurs through the Cl^- ions of NaCl, the so called gap states, is also reconsidered. It is found that the gap states are not merely extensions of broad frontier molecular orbitals allowing for tunneling through the HOMO-LUMO gap of the molecule. Orbitals well below the energy of the HOMO participate in electron tunneling at energies inside the gap. This considerably modifies the topography of molecules when imaged at voltages close to the Fermi level. A tight-binding simulation of the tunneling accounting for relative weights of the gap states and their symmetries is, for the first time, able to reproduce the STM topography images in the HOMO-LUMO gap.

Intrinsic STM-induced electroluminescence (STM-EL) and up-conversion electroluminescence (UCEL) of a single platinum (II) phthalocyanine (PtPc) molecule, a prototypical phosphor, atop NaCl on Au(111) is characterized. It is found that the quantum efficiency, degeneracy of the transition dipole moment, and onset voltage for fluorescence change consider-

ably for varying energy alignment of the PtPc orbitals.

To tune the energy position of the molecular orbitals in a well-defined manner, metal substrates with different work functions are used. Different energy alignment of the orbitals with respect to tip and sample Fermi levels, in principle, controls the electron injection into the molecule which is key to electron-hole recombination and thus, photon emission. These findings refine principles for control of onset voltage, which is essential for the design of low power molecular electronics. At voltages larger than the fluorescence energy, but within the HOMO-LUMO gap, energy transfer from the tip plasmon may also excite the molecule. However, we observe that the associated intensities are much lower than for resonant charge injection into the orbitals.

Hanbury Brown and Twiss interferometry (HBT) is used to analyze the quantum statistics of PtPc fluorescence. An antibunching dip in the $g^{(2)}(\Delta\tau)$ measurement suggests that the single molecule emits photons one at a time, with a time constant of ≈ 300 ps. Recently, it was shown that no such antibunching dip is found in $g^{(2)}(\Delta\tau)$ when the molecule is excited by incident light[96]. The key difference between the electronic- and photo-excitation is the transient spin-doublet state of the cationic state as a first step in exciton generation. Based on these arguments, it is proposed that the antibunching observed for single molecules is associated with the existence of this transient charged state.

UCEL is observed for PtPc at sample voltages lower than the fluorescence energy. Emitting a higher energy photon than available by electron energy seems to conflict with energy conservation. A quadratic dependence of UCEL intensity on the current, and an onset voltage close to the phosphorescence energy suggest that the excitation energy is up-converted to the singlet energy by two tunneling electrons with the triplet acting as a relay state. The fact that only one molecule is involved in the experiment, allows ruling out other mechanisms that may explain energy up-conversion like triplet-triplet annihilation.

Single photon emission under UCEL conditions indicates the existence of a transient charged state in the excitation mechanism. This finding indicates that the excitation from the ground state to the triplet, and then to the singlet, can occur only due to carrier injection since such a process would involve formation of a charged state of the molecule. Moreover, UCEL is observed at both positive and negative voltages for PtPc atop NaCl on Au(111). To explain the intensities and onset voltages for different orbital energy alignment, a new mechanism based on perturbation theory arguments is proposed. This study significantly furthers the understanding of spin-triplet mediated energy up-conversion.

It is surprising that a quadratic current dependence, naturally explained under UCEL conditions, persists even at higher positive voltages where emission by a single electron process would energetically be possible. It is suggested that the linear process remains weak, and is dominated by a highly efficient two electron process.

Besides the role of the triplet state in UCEL, the resultant phosphorescence from its electronic excitation is also observed. In fact, there have not been many reports of STM-induced phosphorescence probably because the triplet emission from phthalocyanines is in the near-infrared range. For PtPc atop NaCl on Ag(111), singlet and triplet emission is observed only

at negative voltages, when resonant tunneling from HOMO to the tip is allowed. The phosphorescence intensities are low in comparison to fluorescence despite the 3:1 ratio in their theoretical excitation probability upon random spin injection. TD-DFT calculations suggest that the transition dipole moment for phosphorescence $T_1 \rightarrow S_0$ is more than an order of magnitude smaller than that for fluorescence $S_1 \rightarrow S_0$.

A tip distance dependent study of relative phosphorescence intensity ($T_1 : S_1$) shows that the coupling to the singlet allows control of magnitude of intersystem crossing to the triplet state. As the tip is moved away from the molecule, the plasmon-exciton coupling decreases, resulting in an increase in the lifetime of the singlet state. It is found that the triplet emission is more sensitive to non-radiative quenching than singlet emission due to its longer lifetime. A combination of these effects leads to an increase in the population of the triplet state, and thus phosphorescence intensities.

Using a wavelength-tunable laser to resonantly excite the molecule to its singlet state, intrinsic photofluorescence of the molecule is observed. A high-resolution photoluminescence spectrum shows a larger number of sharper vibrational modes than electroluminescence. Energy resolved spatial mapping exhibits patterns which can be assigned to modes with different symmetry. Some of these modes are perpendicular to the tip axis, with their transition dipole moment in the plane of the molecule. The plasmonic enhancement is mostly along the tip axis which should mean that these modes have negligible intensities. The observed high intensities can be rationalized by invoking a horizontal component of the tip dipole moment, introducing a lateral plasmonic enhancement, and selection rules enforced by the Raman tensors.

A weak triplet emission is observed for STM-induced resonant photofluorescence even when the tip is placed ≈ 2 nm away from the center of the molecule, where direct excitation of the triplet state due to the tunneling electrons can be ruled out. This is the first observation of intersystem crossing in a tip-controlled experiment and opens new avenues for future analysis with sub-molecular precision.

Lastly, the tip-induced electric field is employed to create discrete electronic states in the band gap of a molecular semiconductor, a thin film of C_{60} molecules. Differential conductance measurements reveal sharp peaks at negative voltages above the HOMO band. Tight-binding calculations suggest that discrete states are split-off from the LUMO band continuum of the C_{60} layer and localized in a few C_{60} molecules on top of the film, directly under the tip. The electron tunneling through the split-off states dominates at large negative voltages $V < -3$ V. A large Coulomb repulsion on these states results in a blockade for consecutive tunneling electrons. The electrons hopping one by one through one of these states may inelastically tunnel and lead to single photon emission. $g^{(2)}(\Delta\tau)$ measurements show an antibunching dip for plasmonic emission corresponding to the inelastic tunneling. The creation of split-off states is a general scheme that may be realized also on thin films of other materials. Design principles for optimized systems are derived from theory. In combination with the photon pair production in the metal-metal tunneling junction at large voltages[171], the discretization of the tunneling current may allow creation of heralded single photons.

Outlook

Some considerations for future work continuing the research of this thesis are presented in the following.

Tip-enhanced photoluminescence from a single phosphor: In this thesis, the photoexcitation is tuned to the energy of the S_1 state, leading to a resonant transition to the lowest singlet excited state. Given the role of vibrational states in intersystem crossing, phosphorescence intensities observed for resonant STM-PL provide only a lower bound on its magnitude. Using higher energy excitation, for example a 532 nm laser, or a tunable laser with its wavelength tuned to the second lowest singlet excited state might allow a direct comparison of T_1:S_1 ratio. Such an analysis may provide a more accurate estimate of the intersystem crossing magnitude and a comprehensive picture of the influence of exciton-plasmon coupling on T_1 emission.

A phosphor that emits in the visible range: Even though the triplet emission from PtPc could be detected, its energy in the near-infrared range (1.275 eV) is $\approx$ 680 meV below the singlet emission (1.952 eV). A poor overlap between the vibrational states of the lowest excited singlet state and the excited triplet state implies that intersystem crossing is unfavorable. In addition, the quantum efficiency of the detector drops by almost an order of magnitude from the red region of the visible spectrum to the near-infrared. Tuning the plasmonic modes of the Au tips such that significant enhancement can be attained both for S_1 and T_1 emission requires considerable tip preparation. These difficulties do not allow a straight-forward study of intersystem crossing and photon correlations of the T_1 emission by HBT and thus, necessitate using a different emitter.

A flat geometry of the molecule is essential for smooth scanning in STM. However, design requirements, like large spin-orbit coupling, or substantial overlap between the vibrational states of singlet and triplet excited states are best satisfied for electron donor-acceptor complexes with a three-dimensional structure. Thus, few efficient, commercially available, and technologically relevant phosphors are suitable for STML studies. Platinum (II) octaethyporphyrin (PtOEP), one of the first phosphorescent complexes which, when embedded in OLEDs, results in high internal quantum efficiency[20], is a promising candidate.

Figure 5.8 shows first results of the PtOEP topography in the HOMO-LUMO gap (fig. 5.8B) and phosphorescence emission (fig. 5.8C). The in-gap image of PtOEP is more complex than the one for PtPc which is presented in Chapter 2 and which only shows topography features at the isoindole units of its molecular frame. The topography image in fig. 5.8B shows a dark halo around the edge of the molecule, and a broken mirror symmetry leading to a chiral pattern. It would then be interesting to compare this with the theoretical tunneling probability through PtOEP.

A sharp T_1 peak is observed by STML at 652 nm wavelength (fig. 5.8C), similar to earlier studies of PtOEP islands on graphene on SiO_2[271]. No S_1 emission line is observed in the STML spectrum on an Au substrate, probably due to absence of plasmonic modes

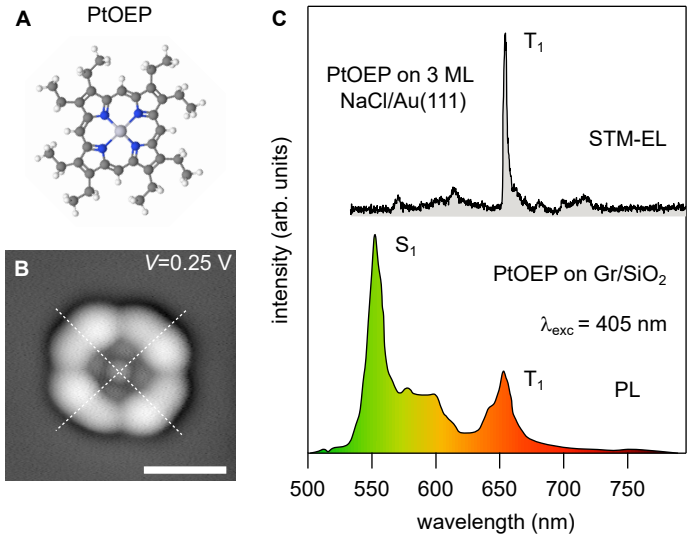

Figure 5.8 — STML of PtOEP atop 3 ML NaCl on Au(111). (A) Ball-and-stick model of PtOEP. (B) Topography image of PtOEP at sample voltage in the HOMO-LUMO gap (set point: $I = 2$ pA, $V = 250$ mV, scale bar: 1 nm). White dashed lines indicate symmetry axes along N atoms. (C) STM-EL spectrum of PtOEP showing T_1 emission line (set point: $I = 30$ pA, $V = -3$ V, $t = 60$ s). Photoluminescence spectrum of PtOEP islands on graphene layer showing both singlet and triplet emission (adapted from Kim *et al.*[271]).

at high energies (above 2.2 eV) for Au. However, two lower intensity peaks at about 570 nm and 630 nm are observed. The peak at 570 nm was recently assigned to the transition from the second lowest excited triplet state to the singlet ground state of PtOEP[272]. Already this preliminary study of PtOEP thus shows a variety of emission phenomena. Since the energy difference between the singlet and the triplet state is of the order of only 50 meV, strong intersystem crossing is expected. Using a Ag tip or Ag substrate, plasmon modes at higher energies may allow the observation of the S_1 emission simultaneously with the T_1 emission and allow a comprehensive characterization of exciton-plasmon coupling and its role in phosphorescence.

Using PtOEP on a Cu(111) substrate, the HOMO energy level may be tuned to ≈ -2.2 V. Such a configuration may cause the T_1 emission to occur already at a sample voltage around -2.2 V, still below the energy of the S_1 state, thus avoiding the complication of Chapter 4, where S_1 and T_1 have the same onset voltage. Analyzing photon statistics of the T_1 emission under these conditions, may provide more information on the role of a transient charged state that is created prior to formation of the T_1 state.

Atomic-scale analysis of emission from atomic defects: In the last decade two dimensional materials with a direct bandgap, transition metal dichalcogenide, have emerged as promising light sources[273]. Besides the intrinsic emission from the layers, single photon emission has been observed from vacancies and carbon defects, for example in *h*-BN[35,173]. However, due to absence of a study using a probe which offers simultaneous atomic-resolution optoelectronic characterization, most studies rely on assignment of the emission to the vacancy defects based on theoretical simulations[274]. An STML study of such defects, and TMD layers in general, would allow a detailed optoelectronic characterization of the defects and their quantum emission (using HBT-STM).

A conductive substrate is necessary for STM to operate. Thus, an analysis of typical samples like TMDs on SiO_2 is not possible. However, recent studies[43,275] show that epitaxially grown TMD monolayers on graphene on an Ir(111) substrate, exhibit sharp emission peaks

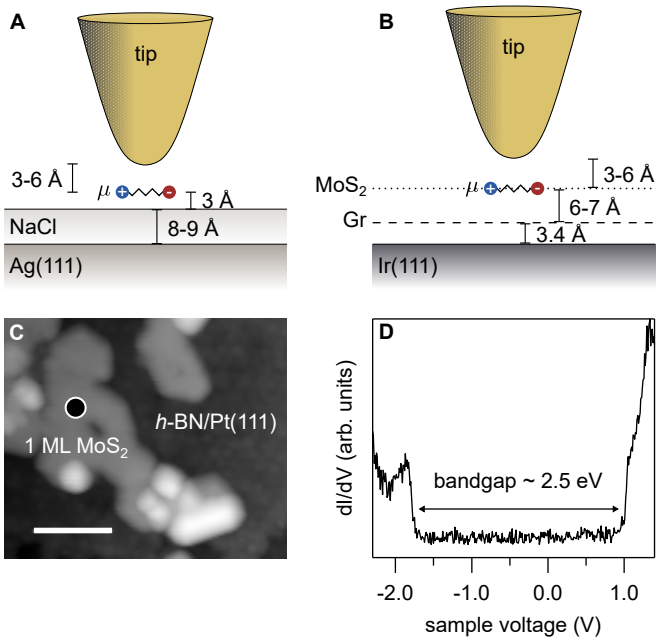

Figure 5.9 — STML of vacancy defects and TMD layers. (A, B) Cartoon showing separation between different substrate layers and the tip for A a molecule atop NaCl on Au(111), and B MoS_2 layer on graphene/Ir(111). (C) Topography image of 1 ML MoS_2 on *h*-BN/Pt(111) (set point: $I = 1$ pA, $V = 1.6$ V, scale bar: 10 nm). (D) Differential conductance spectrum atop MoS_2 (set point: $I = 20$pA, $V = -2.5$ V, $V_{mod} = 20$ mV).

in photoluminescence. A naïve analysis of the separation distances between the different layers shows that the distance of the TMD layer, specifically MoS_2, is roughly the same as a molecule adsorbed atop 3 ML NaCl on Au(111) (see fig. 5.9A and B).

First attempts to grow MoS_2 atop *h*-BN on Pt(111) by molecular beam epitaxy using co-evaporation of sulfur from pyrite (FeS_2), and molybdenum by metal evaporation, are shown in fig. 5.9C and D. Large (few 100 nm^2) islands of *h*-BN with a bandgap of ~ 6 eV can be obtained on Pt(111)[276]. A dI/dV spectrum of MoS_2 (at the black dot in fig. 5.9C) reveals a bandgap of ~ 2.5 eV, close to the theoretical expectation[277] (2.7 to 2.9 eV). However, for most islands a bandgap smaller than 2.5 eV is observed (not shown) due to edge effects resulting from a small size of the MoS_2 islands (few tens of nm^2). This may be the reason why, the light emission observed atop these islands is exclusively plasmonic in nature. Nevertheless, with further optimization of the molecular-beam epitaxy growth parameters, larger islands of TMD materials can be grown, which may then exhibit intrinsic optical properties.

In addition, the coupling to the tip may be used to control the lifetime of single photon emission. Since the time difference between emission events is limited by exciton decay time, decay rate enhancement resulting from coupling to the tip plasmon may be used to manipulate its time constant. Despite the challenging growth conditions, this study shows a lot of promise for future solid state quantum emitters.

The interaction of molecules with TMD layers is also of interest because of charge-transfer excitons which can form at heterointerfaces[278]. In these systems, the exciton generated in one material may dissociate into a spatially separated electron-hole pair across the interface resulting in conversion of light into electricity. A microscopic understanding of charge transfer at TMD-molecular layer interface is imperative for future applications in photovoltaics and photodetectors. Besides that, an efficient coupling between dark and bright TMD excitons, and adsorbed molecules with a large dipole moment has been proposed as a path to

turn dark excitons bright[279]. This would lead to the appearance of a dark exciton peak in presence of a molecule, and thus will be of great interest for chemical sensing applications. The single molecule sensitivity of STM, combined with optical spectroscopy and coherence measurements may elucidate the mechanism behind these, and other so-far undiscovered, processes.

Bibliography

[1] G. G. Stokes, Philos. Trans. R. Soc. **142**, 463 (1852).

[2] E. Becquerel, *La lumière, ses causes et ses effets*, Vol. 1 (Firmin Didot frères, fils et cie, 1867).

[3] D. Brewster, Earth Environ. Sci. Trans. R. Soc. Edinb. **12**, 538 (1834).

[4] F. J. Pisko, *Die Fluorescenz des Lichtes* (Carl Gerold's Sohn, 1861).

[5] E. L. Nichols and E. Merritt, Physical Review (Series I) **19**, 18 (1904).

[6] E. L. Nichols and E. Merritt, Physical Review (Series I) **22**, 279 (1906).

[7] S. Vavilov, Z Phys **22**, 266 (1924).

[8] D. J. Griffiths and D. F. Schroeter, *Introduction to quantum mechanics* (Cambridge university press, 2018).

[9] J. J. Sakurai and J. Napolitano, *Modern Quantum Mechanics*, 2nd ed. (Cambridge University Press, 2017).

[10] F. Perrin, Annales de Physique **10**, 169 (1929).

[11] M. Kasha, Chem. Rev. **41**, 401 (1947).

[12] P. Pringsheim, *Luminescence and phosphorescence* (Interscience Publishers, New York, NY, 1949).

[13] R. S. Becker, *Theory and interpretation of fluorescence and phosphorescence* (Wiley-Interscience, 1969).

[14] A. H. Coons, H. J. Creech, and R. N. Jones, Proc. Soc. Exp. Biol. Med. **47**, 200 (1941).

[15] F. Meyer, H.-J. Spanner, and E. Germer, Metal vapor lamp (1939), US Patent 2182732.

[16] H. C. Borden and G. P. Pighini, Hewlett-Packard Journal **20** (1969).

[17] Australian, State and Territory and New Zealand Governments, Lumens To Watts: Choose brightness | Energy Rating, `https://www.energyrating.gov.au/lighting/lumens-watts` (2020), Last accessed: 04 Apr 2022.

[18] M. Koden, *OLED displays and lighting* (John Wiley & Sons, 2016).

[19] C. W. Tang and S. A. VanSlyke, Appl. Phys. Lett. **51**, 913 (1987).

[20] M. A. Baldo, D. F. O'Brien, Y. You, A. Shoustikov, S. Sibley, M. E. Thompson, and S. R. Forrest, Nature **395**, 151 (1998).

[21] K. Kimura, K. Miwa, H. Imada, M. Imai-Imada, S. Kawahara, J. Takeya, M. Kawai, M. Galperin, and Y. Kim, Nature **570**, 210 (2019).

[22] B. Valeur and M. N. Berberan-Santos, *Molecular Fluorescence: Principles and Applications* (John Wiley & Sons, 2013).

[23] H. Uoyama, K. Goushi, K. Shizu, H. Nomura, and C. Adachi, Nature **492**, 234 (2012).

[24] A. F. Koenderink, Opt. Lett. **35**, 4208 (2010).

[25] M. A. Fusella, R. Saramak, R. Bushati, V. M. Menon, M. S. Weaver, N. J. Thompson, and J. J. Brown, Nature **585**, 379 (2020).

[26] E. Abbe, Archiv f. mikrosk. Anatomie **9**, 413 (1873).

[27] T. Basché, W. Moerner, M. Orrit, and U. Wild, *Single-molecule optical detection, imaging and spectroscopy* (John Wiley & Sons, 2008).

[28] W. E. Moerner and L. Kador, Phys. Rev. Lett. **62**, 2535 (1989).

[29] W. E. Moerner and M. Orrit, Science **283**, 1670 (1999).

[30] G. Binnig, H. Rohrer, C. Gerber, and E. Weibel, Phys. Rev. Lett. **50**, 120 (1983).

[31] C. J. Chen, *Introduction to Scanning Tunneling Microscopy: Second Edition* (Oxford University Press, Oxford, 2007).

[32] K. Bian, C. Gerber, A. J. Heinrich, D. J. Müller, S. Scheuring, and Y. Jiang, Nat. Rev. Methods Primers **1**, 1 (2021).

[33] K. Kuhnke, C. Große, P. Merino, and K. Kern, Chem. Rev. **117**, 5174 (2017).

[34] R. Gutzler, M. Garg, C. R. Ast, K. Kuhnke, and K. Kern, Nat. Rev. Phys. **3**, 441 (2021).

[35] A. Laucht, F. Hohls, N. Ubbelohde, M. F. Gonzalez-Zalba, D. J. Reilly, S. Stobbe, T. Schröder, P. Scarlino, J. V. Koski, A. Dzurak, C.-H. Yang, J. Yoneda, F. Kuemmeth, H. Bluhm, J. Pla, C. Hill, J. Salfi, A. Oiwa, J. T. Muhonen, E. Verhagen, M. D. LaHaye, H. H. Kim, A. W. Tsen, D. Culcer, A. Geresdi, J. A. Mol, V. Mohan, P. K. Jain, and J. Baugh, Nanotechnology **32**, 162003 (2021).

[36] H. J. Kimble, M. Dagenais, and L. Mandel, Phys. Rev. Lett. **39**, 691 (1977).

[37] G. Chen, Y. Luo, H. Gao, J. Jiang, Y. Yu, L. Zhang, Y. Zhang, X. Li, Z. Zhang, and Z. Dong, Phys. Rev. Lett. **122**, 177401 (2019).

[38] A. Farrukh, X.-J. Tian, F.-F. Kong, Y.-J. Yu, S.-H. Jing, G. Chen, Y. Zhang, Y. Liao, Y. Zhang, and Z.-C. Dong, CJCP **34**, 87 (2021).

[39] S. Wang, X. Shan, U. Patel, X. Huang, J. Lu, J. Li, and N. Tao, PNAS **107**, 16028 (2010).

[40] W. Wang, Y. Yang, S. Wang, V. J. Nagaraj, Q. Liu, J. Wu, and N. Tao, Nat. Chem. **4**, 846 (2012).

[41] A. V. Kabashin, P. Evans, S. Pastkovsky, W. Hendren, G. A. Wurtz, R. Atkinson, R. Pollard, V. A. Podolskiy, and A. V. Zayats, Nat. Mater. **8**, 867 (2009).

[42] Y. Shen, J. Zhou, T. Liu, Y. Tao, R. Jiang, M. Liu, G. Xiao, J. Zhu, Z.-K. Zhou, X. Wang, C. Jin, and J. Wang, Nat. Commun. **4**, 2381 (2013).

[43] J. Hall, B. Pielić, C. Murray, W. Jolie, T. Wekking, C. Busse, M. Kralj, and T. Michely, 2D Mater. **5**, 025005 (2018).

[44] G. Binnig, H. Rohrer, C. Gerber, and E. Weibel, Appl. Phys. Lett. **40**, 178 (1982).

[45] G. Binnig, H. Rohrer, C. Gerber, and E. Weibel, Phys. Rev. Lett. **49**, 57 (1982).

[46] R. M. Feenstra and A. P. Fein, Phys. Rev. B **32**, 1394 (1985).

[47] R. S. Becker, J. A. Golovchenko, and B. S. Swartzentruber, Phys. Rev. Lett. **54**, 2678 (1985).

[48] The Nobel Prize in Physics 1986. NobelPrize.org, `https://www.nobelprize.org/prizes/physics/1986/summary/` (1986), Last accessed: 14 Jan 2022.

[49] J. Bardeen, Phys. Rev. Lett. **6**, 57 (1961).

[50] C. M. Bender and S. A. Orszag, *Advanced Mathematical Methods for Scientists and Engineers I: Asymptotic Methods and Perturbation Theory* (Springer, New York, 1999).

[51] W. M. H. Sachtler, G. J. H. Dorgelo, and A. A. Holscher, Surf. Sci. **5**, 221 (1966).

[52] J. Tersoff and D. R. Hamann, Phys. Rev. B **31**, 805 (1985).

[53] W. J. Kaiser and R. C. Jaklevic, IBM J. Res. Dev. **30**, 411 (1986).

[54] J. Repp, G. Meyer, S. M. Stojković, A. Gourdon, and C. Joachim, Phys. Rev. Lett. **94**, 026803 (2005).

[55] J. A. Stroscio, R. M. Feenstra, and A. P. Fein, Phys. Rev. Lett. **57**, 2579 (1986).

[56] X. H. Qiu, G. V. Nazin, and W. Ho, Science **299**, 542 (2003).

[57] J. Lambe and S. L. McCarthy, Phys. Rev. Lett. **37**, 923 (1976).

[58] J. K. Gimzewski, B. Reihl, J. H. Coombs, and R. R. Schlittler, Z. Physik B - Condensed Matter **72**, 497 (1988).

[59] J. K. Gimzewski, J. K. Sass, R. R. Schlitter, and J. Schott, EPL **8**, 435 (1989).

[60] R. Berndt, J. K. Gimzewski, and P. Johansson, Phys. Rev. Lett. **67**, 3796 (1991).

[61] R. Berndt, J. K. Gimzewski, and R. R. Schlittler, Z Phys D - Atoms, Molecules and Clusters **26**, 87 (1993).

[62] N. Nilius, N. Ernst, and H.-J. Freund, Phys. Rev. Lett. **84**, 3994 (2000).

[63] R. Berndt, R. Gaisch, J. K. Gimzewski, B. Reihl, R. R. Schlittler, W. D. Schneider, and M. Tschudy, Science 10.1126/science.262.5138.1425 (1993).

[64] A. J. Heinrich, J. A. Gupta, C. P. Lutz, and D. M. Eigler, Science 10.1126/science.1101077 (2004).

[65] C. Chen, P. Chu, C. A. Bobisch, D. L. Mills, and W. Ho, Phys. Rev. Lett. **105**, 217402 (2010).

[66] Y. Zhang, Y. Luo, Y. Zhang, Y.-J. Yu, Y.-M. Kuang, L. Zhang, Q.-S. Meng, Y. Luo, J.-L. Yang, Z.-C. Dong, and J. G. Hou, Nature **531**, 623 (2016).

[67] J. Doležal, S. Canola, P. Hapala, R. C. de Campos Ferreira, P. Merino, and M. Švec, ACS Nano 10.1021/acsnano.1c08816 (2021).

[68] H. Imada, K. Miwa, M. Imai-Imada, S. Kawahara, K. Kimura, and Y. Kim, Nature **538**, 364 (2016).

[69] S. Cao, A. Rosławska, B. Doppagne, M. Romeo, M. Féron, F. Chérioux, H. Bulou, F. Scheurer, and G. Schull, Nat. Chem. **13**, 766 (2021).

[70] L. Zhang, Y.-J. Yu, L.-G. Chen, Y. Luo, B. Yang, F.-F. Kong, G. Chen, Y. Zhang, Q. Zhang, Y. Luo, J.-L. Yang, Z.-C. Dong, and J. G. Hou, Nat. Commun. **8**, 580 (2017).

[71] Y. Zhang, Q.-S. Meng, L. Zhang, Y. Luo, Y.-J. Yu, B. Yang, Y. Zhang, R. Esteban, J. Aizpurua, Y. Luo, J.-L. Yang, Z.-C. Dong, and J. G. Hou, Nat. Commun. **8**, 15225 (2017).

[72] H. Imada, K. Miwa, M. Imai-Imada, S. Kawahara, K. Kimura, and Y. Kim, Phys. Rev. Lett. **119**, 013901 (2017).

[73] J. Kröger, B. Doppagne, F. Scheurer, and G. Schull, Nano Lett. **18**, 3407 (2018).

[74] Y. Luo, G. Chen, Y. Zhang, L. Zhang, Y. Yu, F. Kong, X. Tian, Y. Zhang, C. Shan, Y. Luo, J. Yang, V. Sandoghdar, Z. Dong, and J. G. Hou, Phys. Rev. Lett. **122**, 233901 (2019).

[75] Y. Luo, F.-F. Kong, X.-J. Tian, Y.-J. Yu, L. Zhang, G. Chen, Y. Zhang, Y. Zhang, and Z.-C. Dong, J. Chem. Phys. **154**, 044309 (2021).

[76] B. Doppagne, M. C. Chong, H. Bulou, A. Boeglin, F. Scheurer, and G. Schull, Science **361**, 251 (2018).

[77] V. Rai, L. Gerhard, Q. Sun, C. Holzer, T. Repän, M. Krstić, L. Yang, M. Wegener, C. Rockstuhl, and W. Wulfhekel, Nano Lett. **20**, 7600 (2020).

[78] Z.-C. Dong, X.-L. Guo, A. S. Trifonov, P. S. Dorozhkin, K. Miki, K. Kimura, S. Yokoyama, and S. Mashiko, Phys. Rev. Lett. **92**, 086801 (2004).

[79] Z. C. Dong, X. L. Zhang, H. Y. Gao, Y. Luo, C. Zhang, L. G. Chen, R. Zhang, X. Tao, Y. Zhang, J. L. Yang, and J. G. Hou, Nat. Photonics **4**, 50 (2010).

[80] P. Merino, C. Große, A. Rosławska, K. Kuhnke, and K. Kern, Nat. Commun. **6**, 8461 (2015).

[81] C. C. Leon, O. Gunnarsson, D. G. de Oteyza, A. Rosławska, P. Merino, A. Grewal, K. Kuhnke, and K. Kern, ACS Nano **14**, 4216 (2020).

[82] P. Merino, A. Rosławska, C. Große, C. C. Leon, K. Kuhnke, and K. Kern, Sci. Adv. 10.1126/sciadv.aap8349 (2018).

[83] K. Kuhnke, V. Turkowski, A. Kabakchiev, T. Lutz, T. S. Rahman, and K. Kern, ChemPhysChem **19**, 277 (2018).

[84] A. Rosławska, P. Merino, C. Große, C. C. Leon, O. Gunnarsson, M. Etzkorn, K. Kuhnke, and K. Kern, Nano Lett. **18**, 4001 (2018).

[85] A. Rosławska, P. Merino, C. C. Leon, A. Grewal, M. Etzkorn, K. Kuhnke, and K. Kern, Nano Lett. **21**, 4577 (2021).

[86] G. Reecht, F. Scheurer, V. Speisser, Y. J. Dappe, F. Mathevet, and G. Schull, Phys. Rev. Lett. **112**, 047403 (2014).

[87] M. C. Chong, G. Reecht, H. Bulou, A. Boeglin, F. Scheurer, F. Mathevet, and G. Schull, Phys. Rev. Lett. **116**, 036802 (2016).

[88] M. C. Chong, N. Afshar-Imani, F. Scheurer, C. Cardoso, A. Ferretti, D. Prezzi, and G. Schull, Nano Lett. **18**, 175 (2018).

[89] A. Gustafsson, M.-E. Pistol, L. Montelius, and L. Samuelson, J. Appl. Phys. **84**, 1715 (1998).

[90] F. Rossel, M. Pivetta, and W.-D. Schneider, Surf. Sci. Rep. **65**, 129 (2010).

[91] E. Dulkeith, A. C. Morteani, T. Niedereichholz, T. A. Klar, J. Feldmann, S. A. Levi, F. C. J. M. van Veggel, D. N. Reinhoudt, M. Möller, and D. I. Gittins, Phys. Rev. Lett. **89**, 203002 (2002).

[92] P. Anger, P. Bharadwaj, and L. Novotny, Phys. Rev. Lett. **96**, 113002 (2006).

[93] M. Barbry, P. Koval, F. Marchesin, R. Esteban, A. G. Borisov, J. Aizpurua, and D. Sánchez-Portal, Nano Lett. **15**, 3410 (2015).

[94] F. Benz, M. K. Schmidt, A. Dreismann, R. Chikkaraddy, Y. Zhang, A. Demetriadou, C. Carnegie, H. Ohadi, B. de Nijs, R. Esteban, J. Aizpurua, and J. J. Baumberg, Science 10.1126/science.aah5243 (2016).

[95] J. Lee, K. T. Crampton, N. Tallarida, and V. A. Apkarian, Nature **568**, 78 (2019).

[96] B. Yang, G. Chen, A. Ghafoor, Y. Zhang, Y. Zhang, Y. Zhang, Y. Luo, J. Yang, V. Sandoghdar, J. Aizpurua, Z. Dong, and J. G. Hou, Nat. Photonics **14**, 693 (2020).

[97] A. Rosławska, P. Merino, A. Grewal, C. C. Leon, K. Kuhnke, and K. Kern, Nano Lett. **21**, 7221 (2021).

[98] C. Bohren and D. Huffman, *Absorption and Scattering of Light by Small Particles* (Wiley, 1998).

[99] P. Johansson, R. Monreal, and P. Apell, Phys. Rev. B **42**, 9210 (1990).

[100] Y. Uehara, Y. Kimura, and S. U. Takeuchi, Jpn. J. Appl. Phys. **31**, 2465 (1992).

[101] P. Johansson, Phys. Rev. B **58**, 10823 (1998).

[102] R. H. Ritchie, Phys. Rev. **106**, 874 (1957).

[103] E. Kretschmann and H. Raether, Z. Naturforsch. A **23**, 2135 (1968).

[104] A. Otto, Z. Physik **216**, 398 (1968).

[105] W. L. Barnes, A. Dereux, and T. W. Ebbesen, Nature **424**, 824 (2003).

[106] R. W. Rendell, D. J. Scalapino, and B. Mühlschlegel, Phys. Rev. Lett. **41**, 1746 (1978).

[107] R. W. Rendell and D. J. Scalapino, Phys. Rev. B **24**, 3276 (1981).

[108] K. Meguro, K. Sakamoto, R. Arafune, M. Satoh, and S. Ushioda, Phys. Rev. B **65**, 165405 (2002).

[109] J. Aizpurua, G. Hoffmann, S. P. Apell, and R. Berndt, Phys. Rev. Lett. **89**, 156803 (2002).

[110] B. N. J. Persson and A. Baratoff, Phys. Rev. Lett. **68**, 3224 (1992).

[111] J. H. Coombs, J. K. Gimzewski, B. Reihl, J. K. Sass, and R. R. Schlittler, J. Microsc. **152**, 325 (1988).

[112] K. H. Gundlach, Solid-State Electronics **9**, 949 (1966).

[113] G. Binnig, K. H. Frank, H. Fuchs, N. Garcia, B. Reihl, H. Rohrer, F. Salvan, and A. R. Williams, Phys. Rev. Lett. **55**, 991 (1985).

[114] M. G. Blaber, M. D. Arnold, and M. J. Ford, J. Phys.: Condens. Matter **22**, 143201 (2010).

[115] C. Zhang, B. Gao, L. G. Chen, Q. S. Meng, H. Yang, R. Zhang, X. Tao, H. Y. Gao, Y. Liao, and Z. C. Dong, Rev. Sci. Instrum. **82**, 083101 (2011).

[116] R. Zhang, Y. Zhang, Z. C. Dong, S. Jiang, C. Zhang, L. G. Chen, L. Zhang, Y. Liao, J. Aizpurua, Y. Luo, J. L. Yang, and J. G. Hou, Nature **498**, 82 (2013).

[117] X.-J. Tian, F.-F. Kong, Y.-J. Yu, S.-H. Jing, X.-B. Zhang, Y. Liao, Y. Zhang, Y. Zhang, and Z.-C. Dong, Appl. Phys. Lett. **117**, 243301 (2020).

[118] Y. Uehara, A. Yagami, K. J. Ito, and S. Ushioda, Appl. Phys. Lett. **76**, 2487 (2000).

[119] K. J. Savage, M. M. Hawkeye, R. Esteban, A. G. Borisov, J. Aizpurua, and J. J. Baumberg, Nature **491**, 574 (2012).

[120] M. van Exter and A. Lagendijk, Phys. Rev. Lett. **60**, 49 (1988).

[121] B. Hecht, H. Bielefeldt, L. Novotny, Y. Inouye, and D. W. Pohl, Phys. Rev. Lett. **77**, 1889 (1996).

[122] J. Aizpurua, S. P. Apell, and R. Berndt, Phys. Rev. B **62**, 2065 (2000).

[123] B. Ren, G. Picardi, and B. Pettinger, Rev. Sci. Instrum. **75**, 837 (2004).

[124] B. Yang, E. Kazuma, Y. Yokota, and Y. Kim, J. Phys. Chem. C **122**, 16950 (2018).

[125] E. Ćavar, M.-C. Blüm, M. Pivetta, F. Patthey, M. Chergui, and W.-D. Schneider, Phys. Rev. Lett. **95**, 196102 (2005).

[126] L. Novotny and B. Hecht, *Principles of Nano-Optics*, 2nd ed. (Cambridge University Press, Cambridge, 2012).

[127] E. M. Purcell, H. C. Torrey, and R. V. Pound, Phys. Rev. **69**, 37 (1946).

[128] E. M. Purcell, Phys. Rev. **69**, 674 (1946).

[129] P. S. Vincett, E. M. Voigt, and K. E. Rieckhoff, J. Chem. Phys. **55**, 4131 (1971).

[130] É. V. Shpol'skiĭ, Sov. Phys. Usp. **3**, 372 (1960).

[131] T.-H. Huang, K. E. Rieckhoff, and E. M. Voigt, Chem. Phys. **36**, 423 (1979).

[132] G. N. Lewis and M. Kasha, J. Am. Chem. Soc. **66**, 2100 (1944).

[133] G. Baryshnikov, B. Minaev, and H. Ågren, Chem. Rev. **117**, 6500 (2017).

[134] B. Doppagne, M. C. Chong, E. Lorchat, S. Berciaud, M. Romeo, H. Bulou, A. Boeglin, F. Scheurer, and G. Schull, Phys. Rev. Lett. **118**, 127401 (2017).

[135] F.-F. Kong, X.-J. Tian, Y. Zhang, Y.-J. Yu, S.-H. Jing, Y. Zhang, G.-J. Tian, Y. Luo, J.-L. Yang, Z.-C. Dong, and J. G. Hou, Nat. Commun. **12**, 1280 (2021).

[136] G. Fischer, *Vibronic coupling: The interaction between the electronic and nuclear motions*, Theoretical chemistry (Academic Press, London, 1984).

[137] J. Franck and E. G. Dymond, Trans. Faraday Soc. **21**, 536 (1926).

[138] E. Condon, Phys. Rev. **28**, 1182 (1926).

[139] G. Herzberg and E. Teller, Z. Phys. Chem. **21B**, 410 (1933).

[140] P. W. Atkins and R. S. Friedman, *Molecular Quantum Mechanics*, fifth edition ed. (Oxford University Press, Oxford, New York, 2010).

[141] U. Fano, Nuovo Cim **12**, 154 (1935).

[142] J. Repp, G. Meyer, F. E. Olsson, and M. Persson, Science 10.1126/science.1099557 (2004).

[143] I. Swart, T. Sonnleitner, and J. Repp, Nano Lett. **11**, 1580 (2011).

[144] M. Imai-Imada, H. Imada, K. Miwa, J. Jung, T. K. Shimizu, M. Kawai, and Y. Kim, Phys. Rev. B **98**, 201403 (2018).

[145] T. Uemura, M. Furumoto, T. Nakano, M. Akai-Kasaya, A. Saito, M. Aono, and Y. Kuwahara, Chem. Phys. Lett. **448**, 232 (2007).

[146] T. Uemura, M. Akai-Kasaya, A. Saito, M. Aono, and Y. Kuwahara, Surf. Interface Anal. **40**, 1050 (2008).

[147] H. F. Hamann, M. Kuno, A. Gallagher, and D. J. Nesbitt, J. Chem. Phys. **114**, 8596 (2001).

[148] H. G. Frey, S. Witt, K. Felderer, and R. Guckenberger, Phys. Rev. Lett. **93**, 200801 (2004).

[149] A. Kinkhabwala, Z. Yu, S. Fan, Y. Avlasevich, K. Müllen, and W. E. Moerner, Nat. Photon. **3**, 654 (2009).

[150] H. Imada, M. Imai-Imada, K. Miwa, H. Yamane, T. Iwasa, Y. Tanaka, N. Toriumi, K. Kimura, N. Yokoshi, A. Muranaka, M. Uchiyama, T. Taketsugu, Y. K. Kato, H. Ishihara, and Y. Kim, Science **373**, 95 (2021).

[151] D. W. Pohl, W. Denk, and M. Lanz, Appl. Phys. Lett. **44**, 651 (1984).

[152] U. Dürig, D. W. Pohl, and F. Rohner, J. Appl. Phys. **59**, 3318 (1986).

[153] E. Betzig and R. J. Chichester, Science **262**, 1422 (1993).

[154] J. Michaelis, C. Hettich, J. Mlynek, and V. Sandoghdar, Nature **405**, 325 (2000).

[155] Y. Zhang, B. Yang, A. Ghafoor, Y. Zhang, Y.-F. Zhang, R.-P. Wang, J.-L. Yang, Y. Luo, Z.-C. Dong, and J. G. Hou, Natl. Sci. Rev. **6**, 1169 (2019).

[156] D. M. Eigler, C. P. Lutz, and W. E. Rudge, Nature **352**, 600 (1991).

[157] S.-W. Hla, J. Vac. Sci. Technol. B Microelectron. Nanometer Struct. Process. Meas. Phenom. **23**, 1351 (2005).

[158] S. Lyu, Y. Zhang, Y. Zhang, K. Chang, G. Zheng, and L. Wang, ArXiv211209554 Cond-Mat Physicsphysics (2021), arXiv:2112.09554 [cond-mat, physics:physics] .

[159] E. R. Menzel, K. E. Rieckhoff, and E. M. Voigt, J. Chem. Phys. **58**, 5726 (1973).

[160] W. Demtröder, *Laser Spectroscopy: Vol. 1 Basic Principles* (Springer, Berlin, Heidelberg, 2008).

[161] A. Jablonski, Nature **131**, 839 (1933).

[162] K. Kuhnke, A. Kabakchiev, W. Stiepany, F. Zinser, R. Vogelgesang, and K. Kern, Rev. Sci. Instrum. **81**, 113102 (2010).

[163] A. Kabakchiev, *Scanning Tunneling Luminescence of Pentacene Nanocrystals*, Ph.D. thesis, EPFL, Lausanne (2010).

[164] R. H. Brown and R. Twiss, Lond. Edinb. Dublin Philos. Mag. J. Sci. **45**, 663 (1954).

[165] R. H. Brown and R. Q. Twiss, Nature **177**, 27 (1956).

[166] R. Hanbury Brown and R. Q. Twiss, Nature **178**, 1046 (1956).

[167] R. H. Brown, R. Q. Twiss, and A. C. B. Lovell, Proceedings of the Royal Society of London. Series A. Mathematical and Physical Sciences **243**, 291 (1958).

[168] M. Fox, *Quantum Optics: An Introduction*, Oxford Master Series in Physics (Oxford University Press, Oxford, New York, 2006).

[169] T. Basché, W. E. Moerner, M. Orrit, and H. Talon, Phys. Rev. Lett. **69**, 1516 (1992).

[170] X. T. Zou and L. Mandel, Phys. Rev. A **41**, 475 (1990).

[171] C. C. Leon, A. Rosławska, A. Grewal, O. Gunnarsson, K. Kuhnke, and K. Kern, Sci. Adv. **5**, eaav4986 (2019).

[172] C. Kurtsiefer, S. Mayer, P. Zarda, and H. Weinfurter, Phys. Rev. Lett. **85**, 290 (2000).

[173] T. T. Tran, K. Bray, M. J. Ford, M. Toth, and I. Aharonovich, Nature Nanotechnology **11**, 37 (2016).

[174] X. Liu and M. C. Hersam, Nat Rev Mater **4**, 669 (2019).

[175] A. Rosławska, C. C. Leon, A. Grewal, P. Merino, K. Kuhnke, and K. Kern, ACS Nano **14**, 6366 (2020).

[176] A. M. Rosławska, *Dynamics of nanoscale systems probed by time-resolved STM-induced luminescence*, Ph.D. thesis, EPFL (2019).

[177] A. Nagashima, N. Tejima, Y. Gamou, T. Kawai, and C. Oshima, Phys. Rev. Lett. **75**, 3918 (1995).

[178] X. W. Tu, G. Mikaelian, and W. Ho, Phys. Rev. Lett. **100**, 126807 (2008).

[179] F. Seitz, *The modern theory of solids* (McGraw-Hill Book Co., New York; London, 1940).

[180] W. A. Harrison, *Solid state theory* (McGraw-Hill, New York, 1970).

[181] W. A. Harrison, *Elementary Electronic Structure* (WORLD SCIENTIFIC, Singapore, 1999).

[182] G. Grosso and G. Parravicini, *Solid state physics* (Academic Press, San Diego, 2000).

[183] A. M. Stoneham, *Theory of Defects in Solids: Electronic Structure of Defects in Insulators and Semiconductors* (Oxford University Press, Oxford, 2001).

[184] J. C. Slater and W. Shockley, Phys. Rev. **50**, 705 (1936).

[185] T. D. Clark and K. L. Kliewer, Phys. Lett. A **27**, 167 (1968).

[186] T. D. Clark, *A calculation of the electronic energy band structure of sodium chloride*, Ph.D. thesis, Iowa State University (1968).

[187] P. K. de Boer and R. A. de Groot, Phys. Lett. A **256**, 227 (1999).

[188] P. K. de Boer and R. A. de Groot, Am. J. Phy. **67**, 443 (1999).

[189] F. E. Olsson, M. Persson, J. Repp, and G. Meyer, Phys. Rev. B **71**, 075419 (2005).

[190] K. Glöckler, M. Sokolowski, A. Soukopp, and E. Umbach, Phys. Rev. B **54**, 7705 (1996).

[191] R. Bennewitz, A. S. Foster, L. N. Kantorovich, M. Bammerlin, C. Loppacher, S. Schär, M. Guggisberg, E. Meyer, and A. L. Shluger, Phys. Rev. B **62**, 2074 (2000).

[192] W. Hebenstreit, J. Redinger, Z. Horozova, M. Schmid, R. Podloucky, and P. Varga, Surf. Sci. **424**, 321 (1999).

[193] J. Repp, *Rastertunnelmikroskopie und -spektroskopie an Adsorbaten auf Metall- und Isolatoroberflächen*, Ph.D. thesis, Freie Universität Berlin (2002).

[194] K. Lauwaet, K. Schouteden, E. Janssens, C. V. Haesendonck, and P. Lievens, J. Phys.: Condens. Matter **24**, 475507 (2012).

[195] Z. Li, H.-Y. T. Chen, K. Schouteden, K. Lauwaet, E. Janssens, C. Van Haesendonck, G. Pacchioni, and P. Lievens, ACS Nano **9**, 5318 (2015).

[196] W. Chen, V. Madhavan, T. Jamneala, and M. F. Crommie, Phys. Rev. Lett. **80**, 1469 (1998).

[197] L. Diekhöner, M. A. Schneider, A. N. Baranov, V. S. Stepanyuk, P. Bruno, and K. Kern, Phys. Rev. Lett. **90**, 236801 (2003).

[198] J. Repp, G. Meyer, and K.-H. Rieder, Phys. Rev. Lett. **92**, 036803 (2004).

[199] F. E. Olsson and M. Persson, Surf. Sci. **540**, 172 (2003).

[200] C. C. Leon, A. Grewal, K. Kuhnke, K. Kern, and O. Gunnarsson, Nat. Commun. **13**, 981 (2022).

[201] K. Lauwaet, K. Schouteden, E. Janssens, C. Van Haesendonck, P. Lievens, M. I. Trioni, L. Giordano, and G. Pacchioni, Phys. Rev. B **85**, 245440 (2012).

[202] E. Madelung, Phys. Z. **19**, 524 (1918).

[203] C. Kittel, P. McEuen, and J. W. . Sons, *Introduction to solid state physics* (John Wiley & Sons, Limited, 2018).

[204] H.-Y. T. Chen and G. Pacchioni, PCCP **16**, 21838 (2014).

[205] C. E. Moore, *Ionization Potentials and Ionization Limits Derived from the Analyses of Optical Spectra* (National Bureau of Standards, 1970).

[206] P. Liljeroth, J. Repp, and G. Meyer, Science **317**, 1203 (2007).

[207] B. Doppagne, T. Neuman, R. Soria-Martinez, L. E. P. López, H. Bulou, M. Romeo, S. Berciaud, F. Scheurer, J. Aizpurua, and G. Schull, Nat. Nanotechnol. , 1 (2020).

[208] G. Blasse, G. J. Dirksen, and P. H. M. de Korte, Mater. Res. Bull. **16**, 991 (1981).

[209] Y. N. Zhuravlev and D. V. Korabel'nikov, Phys. Solid State **51**, 69 (2009).

[210] X. Tao, Z. C. Dong, J. L. Yang, Y. Luo, J. G. Hou, and J. Aizpurua, J. Chem. Phys. **130**, 084706 (2009).

[211] F. Aguilar-Galindo, M. Zapata-Herrera, S. Díaz-Tendero, J. Aizpurua, and A. G. Borisov, ACS Photonics **8**, 3495 (2021).

[212] A. Rosławska, T. Neuman, B. Doppagne, A. G. Borisov, M. Romeo, F. Scheurer, J. Aizpurua, and G. Schull, Phys. Rev. X **12**, 011012 (2022).

[213] J. V. Barth, H. Brune, G. Ertl, and R. J. Behm, Phys. Rev. B **42**, 9307 (1990).

[214] Atom tracking | Nanonis, `https://www.specs-group.com/nc/nanonis/products/detail/atom-tracking/` (2022), Last accessed: 09 Mar 2022.

[215] J. Repp, G. Meyer, S. Paavilainen, F. E. Olsson, and M. Persson, Phys. Rev. Lett. **95**, 225503 (2005).

[216] X.-H. Peng, S. Ganti, A. Alizadeh, P. Sharma, S. K. Kumar, and S. K. Nayak, Phys. Rev. B **74**, 035339 (2006).

[217] J. Doležal, P. Merino, J. Redondo, L. Ondič, A. Cahlík, and M. Švec, Nano Lett. **19**, 8605 (2019).

[218] J. Hölzl and F. K. Schulte, in *Solid Surface Physics*, Springer Tracts in Modern Physics (Springer, Berlin, Heidelberg, 1979) pp. 1–150.

[219] K. Miwa, H. Imada, M. Imai-Imada, K. Kimura, M. Galperin, and Y. Kim, Nano Lett. **19**, 2803 (2019).

[220] G. Schull, N. Néel, P. Johansson, and R. Berndt, Phys. Rev. Lett. **102**, 057401 (2009).

[221] H. Lüth, U. Roll, and S. Ewert, Phys. Rev. B **18**, 4241 (1978).

[222] U. Roll, S. Ewert, and H. Lüth, Chem. Phys. Lett. **58**, 91 (1978).

[223] P. K. Hansma, Phys. Rep. **30**, 145 (1977).

[224] P. Michler, A. Imamoğlu, M. D. Mason, P. J. Carson, G. F. Strouse, and S. K. Buratto, Nature **406**, 968 (2000).

[225] B. Doppagne, *Hyper-Resolved Fluorescence Microscopy with STM*, Ph.D. thesis, Université de Strasbourg (2020).

[226] T. C. Rosenow, K. Walzer, and K. Leo, J. Appl. Phys. **103**, 043105 (2008).

[227] J. H. Brannon and D. Magde, J. Am. Chem. Soc. **102**, 62 (1980).

[228] J. Simon, J.-J. André, J. M. Lehn, and C. W. Rees, *Molecular Semiconductors: Photoelectrical Properties and Solar Cells* (Springer, Berlin, Heidelberg, 1985).

[229] K. Kaiser, L. Gross, and F. Schulz, ACS Nano **13**, 6947 (2019).

[230] J. Doležal, P. Mutombo, D. Nachtigallová, P. Jelínek, P. Merino, and M. Švec, ACS Nano **14**, 8931 (2020).

[231] T.-H. Huang, K. E. Rieckhoff, E.-M. Voigt, and E. R. Menzel, Chem. Phys. **19**, 25 (1977).

[232] K. Kaneto, K. Yoshino, and Y. Inuishi, J. Phys. Soc. Jpn. **37**, 1297 (1974).

[233] K. Kaneto, Y. Ido, and K. Yoshino, J. Phys. Soc. Jpn. **38**, 1042 (1975).

[234] T.-H. Huang, K. E. Rieckhoff, and E.-M. Voigt, Can. J. Phys. **54**, 633 (1976).

[235] G. Schatz and M. Ratner, *Quantum mechanics in chemistry*, Dover books on chemistry (Dover Publications, Mineola, NY, 2002).

[236] R. Chikkaraddy, B. de Nijs, F. Benz, S. J. Barrow, O. A. Scherman, E. Rosta, A. Demetriadou, P. Fox, O. Hess, and J. J. Baumberg, Nature **535**, 127 (2016).

[237] T. Neuman, R. Esteban, D. Casanova, F. J. García-Vidal, and J. Aizpurua, Nano Lett. **18**, 2358 (2018).

[238] Y. Sun, N. C. Giebink, H. Kanno, B. Ma, M. E. Thompson, and S. R. Forrest, Nature **440**, 908 (2006).

[239] M. Garg and K. Kern, Science **367**, 411 (2020).

[240] IsoPlane Teledyne Princeton Instruments, `https://www.princetoninstruments.com/products/isoplane-family/isoplane` (2022), Last accessed: 17 Feb 2022.

[241] R. B. Jaculbia, H. Imada, K. Miwa, T. Iwasa, M. Takenaka, B. Yang, E. Kazuma, N. Hayazawa, T. Taketsugu, and Y. Kim, Nat. Nanotechnol. **15**, 105 (2020).

[242] A. C. Albrecht, J. Chem. Phys. **38**, 354 (1963).

[243] N. I. Nijegorodov and W. S. Downey, J. Phys. Chem. **98**, 5639 (1994).

[244] J. Stark, Ann. Phys. **348**, 965 (1914).

[245] W. E. Lamb and R. C. Retherford, Phys. Rev. **72**, 241 (1947).

[246] A. Babaze, R. Esteban, A. G. Borisov, and J. Aizpurua, Nano Lett. **21**, 8466 (2021).

[247] M. V. Rybin, S. F. Mingaleev, M. F. Limonov, and Y. S. Kivshar, Sci Rep **6**, 20599 (2016).

[248] E. E. Jelley, Nature **138**, 1009 (1936).

[249] G. Scheibe, Angew. Chem. **50**, 212 (1937).

[250] M. Kasha, Radiat. Res. **20**, 55 (1963).

[251] E. G. McRae and M. Kasha, J. Chem. Phys. **28**, 721 (1958).

[252] L.-L. Nian, Y. Wang, and J.-T. Lü, Nano Lett. **18**, 6826 (2018).

[253] H. Günther, *NMR spectroscopy: basic principles, concepts and applications in chemistry* (Wiley-VCH, 2013).

[254] J. Workman Jr. and L. Weyer, *Practical Guide to Interpretive Near-Infrared Spectroscopy* (CRC Press, Boca Raton, 2007).

[255] H. J. Butler, L. Ashton, B. Bird, G. Cinque, K. Curtis, J. Dorney, K. Esmonde-White, N. J. Fullwood, B. Gardner, P. L. Martin-Hirsch, M. J. Walsh, M. R. McAinsh, N. Stone, and F. L. Martin, Nat. Protoc. **11**, 664 (2016).

[256] J. R. Lakowicz, *Principles of fluorescence spectroscopy*, 3rd ed. (Springer US, Boston, MA, 2007).

[257] S. Duan, G. Tian, Y. Ji, J. Shao, Z. Dong, and Y. Luo, J. Am. Chem. Soc. **137**, 9515 (2015).

[258] P. Liu, D. V. Chulhai, and L. Jensen, ACS Nano **11**, 5094 (2017).

[259] S. L. McCall and P. M. Platzman, Phys. Rev. B **22**, 1660 (1980).

[260] B. N. J. Persson, Chem. Phys. Lett. **82**, 561 (1981).

[261] A. C. Albrecht and M. C. Hutley, J. Chem. Phys. **55**, 4438 (1971).

[262] F. Latorre, S. Kupfer, T. Bocklitz, D. Kinzel, S. Trautmann, S. Gräfe, and V. Deckert, Nanoscale **8**, 10229 (2016).

[263] M. G. Boyle, J. Mitra, and P. Dawson, Appl. Phys. Lett. **94**, 233118 (2009).

[264] P. W. Atkins and J. De Paula, *Atkins' Physical chemistry*, 8th ed. (Oxford University Press, Oxford ; New York, 2006).

[265] D.-D. Zhang, J.-L. Xu, and H.-B. Sun, Adv. Opt. Mater. **9**, 2001710 (2021).

[266] I. Aharonovich, D. Englund, and M. Toth, Nat. Photonics **10**, 631 (2016).

[267] C. Große, P. Merino, A. Rosławska, O. Gunnarsson, K. Kuhnke, and K. Kern, ACS Nano **11**, 1230 (2017).

[268] V. Kalmeyer and R. B. Laughlin, Phys. Rev. B **35**, 9805 (1987).

[269] W. I. F. David, R. M. Ibberson, J. C. Matthewman, K. Prassides, T. J. S. Dennis, J. P. Hare, H. W. Kroto, R. Taylor, and D. R. M. Walton, Nature **353**, 147 (1991).

[270] A. F. Hebard, R. C. Haddon, R. M. Fleming, and A. R. Kortan, Appl. Phys. Lett. **59**, 2109 (1991).

[271] B.-H. Kim, D. C. Kim, M.-h. Jang, J. Baek, D. Park, I.-S. Kang, Y. C. Park, S. Ahn, Y.-H. Cho, J. Kim, and S. Jeon, Adv. Mater. **28**, 1657 (2016).

[272] K. Ishii, J. Wada, and K. Murata, J. Phys. Chem. Lett. **11**, 9828 (2020).

[273] S. Manzeli, D. Ovchinnikov, D. Pasquier, O. V. Yazyev, and A. Kis, Nat. Rev. Materials **2**, 1 (2017).

[274] Z. Qiu, K. Vaklinova, P. Huang, M. Grzeszczyk, H. Yang, K. Watanabe, T. Taniguchi, K. S. Novoselov, J. Lu, and M. Koperski, arXiv:2110.07842 [cond-mat] (2021), arXiv:2110.07842 [cond-mat] .

[275] N. Ehlen, J. Hall, B. V. Senkovskiy, M. Hell, J. Li, A. Herman, D. Smirnov, A. Fedorov, V. Y. Voroshnin, G. D. Santo, L. Petaccia, T. Michely, and A. Grüneis, 2D Mater. **6**, 011006 (2018).

[276] W. Auwärter, Surf. Sci. Rep. **74**, 1 (2019).

[277] A. Ramasubramaniam, Phys. Rev. B **86**, 115409 (2012).

[278] T. Zhu, L. Yuan, Y. Zhao, M. Zhou, Y. Wan, J. Mei, and L. Huang, Sci. Adv. **4**, eaao3104 (2018).

[279] M. Feierabend, G. Berghäuser, A. Knorr, and E. Malic, Nat. Commun. **8**, 14776 (2017)

Acknowledgements

I want to extend my sincere gratitude to my teachers and colleagues at Max Planck Institute for Solid State Research, Universität Stuttgart, and the University of Delhi. En route to this dissertation, so many folks lent helping hands to pull me up and push me along.

I am grateful to my thesis advisor, Prof. Klaus Kern. Spending the past six years in Klaus' group has been truly formative. When I joined Klaus' group for the Master's thesis as a wildly uninformed student, I had no idea how fantastic a decision I had stumbled sideways into. Thank you for trusting my abilities before I believed in them myself and for giving me the independence to run with my ideas.

I want to thank the members of my thesis jury: Prof. Oleg Yazyev, Prof. Hugo Dil, Dr. Guillaume Schull, and Dr. Sebastian Stepanow, for their interest and for taking the time to evaluate my work and for their invaluable suggestions.

My supervisor, Dr. Klaus Kuhnke, has taught me to question my claims and keep true to the spirit that science is curiosity mixed with skepticism. I thank him for patiently guiding me through this journey and always entertaining my, at times, half-baked ideas. While I may never achieve his deep insight, I will try and keep patient and be true to that spirit.

I am grateful to Dr. Yousoo Kim and his group for welcoming me to SISL at RIKEN and, later, continuing to support me outside our scientific collaboration. I thank Dr. Hiroshi Imada, Dr. Miyabi Imai-Imada, Dr. Inhae Zoh, Dr. Kensuke Kimura, Dr. Rafael Jaculbia, and other members of SISL for letting me join in on their research work and for their hospitality and sharing the love for food during my stay in Wakō-shi. I would also like to thank Chikako Kuramochi for protecting me from the trying administrative aspects of my visit amidst a global pandemic.

I am forever thankful to Dr. Olle Gunnarsson for his interest and efforts in providing meaning to our experimental findings. Olle's contribution to the work presented in this thesis cannot be overstated. His deep insights and inquisitiveness birthed several projects related to our studies, which I hope we will continue to work on in the future.

I would also like to thank Assoc. Prof. Kuniyuki Miwa for providing theoretical support for single-molecule luminescence experiments and letting me pick his brain on various aspects of molecular emission processes. I thank Prof. Dimas de Oteyza for introducing me to the fascinating properties of Graphene nanoribbons and for fun during his research stay.

I thank Dr. Anna Rosławska, Dr. Christopher Leon, Prof. Markus Ternes, Dr. Rico Gutzler, Dr. Matthias Münks, Dr. Tomasz Michnowicz, Dr. Hiroshi Imada, and Dr. Yuqi Wang for teaching me many topics in scanning probe microscopy, molecular physics and optics, which majorly account for my interest in these areas.

I am thankful to Sabine Birtel and Birgit King for tackling on my behalf all bureaucratic aspects of my employment at MPI Stuttgart and my stay in Germany. I am also thankful to Wolfgang Stiepany, Peter Andler, Marko Memmler, Martin Siemers, Rafail Chaikevitch, and Isabel Wolf for providing their technical expertise to different experimental efforts in the lab. I will always be in awe of how they make everything run so smoothly.

I am happy to leave the *Photon-STM* in the capable hands of Dr. Liqing Zheng (and Mai). I am confident that the stream of beautiful insights and results will continue to flow.

Besides providing the perfect environment for experiments, the Precision Lab also enabled many scientific and worldly discussions (whether intended or not). I would like to thank Dr. Matthias Münks, Dr. Tomasz Michnowicz, Dr. Anna Rosławska, Dr. Shai Mangel, Dr. Jacob Senkpiel, Dr. Sven Szilagyi, Dr. Yuqi Wang, Dr. Christopher Leon, Dr. Manish Garg, Dr. Yang Luo, Dr. Alberto Martin Jiménez, Maximilian Uhl, Marcel Pristl, Tobias Wollandt, Dr. Haonan Huang, Dr. Sujoy Karan, Soroush Arabi, Moritz Edte, Aditya Desai, Dr. Pablo Merino, Jz-Yuan Juo, Dr. Robert Drost, Dr. Soon Jung Jung, Dr. Christian Ast, and many others for all the fun. Over the years at MPI, I have been lucky to befriend many of my colleagues. Besides the ones already mentioned, I would like to thank Dr. Alessio Scavuzzo, Dr. Piotr Kot, Lukas Powalla, Dr. Lukas Schlipf, Dr. Sebastian Koslowski, Dr. Domenico Paone, Janis Siebrecht, Maneesha Ismail, Dinesh Pinto, Dr. Luigi Malavolti, Dr. Kelvin Anggara, Dr. Hannah Ochner, Dr. Daniela Ţabrea, Camiel van Efferen, Dr. Christian Schön, Dr. Marko Burghard, and Dr. Aparajita Singha for always maintaining a great environment to work and for many outings in and outside of work.

On a personal note, I want to thank Anna, Tomasz, Sven, Alessio, Piotr, Lukas, Matthias, Moritz, Marcel, and other co-participants of the *Nalewka* meetings for good times outside the lab, and Sven (and Melanie) for helping shed the gains from those outings. Thanks for listening to all my rants without much judgment and for your guidance.

I also appreciate a whole cast of people who helped behind the scenes of the science. Outside of work, Lucas Penn, David Riobó Barba, Aisha Khalid, Peggy Stinson, Isooda Ajdari, Tanmay Goel, Mina Delfanazari, and many others kept me sane and grounded. I would like to collectively thank all my friends in Stuttgart, Tokyo, and Delhi for countless outings and for always being up for exploring food. I learned, and continue to learn, a great deal from each and every one of you. Thank you all for bearing with me.

I want to thank my long-time friend Abhinandan Dass who has shared his journey with me from the very beginning. Thanks for being the voice of reason during the toughest times.

I am grateful to Sylvia Butkiewicz for her support, guidance, and encouragement in personal and professional matters. She has pushed me to become a better version of myself (still debatable) and overcome countless challenges.

Last but not least, I would like to express my deepest gratitude to my parents and my family back in India. The thankless sacrifices you have made for me are too many to thank for individually. Thank you for believing in me no matter what path I choose. I would like to especially thank my sister, Chetna, and brother-in-law, Akshay, whose support assures me that I can work without any worry. I would like to take the opportunity to congratulate them on the birth of their newborn. I look forward to seeing you all soon.

Stuttgart, June 23, 2022 Abhishek Grewal

Curriculum Vitæ

Personal details

Abhishek Grewal
June 10, 1994, born in New Delhi, India

Education

2018–2022	**PhD Physics**
	École polytechnique fédérale de Lausanne, Lausanne, Switzerland
2015–2017	**MSc Physics**
	Univestiät Stuttgart, Stuttgart, Germany
2012–2015	**BSc (Hons) Physics**
	University of Delhi, New Delhi, India

Work experience

Since Jan. 2018	*Max-Planck-Insitut für Festkörperforschung*, Stuttgart, Germany
	Research associate, Nanoscale Science Department
Jan.–Aug. 2020	*RIKEN* (理化学研究所), Wakō-shi, Japan
	Visiting researcher, Surface and Interface Science Laboratory
Aug. 2016–Dec. 2017	*Max-Planck-Insitut für Festkörperforschung*, Stuttgart, Germany
	Research assistant, Nanoscale Science Department
Feb.–June 2016	*1. Physikalisches Institut, Univestiät Stuttgart*, Stuttgart, Germany
	Research assistant, Microwave Lab
Sep.–Dec. 2014	*University of Delhi*, New Delhi, India
	Research assistant, Associate Prof. Sukanta Dutta
Nov.–Dec. 2013	*Indian Institute of Technology*, Roorkee, India
	Internship, Insitute Instrumentation Centre

Publications

A. Grewal, C. C. Leon, O. Gunnarsson, K. Kuhnke, K. Kern. *Orbital engineering of single molecule luminescence*. (in preparation)

A. Grewal, H. Imada, K. Miwa, M.-I. Imada, K. Kimura, R. Jaculbia K. Kuhnke, K. Kern, Y. Kim. *Single molecule phosphorescence and intersystem crossing in a coupled exciton-plasmon system*. (in preparation)

A. Grewal, C. C. Leon, K. Kuhnke, K. Kern, O. Gunnarsson. *Character of gap states of molecules on surfaces*. (in preparation)

A. Grewal, C. C. Leon, K. Kuhnke, K. Kern, O. Gunnarsson. *Vacuum propagation of electrons in scanning tunneling microscopy*. (in preparation)

C. C. Leon*, A. Grewal*, K. Kuhnke, K. Kern, and O. Gunnarsson, *Anionic Character of the Conduction Band of Sodium Chloride*, Nat. Commun. **13**, 981 (2022).

A. Grewal, Y. Wang, M. Münks, K. Kern, and M. Ternes, *Local Stiffness and Work Function Variations of Hexagonal Boron Nitride on Cu(111)*, Beilstein J. Nanotechnol. **12**, 559 (2021).

A. Rosławska, P. Merino, A. Grewal, C. C. Leon, K. Kuhnke, and K. Kern, *Atomic-Scale Structural Fluctuations of a Plasmonic Cavity*, Nano Lett. **21**, 7221 (2021).

A. Rosławska, P. Merino, C. C. Leon, A. Grewal, M. Etzkorn, K. Kuhnke, and K. Kern, *Gigahertz Frame Rate Imaging of Charge-Injection Dynamics in a Molecular Light Source*, Nano Lett. **21**, 4577 (2021).

P. Merino, A. Rosławska, A. Grewal, C. C. Leon, C. Gonzalez, K. Kuhnke, and K. Kern, *Gold Chain Formation via Local Lifting of Surface Reconstruction by Hot Electron Injection on $H_2(D_2)$/Au(111)*, ACS Nano **14**, 15241 (2020).

A. Rosławska*, C. C. Leon*, A. Grewal, P. Merino, K. Kuhnke, and K. Kern, *Atomic-Scale Dynamics Probed by Photon Correlations*, ACS Nano **14**, 6366 (2020).

C. C. Leon, O. Gunnarsson, D. G. de Oteyza, A. Rosławska, P. Merino, A. Grewal, K. Kuhnke, and K. Kern, *Single Photon Emission from a Plasmonic Light Source Driven by a Local Field-Induced Coulomb Blockade*, ACS Nano **14**, 4216 (2020).

J. Lawrence, P. Brandimarte, A. Berdonces-Layunta, M. S. G. Mohammed, A. Grewal, C. C. Leon, D. Sánchez-Portal, and D. G. de Oteyza, *Probing the Magnetism of Topological End States in 5-Armchair Graphene Nanoribbons*, ACS Nano **14**, 4499 (2020).

C. C. Leon*, A. Rosławska*, A. Grewal, O. Gunnarsson, K. Kuhnke, and K. Kern, *Photon Superbunching from a Generic Tunnel Junction*, Sci. Adv. **5**, eaav4986 (2019).

P. Merino, A. Rosławska, C. C. Leon, A. Grewal, C. Große, C. González, K. Kuhnke, and K. Kern, *A Single Hydrogen Molecule as an Intensity Chopper in an Electrically Driven Plasmonic Nanocavity*, Nano Lett. **19**, 235 (2019).

*Equal contribution